

**RYDBERG-MEDIATED ATOMIC ENSEMBLE ENTANGLEMENT
AND HYPERFINE QUBIT DETECTION**

by

Minho Kwon

A dissertation submitted in partial fulfillment of
the requirements for the degree of

Doctor of Philosophy

(Physics)

at the

UNIVERSITY OF WISCONSIN–MADISON

2019

Date of final oral examination: 2019/04/17

The dissertation is approved by the following members of the Final Oral Committee:

Mark Saffman, Professor, Physics

Thad Walker, Professor, Physics

Deniz Yavuz, Professor, Physics

Mikhail Kats, Assistant Professor, Electrical and Computer Engineering

© Copyright by Minho Kwon 2019
All Rights Reserved

To my parents.

ACKNOWLEDGMENTS

The work presented in thesis would have been impossible without the contribution from many people.

First, I would like to thank my advisor, Mark Saffman, for his insightful guidance and patience throughout my doctoral study. I have learned numerous things from him and things his valuable advice made me become a better researcher. Mark balances himself extremely well between the role of a group leader and a physicist, and I have been emulating him so that I can be as productive and successful as him.

I would like to thank my co-advisor, Thad Walker, for sharing his enthusiasm and insights. His advice were critical ingredients to solve problems I encountered and to deepen my understanding on the underlying physics.

I thank Deniz Yavuz for kindly accepting my request to be on the committee and his early efforts on our experiments.

Now I want to thank my lab mates in Saffman group. Every one of them contributed in a unique way and I appreciate all of them. I appreciate Alex Gill's early efforts on the apparatus and many electronics he developed. Matt Ebert was a super grad student and I appreciate his integrated understanding of the experiment. Rb lab's productivity couldn't be maintained without Chris Young's enthusiasm and thrust. I appreciate Preston's detail-oriented work ethics. Also, thanks to Peiyu for helping me constructing the SHG and self-heterodyne system. Sebastian Malewicz, Brandon Radzom and Ben Kufel are excellent undergrads and I appreciate their contribution to making the high performing temperature-controlled box. Special thanks to Sebastian for making the Raspberry Pi camera

custom mount. I would like to thank our lab assistant Laura Fleming for her quick turn-around time, high standard, and kind consultation on technical matters. I had privilege to work with many stellar researchers, Larry Isenhower, Jonathan Pritchard, Tian Xia, Donald Booth, Yuan Sun, Trent Graham and Garrett Hickman. They made the lab significantly more enjoyable and productive. During the short overlap with Michael Gibbons, we shared the excitement when we saw frequency doubled light from the PPKTP crystal.

Also, it has been my great pleasure to work with friendly and knowledgeable fellow grad students: Martin Lichtman, Kara Maller, Alex Carr, James Hostetter, Josh Isaacs, Chris Yip, Xiaoyu Jiang, Juan Bohorquez and Cody Poole. I really enjoyed working with talented undergrad students : William Milner, Alphonse Marra, Huaxia Zhou, Liev Birman, Sydney Lybert.

Thanks to my office mate, Diptaranjan “Dipto” Das, for rejuvenating chats when we rest in the office.

To all support staffs in the Department of Physics. I would like to express my special gratitude to Ann Austin and Keeley Bannon, for their commitment and taking care of bureaucratic matters very nicely.

I was fortunate to have friends who can just listen and emotionally support me here at Madison: Youngjun Ahn, John Bbang, Junhyo Cho, Namsuk Cho, Yoonchul Choi, Jeyoon Jang, June Jeon, Kyeong-Jun Jeong, Jihye Kam, Bom Kim, Haein Kim, Junsung Kim, Sangjung Kim, Sunjung Kim, Suro Kim, Namhyo Kim, Nana Kim, Jeehyeon Lee, Jihye Lee, Kyubin Lee, Soomin Lee, Yujin Lee, Joohyun Park, Kyusic Park, Meenmo Kang, Sungho Yoon, Jung Young You.

Special thanks to Helena Seol, who made my life in Madison more meaningful. I would like to thank my Michigan Rydberg friend, Nithiwadee “Pound” Thaicharoen, for therapying advices beyond Rydberg.

There were people who inspired me to start this long journey. To Hui Deng and Paul Bierdz, for bootstrapping me and their kind support throughout my doctoral degree. To my lifelong friends Dongwon Kim and Dong Uk Choe in Korea. Warm welcome and encouragements from you guys were invaluable. I would like to thank my special EPM mate, Wooseung “Fkiller” Lee.

I cannot imagine where I would be without my family and their constant and unconditional support. My dad and mom deserve the most credit for any success I achieve. I thank my brother, Minsung Kwon, for his kind support and being with my parents while I am studying abroad. My grandmother and aunts believed in my potential and it empowered me to overcome any obstacles along this journey.

There are countless others that I can fill up the pages, but I must finish the rest of the thesis, so I will wrap up. I thank to the people of the United States, as this work is supported by National Science Foundation grant numbers PHY-1104531, PHY-1521374, and Air Force Office of Scientific Research Quantum Memories MURI. This collaborative [Overleaf](#) LaTeX platform has increased my writing productivity by an order of magnitude, and I appreciate their efforts.

Thank you all!

CONTENTS

Contents v

List of Tables xi

List of Figures xii

Abstract xviii

1	Motivation and Introduction	1
1.1	<i>Ensemble Quantum Computation</i>	2
1.2	<i>Ensemble Quantum Communication</i>	3
1.3	<i>Summary</i>	5
I Background and Theory		7
2	Rydberg Atoms	8
2.1	<i>Alkali atom Rydberg states</i>	8
2.2	<i>Rydberg atom wavefunctions</i>	9
2.3	<i>Dipole Matrix elements</i>	9
2.4	<i>Ground-Rydberg Rabi frequency including Hyperfine structure</i>	12
2.5	<i>Stark shifts</i>	13
2.6	<i>Dynamic Polarizability</i>	15
2.7	<i>Zeeman shifts</i>	17
3	Rydberg Interaction	21
3.1	<i>Dipole-Dipole interactions</i>	21
3.1.1	Long-range interaction	22
3.1.2	Short-range interaction	23
3.1.3	Even-shorter range interaction	23
3.2	<i>Rydberg blockade and Superatoms</i>	24

3.3	<i>Hamiltonian for Intra-Ensembles</i>	26
3.4	<i>Hamiltonian for Inter-Ensembles</i>	27
4	Quantum Optics	29
4.1	<i>Collective atom-light interaction</i>	29
4.1.1	Radiative eigenstate analysis	34
4.1.2	Directional photon emission	36
II	Experiment Setup	43
5	Cooling, trapping, optical pumping and manipulation of atoms	44
5.1	<i>Magneto Optical Trap</i>	45
5.1.1	2D MOT	45
5.1.2	UV Light Induced Atom Desorption	45
5.1.3	3D MOT	46
5.1.4	Cooling and Repumper lasers	47
5.2	<i>Red-detuned Optical Dipole Trap</i>	50
5.3	<i>Blue-detuned 1D Optical Lattice</i>	52
5.3.1	1D Lattice Design	53
5.4	<i>State preparation and coherent manipulation</i>	56
5.4.1	Clock state Optical Pumping	56
5.4.2	Global rotations with Microwave	56
5.4.3	Local qubit rotation with Raman Laser	59
5.4.4	Two-photon Rydberg excitation	60
6	Experiment system characterization	63
6.1	<i>Overview of single atom experiments</i>	63
6.2	<i>Single atom imaging</i>	65
6.2.1	Camera noise	69
6.2.2	Determination of region of interests	71
6.2.3	Dipole emission pattern	71

6.3	<i>Single-atom Rydberg Spectroscopy</i>	73
6.4	<i>Ground State Coherence</i>	73
6.5	<i>Rydberg Ramsey</i>	76
6.6	<i>Single atom Ground-Rydberg Rabi oscillation</i>	78
6.7	<i>Electromagnetic interference on Rydberg atoms</i>	79
6.7.1	External fields on 111d state	80
6.7.2	External fields on 97d state	81
7	Frequency doubling	84
7.1	<i>960/480 PPKTP doubling cavity</i>	87
7.1.1	Quasi-Phase matching	87
7.1.2	Enhancement cavity Design	87
7.1.3	Hansch-Couillaud Cavity stabilization	93
7.2	<i>1540/770 LBO doubling cavity</i>	93
7.2.1	Type-I Non-Critical Phase matching	96
7.2.2	Cavity Design	97
7.2.3	Pound-Drever-Hall Cavity stabilization	98
7.2.4	Optical setup	103
	III Ensemble Experiments and Calculations	107
8	Ensemble qubit preparation	108
8.1	<i>Collectively enhanced Rabi oscillation</i>	108
8.2	<i>Composite pulse</i>	110
8.3	<i>Ensemble composite pulse Rabi oscillation</i>	112
9	Collective spin dynamics of Ensemble qubit	114
9.1	<i>Microwave tomography as entanglement witness</i>	114
9.1.1	Separable state rotation	114
9.1.2	Singly excited state Rotation	117
9.2	<i>W-state Rotation</i>	119

9.3	<i>Coherence of ensemble qubit</i>	122
9.4	<i>Limitations</i>	124
10	Ensemble-Ensemble blockade	129
10.1	<i>Experiment Sequence</i>	129
10.2	<i>Experiment Results</i>	129
10.3	<i>Blockade leakage and Reverse blockade</i>	130
IV Single-atom Qubit Experiments		136
11	State-dependent fluorescence detection of Hyperfine Qubits	137
11.1	<i>Motivation</i>	137
11.2	<i>Experiment Procedure</i>	140
11.3	<i>Results</i>	144
11.4	<i>Discussion</i>	146
11.4.1	<i>Transient depumping</i>	147
11.4.2	<i>Solution to Transient depumping</i>	148
11.5	<i>Minimization of State-Mixing</i>	148
11.5.1	<i>Optimization of Light Polarization</i>	150
11.5.2	<i>Magnetic field optimization</i>	152
11.5.3	<i>Fictitious magnetic field from vector light shift</i>	153
11.5.4	<i>Excited manifold state mixing from Tensor light shift</i>	158
11.6	<i>Resonant and off-resonant scattering rates</i>	159
11.6.1	<i>Unpolarized illumination</i>	160
11.6.2	<i>Circularly-polarized illumination</i>	161
11.7	<i>Site-Selective Readout for Error Correction</i>	165
12	Automatic Alignment System	167
12.1	<i>Configuration</i>	168
12.1.1	<i>Motor control system</i>	168
12.1.2	<i>Image acquisition system</i>	171

12.1.3 Reimaging optical system	171
12.2 Alignment system characterization	172
12.2.1 Closed-loop Picomotor operation	174
12.2.2 Misalignment detection with cameras, 780 photons	175
12.2.3 Misalignment detection with atoms, 780 photons	176
12.2.4 Misalignment detection with cameras, 480 photons	180
12.2.5 Misalignment detection with atoms, 480 photons	181
12.3 Results	182
12.3.1 Relative pointing stability between 1064 and 780 beams	182
12.3.2 Pointing stability of 480 beam	185
12.4 Limitations	185
12.4.1 Too much friction on X-Y translation stage	185
12.4.2 Chromatic focal shift on confocal system	186
12.4.3 Temperature Correction	187
12.4.4 Notes on non-confocal imaging system	190
V Conclusion and Outlook	192
13 Conclusion	193
A Rydberg filtering cavity	196
B Cavity Lock monitors	199
B.1 <i>Transmission monitor</i>	199
B.1.1 Raspberry Pi Camera	200
B.1.2 Custom Mount	200
B.1.3 Setting up	202
B.2 <i>Frequency monitor</i>	202
C The Box	204
C.1 <i>Thermal control</i>	204
C.2 <i>EMI shielding</i>	204

D Laser characterization 208*D.1 Heterodyne measurements* 208*D.2 Self-heterodyne measurements* 210**E** Laser frequency chart 211**F** Home-made Teensy Temperature controller 214**References** 220

LIST OF TABLES

2.1 Scaling properties of Rydberg states	8
5.1 Optics for creating 770 lattice	53
7.1 960/480 Cavity Optics detail	91
7.2 Summary of numbers relevant to the performance of the 960/480 frequency doubler. PPKTP purchased from Raicol Crystals	92
7.3 Summary of performance of the 1540/770 frequency doubler at best working condition	96
7.4 1540/770 Cavity Optics detail	101
7.5 770 light source to fiber optical components	105
11.1 State selective readout results in the central site(#2) averaged over 2000 measurements	144
11.2 Loss-corrected detection fidelities for the other four shallower traps . .	144
12.1 Reimaging setup for 1064 FORT and 780 addressing beams	172
A.1 Purchased optics for filtering cavity setup	196
E.1 Summary of Laser and AOM frequencies in the current setup.	211
E.2 Calculated Rydberg two-photon resonance	213

LIST OF FIGURES

1.1	Diagram of Part III and IV	5
2.1	Radial wavefunctions of $nd_{5/2}$ Rydberg states of ^{87}Rb	10
2.2	Dynamic polarizability of ground state Rubidium atom and Rydberg state	17
2.3	Zeeman maps of Rydberg states, $97d_{5/2}$	20
3.1	Angular dependency of C_6 coefficients between two interacting $ 84D_{5/2}, m_j\rangle$ atoms	21
3.2	Energy level of atom-pair for different states	25
3.3	Single atom vs single super-atom	26
3.4	Geometry of our atoms and lasers for trapping and Rydberg excitation.	27
4.1	Level diagram and atom configuration	40
4.2	Cooperative emission from 10 atoms in 1-aim array	40
5.1	Main apparatus and the box	44
5.2	Square cell assembly. 2D-MOT and push beam.	46
5.3	Magneto-optically trapped atoms dependency to the presence of UV light	47
5.4	Time of Flight of Rb cloud	49
5.5	Expanding atomic cloud as a function of Time of Flight	49
5.6	3D MOT Loading versus 2D MOT detuning	50
5.7	Parametric heating experiment of 1038 nm ODT to identify trap frequencies	51
5.8	Dynamic polarizability of Ground state and Rydberg atoms	52
5.9	1D lattice imaged with Erich Urban's calibrated imaging system	54
5.10	Sliced intensity profile of the 770 lattice	54
5.11	Peak trap barrier versus optical power in the 770 1D Lattice beams.	55
5.12	Trap frequency and atomic density in 1D Lattice	55
5.13	Optical pumping versus depumping curve	57
5.14	Microwave setup	59

5.15 Global qubit rotations performed driven by a microwave pulse, showing driven coherence time of $\sim 10\text{ms}$	60
5.16 Rabi oscillation between clock states by Raman laser	61
5.17 Two-photon excitation scheme for D states	62
6.1 Optical train for addressing, ODT beams and imaging system	64
6.2 Generic experiment sequence for the new apparatus with hexagonal cell	66
6.3 Atom fluorescence with and without the repumping light	67
6.4 EMCCD Camera noise histograms	69
6.5 Fluorescence from individual atoms resolved by Independent Component Analysis	72
6.6 Two-photon Spectroscopy of Rydberg 111d states with and without dipole trap during excitation pulse	74
6.7 Two-photon Spectroscopy of Rydberg 84d states	75
6.8 Zeeman map of $ 97d_{5/2}, m_j = 5/2\rangle$	76
6.9 Ground Hyperfine Clock states coherence at different bias magnetic field.	77
6.10 Atom temperature and Ground Clock state coherence	77
6.11 Ground-Rydberg Ramsey experiment. $ 2, 0\rangle \leftrightarrow 84d_{3/2}, m_j = 3/2\rangle$, single atom. Data from 2018-09-05	78
6.12 Ground-Rydberg Rabi Oscillation 84d states	79
6.13 Dipole-allowed transitions from nd _{5/2} state and strong rf sources in the lab	80
6.14 Rabi flopping and two-photon spectroscopy of $ 2, 0\rangle \leftrightarrow 111d_{5/2}, m_j = 5/2\rangle$ transition, with and without near-resonant external field	81
6.15 Raman external cavity diode laser system with rf modulation input . .	82
6.16 Severely dephasing Rabi oscillations between $ 2, 0\rangle \leftrightarrow 97d_{5/2}, m_j = 5/2\rangle$ states due to external microwave source	83
7.1 PPKTP dimension, orientations and poled domains	88
7.2 Poling period and phase-matching temperature	88
7.3 Single pass PPKTP SHG	89
7.4 PPKTP doubling cavity. Tangential and Sagittal waist as a function of the curved mirror spacing, L_2	90

7.5	960/480 bow-tie ring cavity and input optical setup	90
7.6	Spatial beam profile of 480 nm from the crystal	92
7.7	480 nm spatial profile after collimated with f=100mm lens. Showing circular profile.	93
7.8	PPKTP Phase matching temperature versus 960 laser frequency	94
7.9	Bichromatic, doubly resonant scanning Fabry-Perot cavity setup to diagnose unstable 1540 DFB laser	95
7.10	Fiber-optical configuration of 1540 nm coherent light source.	95
7.11	LBO axis definition	97
7.12	LBO Type-I Non-Critical Phase Matching	98
7.13	LBO doubling cavity. Tangential and Sagittal waist as a function of the curved mirror spacing, L_2 . Chosen $L_2=6.6$ cm.	99
7.14	Bow-tie cavity for 1540/770 doubling cavity.	99
7.15	1540/770 SHG cavity output power versus input coupler transmission	100
7.16	Mechanical design of 1540/770 SHG LBO Cavity Assembly	100
7.17	Creating PDH error signal for 1540/770.	102
7.18	Cavity transmission of fundamental and PDH error signal.	103
7.19	Modified fast servo gain state for 1540/770 PDH lock	104
7.20	Thermal effects distorting the cavity transmission while ramping the cavity length	104
7.21	Wavelength-dependency of Photoacoustic absorption in LBO Crystal	105
7.22	Beam parameter product measurement of 770nm from SHG Cavity	105
7.23	Spatial beam profile of 770 nm from the cavity	106
8.1	Imhomogeneous collectively enhanced Rabi oscillations and Poissonian atom number distribution	109
8.2	Visualized qubit rotation with normal and composite pulse sequence, assuming 20% undershoot in the pulse area. Desired operation is to flip the qubit from the north pole to the south.	110
8.3	Calculated Ensemble Rydberg Rabi oscillations of with Poissonian atom number distribution	111

8.4	RF and electro-optical setup for composite pulse scheme	112
8.5	Comparison between normal and composite pulse on Single-atom Rydberg Rabi oscillation	113
8.6	Comparison between normal- and the composite-pulse driving collective Rabi oscillations between $ 2, 0\rangle$ and $ 111d_{5/2}, m_j = 5/2\rangle$	113
9.1	Microwave Tomography of the coherent spin state	116
9.2	Microwave Tomography of possible constituents of Atomic Fock state:Non-localized vs localized single excitation states	119
9.3	Probability of measuring 0 after rotating a state prepared by our W-state preparation pulses	120
9.4	Experiment sequence to measure coherence time using Ramsey style interferometer	122
9.5	Ramsey interference measurement of qubit coherence for oscillation as a function of the gap time	123
9.6	Atom number dependency of atomic ensembles in different entanglement class.	124
9.7	Evolution of tomographic signature of a state prepared with W-state protocol	125
9.8	Pair-state calculation of 97d97d	126
9.9	Pair-state calculation of 84d84d	127
10.1	Ensemble blockade experiment configuration and pulse sequences . .	130
10.2	Collective Rabi oscillations on Target site while switching the Control qubit on and off	131
10.3	Collective Rabi oscillations on Target site while switching the Control qubit on and off. Post-selected on successful Control Transfer.	132
10.4	Reduction of Control ensemble returning to $ 1, 0\rangle$ state, as a function of Target ensemble Rydberg pulse area.	133
10.5	Pair-state calculation of 97D97D, 90°	134
10.6	Pair-state calculation of 84D84D, 90°	135
10.7	Pair-state calculation of 111D111D, 90°	135

11.1 Experimental setup around hexagonal vacuum cell	141
11.2 Regions of interest and fluorescence statistics seen by EMCCD Camera	145
11.3 Probability of atom retention after non-destructive readout as a function of trap depth.	146
11.4 State dynamics during the state-selective readout	149
11.5 Growth of the probability of being depumped to the dark state ($F = 1$) for two different stretched Zeeman states	153
11.6 Larmor precession of $ 2, +2\rangle$ showing finite overlap to $ 2, +1\rangle$	156
11.7 Dependence of mean number of resonant photons per Raman photon on probe light parameters.	162
11.8 Proposed site-specific readout using shelving technique	166
12.1 Long-term alignment drift of two Rydberg beams at atom plane.	167
12.2 Top level view of the AAS system as of 2019-03-22	169
12.3 Optical setup of Automatic Alignment System	173
12.4 Confocal Setup. Propagation of gaussian beams from atom plane through the imaging system	174
12.5 Open-loop picomotor repeatability	175
12.6 Reimaged beams onto the CCD camera	176
12.7 Detecting beam misalignment with atoms	178
12.8 Horizontal position-dependent differential ac stark shift, and corresponding error signal	179
12.9 480 beam on EMCCD camera and centroid analysis	181
12.10AAS closed-loop 1C horizontal variation, temperature corrected	183
12.11AAS closed-loop 1C vertical variation, temperature corrected	183
12.12Histogram of misalignment for temperature ramping of the optical system.184	184
12.13Timeseries of misalignment for temperature ramping of the optical system184	184
12.14Qioptiq X-Y stage for beam positioning. Problematic interfaces are marked as red dashed rectangles.	186
12.15Closed-loop alignment versus temperature. Linear temperature correction188	188

12.16	Closed-loop alignment versus temperature. Quadratic temperature correction	189
12.17	Previous-generation non-confocal reimaging system	190
12.18	Non-confocal setup. Propagation of gaussian beams from atom plane through imaging system	191
A.1	Scanning FP transmission through 960 filtering cavity	197
A.2	Miniature vacuum assembly for hosting ~ 100 mm long filtering cavity	198
B.1	Spectral sensitivity of Raspberry Pi NoIR Camera	200
B.2	Assembled Raspberry Pi camera and the custom mount	201
B.3	Transmission through the reference cavity. Typically the input cavity coupling is optimize fundamental Gaussian mode.	202
C.1	Box enclosure and main apparatus seen from the side	205
C.2	Electrical and water connections.	206
C.3	Temperature stability of actively controlled box	207
C.4	RF attenuation of the box	207
D.1	Heterodyne setup	208
D.2	Beatnote between two Rydberg lasers, 780A and 780B while they are stabilized to the ULE reference cavity	209
D.3	Beatnote between two Rydberg lasers, 780A and 780B while they are stabilized to the ULE reference cavity, zoomed in	209
D.4	Self-Heterodyne setup. Credit :Peiyu Yang	210
F.1	Home-made TEC controller(Prototype) stabilizing the temperature of an acousto-optical modulator	214
F.2	Functional diagram of Temperature Controller	215
F.3	Teensy TEC controller PID tuning curves. Data from 2016-03-16	216
F.4	Performance of home-made Teensy TEC controller	217
F.5	Board layout of Teensy TEC controller	218
F.6	Schematic of Teensy TEC controller	219

ABSTRACT

This thesis reports progress towards using hyperfine-encoded neutral atomic ensembles for quantum information applications. Ensemble qubits are alternative building blocks to encode and process quantum information, while circumventing the challenges preparing a low-entropy qubit register with single-atom qubits. While ensemble approach inherits the single-atom quantum gate protocols, cooperative atom-light interaction makes it favorable platform to implement atom-photon interface, such as quantum memory.

We have demonstrated semi-deterministic preparation of W-state, which we use as an ensemble qubit. Observed 50-60% preparation fidelity shows discrepancy to expected $> 80\%$ fidelity taking account of known imperfections. We suspect Ground-Rydberg and Rydberg-Rydberg molecular interactions within the ensemble modify the dynamics. State tomography and Ramsey experiment clearly identified that the majority of constituents in an ensemble are indeed entangled. We report the first measurement of W-state coherence time as $T_2^* = 2.6$ ms for $\bar{N}=7.6$ atoms, which is long enough to perform ~ 2600 Rydberg-mediated quantum gate operations.

The first demonstration of Rydberg blockade between two ensembles happened in the same apparatus. We observe blockade fidelity of 0.89(uncorrected) and near-unity fidelity when post-selected on successful N=1 Fock state preparation of control ensemble. For weakly blockaded cases, Target ensemble remained as a perturber inhibiting Control ensemble from de-excitation. We discuss the efficacy of optical lattice insertion to suppress molecular interactions that might have been affecting the Rydberg dynamics. Directionality of cooperative emission from entangled

atoms in a four-wave mixing scheme is discussed.

High fidelity, parallel, low loss fluorescence detection of hyperfine ground state of rubidium atoms is presented. Enforced cycling transition scattering minimally alters the internal states. We achieve mean state detection fidelity of 97% (uncorrected) and 98.7% (SPAM error corrected), with atom loss rate < 2% and hyperfine-changing rate < 2%. This scalable technique is also compatible with ensemble qubits and error correcting schemes.

Technical developments on apparatus, lasers, supporting hardware and software are discussed. Automatic beam alignment system is implemented to correct long-term drift of tightly focused addressing beams. Achieved 1σ pointing stability of 60 nm between dipole traps and 780 addressing beam. Two home-made, high-performing, cavity-enhanced frequency doubling systems were constructed to meet experimental demand. We observe 960/480 system output as high as 180 mW with 600 mW fundamental, and 1540/770 system output as high as 13.97 W from 19 W fundamental.

1 MOTIVATION AND INTRODUCTION

Experiments with qubits encoded in hyperfine states of neutral atoms are active area of research as a route towards scalable quantum information processing[1]. One of the challenges that was only recently solved are deterministic preparation of atoms in array. Stochastic processes relying on collisions and dissipative dynamics[2–7] were typically employed, achieving sub-poissonian loading at limited extent. As an alternative, ensembles are suggested as building blocks[8, 9] to encode and process quantum information, as it is less challenging to prepare an array of ensembles. Ensemble uses a collection of identical, indistinguishable particles as constituents, where each particle has two-level internal state capable of storing quantum information. Ensemble qubit uses the total number of excitations among its constituents for encoding, typical choice being 0-excitation($\equiv |\bar{0}\rangle$) and 1-excitation($\equiv |\bar{1}\rangle$) forming a two-level system for a collection of particles, therefore a qubit. Single- and Two-qubit gate operations on ensemble qubits are possible with a twist on existing single-atom protocols.

DiVincenzo's criteria lists seven conditions that an experimental setup must meet to construct a quantum computer, five of which are for quantum computation, and the last two are for quantum communication.

1. Scalable physical system with well characterized qubit
2. Ability to initialize qubits
3. Long coherence relative to gate time

4. Universal set of quantum gates
5. Qubit-specific measurement capability
6. The ability to map stationary qubit to flying one, and vice versa
7. The ability to faithfully transmit flying qubits between specified locations

We split the criteria into two categories and check if ensembles can qualify for quantum computation (Section 1.1), and quantum memory (Section 1.2).

1.1 Ensemble Quantum Computation

Neutral atoms are known to be a scalable physical platform. Scalability of single neutral atom qubits become more evident from explosive demonstrations of the preparation and control of order tens of qubits in 1D[10], 2D[11–15] and 3D[16] optical tweezer array. Compared to the single-atom filling tasks, loading ensembles are less challenging as one has to simply overlap a cloud of cold atoms with optical tweezers for short period of time.

Single atom qubits are often initialized to hyperfine ground states, readily achieved by optical pumping. For our choice of atoms(⁸⁷Rb) and Ensemble qubit encoding scheme, initialization to 0-excitation state or $|\bar{0}\rangle$ uses same optical pumping technique. However, the other logical state $|\bar{1}\rangle$ is a maximally entangled state where single excitation is non-localized, often called W-state $|W\rangle$. This thesis reports progress towards semi-deterministic preparation of the state, thereby fulfilling the missing piece satisfying the criteria.

Coherence time of hyperfine-encoded single-atom qubits are demonstrated from ms to several seconds level[17], and typical gate time being $\sim 1\mu s$, thus meeting the criteria. Ensemble qubits have additional dephasing mechanisms due to collisions, but compared to GHZ-coded states where spectral(phase) sensitivity is enhanced, W-state encoded qubits have same sensitivity as single atom. This thesis presents experimental measurement of W-state ensemble qubit, showing long enough coherence time to operate a few thousands of Rydberg-mediated gates.

Regarding the last criteria, qubit specific detection, there are proposed schemes for single-atoms by shelving to metastable states, using spin-dependent force, and more. In this thesis, we present demonstration of hyperfine conserving, parallel, low loss detection of single-atom hyperfine qubits. This technique is compatible with ensemble qubit detection. Site-specific readout is also possible but with at some overheads requiring coherent state manipulation.

1.2 Ensemble Quantum Communication

The last two divincenzo's criteria requires physical system to be capable of quantum communication, an ability to efficiently transfer qubit from one place to another. This is critical step to interconnect quantum computers which are otherwise isolated, incapable of sharing locally computed results and ultimately limiting the scalability. Single photons are excellent flying qubits but exponential loss in fiber optics or free-space eventually limits the communicable range, which an optical amplifier cannot extend due to No-cloning theorem[18]. However, quantum re-

peaters can take the role of optical amplifier as a mean of extending the range of entanglement distribution. Quantum repeaters can firstly create entanglement between short elementary links, then swap the entanglements between the other neighboring links sequentially all the way to the destination [19]. One critical ingredient is a quantum memory to store the photonic qubit for intermediary operations e.g. entanglement swapping. Atomic ensemble become attractive platform as the heralded atom-photon entanglement can be generated by DLCZ[19, 20] protocol and Raman memory. Although Raman memory[21, 22] and Electromagnetically Induced Transparency(EIT) based memory [23] have shown high fidelity and collection efficiency[24], coherence time is usually on the order of μs , limited by atomic coherence. Furthermore, probabilistic nature of spontaneous emission significantly limits the entanglement generation rate. Deterministic generation of atom-photon entanglement with cold atomic ensembles were proposed[25, 26], and experimentally demonstrated[27] using collectively enhanced emission and Rydberg blockade. Entangling single atom qubit to an ensemble qubit can allow fast and highly efficient readout possible owing to interference between quantum emitters, proposed by[28], which has not been demonstrated. Collective quantum emitter containing single excitation can emit a photon with modified emission pattern, and can be engineered to be highly directional[29–31]. Moreover, additional degree of freedom[32–34] can potentially extend a channel capacity. Inspired by the proposals[35–37]and advances in the field, we focus on experimental realization of quantum memory and quantum repeater based on atomic ensembles, and discuss the remaining challenges.

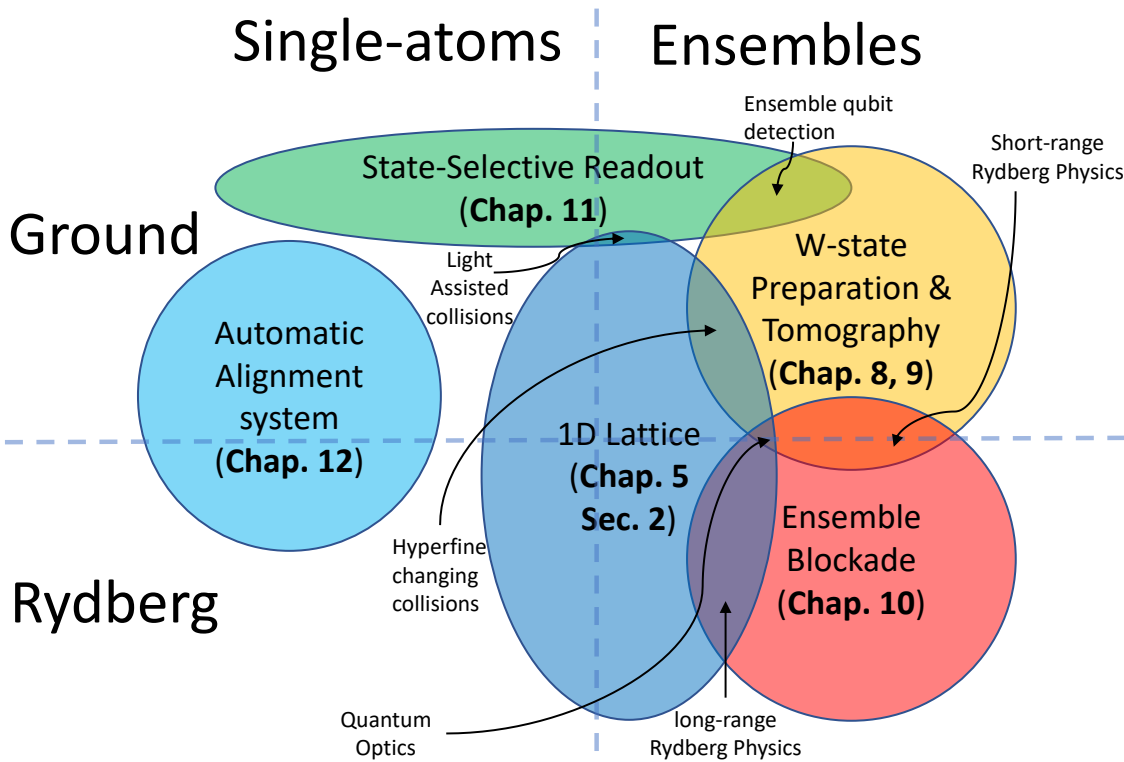


Figure 1.1: Diagram of Part III and IV

1.3 Summary

Part I illustrates key physics related to this work, ranging from Single Rydberg atom physics in Chapter 2, Rydberg pair interactions in chapter 3, and Quantum optics using Rydberg atoms in chapter 4. Part II shows important characterization results from upgraded apparatus. Part III contains main experiments of our ensemble preparation in Chapter 8, ensemble coherence and spin dynamics in Chapter 9 and ensemble blockade in Chapter 10.

Part IV has single-atom qubit experiments from upgraded apparatus. Chapter 11 discusses parallel, low-loss detection of hyperfine qubits. Chapter 12 has automatic

alignment system. Grand conclusion and future outlook is on Part **V**.

Part I

Background and Theory

2 RYDBERG ATOMS

2.1 Alkali atom Rydberg states

Binding energy of the Rydberg electron in Alkali atoms can be written as

$$E = -\frac{\text{Ry}}{(n^*)^2} \quad (2.1)$$

where Ry is the Rydberg constant, $n^* = (n - \delta_{n,l,j})$ is effective principal quantum and quantum defects. Quantum defects are empirically determined from spectropic measurements and can be written as

$$\delta_{nlj} = \delta_0 + \frac{\delta_2}{(n - \delta_0)^2} + \frac{\delta_4}{(n - \delta_0)^4} + \dots \quad (2.2)$$

where $\delta_0, \delta_2, \dots$ are dependent upon l and j .

Table 2.1: Scaling properties of Rydberg states

Property	Scaling
Binding energy	n^{-2}
Orbital radius	n^2
Energy level splitting	n^{-3}
Radiative lifetime	n^3
Polarizability	n^7
Rabi frequency	$n^{-3/2}$

2.2 Rydberg atom wavefunctions

The wavefunction for the valence electron is described by Schrodinger equation, given in atomic units (a.u.) as

$$\left[-\frac{1}{2\mu} \nabla^2 + V(r) \right] \psi(r, \theta, \phi) = U\psi(r, \theta, \phi) \quad (2.3)$$

where μ is the reduced mass of the electron, r is the radial coordinate and $V(r)$ is the core potential. Since $V(r)$ has no angular dependence, the wavefunction is separable, giving $\psi(r, \theta, \phi) = R(r)Y_l^{m_l}(\theta, \phi)$, where $Y_l^{m_l}(\theta, \phi)$ is a spherical harmonic dependent upon the orbital angular momentum l of the Rydberg state. Inserting this into Equation 2.3 gives the equation for the radical wavefunction of the electron

$$\left[-\frac{1}{2\mu} \left(\frac{d^2}{dr^2} + \frac{2}{r} \frac{d}{dr} \right) + \frac{l(l+1)}{2\mu r^2} + V(r) \right] R(r) = UR(r) \quad (2.4)$$

2.3 Dipole Matrix elements

Transitions between atomic states primarily occur due to coupling with the electric dipole moment $\mu = er$ of the valence electron, which is a factor of $(\alpha/2)^2$ stronger than the magnetic dipole coupling[39]. The strength of the coupling between states $|nlm_l\rangle$ and $|n'l'm'_l\rangle$ is given by the dipole matrix element $\langle nlm_l | \mu | n'l'm'_l \rangle$, which is dependent upon the overlap of the wavefunctions with the electric dipole moment. From knowledge of the dipole matrix elements, it is possible to calculate transition probabilities, radiative lifetimes and many other properties of the atomic states[40].

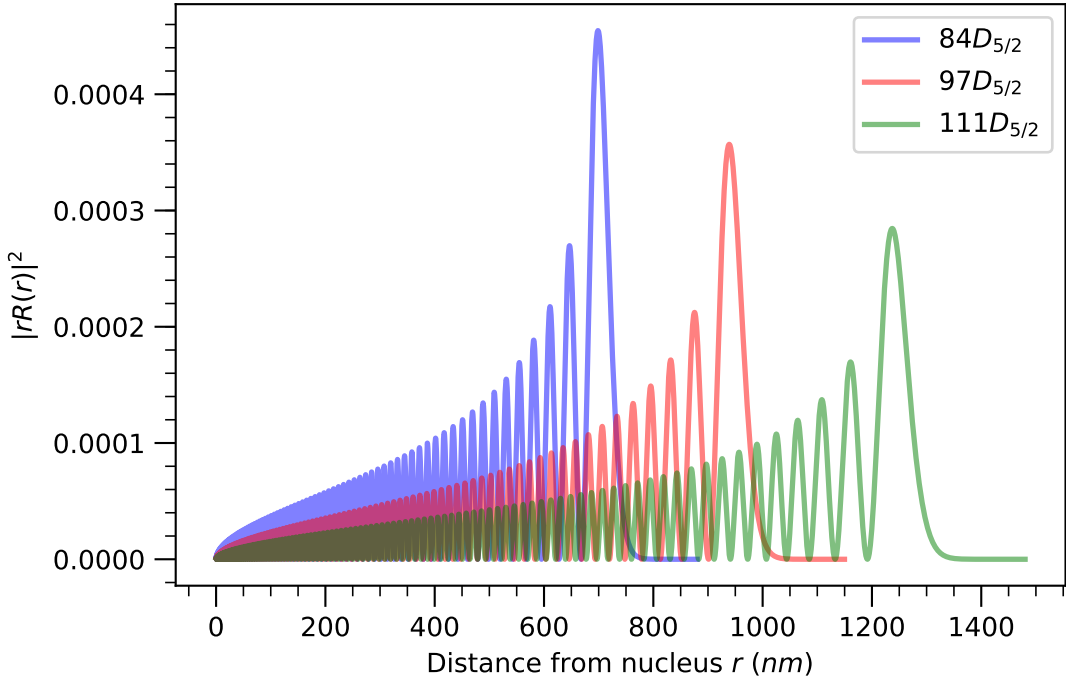


Figure 2.1: Radial wavefunctions of $nD_{5/2}$ Rydberg states of ^{87}Rb , using [38]

The dipole operator is $\mu = er \cdot \hat{\mathbf{e}}$, where $\hat{\mathbf{e}}$ is the electric field polarization unit vector. Transforming into the spherical basis, the dipole operator can be decomposed into the operators μ_q , with $q \in \{-1, 0, +1\}$ corresponding to $\{\sigma^+, \pi, \sigma^-\}$ transitions, given by

$$\begin{aligned} \mu_{-1} &= 1/\sqrt{2} (\mu_x - i\mu_y) \\ \mu_0 &= \mu_z \\ \mu_1 &= 1/\sqrt{2} (\mu_x + i\mu_y) \end{aligned} \tag{2.5}$$

These operators are related to the spherical harmonics by $\mu_q = er \sqrt{4\pi/3} Y_1^q(\theta, \phi)$, which form a set of rank-1 irreducible tensors. As a result of Wigner-Eckart the-

orem can be used to separate dipole matrix element into an angular coupling and a reduced matrix element $\langle l||er||l' \rangle$ which depends only on l and the radial wavefunction

$$\langle nlm_l | \mu_q | n'l'm'_l \rangle = (-1)^{l-m_l} \begin{pmatrix} l & 1 & l' \\ -m_l & q & m'_l \end{pmatrix} \langle l || \mu || l' \rangle \quad (2.6)$$

where the brackets denote the Wigner-3j symbol. Using the properties of the Wigner-3j symbol, the selection rules of the electric dipole can be derived as

$$\langle l || \mu || l' \rangle = (-1)^{-1} \sqrt{(2l+1)(2l'+1)} \begin{pmatrix} l & 1 & l' \\ 0 & 0 & 0 \end{pmatrix} \langle nl | er | n'l' \rangle \quad (2.7)$$

where the radial matrix elements $\langle nl | er | n'l' \rangle$ represent the overlap integral between the radial wavefunctions and the dipole moment

$$\langle nl | er | n'l' \rangle = \int_{r_i}^{r_o} R_{n,l}(r) er R_{n,l'}(r) r^2 dr \quad (2.8)$$

where r_i and r_o are inner and outer radii of integration. Spin-orbit interaction further breaks degeneracy of the l states, which split according to $j = l + s$. As the electric field only couples to the orbital angular momentum(l) of the electron, it is necessary to transform from the fine-structure basis into the uncoupled basis to evaluate the dipole matrix elements. Using the Wigner-Eckart theorem, the matrix element can be expressed in terms of the reduced matrix element $\langle j || \mu || j' \rangle$, related

to the other expression as

$$\langle j || \mu || j' \rangle = (-1)^{l+s+j'+1} \delta_{s,s'} \sqrt{(2j+1)(2j'+1)} \left\{ \begin{array}{ccc} j & 1 & j' \\ l' & s & l \end{array} \right\} \langle l || \mu || l' \rangle \quad (2.9)$$

where $\{\dots\}$ denote a Wigner-6j symbol. Combining these equations, the dipole matrix element in the fine-structure basis is

$$\begin{aligned} \langle nljm_j | \mu_q | n'l'j'm'_j \rangle &= (-1)^{j-m_j+s+j'+1} \sqrt{(2j+1)(2j'+1)(2l+1)(2l'+1)} \\ &\times \left\{ \begin{array}{ccc} j & 1 & j' \\ l' & s & l \end{array} \right\} \left(\begin{array}{ccc} j & 1 & j' \\ -m_j & q & m'_j \end{array} \right) \left(\begin{array}{ccc} l & 1 & l' \\ 0 & 0 & 0 \end{array} \right) \langle nlj' | er | n'l'j' \rangle \end{aligned} \quad (2.10)$$

Expectation value of $\langle r^k \rangle$ can be numerically integrated, or analytically obtained from Krammers recursion relations. A few interesting cases are $k = -1, 1$, and 2 .

2.4 Ground-Rydberg Rabi frequency including Hyperfine structure

We wish to calculate two-photon Rabi frequency that couples ground state in hyperfine basis $|f_g, m_f\rangle$ to Rydberg state in fine structure basis $|n, l, j, m_j\rangle$.

$$\begin{aligned} \Omega_{f_g, m_g}^{j, m_j} &= \sum_{f_r, m_r} = C_{jm_j Im_I}^{f_r m_r} \Omega_{f_g, m_g}^{f_r, m_r} \\ &= \Omega_{common} \sum_{f_r} C_{jm_j Im_I}^{f_r, m_g + q_1 + q_2} \tilde{\Omega}_{f_g, m_g}^{f_r, m_g + q_1 + q_2} \end{aligned} \quad (2.11)$$

where

$$\begin{aligned}\Omega_{common} &= \frac{\varepsilon_1 \varepsilon_2 \langle n_r L_r S J_r || r || n_p L_p S J_p \rangle \langle n_p L_p S J_p || r || n_g L_g S J_g \rangle}{2\hbar^2 \Delta_1} \\ \tilde{\Omega}_{f_g, m_g}^{f_r, m_g + q_1 + q_2} &= \sum_{f_p} c_{Ij_g f_g}^{j_p f_p} c_{Ij_p f_p}^{j_r f_r} C_{f_p, m_g + q_1, 1, q_2}^{f_r, m_g + q_1 + q_2} C_{f_g, m_g, 1, q_1}^{f_p, m_g + q_1} \frac{\Delta_1}{\Delta_1 - \Delta_{fp}}\end{aligned}\quad (2.12)$$

where $C_{...}^{...}$ is a Clebsch-Gordan coefficient and

$$c_{Ij_f}^{j', f'} = (-1)^{1+I+f+j'} \sqrt{2f+1} \left\{ \begin{array}{ccc} j & 1 & f \\ f' & 1 & j' \end{array} \right\} \quad (2.13)$$

and a one-photon detuning from the center of mass of the p state

$$\begin{aligned}\Delta_1 &= \omega_1 - \omega_{pg} \\ \Delta_{fp} &= \omega_{fp} - \omega_p = 2\pi \times \frac{A}{2} [f_p(f_p + 1) - I(I + 1) - j_p(j_p + 1)]\end{aligned}\quad (2.14)$$

We consider exciting $nd_{5/2}$ state via $5p_{3/2}$ state.

2.5 Stark shifts

When two-level system with energies E_1 and E_2 is being coupled with the coupling strength Ω , Hamiltonian of the modified system is

$$\begin{bmatrix} E_1 & \Omega \\ \Omega^* & E_2 \end{bmatrix}\quad (2.15)$$

where diagonalization gives new eigen-energies

$$\lambda_{\pm} = \frac{(E_1 + E_2) \pm \sqrt{(E_1 - E_2)^2 + 4\Omega^2}}{2} \quad (2.16)$$

In case of Electric dipole-allowed(E1) atomic transition separated by $E_2 - E_1 = \hbar\omega_0$ coupled with a vector optical field $E = (\varepsilon(\mathbf{r}, t)/2) e^{-i\omega t} + (\varepsilon^*(\mathbf{r}, t)/2) e^{i\omega t}$, Hamiltonian of the system is

$$\begin{aligned} H_a &= U_g |g\rangle \langle g| + U_e |e\rangle \langle e| \\ H_{E1} &= -\hat{d} \cdot \mathbf{E} \end{aligned} \quad (2.17)$$

where \hat{d} is dipole operator and in this case $\hat{d} = d_{eg} |e\rangle \langle g| + d_{eg}^* |g\rangle \langle e|$, where $d_{eg} = \langle e | \hat{d} | g \rangle$ is dipole matrix element. If the detuning $\delta = \omega - \omega_{eg}$ is small and applicable for rotating wave approximation, the rapidly oscillating terms are neglected. This generates effective atom-field Hamiltonian with reduced effective Rabi frequency.

$$H_{dressed} = \hbar \begin{bmatrix} \delta & \Omega/2 \\ \Omega/2 & 0 \end{bmatrix} \quad (2.18)$$

with eigen-energies of $\lambda_{\pm} = \hbar/2 (\delta \pm \sqrt{\delta^2 + \Omega^2})$. For Electric dipole(E1) matrix element vanishing atomic transitions, it might still be driven with higher order couplings, if magnetic dipole(M1) or electric quadrupole(E2) matrix have non-zero matrix elements. Similar treatment can be done for M1 transition, but now atom will be coupled to the magnetic part(B), instead of electric field(E). With oscillating

magnetic field, interaction Hamiltonian is then

$$H_{M1} = -\hat{\mu} \cdot \mathbf{B} \quad (2.19)$$

where $\hat{\mu}$ is magnetic dipole operator.

2.6 Dynamic Polarizability

Interaction of bound electron with an external oscillating field can shift the energy levels. Using the 2nd order perturbation theory the scalar, vector and tensor dynamic polarizabilities in fine structure basis are

$$\begin{aligned} \alpha_0(\omega) &= \frac{2e^2}{3\hbar(2j_a + 1)} \sum_{n_b, j_b} \frac{\omega_{ba}}{\omega_{ba}^2 - \omega^2} |\langle n_b j_b | \hat{r} | n_a j_a \rangle|^2 \\ \alpha_1(\omega) &= -\frac{e^2}{\hbar} \left[\frac{6}{(2j_a + 1)(j_a + 1)j_a} \right]^{1/2} \sum_{n_b, j_b} (-1)^{j_a + j_b} S_{1j_a 1}^{j_a 1 j_b} \frac{\omega}{\omega_{ba}^2 - \omega^2} |\langle n_b j_b | \hat{r} | n_a j_a \rangle|^2 \\ \alpha_2(\omega) &= \frac{e^2}{\hbar} \left[\frac{40(2j_a - 1)j_a}{3(2j_a + 3)(2j_a + 1)(j_a + 1)} \right]^{1/2} \sum_{n_b, j_b} (-1)^{j_a + j_b} S_{1j_a 1}^{j_a 1 j_b} \frac{\omega}{\omega_{ba}^2 - \omega^2} |\langle n_b j_b | \hat{r} | n_a j_a \rangle|^2 \end{aligned} \quad (2.20)$$

Dynamic polarizability of loosely bounded electrons in Rydberg atoms can be described by ponderomotive interaction thereby being

$$\alpha_{Ry} = -\frac{e^2}{m_e \omega^2} \quad (2.21)$$

and ponderomotive energy shift

$$U = -\frac{1}{4}\alpha_{cgs}|\varepsilon|^2 \quad (2.22)$$

where m_e is mass of electron, ω is angular frequency of oscillating electric field, and ε is an amplitude of electric field in cgs unit.

Polarizability of ground state atoms due to far-off resonant trap(FORT) can have simpler form due to large detuning from D1 and D2 lines. ac stark shifts can take approximate form $U \sim \frac{I}{\Delta_{eff}}$, where Δ_{eff} is effective detuning from the alkali doublets, and valid approximation for $\Delta_{fs} \ll \Delta_{eff}$. Then differential ac stark shift for average trap depth U for upper and lower hyperfine levels can be approximated as

$$\delta_{1064} \sim U \left(\frac{1}{1 + \frac{\Delta_{fs}}{2\Delta_{eff}}} - \frac{1}{1 - \frac{\Delta_{fs}}{2\Delta_{eff}}} \right). \quad (2.23)$$

valid where $\Delta_{fs} \ll \Delta_{eff} \ll \Delta_{eff}$. Even more simplified form that is only proportional to the ratio between $\eta = \Delta_{fs}/\Delta_{eff}$ is

$$\delta_{1064} \sim -\eta U \quad (2.24)$$

With typical experimental parameters $U = k_B \times -1\text{mK}$, $\Delta_{fs} = 2\pi \times 6.834 \text{ GHz}$, $\Delta_{eff} = 2\pi \times -102.47 \text{ THz}$, $\eta = -1/14994$ and we obtain

$$\delta_{1064,1mK}/(2\pi\hbar) = - \left(\frac{1}{-14994} \right) \times (-20.8\text{MHz}) = -1.39\text{kHz} \quad (2.25)$$

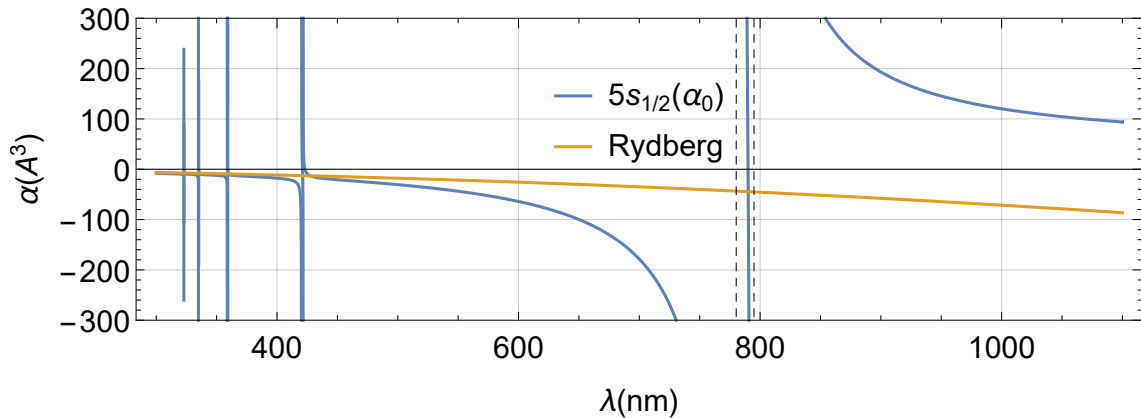


Figure 2.2: Dynamic polarizability of ground state Rubidium atom and Rydberg state in 300-1100 nm range

Due to uneven diffraction efficiency of our FORT diffractive optical element, traps have slightly different depth. This generates site-dependent shifts that is comparable to Microwave Rabi frequency $\Omega_{MW} \sim 2\pi \times 3\text{kHz}$. Therefore, we lower the trap depth to reduce inhomogeneous lineshifts. Magnetic field is uniform in the scale of our interest.

2.7 Zeeman shifts

Rydberg Zeeman shift consists paramagnetic term, giving linear shifts, and diamagnetic term, which gives quadratic shifts thereby more pronounced at high-B and high-principal number. We typically operate at weak field (a few gauss) where diamagnetic contribution can be neglected. In fine-structure basis, Zeeman interaction is merely $H_B = \mu_B g_J m_J B$ where g_J is g-factor for Rydberg electron, B is bias

magnetic field. As a guidance, Hamiltonian including Diamagnetic term reads

$$\hat{H}_m = \frac{\mu_B}{\hbar} \left(g_L \hat{\mathbf{L}} \cdot \mathbf{B} + g_S \hat{\mathbf{S}} \cdot \mathbf{B} \right) + \frac{e^2}{2m} \mathbf{A} \cdot \mathbf{A} \quad (2.26)$$

with the replacement $\mathbf{A} = \frac{1}{2}(\hat{\mathbf{B}} \times \hat{\mathbf{r}})$ and the quantization axis set by the magnetic field $\mathbf{B} = B\mathbf{e}_z$,

$$\hat{H}_m = \frac{\mu_B}{\hbar} \left(g_L \hat{\mathbf{L}}_z B + g_S \hat{\mathbf{S}}_z \cdot \mathbf{B} \right) + \frac{2\mu_B^2}{a_0^2 E_H} \frac{(\rho^2 B^2)}{8} \quad (2.27)$$

where $\rho^2 = r^2 \sin^2 \theta$. Transition from linear to non-linear shift happens with the field strength roughly at

$$B \sim 2n^{-4} \quad (2.28)$$

The latter term gives nonlinear shift and couples $\Delta l = 0, \pm 2$ states. Matrix elements for diamagnetic term reads[41]

$$\begin{aligned} & \langle n' l' m'_l | \hat{H}_D | n l m_l \rangle \\ &= \frac{2\mu_B^2}{a_0^2 E_H} \langle n' l' m'_l | \frac{\rho^2 B^2}{8} | n l m_l \rangle \end{aligned} \quad (2.29)$$

Depends on the strength of the magnetic field, this term can mix the states between different l , and even different n at very strong field. Using separation of variables, we can use the following identities

$$\langle n l | r^2 | n l \rangle = \frac{n^2 a_\mu^2}{2} [5n^2 - 3l(l+1) + 1] \quad (2.30)$$

and

$$\langle l'm'_l | \sin^2 \theta | l, m_l \rangle = \frac{4\sqrt{\pi}}{3} \langle l'm'_l | Y_{00} | lm_l \rangle - \frac{4\sqrt{\pi}}{3\sqrt{5}} \langle l'm'_l | Y_{20} | lm_l \rangle \quad (2.31)$$

where the first term is evaluated as

$$\frac{2}{3} \delta_{mm'} \delta_{ll'} \quad (2.32)$$

and the second term is

$$\begin{aligned} & -\delta_{mm'} \frac{4\sqrt{\pi}}{3\sqrt{5}} [\delta_{ll'} \sqrt{\frac{5}{4\pi}} C_{l020}^{l0} C_{lm20}^{lm} \\ & + \delta_{l',l+2} \sqrt{\frac{5(2l+1)}{4\pi(2l+5)}} C_{l020}^{l+2,0} C_{lm20}^{l+2,m} \\ & + \delta_{l',l-2} \sqrt{\frac{5(2l+1)}{4\pi(2l-3)}} C_{l020}^{l-2,0} C_{lm20}^{l-2,m}] \end{aligned} \quad (2.33)$$

We consider *S* and *D* states as they are dipole-allowed states that can be two-photon excited from $5^2s_{1/2}$ of ^{87}Rb . [42] Typically we operate below 20 G, which is below *l*- and *n*-mixing regime, and diamagnetic term can be safely neglected.[43]

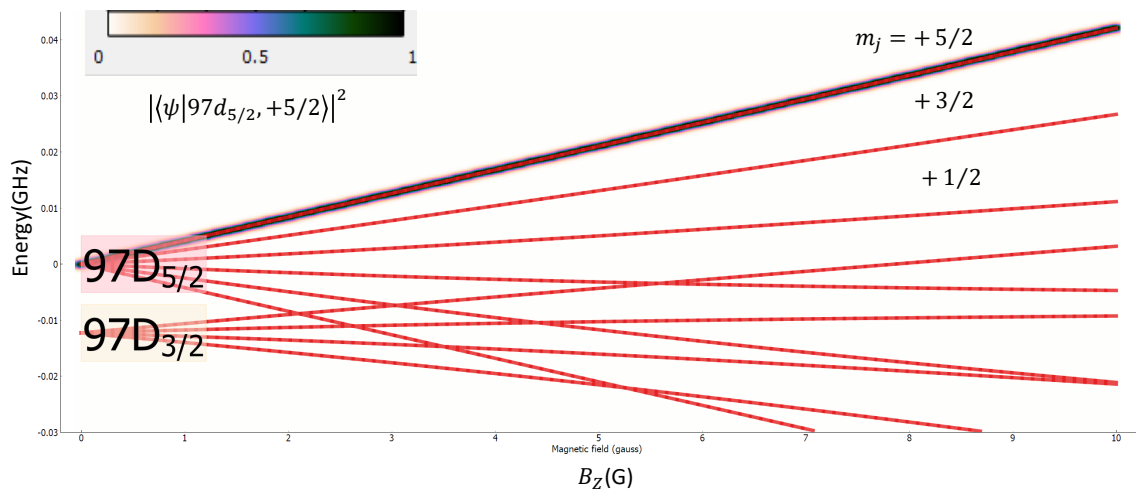


Figure 2.3: Zeeman map of Rydberg states, $97d_{5/2}$ and $97d_{3/2}$ at weak external magnetic field. Diamagnetic shifts included. State overlap to unperturbed $|97d_{5/2}, m_j = 5/2\rangle$ is visualized. Calculated using [Pair-interaction\[43\]](#)

3 RYDBERG INTERACTION

3.1 Dipole-Dipole interactions

For two atoms separated by distance \mathbf{R} the dipole-dipole interaction is given by

$$V(\mathbf{R}) = \frac{\mu_1 \cdot \mu_2}{R^3} - \frac{3(\mu_1 \cdot \mathbf{R})(\mu_2 \cdot \mathbf{R})}{R^5} \quad (3.1)$$

where the dipole matrix element $\mu_{1,2}$ describe transitions from the initial Rydberg states $|r\rangle$ to other dipole-coupled states $|r'\rangle, |r''\rangle$ respectively. The dipole-coupled pair-states have an energy difference Δ given by $\Delta = E_{r'} + E_{r''} - 2E_r$, with the dominant contribution to the atom-atom interaction arising from the pair state

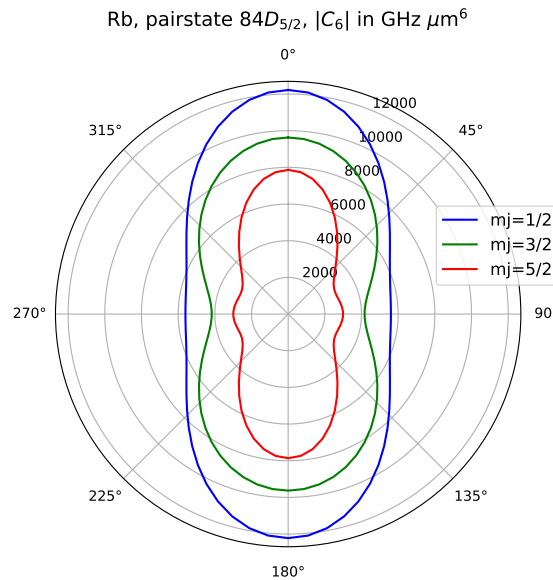


Figure 3.1: Angular dependency of C_6 coefficients between two interacting $|84d_{5/2}, m_j\rangle$ atoms[38]

of with smallest absolute defect $|\Delta|$. Reducing this to a simple two-pair problem, the Hamiltonian for the states $|rr\rangle, |r'r''\rangle$ is given by

$$H = \begin{bmatrix} 0 & V(R) \\ V(R) & \Delta \end{bmatrix} \quad (3.2)$$

Yielding new eigenenergies

$$\lambda_{\pm} = \frac{\Delta \pm \sqrt{\Delta^2 + 4V(R)^2}}{2} \quad (3.3)$$

where λ_- is perturbed $W_{|rr\rangle}$ and λ_+ is perturbed $W_{|r'r''\rangle}$.

3.1.1 Long-range interaction

In long-range $V(R) \ll \Delta$ or van der Waals regime, the original pair state $|rr\rangle$ energy is shifted as

$$\Delta W_{rr} = -\frac{V(R)^2}{\Delta} = -\frac{C_6}{R^6} \quad (3.4)$$

The sign of the interaction is determined by Δ . In this limit, the strength of the interaction is characterized by C_6 parameter which scales proportional to n^{*11} . This dependency can be understood as combined scaling of $V(R) \propto \mu^2 \propto n^{*4}$ and the energy defect $\Delta \propto n^{*-3}$.

3.1.2 Short-range interaction

In Short-range $V(R) \gg \Delta$ or resonant dipole-dipole regime, the shift is

$$\Delta W = \pm V(R) = \pm \frac{C_3}{R^3}. \quad (3.5)$$

Interaction has $1/R^3$ dependence associated with a pair of static dipoles, scaling as $C_3 \propto n^{*4}$. Transition between $1/R^3$ and $1/R^6$ regime is characterized by van der Waals radius(R_{vdW}) which is

$$R_{vdW} = (|C_6|/\Delta)^{1/6} \propto n^{*7/3} \quad (3.6)$$

In ensemble case, each pair-interaction will contribute to the total shift. Qualitative difference between van der Waals and resonant dipole-dipole regime is that in the vdW, nearest-neighbor interaction dominates. In resonant regime, one has to consider integrate over all pairs to accurately describe the ensemble system. For short-range calculations, high order ($1/R^n$) with $n \geq 4$ interactions comes into play, and accurate calculation of pair-state eigenstates require inclusion of those states, making the task computationally very challenging.

3.1.3 Even-shorter range interaction

Electron wavefunction of Rydberg atom increases spatial extent that scales with the principal quantum number n . Le Roy radius[44], a characteristic separation where electronic wavefunctions between a pair of Rydberg atoms start to overlap,

is defined as

$$R_{LR} = 2 \left(\sqrt{\langle r_1^2 \rangle} + \sqrt{\langle r_2^2 \rangle} \right) \quad (3.7)$$

where r_1 and r_2 are electron coordinates for the first and the second of two interaction atoms. For Alkali atoms Le Roy radius has upper bound of

$$R_{LR} = a_0 \sqrt{8n^2(5n^2 + 1 - 3l(l+1))}. \quad (3.8)$$

Above this radius, molecular potential can take asymptotic form of the sum of $1/R^k$ terms, such as

$$V(R) = \mathcal{D} - \sum_k C_k / R^k \quad (3.9)$$

where \mathcal{D} is a molecular disassociation limit and C_k are corresponding coefficients. If internuclear distance is shorter than Le Roy radius, above expression breaks down and vibrational levels cannot be described by LeRoy-Bernstein theory[44].

3.2 Rydberg blockade and Superatoms

Rydberg interaction perturbs the energy levels. If the perturbation is large enough such that the effective detuning Δ_r is larger than the coupling Ω , efficient and coherent excitation to the Rydberg state will be suppressed, as show in 3.2. This suppression due to Rydberg interaction is called “Rydberg Blockade”.

If the original Rydberg state becomes detuned enough due to the pair-interaction, such that $\Omega \ll \Delta_r$, accessible state is singly excited to Rydberg where participating atoms have equal and symmetric coupling. Blockaded ensemble can be modeled

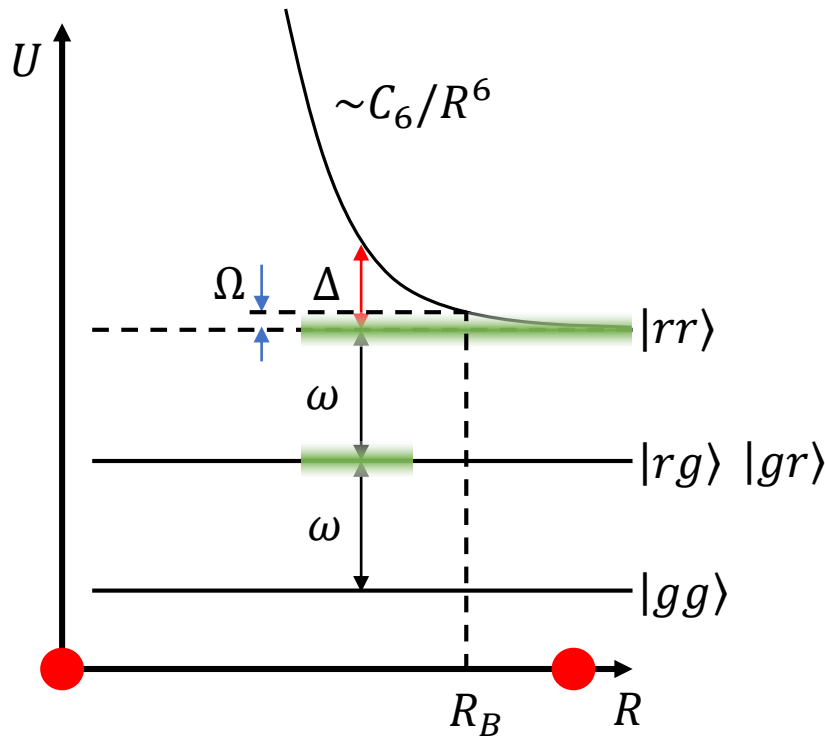


Figure 3.2: Energy level of atom-pair for different states. Illustration for Rydberg excitation blockade

as two-level system but with enhanced Rabi frequency, scaled by the participants within the Blockade volume, as illustrated in Figure 3.3.

Another important characteristic distance is van der Waals radius(R_{vdW}) where the dominating interaction changes from resonant dipole-dipole interaction to van der Waals interaction.

Size of electronic wavefunction for principal number $n \sim 100$ can reach $\sim 1\mu m$. In our ensemble experiments it is natural to have multiple atoms in a same site, thereby atom-pair distance can be much smaller than their wavefunction. In this regime, short-range and molecular interaction become non-negligible. Autoioniza-

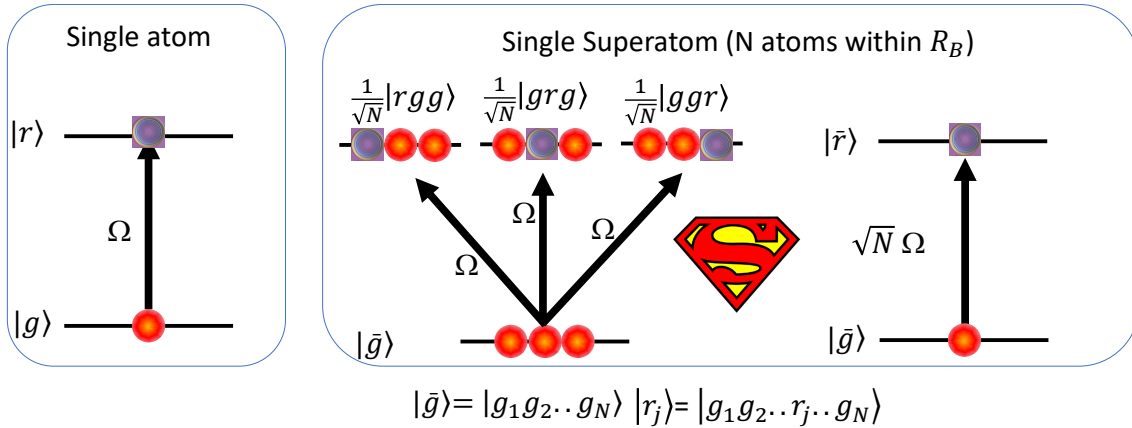


Figure 3.3: Single atom vs single super-atom

tion[45, 46], molecular resonance[47]

Our trap geometry and anisotropic interaction of $l = 2$ Rydberg state makes intra- and inter- ensembles to be treated differently. For atoms in the same site, they are in ($R < R_{vdW}$) regime that distance between atoms are smaller than van der Waals radius, or even Le Roy Radius. However, for inter-ensemble, atoms between different site, are far enough ($R > R_{vdW}$) to perturbatively calculate the pair-state interaction.

3.3 Hamiltonian for Intra-Ensembles

Due to the geometry of our dipole trap(3.4) and anisotropic Rydberg interaction, interatomic distance R of atom pairs in a same site is R_{vdW} where short-range interaction is dominating. In this short-range regime, we can further break down this into two categories where molecular interaction kicks in($R < R_{LR} < R_{vdW}$), and where the resonant dipole-dipole R^{-3} interaction is dominating ($R_{LR} < R < R_{vdW}$).

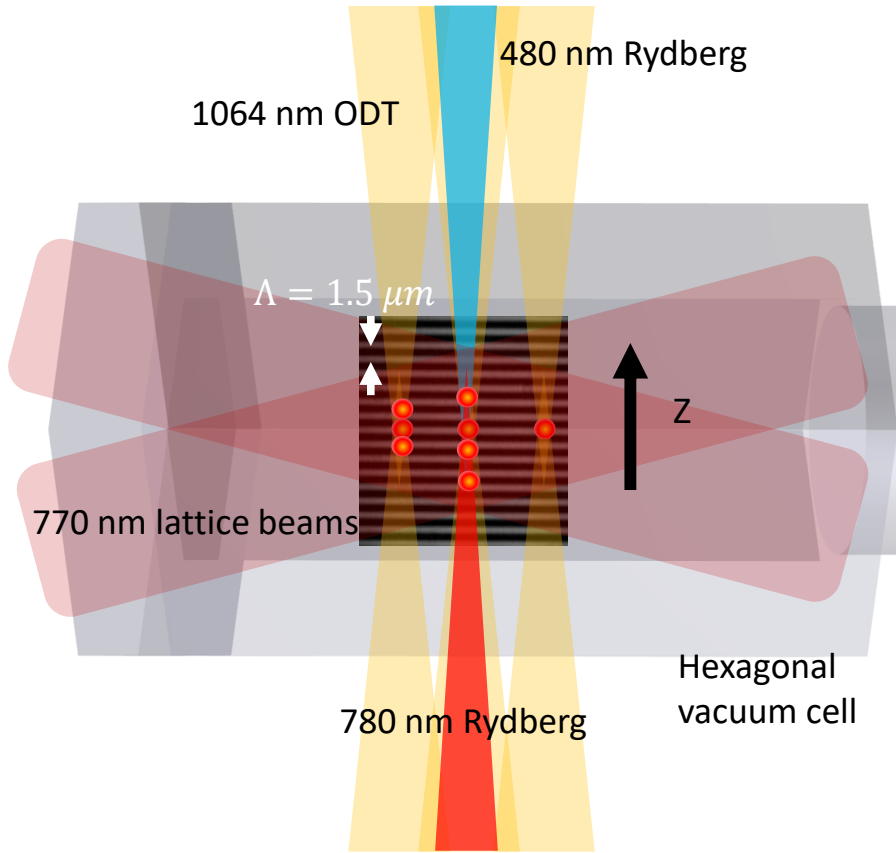


Figure 3.4: Geometry of our atoms and lasers for trapping and Rydberg excitation.

3.4 Hamiltonian for Inter-Ensembles

Rydberg interaction between two ensembles, or superatoms, are van der Waals interaction because of much larger separation than intra-ensemble case. Interaction is simply C_6/R^6 ($R > R_{vdW}$) and this is the regime where many Rydberg-based quantum simulator and computing platform are operating at. Shining laser on the atoms that are resonant with the transition between the ground state $|g\rangle$ and a Rydberg state $|r\rangle$, the system Hamiltonian is

$$H = \sum_i \frac{\hbar\Omega}{2} \sigma_x^i + \sum_{i < j} V_{ij} n^i n^j \quad (3.10)$$

acting on pseudo-spin states $|\uparrow\rangle_i$ and $|\downarrow\rangle_i$ corresponding to states $|g\rangle$ and $|r\rangle$ of atom i , respectively. Here, Ω is the Rabi frequency of the laser coupling, the $\sigma_\alpha^i (\alpha = x, y, z)$ are Pauli matrices acting on atom i , and $n^i = (1 + \sigma_z^i)/2$ is the number of Rydberg excitations (0 or 1) on site i . The term V_{ij} arises from the van der Waals interaction between atom i and j when they are both in $|r\rangle$, and scales as $C_6(\theta)|\mathbf{r}_i - \mathbf{r}_j|^{-6}$ with the separation between the atoms $\mathbf{r}_i - \mathbf{r}_j$. Time evolution of the system can be readily simulated using QuTip[48] or other framework.

4 QUANTUM OPTICS

We briefly discuss the interaction between atoms and light at single photon regime. Physical system of our particular interest is a collection of optically trapped cold atoms, containing non-localized single excitation. We are interested in engineering the system to implement directional, deterministic single photon source. Raman memory approach in waveguide has recently been demonstrated[49], and we will be considering Rydberg-mediated, deterministic, free-space source.

4.1 Collective atom-light interaction

When identical atoms are tightly confined in a volume, shorter than the wavelength of photon they emit, they will decay much faster[50] than single atom case. Radiation properties are modified by neighboring atoms in the vicinity, as they interact with same radiation mode, and enhanced collective atomic decay grows as the number of atoms increases. Instructive analysis with three atoms[51] case can be found. Dicke state cannot exactly be an exponentially decaying eigenstate in N-atom system if N is greater or equal to 4 because there is no atomic space distribution that can make identical interaction between any two atoms.

Model and Hamiltonian

Let us first consider a simplified setup that allows us to focus on the most prominent feature of superradiance. We consider N atoms in two level system in a weak excitation regime, that no more than one atom can be excited. Hamiltonian of the

system is

$$H = H_0 + H_{int}. \quad (4.1)$$

H_0 is unperturbed hamiltonian and H_{int} is the interaction Hamiltonian.

$$H_0 = \sum_{j=1}^N \hbar\omega_{eg} |e_j\rangle \langle e|_j + \sum_{\mathbf{k}} \hbar\omega_{\mathbf{k}} a_{\mathbf{k}}^\dagger a_{\mathbf{k}} \quad (4.2)$$

$\hbar\omega_{eg} = E_e - E_g$ is the energy of the atomic transition between ground and excited state. $\hbar\omega_{\mathbf{k}}$ is the energy of \mathbf{k} -mode photon. In the rest of text, $\hbar = 1$ convention is used simplify the expressions. Interaction Hamiltonian reads

$$H_{int} = \sum_{j=1}^N \sum_{\mathbf{k}} g_{\mathbf{k}} (|e_j\rangle \langle g| e^{i\omega_{eg}t} + |g\rangle \langle e_j| e^{-i\omega_{eg}t}) (a_{\mathbf{k}}^\dagger e^{i\omega_{\mathbf{k}}t - i\mathbf{k}\cdot\mathbf{r}_j} + a_{\mathbf{k}} e^{-i\omega_{\mathbf{k}}t + i\mathbf{k}\cdot\mathbf{r}_j}) \quad (4.3)$$

where $|e_j\rangle \langle g|$ ($|g\rangle \langle e_j|$) is atomic raising(lowering) operator of j -th atom, and $a_{\mathbf{k}}^\dagger$ ($a_{\mathbf{k}}$) is creation(annihilation) operator associated with \mathbf{k} -th mode photon. Rearranging the terms to co-rotating term($\omega_{eg} - \omega_{\mathbf{k}}$) and counter-rotating terms($\omega_{eg} + \omega_{\mathbf{k}}$), we have

$$\begin{aligned} H_{int} = & \sum_{j=1}^N \sum_{\mathbf{k}} g_{\mathbf{k}} \left[|g\rangle \langle e_j| a_{\mathbf{k}}^\dagger e^{i(\omega_{\mathbf{k}} - \omega_{eg})t} e^{-i\mathbf{k}\cdot\mathbf{r}_j} + |e_j\rangle \langle g| a_{\mathbf{k}} e^{-i(\omega_{\mathbf{k}} - \omega_{eg})t} e^{i\mathbf{k}\cdot\mathbf{r}_j} \right] \\ & + \left[|g\rangle \langle e_j| a_{\mathbf{k}} e^{-i(\omega_{\mathbf{k}} + \omega_{eg})t} e^{i\mathbf{k}\cdot\mathbf{r}_j} + |e_j\rangle \langle g| a_{\mathbf{k}}^\dagger e^{i(\omega_{\mathbf{k}} + \omega_{eg})t} e^{-i\mathbf{k}\cdot\mathbf{r}_j} \right] \end{aligned} \quad (4.4)$$

Terms in the first parenthesis is co-rotating term that governs a single photonic state and single atomic excitation. The second parenthesis terms are so called counter-rotating terms governing interaction of two atomic excitation and a virtual

photonic state, which violates energy conservation therefore a virtual process. In a small ensemble regime $d \ll \lambda_{eg}$ the virtual process takes important role in the dynamics, as these literatures say[27][52]. Literatures with Rotating Wave Approximation(RWA)[53]. It changes the kernel of interaction. When atoms are well separated $d > \lambda_{eg}$, the virtual process can be safely neglected and the RWA gives the hamiltonian

$$H_{int,RWA} = \sum_{j=1}^N \sum_{\mathbf{k}} g_{\mathbf{k}} \left[|g\rangle \langle e_j| a_{\mathbf{k}}^\dagger e^{i(\omega_k - \omega_{eg})t} e^{-i\mathbf{k}\cdot\mathbf{r}_j} + |e_j\rangle \langle g| a_{\mathbf{k}} e^{-i(\omega_k - \omega_{eg})t} e^{i\mathbf{k}\cdot\mathbf{r}_j} \right] \quad (4.5)$$

In the following discussion, we do not apply RWA in order to fully illustrate the physics.

Time evolution of atomic and field amplitudes

Suppose we have an atomic ensemble in a singly excited state so only one of the atoms is in the optically excited state and all others are in the ground state. Then we can represent such state as a superposition of having single atomic excitation with no photon and all atoms in the ground state with a single photon.

$$|\psi(t)\rangle = \sum_{j=1}^N \alpha_j(t) |e_j; 0\rangle + \sum_{\mathbf{k}} \kappa_{\mathbf{k}}(t) |g; 1_{\mathbf{k}}\rangle \quad (4.6)$$

where $|e_j; 0\rangle \equiv |g_1 g_2 \cdots e_j \cdots g_N\rangle |0\rangle$ and $|g; 1_{\mathbf{k}}\rangle \equiv |g_1 g_2 \cdots g_N\rangle |\mathbf{k}\rangle$, with $|0\rangle$ stands for the vacuum and $|\mathbf{k}\rangle$ for one photon in the \mathbf{k} th mode of the EM field. We set initial conditions $\sum_{j=1}^N |\alpha_j(0)|^2 = 1$ and $\kappa_{\mathbf{k}}(0) = 0$ saying that initially no photon is

in the system. Substituting the equation into Schrodinger equation gives coupled differential equations for the atomic amplitudes $\alpha_j(t)$ and the field amplitude $\kappa_{\mathbf{k}}(t)$ as the following.

$$\begin{aligned}\dot{\alpha}_j(t) &= -i \sum_{\mathbf{k}} g_{\mathbf{k}} \kappa_{\mathbf{k}}(t) e^{-i(\omega_k - \omega_{eg})t + i\mathbf{k} \cdot \mathbf{r}_j} \\ \dot{\kappa}_{\mathbf{k}}(t) &= -i \sum_{j=1}^N g_{\mathbf{k}} \alpha_j(t) e^{i(\omega_k - \omega_{eg})t - i\mathbf{k} \cdot \mathbf{r}_j}\end{aligned}\quad (4.7)$$

Integrating the photonic equation over time, using the initial condition($\kappa_{\mathbf{k}}(0) = 0$) gives

$$\kappa_{\mathbf{k}}(t) = -i \int_0^t dt' \sum_{j=1}^N g_{\mathbf{k}} \alpha_j(t') e^{i(\omega_k - \omega_{eg})t' - i\mathbf{k} \cdot \mathbf{r}_j} \quad (4.8)$$

Substituting this into the atomic equation, we decouple the equation

$$\dot{\alpha}_j(t) = - \sum_{\mathbf{k}} \sum_{j'=1}^N \int_0^t dt' |g_{\mathbf{k}}|^2 \alpha_{j'}(t') e^{-i(\omega_k - \omega_{eg})(t' - t) + i\mathbf{k} \cdot (\mathbf{r}_j - \mathbf{r}_{j'})} \quad (4.9)$$

We assume the atomic distribution is small enough that we can neglect the time of photon flights. With the identity $\int d\tau e^{i\omega\tau} = \pi\delta(\omega) + iP(\frac{1}{\omega})$ Then applying Markov approximation gives,

$$\dot{\alpha}_i(t) = -\gamma \sum_{j=1}^N \Gamma_{ij} \alpha_j(t) \quad (4.10)$$

where the single atom spontaneous decay rate is $\gamma = \frac{V_{photon} k_0^2 g_{k_0}^2}{\pi c}$, and $N \times N$ matrix atomic decay operator Γ_{ij} is written as

$$\Gamma_{ij} = \frac{\sin(k_0 |\mathbf{r}_i - \mathbf{r}_j|)}{k_0 |\mathbf{r}_i - \mathbf{r}_j|} - i \frac{\cos(k_0 |\mathbf{r}_i - \mathbf{r}_j|)}{k_0 |\mathbf{r}_i - \mathbf{r}_j|} (i \neq j) \quad (4.11)$$

with $\Gamma_{ij}=1$ if $i = j$. If the atomic excitation is prepared with a resonant plane-wave, optical phases will depend upon the atom locations. It is convenient to incorporate the spatial phase factor to the definition of excited states as the following.

$$\begin{aligned} e^{i\mathbf{k}_0 \cdot \mathbf{r}_j} |e_j\rangle &\rightarrow |e'_j\rangle \\ \beta_j &= e^{-i\mathbf{k}_0 \cdot \mathbf{r}_j} \alpha_j \end{aligned} \quad (4.12)$$

This enables us to write the atomic amplitude decay equation to be

$$\dot{\beta}_i(t) = -\gamma \sum_{j=1}^N \Gamma_{ij} e^{-i\mathbf{k}_0 \cdot (\mathbf{r}_i - \mathbf{r}_j)} \beta_j(t) \quad (4.13)$$

Now, one can calculate arbitrary time evolution by knowing the atomic distribution and the initial population $\beta_j(t = 0)$ on each excited state $|e_j\rangle$. Once they are figured out, photonic amplitudes can be obtained by substituting $\beta_j(t)$ to the differential equation. It yields

$$\kappa_{\mathbf{k}}(t) = -ig_{\mathbf{k}} \sum_{j=1}^N \int_0^t dt' \beta_j(t') e^{i(\omega_k - \omega_{eg})t'} e^{-i(\mathbf{k} - \mathbf{k}_0) \cdot \mathbf{r}_j} \quad (4.14)$$

Unfortunately, $|e_j\rangle$ are not the exact eigenstates of Γ_{ij} . This means each atomic

amplitude is a superposition of different exponentially decaying states. If atom distribution is tightly confined within the wavelength, one eigenstate dominates with the enhanced decay rate $N\gamma$. If atoms are spreaded out randomly, they form subsystems that decays all differently therefore the enhancement of decay decreased, as predicted by the trace conservation. Nevertheless, eigenstate analysis gives a good idea of time evolution. This will be discussed in the following section.

4.1.1 Radiative eigenstate analysis

Behavior of the collective interactions between atoms and the photon they emit can be fully revealed by solving the matrix equation when atoms positions(or distribution)and their initial states are provided. We assume that the state is prepared by absorbing a photon. As discussed before, different phase will arise from the different timing of excitation for each atom $e^{i\mathbf{k}_0 \cdot \mathbf{r}}$. Rewritting the atomic amplitude differential equation in a matrix form,

$$\dot{A} = \gamma \Gamma A \quad (4.15)$$

where the vector A is

$$A = \begin{pmatrix} \alpha_1(t) \\ \alpha_2(t) \\ .. \\ \alpha_N(t) \end{pmatrix} \quad (4.16)$$

and the decay matrix Γ is

$$\Gamma = \|\Gamma_{ij}\| = \begin{pmatrix} 1 & \Gamma_{12} & \dots & \Gamma_{1N} \\ \Gamma_{21} & 1 & \dots & \Gamma_{2N} \\ \dots & \dots & \dots & \dots \\ \Gamma_{N1} & \dots & \dots & 1 \end{pmatrix} \quad (4.17)$$

Diagonalization of the decay operator Γ gives eigenvectors $|\nu_n\rangle$, ($n = 1, \dots, N$) with associated eigenvalues Γ_n . If initial state is prepared in an eigenstate $A(0) = |\nu_n\rangle$, time evolution of the state is $A(t) = e^{-\gamma\Gamma_n t} A(0)$, meaning that the population decays with the rate $\gamma Re\Gamma_n$. The real part of Γ_n determines the decay rate, and the imaginary part is from collective Lamb shift that induces coherent population transfer to other excited states. For arbitrary initial state, the general solution of the Schrodinger equation can be written as

$$|\psi(t)\rangle = \sum_{j=1}^N \alpha_j(t) |e_j\rangle + \sum_{\mathbf{k}} \kappa_{\mathbf{k}}(t) |1_{\mathbf{k}}\rangle \quad (4.18)$$

or

$$|\psi(t)\rangle = \sum_{j=1}^N \beta_j(t) |e'_j\rangle + \sum_{\mathbf{k}} \kappa_{\mathbf{k}}(t) |1_{\mathbf{k}}\rangle \quad (4.19)$$

which can be represented in terms of eigenvectors.

$$|\psi(t)\rangle = \sum_{n=1}^N C_n e^{-\gamma\Gamma_n t} |\nu_n\rangle \quad (4.20)$$

The coefficients C_n ($n = 1, 2, \dots, N$) are determined by the initial condition. The decay

operator Γ is complex symmetric matrix, and real symmetric when Lamb shifts are neglected. If the interatomic distances are large enough $k_0 R \gg 1$ so the virtual process term can be neglected, it can be approximated to Hermitian. Eigenvectors of the matrix then can be chosen mutually orthonormal, yielding $C_n = \langle \nu_n | \psi(0) \rangle$. Substituting

$$\begin{aligned} \alpha_j(t) &= \langle e_j | \psi(t) \rangle = \sum_{n=1}^N C_n(t) \langle e_j | \nu_n \rangle \\ &= \sum_{n=1}^N C_n e^{-\gamma \Gamma_n t} \langle e_j | \nu_n \rangle \\ &\quad \sum_{n=1}^N C_n \nu_n^{(j)} e^{-\gamma \Gamma_n t} \end{aligned} \tag{4.21}$$

where $\nu_n^{(j)} = \langle e_j | \nu_n \rangle$, meaning the projection of $|\nu_n\rangle$ onto j -th excited state.

4.1.2 Directional photon emission

Excited atom spontaneously decays to its ground state and emit a photon to random direction e.g. 4π sr. When a cloud of excited atoms incoherently decays, they will also emit photons to the random direction. However, if they are correlated so they decay in a coherent fashion, this is analogous to a collection of coherent emitters like an antenna array. Just like the radiation pattern of antenna can be varied by tuning the phase of each emitter, the photon angular distribution from the atoms can be tuned to have strong directionality. In Dicke sample, atoms prepared with a single photon absorption that are confined in a small volume less than λ , the phase between each atom is close to unity $e^{i\mathbf{k}_0 \cdot \mathbf{r}} \sim 1$ therefore they exhibit

correlated spontaneous emission. For larger samples, carefully positioning atoms will still prepare approximate Timed-Dicke state that will decay rapidly. Regularly positioning neutral atoms can be achieved using Optical Lattices[54]. List some techniques that can form favorable geometry i.e quantum dots. photonic crystal. one-dimensional ion trap string. Suppose we have N atoms where the position vector of each atom is r_j . Using lasers we can prepare symmetric singly excited state that contains momentum $\exp\{i\mathbf{k}_0 \cdot \mathbf{r}\}$. This state preparation can be done with two photon absorptions(ω_1, \mathbf{k}_1) and (ω_2, \mathbf{k}_2) from hyperfine ground state to Rydberg state, followed by a single photon emission (ω_3, \mathbf{k}_3) to an intermediate state. Then the atomic ensemble has symmetric singly excited state between the ground state and intermediate state, where j -th atom has $\exp\{i\mathbf{k}_0 \cdot \mathbf{r}\}$ provided that $(\mathbf{k}_0 = \mathbf{k}_1 + \mathbf{k}_2 - \mathbf{k}_3)$. If the state cooperatively decays to the ground state, the last photon (ω_4, \mathbf{k}_4) satisfies the energy conservation: $\omega_4 = \omega_1 + \omega_2 - \omega_3$ and the momentum conservation $\mathbf{k}_4 = \mathbf{k}_0$. Here we quantitatively calculate the angular photon distribution. In the assumption that the system decays as a whole so each atom being a coherent emitter, probability of the photon being emitted to \mathbf{k}_4 can be written as[28]

$$I_{\mathbf{k}_4} \propto \frac{1}{N} \left| \sum_{j=1}^N e^{-i(\mathbf{k}_4 - \mathbf{k}_0) \cdot \mathbf{r}_j} \right|^2 \quad (4.22)$$

Upper argument will be a good approximation when initial state $|\psi(0)\rangle$ has large overlapping $\langle \nu_n | \psi(0) \rangle \sim 1$ with one of superradiant eigenstate $|\nu_n\rangle$. This occurs when atoms are very tightly confined just like Dicke sample, or lattice configuration. The difference between them are the presence of contribution from exchanging virtual photons. In the Dicke sample, both real photons and virtual photons can be

uniformly exchanged among atoms because they are so close to each other. If the sample gets larger, the interaction becomes inhomogeneous so the superradiance quickly vanishes. If one can place atoms regularly so the photon exchange is uniform, there will be states that highly overlaps with the rapidly decaying eigenstate. In general, many radiative eigenstate appear and they decay all differently with the rate $Re(\gamma\Gamma_n)$ and the frequency shift $Im(\gamma\Gamma_n)$. It is therefore useful to analyze by decomposing initial state to radiative eigenstates. Let us consider the eigenvector decomposition of the initial state and put into the photonic part $\kappa_{\mathbf{k}}(t)$. We get

$$\kappa_{\mathbf{k}}(t; \omega_k) = -i \int_0^t dt' \sum_{j,n}^N g_{\mathbf{k}} C_n e^{-\gamma\Gamma_n t'} \nu_n^{(j)} e^{i(\omega_k - \omega_{eg})t' - i\mathbf{k}\cdot\mathbf{r}_j} \quad (4.23)$$

In a similar treatment, we get

$$\kappa_{\mathbf{k}}(t; \omega_k) = -i \sum_{j,n}^N g_{\mathbf{k}} \frac{(1 - e^{-\gamma\Gamma_n t}) C_n \nu_n^{(j)} e^{-i\mathbf{k}\cdot\mathbf{r}_j}}{\gamma\Gamma_n - i(\omega_k - \omega_{eg})} \quad (4.24)$$

To see where the photon ends up, take the limit $t \rightarrow \infty$

$$\kappa_{\mathbf{k}}(\infty; \omega_k) = -i \sum_{j,n}^N g_{\mathbf{k}} \frac{C_n \nu_n^{(j)} e^{-i\mathbf{k}\cdot\mathbf{r}_j}}{\gamma\Gamma_n - i(\omega_k - \omega_{eg})} \quad (4.25)$$

Integrating the whole spectrum $\int_{-\infty}^{\infty} d\omega_k$, one finally arrives to

$$\kappa_{\mathbf{k}}(\infty) = -i \sum_{j,n}^N g_{\mathbf{k}} \frac{C_n \nu_n^{(j)} e^{-i\mathbf{k}\cdot\mathbf{r}_j}}{\gamma Re(\Gamma_n)} \quad (4.26)$$

Therefore probability of emitting a photon to \mathbf{k} is

$$|\kappa_{\mathbf{k}}(\infty)|^2 = \left| \sum_{j,n}^N g_{\mathbf{k}} \frac{C_n \nu_n^{(j)} e^{-i\mathbf{k} \cdot \mathbf{r}_j}}{\gamma R e(\Gamma_n)} \right|^2 \quad (4.27)$$

Half-opening angle of the forward emission cone quickly reaches to diffraction-limited with tens of atoms. It is the angle from $\theta = 0$ to the angle where the power local minimum is. Gray horizontal line is the divergence half-angle assuming that fundamental gaussian beam is formed from the gaussian atom distribution.

$$\theta_{x,y} = \frac{\lambda}{\pi w_0^{x,y}} = \frac{\lambda}{\pi 2\sigma_{x,y}} \quad (4.28)$$

where $w_0^{x,y}$ are the waist radii of gaussian beam for each transverse direction. Note that radiating mode has twice of the atomic waist radii $\sigma_{x,y}$.

For irregularly distributed atoms, cooperativity rapidly decreases as the sample becomes larger than the radiation wavelength, because interactions between atoms are becoming more inhomogeneous. Instead of coherently decaying as a whole, they will become a part of subsystems which is a radiative eigenstate of the decaying operation. To further extend superradiance to larger sample, we introduce a 3D lattice where the distance between atoms are well controlled.

In reality there are other atomic levels where atoms can decay to, but does not participate in collective enhancement. To capture the full physical picture, one has to take account those other competing decay channels, vector treatment of light polarization, dipole radiation pattern, virtual processes including dipole-dipole interactions and collective Lamb shifts.

In the four-wave mixing scheme shown on Figure 4.1b, general solution of this

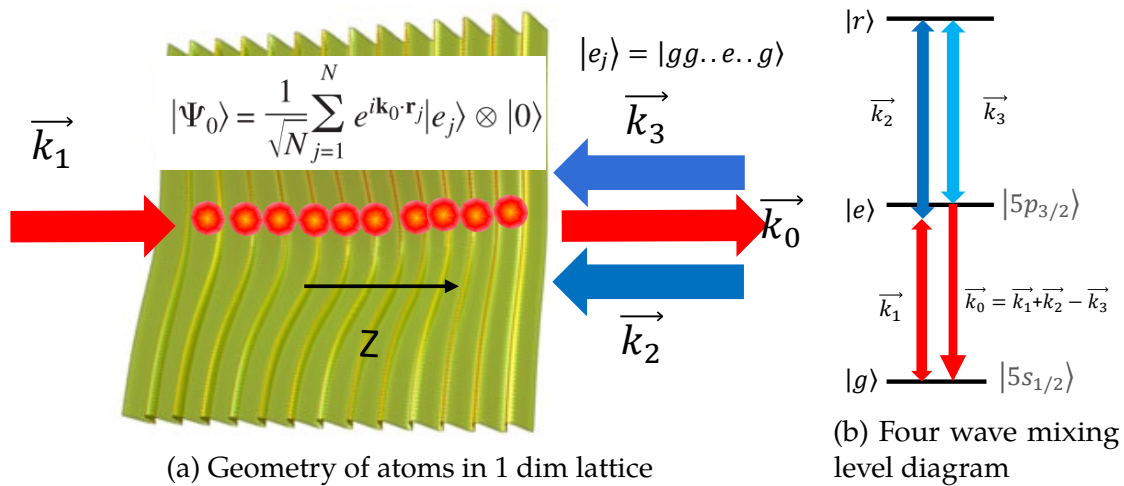


Figure 4.1: Level diagram and atom configuration

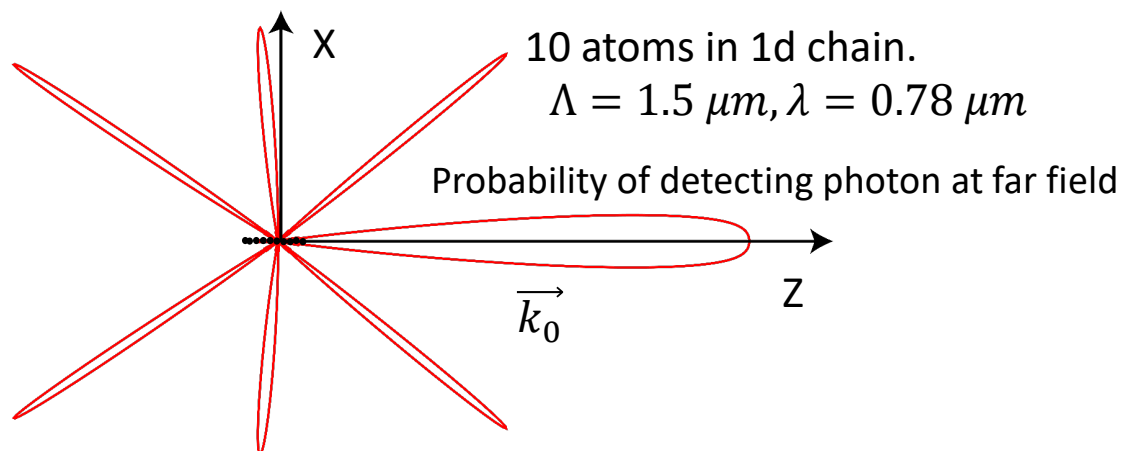


Figure 4.2: Cooperative emission from 10 atoms in 1-aim array

system is represented as

$$\begin{aligned}
|\psi(t)\rangle = & \sum_{j=1}^N r_j(t) e^{-i\omega_{rg}t} |r_j\rangle |0\rangle \\
& + \sum_{\vec{k},s} (\kappa_{g,\vec{k},s}(t) |g\rangle + \kappa_{g_\perp,\vec{k},s}(t) |g_\perp\rangle) e^{-i\omega_k t} |1_{\vec{k},s}\rangle \\
& + \sum_{j=1}^N \sum_{q=-1}^1 \beta_j^q(t) e^{-i\omega_{eg}t} |e_j^q\rangle |0\rangle \\
& + \sum_{n=1}^N \sum_{m=n+1}^N \sum_{q,\mu=-1}^1 \alpha_{mn\vec{k}s}^{q\mu}(t) e^{-i(\omega_k+2\omega_{eg})t} |e_n^q e_m^\mu\rangle |1_{\vec{k},s}\rangle
\end{aligned} \tag{4.29}$$

where $|r\rangle$ denotes a long lived Rydberg state we start from, $|e^q\rangle$ ($q = -1, 0, 1$) are Zeeman sublevels of an excited state, $|g\rangle$ is the ground state we originally prepared, $|g_\perp\rangle$ is short hand notation for the other ground states.

Atomic Structure

Let us first consider where the singly excited entangled state can decay to. Collective enhancement only occurs to the decay to its original state. We investigate and compare the efficiency of each excitation scheme. Our protocol begins with hyperfine ground states initialized by optical pumping. Sets of computational basis states are either clock states ($|1\rangle = |F = 2, m_f = 0\rangle$ and $|0\rangle = |F = 1, m_f = 0\rangle$) or Stretched states ($|1\rangle = |F = 2, m_f = 2\rangle$ and $|0\rangle = |F = 1, m_f = 1\rangle$). From here, two photon excite the atoms to a Rydberg W-state. This Rydberg W-state can be mapped down in the hyperfine manifold for storage, or can exhibit superradiant decay on its way back to the reservoir state. When Rydberg W-state goes through stimulated

emission of a 480nm photon, it is mapped to one of the hyperfine states in the intermediate p levels, i.e. $p_{1/2}$ or $p_{3/2}$, spontaneous decay will bring the p level W-state to the ground state. This is the moment when the collectively enhanced decay occurs. Because of symmetricity of W-state, the rate of decay back to the reservoir state is enhanced by the number of atoms, while other decay channels exhibit natural decay rate. These channels compete with the superradiant channel, therefore effectively decreasing the number of atoms participating in the decay. In order to efficiently utilize superradiance, we want the competing channels to be suppressed. Coupling schemes that will maximize the superradiant feature. Directionality and cooperativity strongly depends on the geometric arrangements[55] of atoms.

Part II

Experiment Setup

5 COOLING, TRAPPING, OPTICAL PUMPING AND MANIPULATION OF ATOMS

We study science happening at a few μm scale, although actual apparatus is much larger than that. This chapter provides top-down view of our apparatus, starting from laser cooling to optical pumping. The main apparatus can be seen Figure 5.1, contained in a protective box. For those readers who are interested to know details of vacuum construction and optical layout designs are encouraged to see Matt Ebert's thesis[56], and I will cover updated layout for any modified setup.

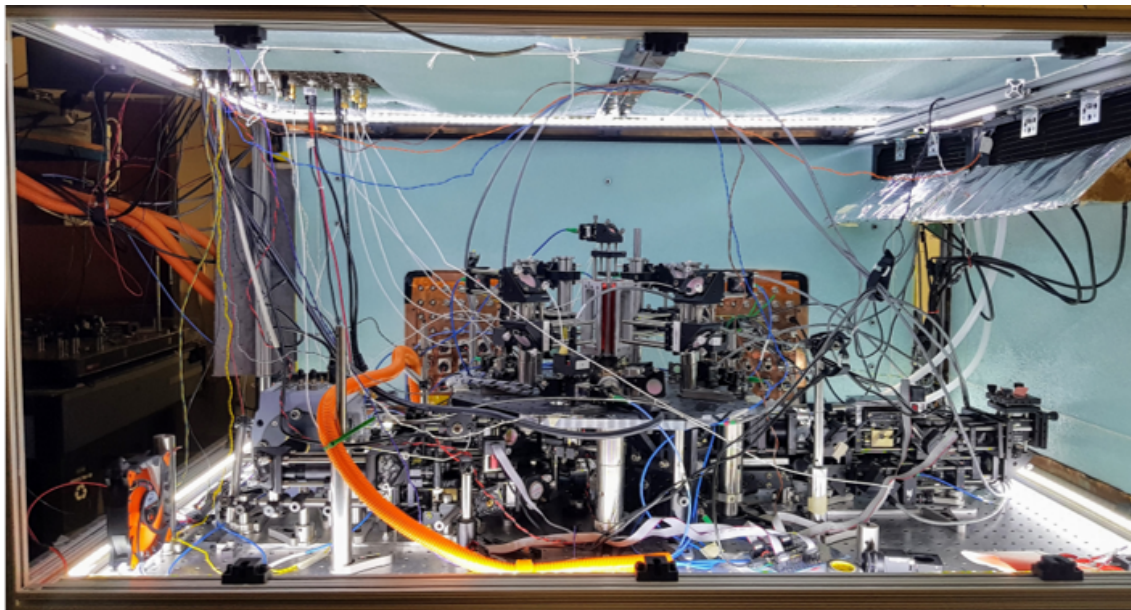


Figure 5.1: Main apparatus and the box

5.1 Magneto Optical Trap

Our setup is comprised of double MOT configuration in order to achieve low pressure and efficient atom loading at the same time. The double MOT has two vacuum cells, one of which having higher pressure serves as a atom source and the other one with lower pressure is to perform science. They are inter-connected by a small hole to limit conductivity, enabling differential pumping technique.

5.1.1 2D MOT

Two-dimensional MOT is generated in a square glass cell located above the hex cell, where we host scientific experiments. Two pairs of MOT beams come perpendicular to each side of the square cell, transversely cooling atoms. This creates a beam of cold atoms axially, and is forced to flow toward the other vacuum cell when another weak beam from the top is in place. Typical pressure is around 10^{-8} Torr.

5.1.2 UV Light Induced Atom Desorption

We have extra knob to modulate the atom loading rate by Light Induced Atom Desorption(LIAD)[[57](#), [58](#)]. LIAD modifies the background vapor pressure by replenishing the atoms that were stuck on to the glass surface back to the vacuum. Typically UV lights are used for LIAD as they are more energetic and efficient knocking atoms from the surface. We use Thorlabs [M405L2-C2-UV](#) (405 nm) Collimated LED. shining the square 2D-MOT glass cell, purchased from [Triad Technology](#). We observed the fluorescence of atomic cloud in-situ while turning the UV on and off.

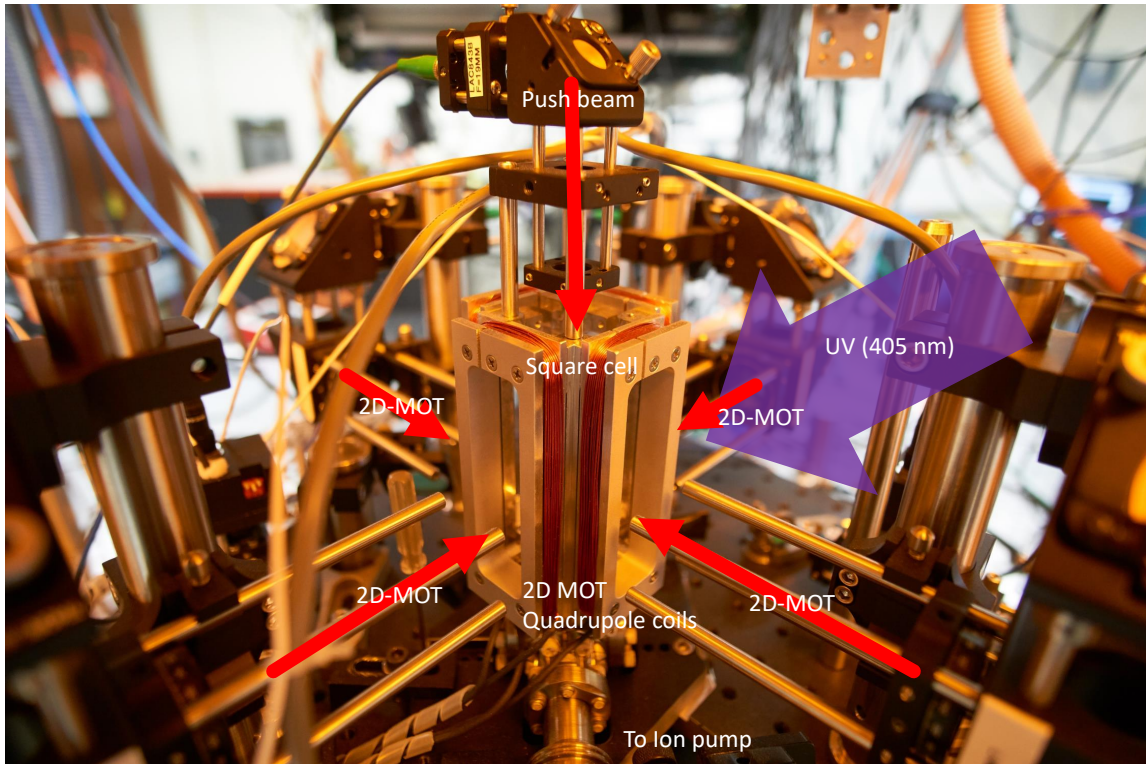


Figure 5.2: Square cell assembly. 2D-MOT and push beam.

The result showed on Figure 5.3 is very similar to [59].

5.1.3 3D MOT

Pre-cooled atoms are transported to the hexagonal glass cell which is placed underneath of the 2D MOT through a pinhole. These atoms are doppler cooled by six MOT beams and magnetically trapped by quadrupole field gradient, eventually forming a cloud at the potential minimum. This process is called ätom loading. Atom loading becomes inefficient when the pre-cooled atoms are not provided, because 3D MOT has low Rb vapor pressure meaning there are few atoms to catch.

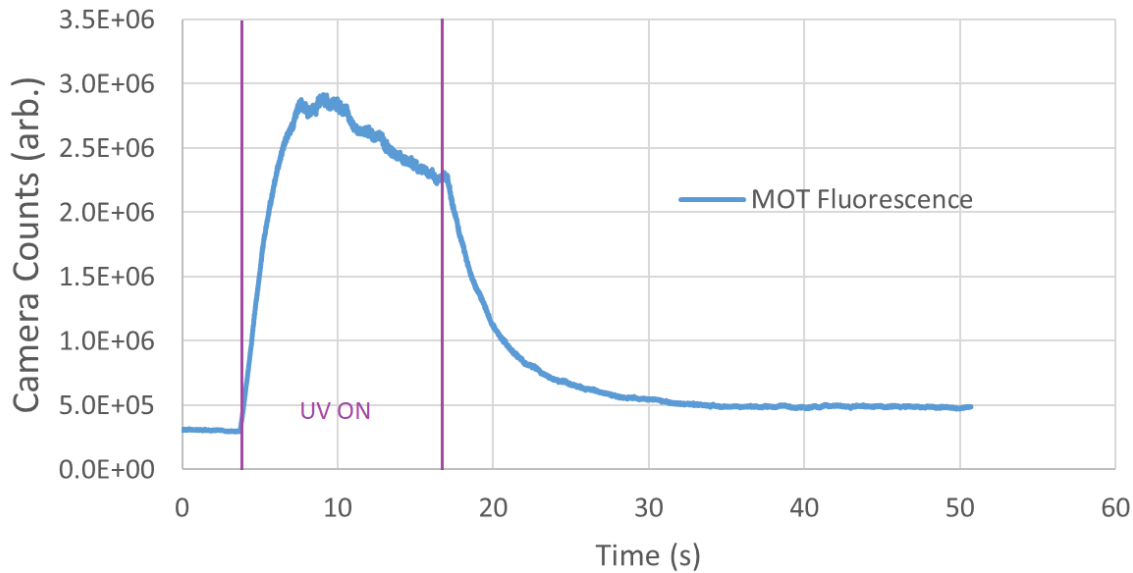


Figure 5.3: Magneto-optically trapped atoms dependency to the presence of UV light.

Here we describe the efforts made to make the process as efficient as possible.

5.1.4 Cooling and Repumper lasers

Cooling and repumping lasers are DFB diode lasers purchased from Eagleyard. Integrated TEC and small heat capacity makes them thermally controllable with high bandwidth, thereby compensating environmental swing very reliably. Poor HVAC of Chamberlin had been extremely troublesome and one of the biggest barrier of productivity, as our previous home-made ECDL got easily perturbed by those events. we are happy that we moved to DFB, showing excellent thermal stability. One drawback is their high sensitivity to current noise and rf pick-offs, optical feedback. One should pay extra attention when dealing with these laser

diode.

Time of Flight

Atomic cloud in a MOT is being cooled and trapped by the magnetic field. When they are removed, atoms move freely and as a macroscopic result, the cloud expands. Since the rate of expansion depends upon the temperature of atoms, one can extract it by taking two camera shots of the cloud, before the release and after the release with finite wait time^{5.4}. Atoms are loaded from background for a few secs, then cooling and repumper beam and quadrupole field are turned off to let atoms to expand. After a few ms, only the cooling and repumper light is back on to collect fluorescence. Then the Gaussian half-width of the atomic cloud expands as

$$w(t) = w_r \sqrt{1 + \frac{4k_B T t^2}{m w_r^2}} \quad (5.1)$$

where w_r is size at $t = 0$, and Gaussian waist by fitting to $(e^{-x^2/w^2(t)})$, T is atom temperature, t is evolution time, m is the mass of atom.

Corresponding to atom temperature of $(16(2)), 11.7(7)\mu K$ for horizontal and vertical direction.

Loading curves

Two important parameters characterizing the MOT are loading rate and loss rate. To extract them we utilize the technique from [60], which measures time constants for loading and losing. 3D MOT Loading only from the hex cell is fairly slow, due

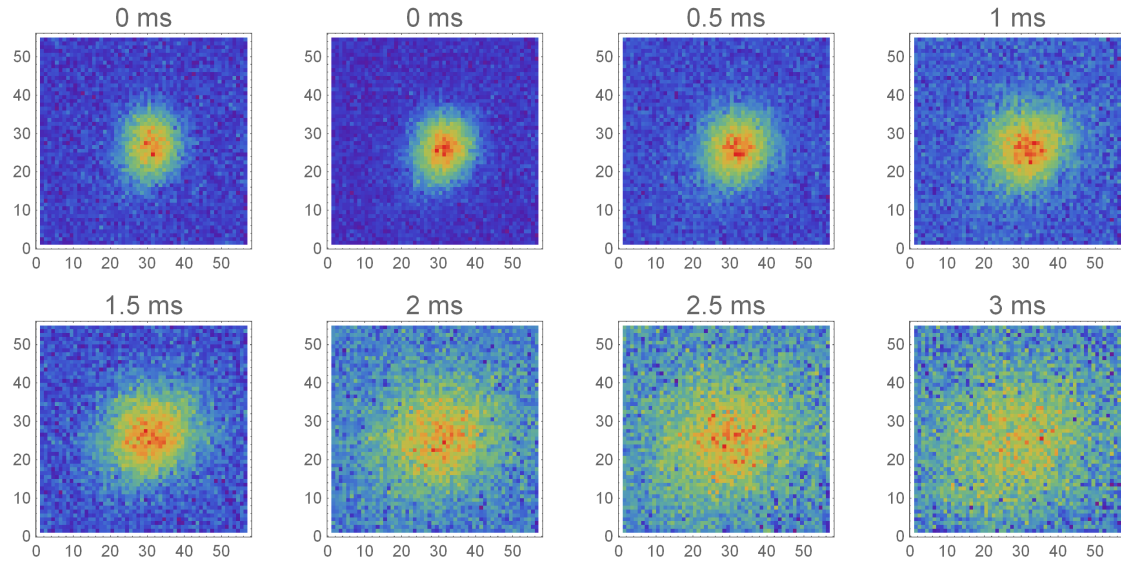


Figure 5.4: Time of Flight(TOF) of Rb cloud. (X,Y) dimensions are in camera pixels. Each pixel corresponds to $13\mu\text{m}$. $\delta = -2\pi \times 11\text{MHz}$, $I_{total} = 4.5\text{mW/cm}^2$. Captured from Andor Luca camera with 0.5ms exposure, $\times 20$ EM gain, averaged over 50 shots, background subtracted. Data from 2015-11-04

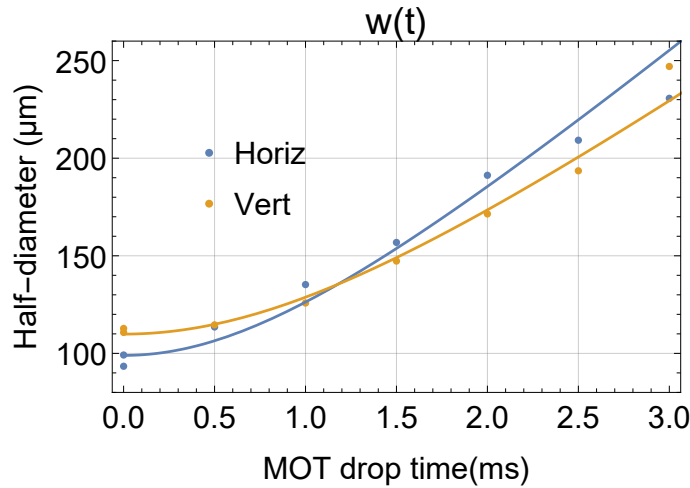


Figure 5.5: Expanding atomic cloud as a function of Time of Flight. Fitted with Equation 5.1. Data from 2015-11-04.

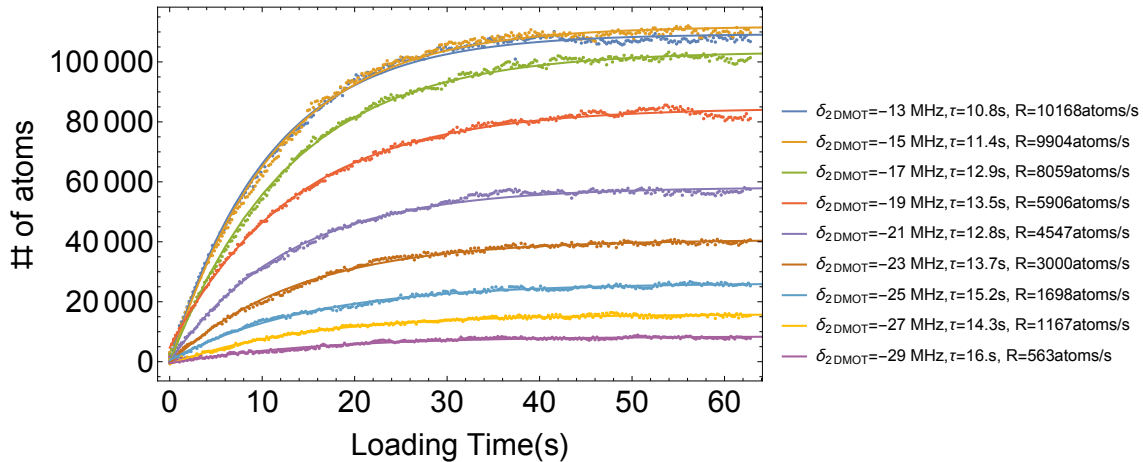


Figure 5.6: 3D MOT Loading versus 2D MOT Cooling light detuning. Single atom signal has been calibrated to convert the camera counts into the number of atoms. Extracted loss rates are $\alpha = 6.2 \times 10^{-2} / \text{s}$ (single body), $\beta = 2.1 \times 10^{-7} / \text{atom/s}$ (two body). Maximum loading rate $R = 10^4$ atoms. Captured from Andor Ixon EMCCD camera, no EM gain, 20ms exposure. 3D Cooling light detuning $\delta_{3D} = -13$ MHz. Sum of the six MOT beam intensity is 41mW/cm^2 . Ion pump pressure reading 8.2×10^{-9} Torr. UV LIAD is not used. Data from 2016-02-18.

to its low pressure typically around 10^{-9} Torr. When 2D MOT sources atoms, the loading is enhanced. The loading rate can be effectively tuned by the detuning of 2D MOT light respect to F=2 to F'=3 transition. This figure shows the number of atoms in 3D MOT after they are turned on.

5.2 Red-detuned Optical Dipole Trap

High power 1064 nm(or 1038 nm) single frequency fiber laser is used to trap ground state atoms. 13 W fiber amplifier(Optilab YDFA-40B-R) is seeded by 60mW 1064nm fiber-coupled DFB laser purchased from QPC Lasers. Generated light goes through switching AOM and waveplate based intensity noise-eater, finally delivered to the

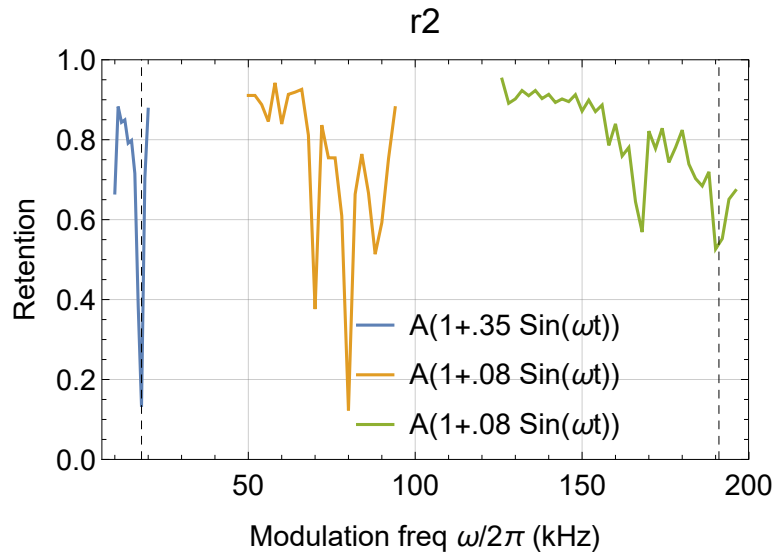


Figure 5.7: Parametric heating experiment of 1038 nm ODT to identify trap frequencies. Center site. Observed resonances at the trap modulation frequency $\omega/2 = 2\pi \times (9, 35, 40, 83, 95)$ kHz. Trap modulation time was 85 ms. Total of 750 mW distributed over 5 sites. The result is consistent with ~ 330 mW of 1038 nm on the center spot, generating 5.7 mK deep trap. We typically operate around 1-2 mK deep trap. Data from 2017-04-13.

main apparatus. Delivered light goes through a diffractive element to make five tightly focused spots at atom plane. See Figure 6.1 for optical set up.

Trap frequency measurements, Figure 5.7, suggest that the beam waists $w_0 \sim 2.5\mu\text{m}$, $z_R = \frac{\pi w_0^2}{\lambda} \sim 18\mu\text{m}$. Parametric heating experiment has been done by modulating the trap depth at the frequency ω , and resonance occurs where it is twice of the trap frequencies. Multiple resonance were observed and we attribute them to anharmonicity of the trap and imperfect DDS RAM mode control.

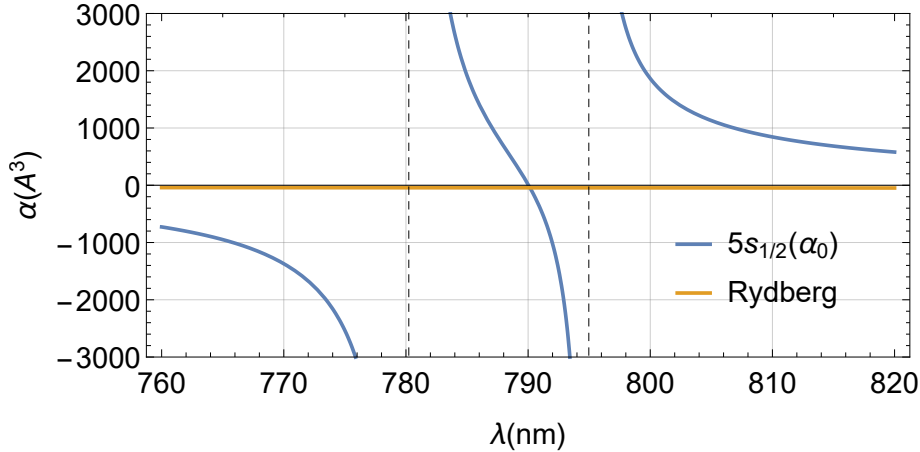


Figure 5.8: Dynamic polarizability of Ground state and Rydberg atoms near D1 and D2 lines(Dashed). Scalar $\alpha_0(\omega)$ polarizability is presented for Ground state atom. $\alpha_0(5s_{1/2} 770\text{nm}) = -1370\text{\AA}^3$, $\alpha_0(\text{Ryd}770\text{nm}) = -42\text{\AA}^3$

5.3 Blue-detuned 1D Optical Lattice

To trap atoms in a periodic lattice, we use 770nm laser which is 10nm blue-detuned from Rb D2 line at 780.24 nm. To satisfy the high power requirement, cavity enhanced frequency doubling cavity is employed providing a few watt of continuous-wave, single frequency 770nm light. Rydberg atoms experience ponderomotive force and exhibits negative polarizability for all wavelength, thereby low-intensity seeker. Ground state atoms can be high(low)-intensity seeker for given trapping light if the sign of dynamic polarizability is positive(negative) respectively.

Symbol	Description	Part Number
f_1	Fiber collimator	Thorlabs F260APC-780
f_2	f=250mm Lens	Newport KPX073AR.16

Table 5.1: Optics for creating 770 lattice

5.3.1 1D Lattice Design

Optical lattice is created by interfering two linearly polarized Gaussian beam of wavelength λ at a relative angle θ that determines the lattice constant

$$\Lambda = \frac{\lambda}{2 \sin(\theta/2)}. \quad (5.2)$$

With design choice of $\lambda = 770\text{nm}$ and $\theta = 30^\circ$, estimated lattice spacing is $\sim 1.48\mu\text{m}$. This technique has been used to trap atoms in 3D geometry as well[61]. We may expand our lattice to 2D or 3D by adding more pairs of beams, but with frequency shift imposed on each arms to avoid inter-modulation. Constructed 1D lattice pattern is captured using Erich Urban's calibrated imaging system, shown on Figure 5.9. Spatial profile along our quantization axis(z) shows expected sinusoidal interference pattern on Figure 5.10. $\lambda/2$ waveplates on each arm were optimized to maximize the amplitude. This is particularly important to minimize the residual ac stark shift on atoms, as they are low intensity seeker and finite but non-zero ac stark shift may affect atomic coherence.

Expected axial confinement from 770 lattice at certain optical power is presented on Figure 5.12, showing that for $200\mu\text{K}$ barriers, $\sigma_z \sim 200\text{nm}$.

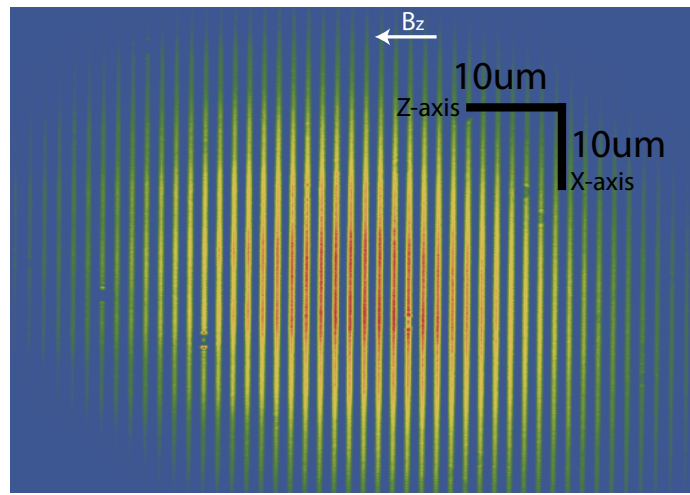


Figure 5.9: 1D lattice imaged with Erich Urban's calibrated imaging system. Light wavelength $\lambda = 770\text{nm}$ and measured lattice spacing $\Lambda = 1.59\mu\text{m}$. Gaussian beam sizes are $(w_x, w_z) = (38.7, 34.8)\mu\text{m}$. Imaged onto Watec Camera. Note the asymmetric pixel size of the camera. B_z indicates the quantization axis set by bias magnetic field.

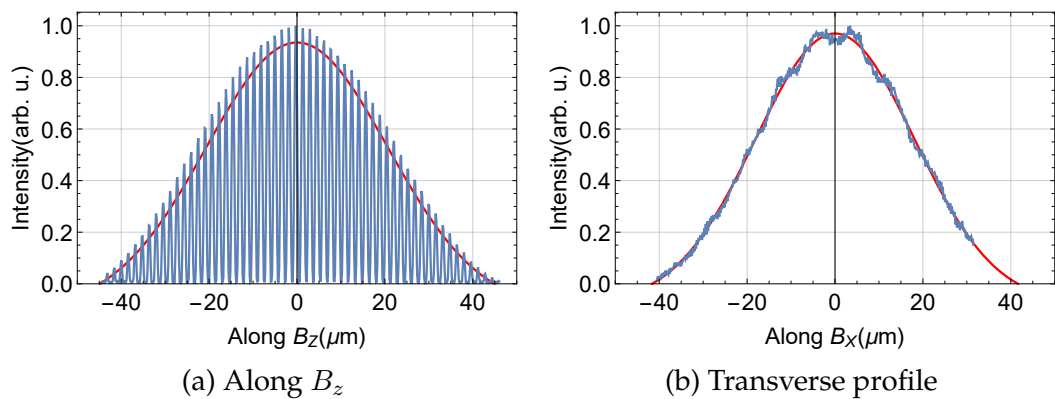


Figure 5.10: Sliced intensity profile of the 770 lattice

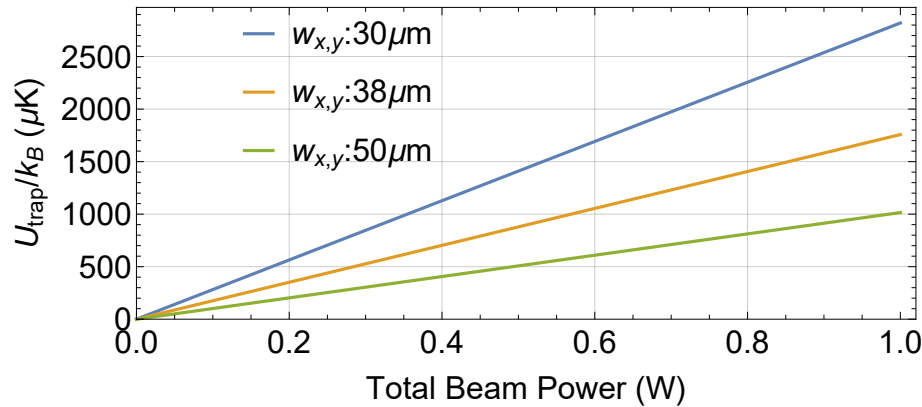


Figure 5.11: Peak trap barrier versus optical power in the 770 1D Lattice beams.

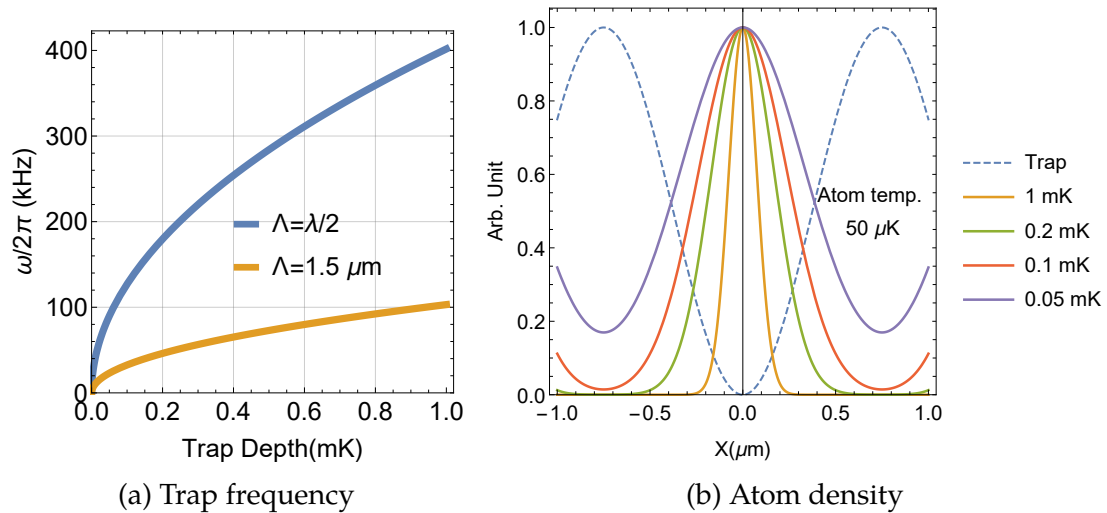


Figure 5.12: Trap frequency and atomic density in 1D Lattice. Wavelength of the lattice beam is $\lambda = 770\ \text{nm}$ and designed lattice constant is $\Lambda = 1.5\ \mu\text{m}$.

5.4 State preparation and coherent manipulation

5.4.1 Clock state Optical Pumping

Unless specified, all experiments begin from “Clock” state, which is magnetically insensitive to first order. After loading atoms to optical tweezers, atoms are in random Zeeman states. By shining linearly polarized light whose electric polarization matched with atomic quantization axis set by bias magnetic field, atoms are optically pumped to the “Dark” state($F = 2, m_F = 0$). The probability of preparing atoms at the desired state, state preparation fidelity, depends on polarization purity of the light and quantization axis mismatch. With highly linearly polarized light, fine-tuning of bias field is performed by minimizing depumping signal while scanning shim coil currents. State preparation fidelity is determined by the rate of two competing processes, optical pumping and depumping. Those rates can be experimentally measured by fitting the pumping and depumping curves to exponentially decaying function.

5.4.2 Global rotations with Microwave

One can also use magnetic dipole transition(M1) to drive transitions between hyperfine states. Now interaction term becomes $V = \vec{\mu} \cdot \vec{B}$. It is our interest what Rabi frequency will we get for given microwave power. Rabi frequency can be written as $\Omega = \langle i | V | f \rangle$ where i is initial state and f denotes final state and V is the interaction

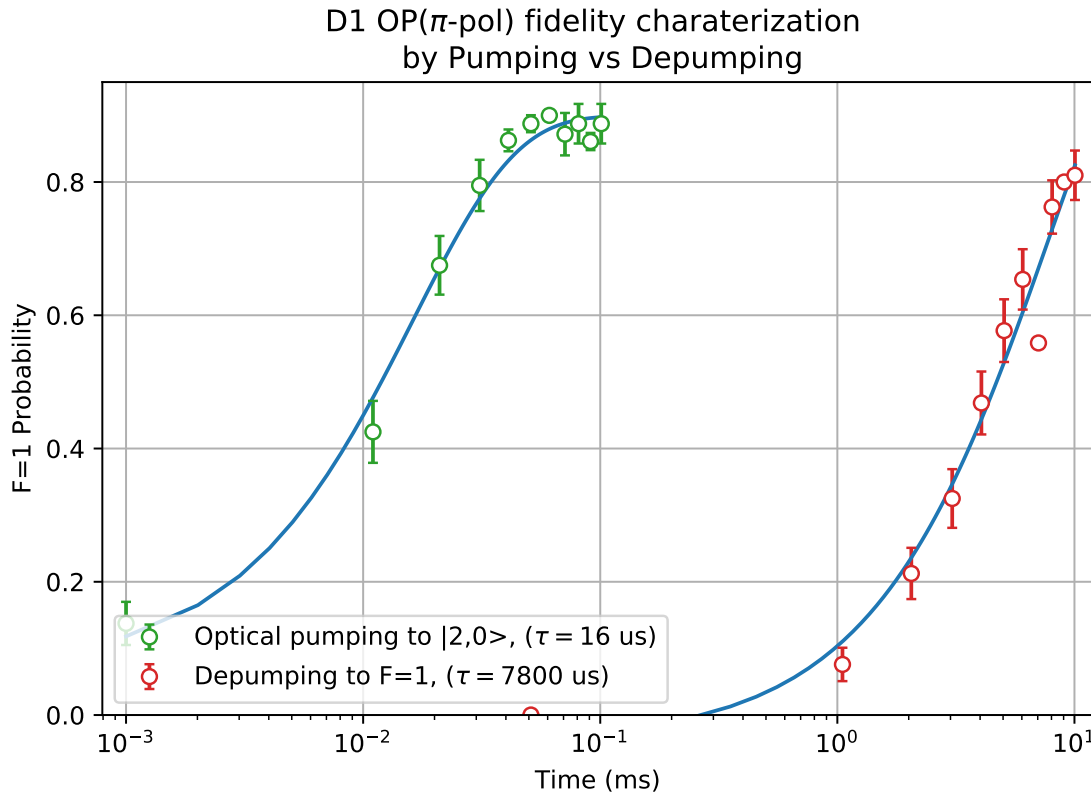


Figure 5.13: Optical pumping versus depumping curve. The ratio of these two competing process determine the fidelity

hamiltonian. For $5s_{1/2}$ level, the magnetic dipole interaction term is given as

$$V = -(\vec{\mu}_L + \vec{\mu}_S + \vec{\mu}_I) \cdot \vec{B} \quad (5.3)$$

where $\vec{\mu}_L = \frac{\mu_B}{\hbar} g_L \mathbf{L}$, $\vec{\mu}_S = \frac{\mu_B}{\hbar} g_S \mathbf{S}$ and $\vec{\mu}_I = \frac{\mu_B}{\hbar} g_I \mathbf{I}$ are orbital magnetic moment, spin magnetic moment and nucleus magnetic moment respectively. Suppose we have a weak magnetic field B_0 defining the quantization axis along z-direction. Then the

microwave radiation creates a magnetic field at the atom of the form

$$\mathbf{B} = B_0 \cos(\mathbf{k} \cdot \mathbf{x} - \omega t) \hat{\mathbf{z}} \quad (5.4)$$

For $S_{1/2}$ state, $L = 0$ therefore $\mu_L = 0$. With the weak bias field, now the interaction can be written as

$$V = \frac{\mu_B B_1}{\hbar} (g_S S_z + g_I I_z) \cos(\omega t) \quad (5.5)$$

For clock state transition,

$$\begin{aligned} |F = 2, m_F = 0\rangle &= \frac{1}{\sqrt{2}} \left[\left| -\frac{1}{2}, +\frac{1}{2} \right\rangle + \left| +\frac{1}{2}, -\frac{1}{2} \right\rangle \right] \\ |F = 1, m_F = 0\rangle &= \frac{1}{\sqrt{2}} \left[\left| -\frac{1}{2}, +\frac{1}{2} \right\rangle - \left| +\frac{1}{2}, -\frac{1}{2} \right\rangle \right] \end{aligned} \quad (5.6)$$

Then the Rabi frequency Ω coupling the two clock states is

$$\Omega_{MW} = \langle 2, 0 | V | 1, 0 \rangle = -\frac{\mu_B B_0}{2\hbar} (g_S - g_I) \quad (5.7)$$

where electron spin g-factor $g_S \sim 2.002$, and nuclear g-factor $g_I \sim 0$. By knowing the irradiance $E_e = \frac{P}{A} W/m^2$ of the radiation at the point where the atom sits, the Rabi frequency can be estimated as

$$\Omega_{MW} = 2\pi \times 204.093 \sqrt{E_e} (Hz) \quad (5.8)$$

For example, 3 W of uniform radiation in a rectangular opening($2'' \times 1.5''$) of

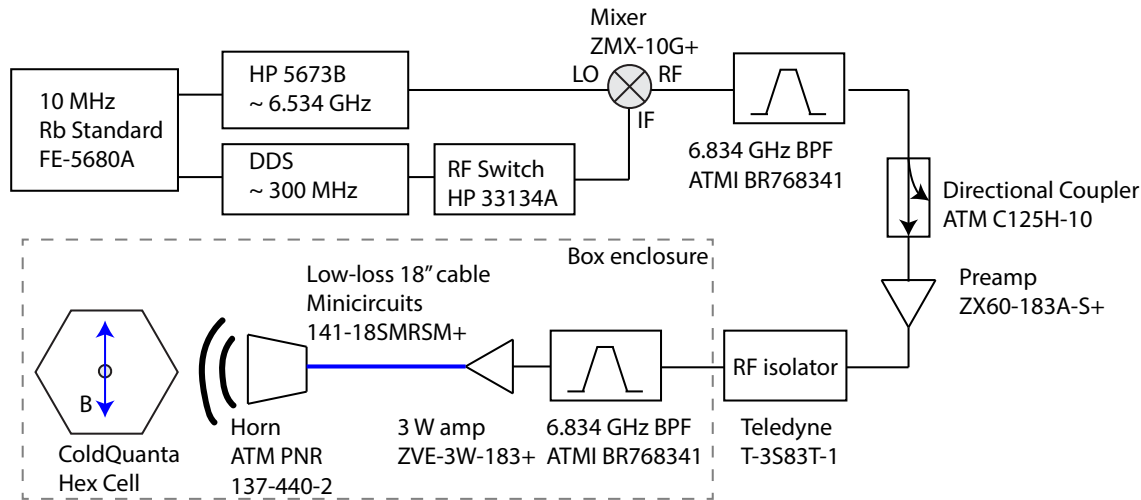


Figure 5.14: Microwave setup

ATM 137-440-2 Microwave horn gives $\Omega = 2\pi \times 8.035\text{kHz}$. The exiting aperture is narrower for horn designed to operate at higher frequencies. In Cesium, hyperfine splitting is 9.2GHz so if one uses ATM 112-440-6, designed for that frequency, the aperture is smaller ($1.63'' \times 1.18''$). This gives 10.034kHz of Rabi frequency. However the actual Rabi frequency is most likely be slower due to attenuation and reflections on the vacuum cell interfaces.

5.4.3 Local qubit rotation with Raman Laser

Alternative way of coherent manipulation of hyperfine ground states are using a Raman laser. Dipole-forbidden, magnetic dipole transition can be accessed by two-photon process. Because we are using lights, they can address atoms in individual sites separated by a few microns. We perform T2 measurement and obtained a result consistent with the result from microwave experiment.

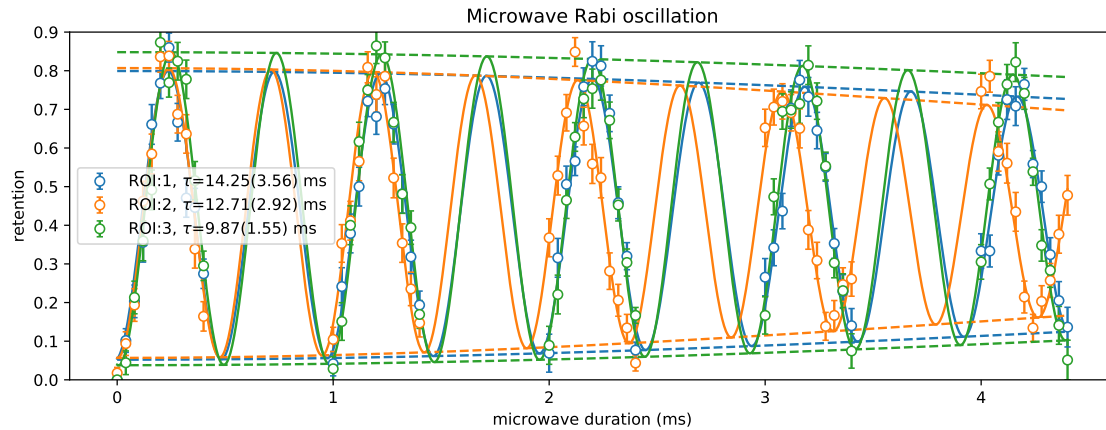


Figure 5.15: Global qubit rotations performed driven by a microwave pulse, showing driven coherence time of ~ 10 ms.

780 nm Raman laser uses same path as 780 nm Rydberg laser, making it useful for aligning them to atoms. The quality of Rabi flopping driven by Raman laser provide an assessment of inhomogeneity of the coupling or ac stark shift gradient. Observed decay of Rabi amplitude (Figure 5.16) is consistent with known axial atom distribution $\sigma_z \sim 7\mu\text{m}$ and 780 beam parameters.

5.4.4 Two-photon Rydberg excitation

Hyperfine ground states are two photon excited to accessible Rydberg states depends upon the scheme. Dipole selection rule($\Delta l = 0, \pm 2$) limits accessible states to $nS_{1/2}$ and $nD_{3/2}, nD_{5/2}$. D -states are chosen as they exhibit larger transition dipole moments. Excitation is achieved by two σ^+ photons with intermediate detuning of ~ -2 GHz. The scheme being used in thesis is shown in Figure 5.17.

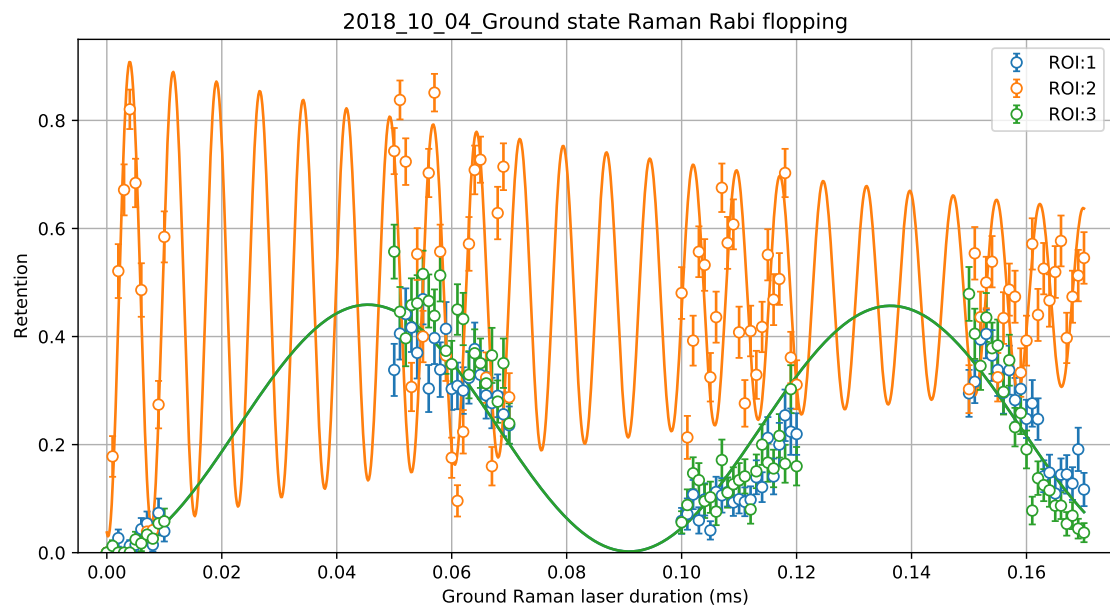


Figure 5.16: Rabi oscillation between clock states by Raman laser, detuned by ~ -60 GHz from $5s_{1/2} \rightarrow 5p_{3/2}$. Atoms in the neighboring sites are affected by gaussian wing of the Raman beam due to the differential ac stark shift of the Raman beam itself adjacent sites do not exhibit full population transfer. Data from 2018-10-04.

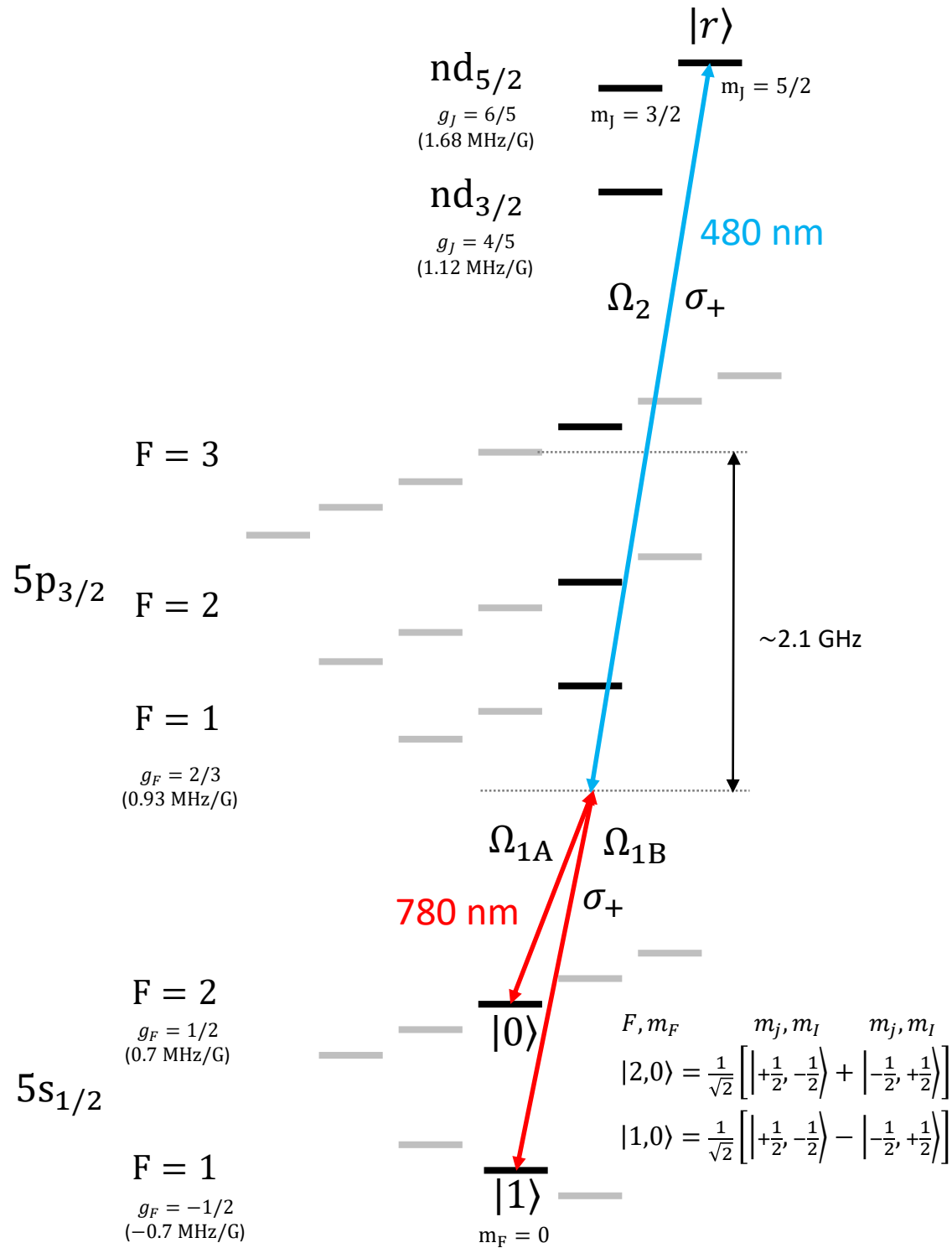


Figure 5.17: Two-photon excitation scheme for D states

6 EXPERIMENT SYSTEM CHARACTERIZATION

This chapter provides detailed characterization of the apparatus through single atom experiments. Laser cooled, magnetically trapped atoms are transferred to optical dipole trap, then optically pumped to the clock states. With those prepared single atoms, we detect them by collecting scattered light, perform spectroscopy and coherent excitation to Rydberg states.

6.1 Overview of single atom experiments

High level, visualized diagram of generic experiment sequence is shown in Figure 6.2. To help understanding of the relevant optical system, reprinted Figure 6.1 is presented. For those readers interested in details of components are advised to see the reference. As of 2019-04-22, generic experiment protocol begins with a short UV pulse on the square cell, knocking Rb atoms stuck on the glass wall. After allowing 2D and 3D MOT to accumulate cold atoms, dipole trap is turned on and transfer process begins. Brief time overlap $\sim 5\text{ms}$ is enough to capture atoms. Then Anti-Helmholtz coil(14G/cm) of 3D-MOT shuts off, letting uncaptured cold atoms to fall off. 2D MOT coils are continuously turned on, each drawing (-3, +3, -2.2, +2.8) amps. With a bias magnetic field turned on, we perform single atom imaging for population measurement typically taking $\sim 5\text{ ms}$, followed by optical pumping which takes $\sim 2\text{ms}$. Science phase can be configured with Rydberg lasers, Raman laser, microwave, and dynamic switching of ODT at will. Experiment cycle ends with final population measurement and clearing the trap, simply by dropping the

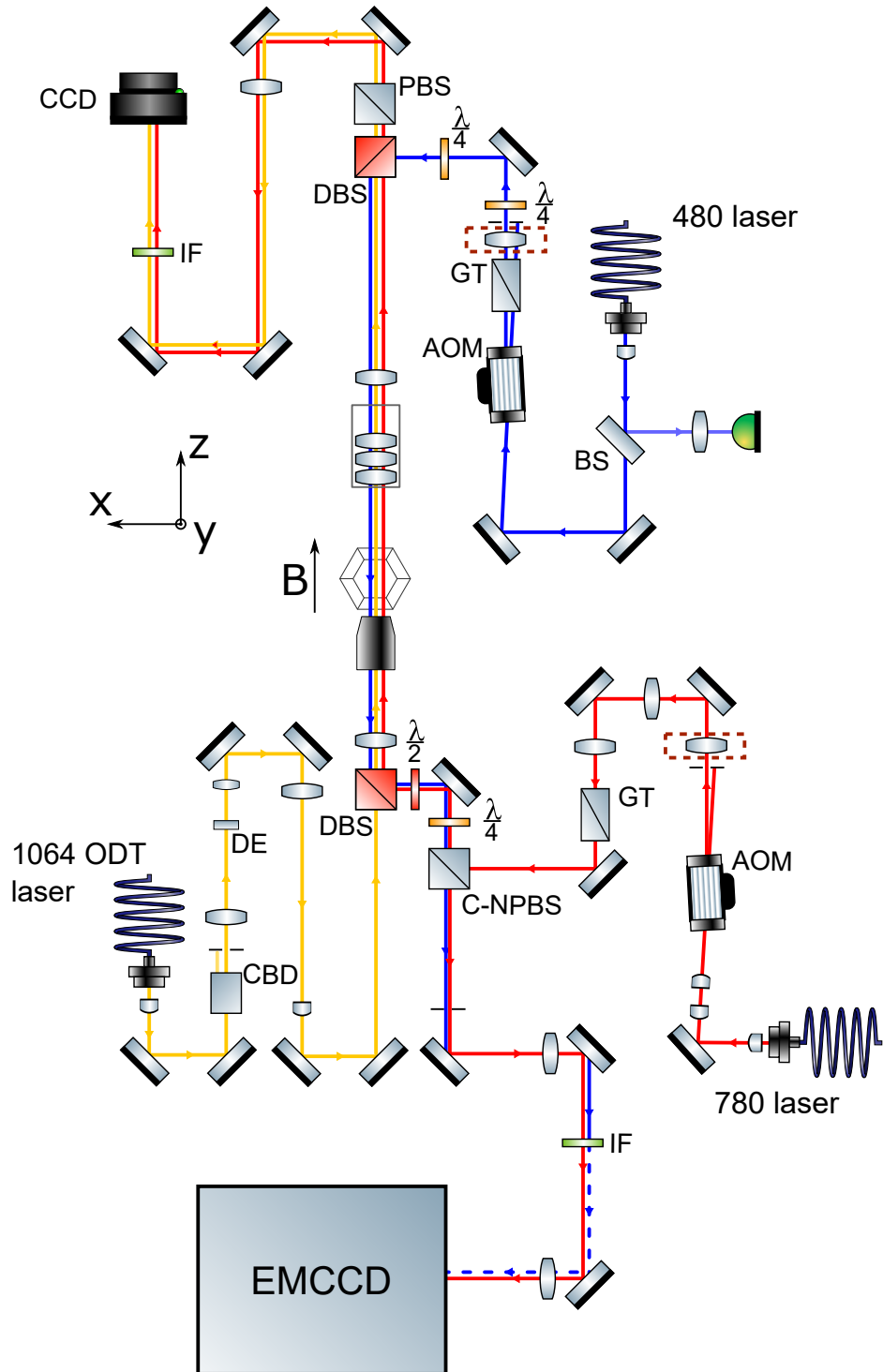


Figure 6.1: Reprinted from Ebert's thesis[56]. Optical train for addressing, ODT beams and imaging system.

ODT power. At the very beginning and the end, 780 and 480 beams are turned on very briefly to sample their location and noise-eaters.

6.2 Single atom imaging

The camera signal distributions for the cases of bright $|B\rangle$ and dark $|D\rangle$ states after probing for a time t are given by Poissonian distributions with means

$$\begin{aligned}\mu_D(t) &= (\gamma_D + \gamma_{bg})t + \mu_{CIC}, \\ \mu_B(t) &= (\gamma_B + \gamma_{bg})t + \mu_{CIC},\end{aligned}\tag{6.1}$$

where γ_{bg} , γ_D , and γ_B are the background, dark state, and bright state photo-electron production rates and μ_{CIC} is the background photo-electron rate due to clock induced charge (CIC). CIC is a Poissonian noise source intrinsic to EMCCD cameras and is independent of the exposure time. The photo-electron production rate from $|D\rangle$, given by γ_D , is negligible compared to γ_B and γ_{bg} , therefore we set $\gamma_D = 0$ for this section and consider the dark state distribution as a background distribution for the bright state. Both the large average number of photo-electrons, $\mu_D \sim 100$, and fluctuations in probe intensity and detuning broaden the expected single-atom signal. Therefore we can treat the photo-electron distributions, $S_B(s)(S_D(s))$, as Gaussian: $G(s, \mu, \sigma) = (2\pi\sigma^2)^{-1/2}e^{-(s-\mu)^2/2\sigma^2}$. For our system, the effect of spurious noise from CIC is lower than other sources of background $\gamma_{bg}t > \mu_{CIC}$ for our exposure times, therefore we can simplify the analysis by assuming a Gaussian distribution for all noise sources, see Figure 6.4. The width of the distributions,

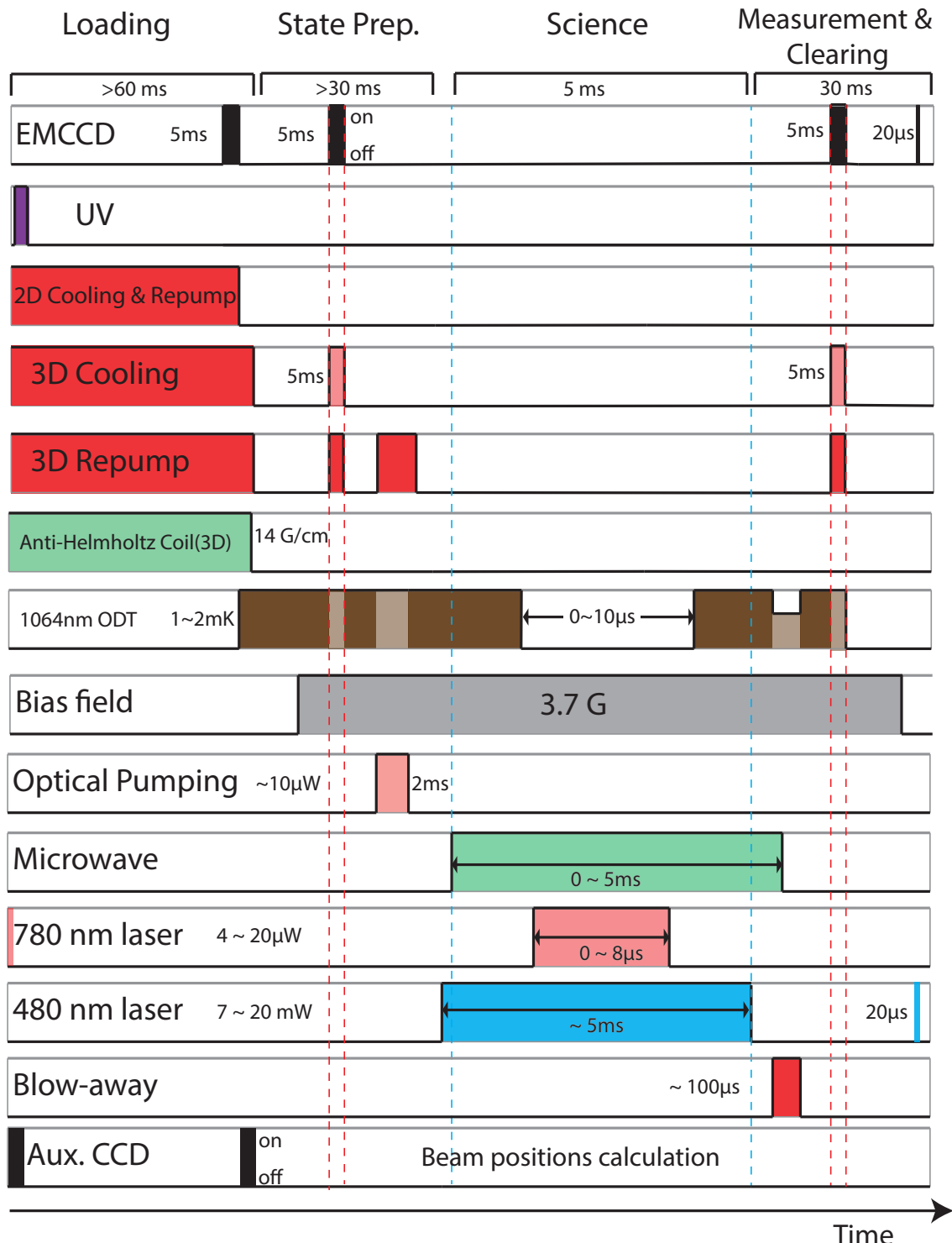


Figure 6.2: Generic experiment sequence for the new apparatus with hexagonal cell. Previous apparatus has same steps but without 2D MOT loading procedure. Opacity of the shaded region is a visualization of duty cycle.

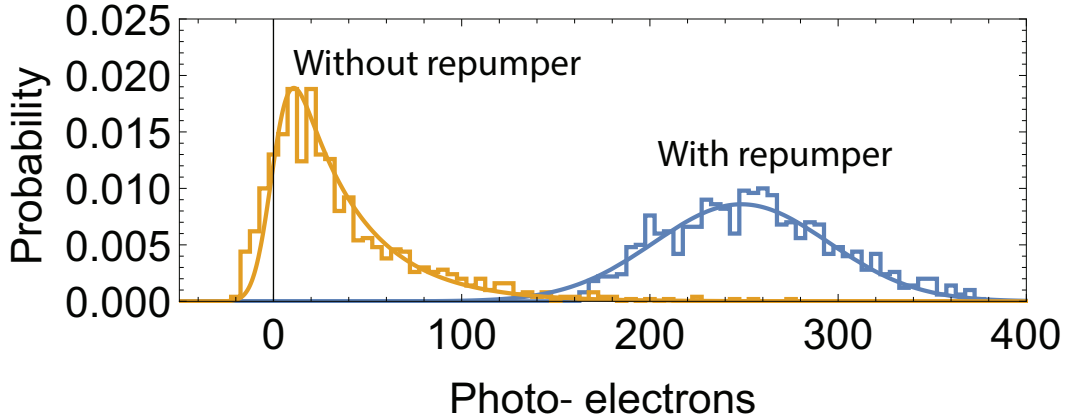


Figure 6.3: Signal from a $t = 4$ ms exposure of $|B\rangle$ with isotropic polarization, detuning $\delta \sim -1.5\gamma$, and intensity $s_0 \sim 10$, with (blue) and without (yellow) the extra $|D\rangle \leftrightarrow |e_D\rangle$ hyperfine repumping light. The blue solid line is a fit to a Gaussian distribution with no loss, and is used to extract parameters for the fit to the yellow curve. The yellow curve is a fit for the loss rate α in Equation (6.5) convolved with the background Gaussian distribution, all other parameters are fixed. The result of the fit yields a depumping rate of $\alpha = 1.8(1)$ ms $^{-1}$. The large loss rate for the case of isotropic polarization emphasizes the necessity of strict polarization control.

$\sigma_B(\sigma_D)$, are determined experimentally by fitting the distributions given by

$$\begin{aligned} S_D(s) &= G(s, \mu_D, \sigma_D), \\ S_B(s) &= G(s, \mu_B, \sqrt{\sigma_B^2 + \sigma_D^2}), \end{aligned} \tag{6.2}$$

to the relevant camera signal distributions with no loss.

The width of the background must be deconvolved from the width of the bright state distribution to correctly include the effect of losses during the measurement, although typically $\sqrt{\sigma_B^2 + \sigma_D^2} \approx \sigma_B$. For $|B\rangle$ a lossless measurement can be done by leaving the $|D\rangle \leftrightarrow |e_D\rangle$ hyperfine repumping light on during the camera exposure.

When losses during readout are included the bright state distribution, $S_B(s)$,

changes from Gaussian to something more complicated. If the atom in $|B\rangle$ is lost or depumped into $|D\rangle$ at time $t' < t$, then the atom will cease scattering photons and will only accumulate photo-electrons at γ_{bg} for a time $t - t'$. Therefore the mean signal for an atom initially in $|B\rangle$ undergoing a loss event at time t' is given by $\mu_B^*(t') = \gamma_B t' + \gamma_{bg} t + \mu_{CIC}$. This effectively adds a tail to the ideal Gaussian distribution. The normalized tail distribution, S_B^* , is given by

$$S_B^* = \left(\frac{\alpha}{1 - e^{\alpha t}} \right) \int_0^t dt' e^{-\alpha t'} G(s, \mu_B^*(t'), \sigma_B^*(t')), \quad (6.3)$$

where α is the combined heating induced loss and depumping rate and $\sigma_B^*(t') \equiv \sqrt{\sigma_B^2(t'/t) + \sigma_D^2}$. To the best of our knowledge, this integral cannot be solved analytically unless $\sigma_{bg} = 0$. For simplicity we also set $\gamma_{bg}, \mu_{CIC} = 0$ and Equation 6.3 becomes

$$S_B^* \simeq \frac{\alpha}{2(1 - e^{-\alpha t})} \sqrt{\frac{t}{\chi}} e^{s\gamma_B t/\sigma_B^2} [A_+ - A_-], \quad (6.4)$$

where $\chi \equiv \gamma_B^2 t + 2\alpha\sigma_B^2$ and

$$A_{\pm} \equiv e^{\pm(s/\sigma_B^2)\sqrt{\chi t}} \left[\text{erf} \left(\frac{s \pm \sqrt{\chi t}}{\sqrt{2}\sigma_B} \right) - 1 \right].$$

The original distribution with finite background can be recovered by convolving S_B^* with the background distribution $G(s, \gamma_{bg}t + \mu_{CIC}, \sigma_D)$. In the case of small loss this is a small effect and the time-intensive convolution operation is not necessary.

The full camera signal distribution model, S_B , can be obtained now by a weighted

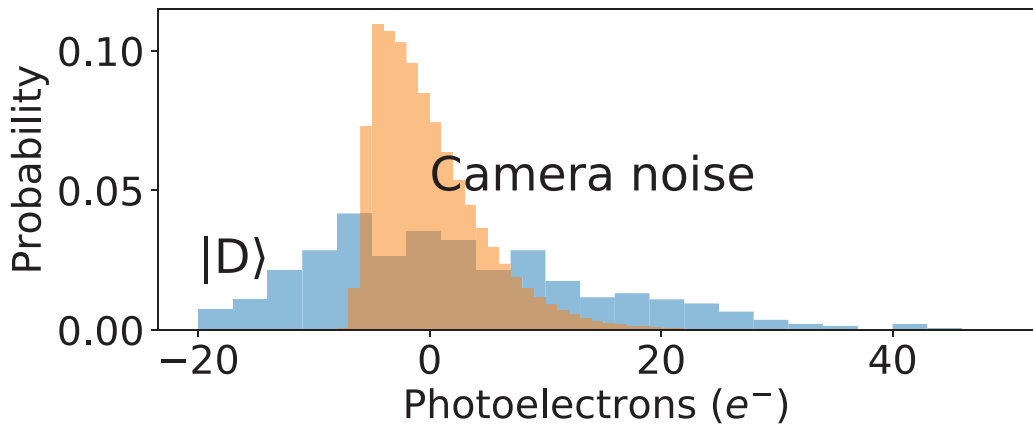


Figure 6.4: A comparison of the intrinsic camera noise in the 5 pixel region of interest (ROI) with the camera shutter closed (Yellow), and the photo-electron distribution for $|D\rangle$ (Blue). The data are centered about the mean of the distribution. Intrinsic camera noise is $\sim 22(e^-)^2$, while the dark state has variance of $\sim 196(e^-)^2$, due to additional noise in the experimental setup.

sum of the distribution with no loss, $S_B^{(0)} \equiv G(s, \mu_B, \sigma_B)$, and the tail distribution with a loss event, S_B^* :

$$S_B(s) = e^{-\alpha t} S_B^{(0)}(s) + (1 - e^{-\alpha t}) S_B^*(s) \quad (6.5)$$

An example histogram for $|B\rangle$ is shown under conditions of large depumping losses compared to no depumping loss in Figure 6.3.

6.2.1 Camera noise

EMCCD cameras have multiple sources of noise which broaden the camera count distribution including dark counts, CIC, EM gain register noise, and analog to digital converter (ADC) noise. Modeling is possible though complicated[62]. Cooling the

detector to -70 C reduces dark counts to a rate that is negligible on the scale of our $t < 10$ ms camera exposures. CIC is a Poissonian process, caused by impact ionization when reading out camera pixels, that gives the background photo-electron signal a long tail, see Figure 6.4. The long CIC tail is independent of exposure time and therefore sets a limit on how many photo-electrons must be collected to make a high fidelity threshold-based measurement. CIC events should lack any spatial correlation with photo-electron events, so the effect could be reduced further by including spatial information, such as an auto-correlation, into a multi-dimensional threshold cut.

By taking images with the shutter closed, the unavoidable CIC and ADC noise level of the camera is found to have a standard deviation of ~ 5 photo-electrons. The effect of environmental noise sources such as room lights, probe scattering from surfaces, and fluorescence from untrapped background atoms are minimized by a narrow bandpass interference filter and a spatial filter, but still contribute to the background at a combined rate of 29 photo-electrons/ms averaged over the exposure time. Arbitrarily selecting more pixels for ROI will add these noise sources on top of the signal and broaden the histogram peaks, limiting the maximal fidelity. Fluorescence from neighboring sites can contribute to the signal as well. This crosstalk is 2% of the single atom signal per site. For instance with a $\sim 150 e^-$ single atom signal, the neighboring site shows a $\sim 3 e^-$ signal.

6.2.2 Determination of region of interests

In a noise-free detector all pixels that contain signal could be included in the ROI. In practice detector noise prevents this because including more pixels leads to more noise. To maximize Signal-to-Noise Ratio (SNR), a few dominant pixels are chosen for the ROI. Since our trap location is stable, we can set the regions of interests based on high SNR optical molasses imaging. We take several thousand camera shots containing stochastic loading events on five sites. Since atom loading events are uncorrelated we perform independent component analysis (ICA)[63] to infer the locations of the independent emitters. The result of the analysis is shown in Figure 6.5. Most of the signal from each site is localized onto 4-5 pixels.

Intrinsic camera noise is uniform over pixels so the number of included pixels determines the noise contribution from the camera. To keep the effect the same at all five sites we choose the same number of pixels at each site. The maximum number of pixels that gave us non-overlapping ROIs was five, which contained 76 – 92% of the photo-electron counts based on the ICA.

6.2.3 Dipole emission pattern

The dipole emission pattern is not isotropic, and therefore a simple solid angle estimate based on the lens numerical aperture (NA) is not sufficient. When emitting a circularly polarized photon, the emission pattern is that of a rotating dipole. The fraction of light collected by a lens with numerical aperture NA is:

$$\text{CE} = \int_{\theta_i}^{\theta_f} \int_{-\phi_0}^{\phi_0} \frac{3}{16\pi} (\cos^2 \theta + 1) d\phi \sin \theta d\theta \quad (6.6)$$

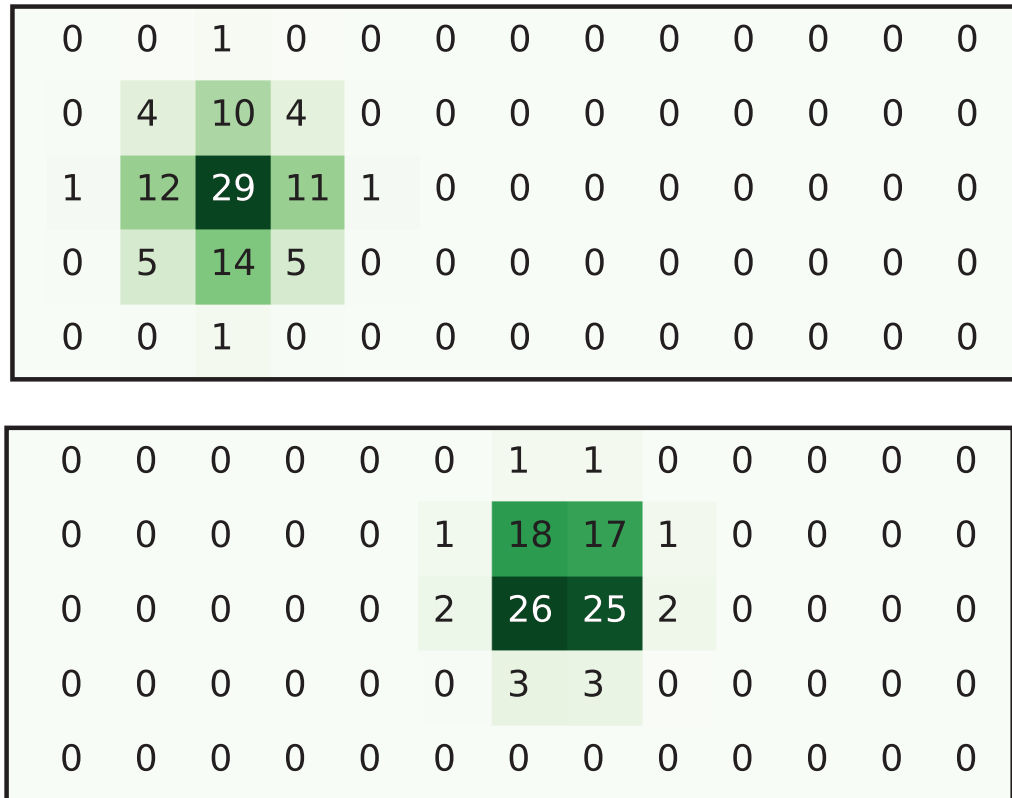


Figure 6.5: Fluorescence from individual atoms resolved by Independent Component Analysis(ICA). Numbers are the percentage of normalized signal received by that pixel. ICA results for ROI#0(upper) and #2(lower) are shown.

where CE denotes collection efficiency, θ is polar angle from the atom's quantization axis and ϕ is azimuthal angle. For a lens with a given NA, $\theta_i = \frac{\pi}{2} - \arcsin(\text{NA})$, $\theta_f = \frac{\pi}{2} + \arcsin(\text{NA})$, $\phi_0 = \arcsin\left(\sqrt{\frac{\text{NA}^2}{\sin^2\theta} - \frac{1}{\tan^2\theta}}\right)$. In our configuration, the quantization axis makes an angle α with the optical axis of collection. Therefore in the lens' spherical coordinates the integrand in parentheses becomes

$$\cos^2\theta \rightarrow [\cos(\alpha)\cos(\theta) - \sin(\alpha)\sin(\theta)\cos(\phi)]^2 \quad (6.7)$$

In our setup $\alpha = 60^\circ$ and $\text{NA} = 0.40$, which yields a collection efficiency of $\text{CE} = 3.94\%$ which is slightly less than for the case of isotropic emission which would give $\text{CE} = 4.17\%$.

6.3 Single-atom Rydberg Spectroscopy

First step before manipulation of single atom Rydberg states are to perform spectroscopy to find the Rydberg levels. Laser-cooled, optically trapped Single atom has cleaner environment for spectroscopy and also provides means to detect the Rydberg atom. Because ground state atoms are trapped by red-detuned light, they are high-intensity seekers. However, ponderomotive interaction of valance electron of Rydberg atoms are low-intensity seeker. Therefore Rydberg atoms are anti-trapped from the optical tweezers. Detecting the loss of atoms after applying Rydberg excitation pulses gives indirect way to detect them. Typically dipole trap is turned off for short period of time during Rydberg excitation pulses to allow cleaner environment. Figure 6.6 is a good representative case to compare trap-on and off case, showing that the presence of red-detuned dipole trap requires more energetic Rydberg beams to excite atoms.

6.4 Ground State Coherence

The qubit state being used is “Clock state”, and is less perturbed by environment than other states because of its insensitivity to the linear Zeeman shift. However, quadratic Zeeman shift and light shifts do exist and their instability can affect the

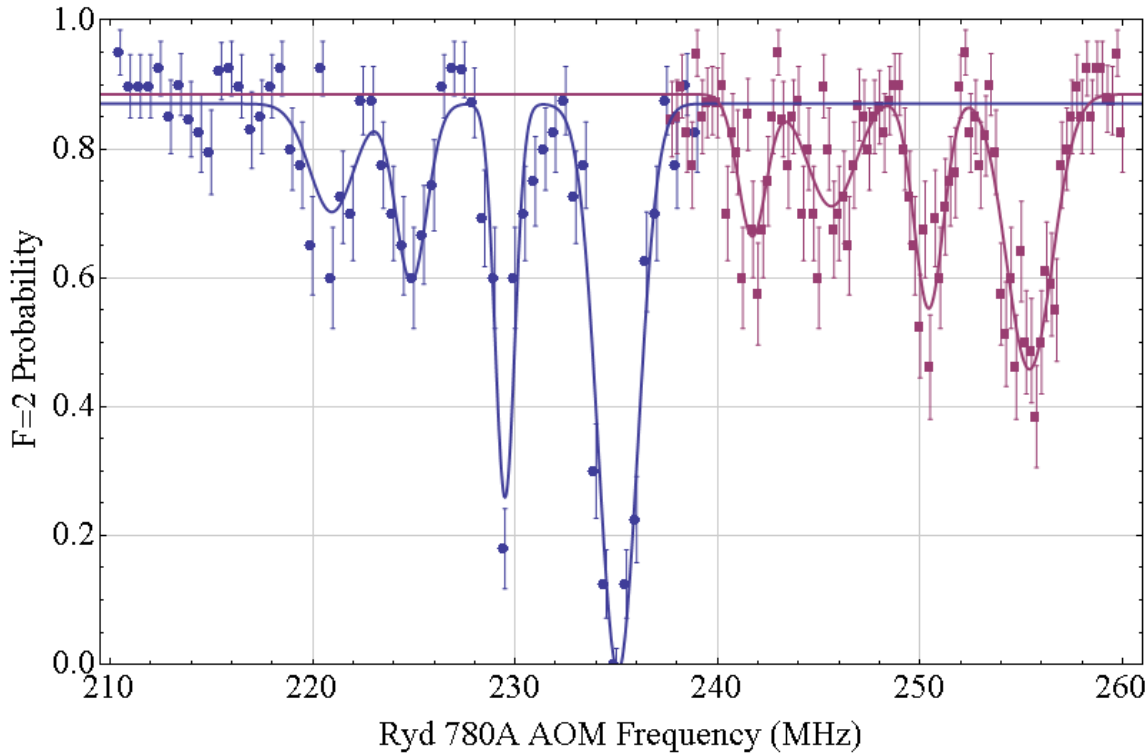


Figure 6.6: Rydberg two-photon spectroscopy of 111d states with and without dipole trap during excitation pulse. Trap on(Purple) and Trap off(Blue). Data from 2014-07-30

coherence of the qubit. Fluctuations of magnetic field is contributes to quadratic Zeeman shift, and atomic motion within optical dipole trap also gives inhomogeneous dephasing mechanism. In other words, coherence time of ground states can be used as a sanity check and extract the temperature atoms and magnetic field stability in the apparatus. Coherence is measured by Ramsey-style experiment where two $\pi/2$ pulses are separated by a time delay, and watching the envelope of oscillation decaying as a function of the gap. Fitting the contrast of oscillation[64], T_2^* can be obtained.

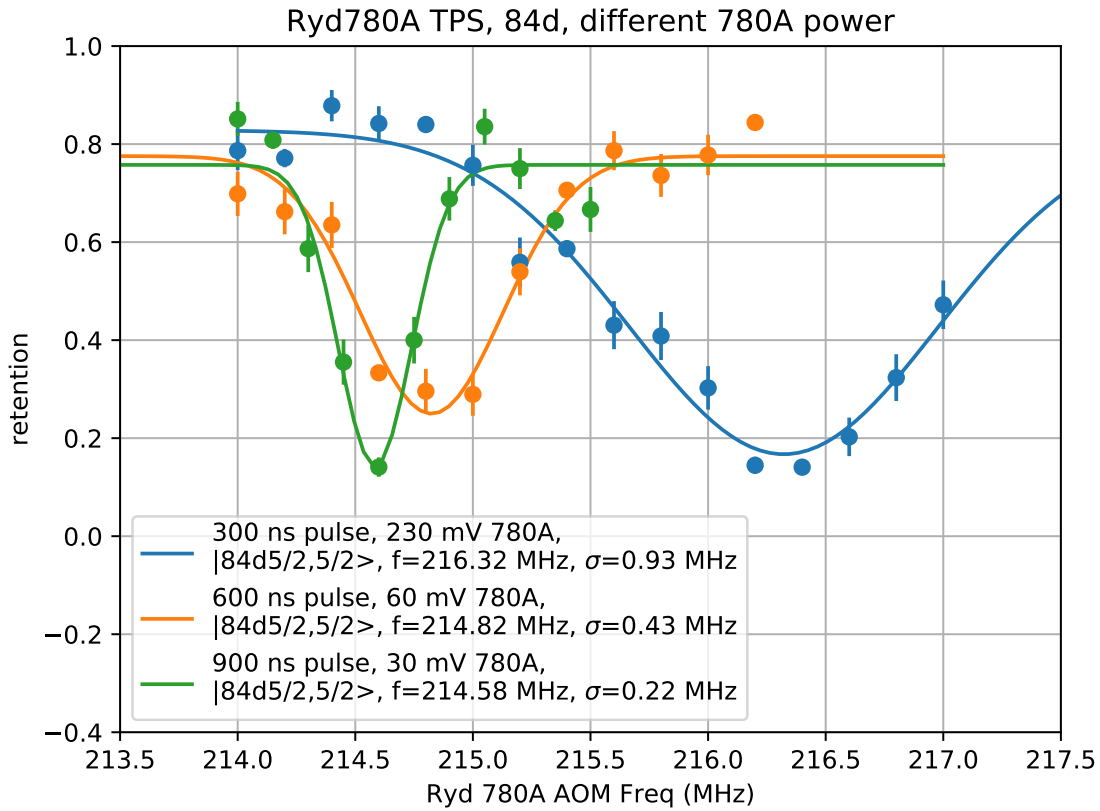


Figure 6.7: Two-Photon Spectroscopy to search Rydberg transitions. Looking for 84D states with different 780 optical power.

$$\alpha(t) = \left[1 + 0.95 \left(\frac{t}{T_2^*} \right)^2 \right]^{-3/2} \quad (6.8)$$

Temperature-limited dephasing time[64] is

$$T_2^* = 0.97 \frac{2\hbar}{\eta k_B T} \quad (6.9)$$

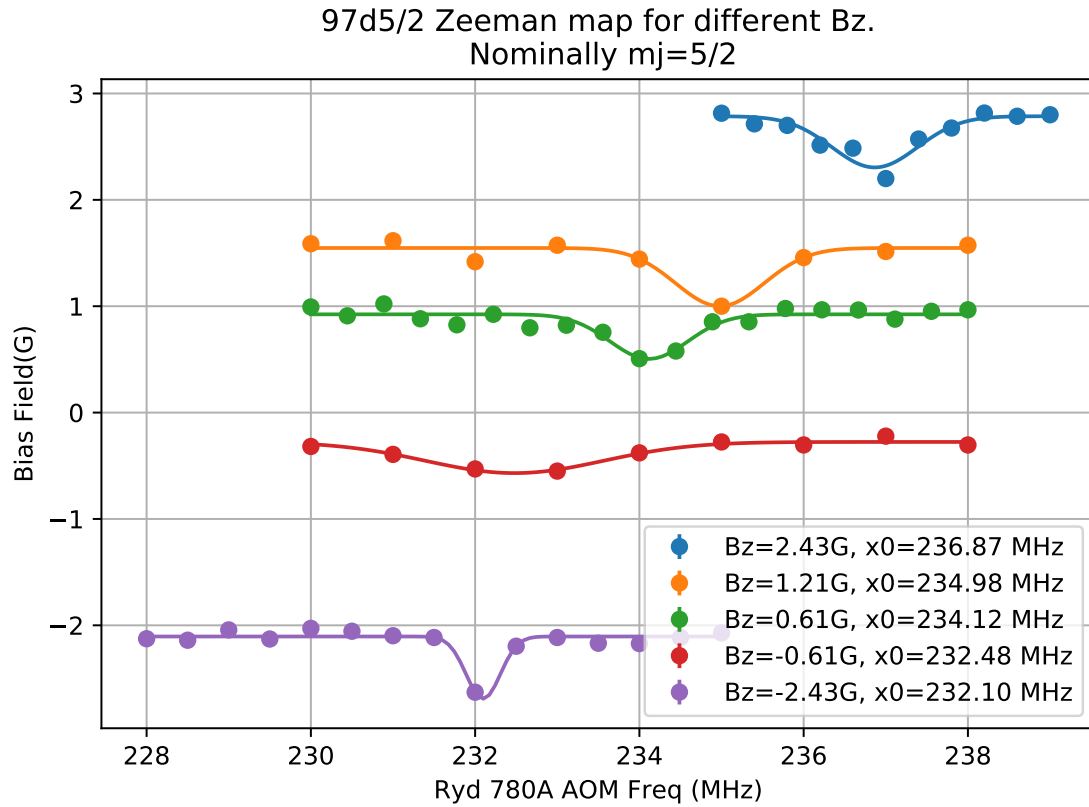


Figure 6.8: Zeeman map of $|97d_{5/2}, m_j = 5/2\rangle$. Y-axis also represents Rydberg loss. Data from 2018-04-25.

where η is the ratio of the hyperfine splitting ω_{hfs} and effective dipole trap detuning Δ_{eff} . In our case $\omega_{hfs} = 2\pi \times 6.834\text{GHz}$ and 1064 nm ODT gives $\eta \sim 6.67 \times 10^{-5}$, see derivation at (Section 2.25).

6.5 Rydberg Ramsey

Ground-Rydberg Ramsey provides direct measurement of differential ac stark shift between the states. Exemplary case is shown on Figure 6.11, where the Rydberg

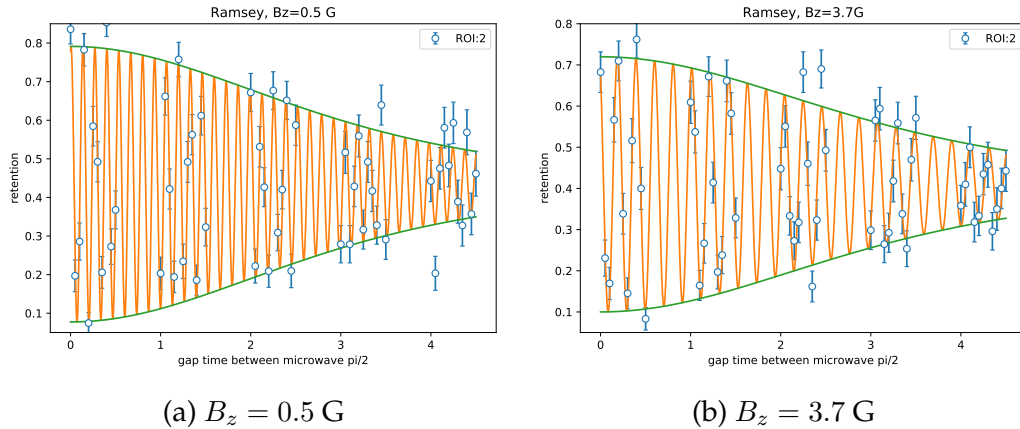


Figure 6.9: Ground Hyperfine Clock states coherence at different bias magnetic field.

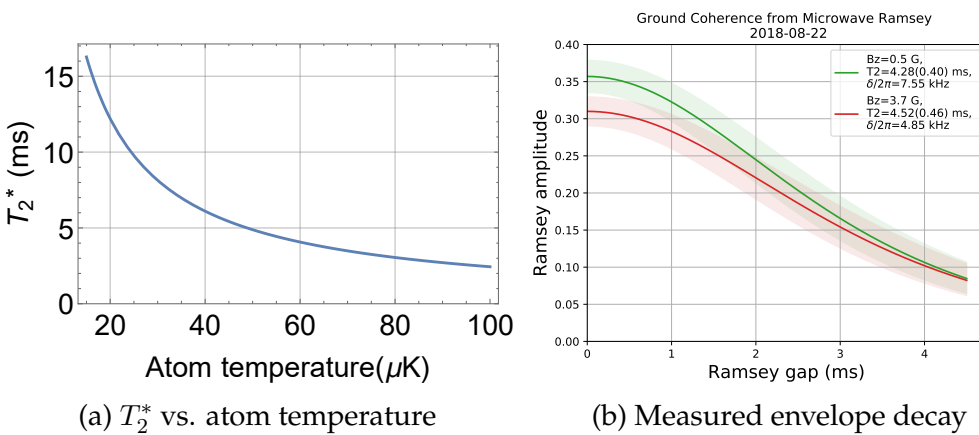


Figure 6.10: Atom temperature and Ground Clock state coherence. Measured $T_2^* =$ for $B_z = 0.5$ and 3.7 G . suggesting the atom temperature $T_{\text{atom}} \leq 60 \mu\text{K}$

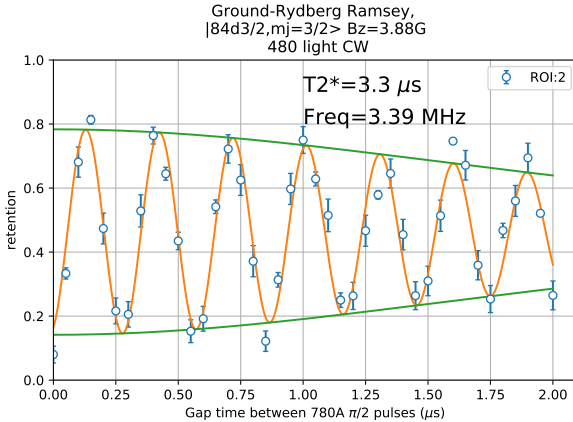


Figure 6.11: Ground-Rydberg Ramsey experiment. $|2, 0\rangle \leftrightarrow |84d_{3/2}, m_j = 3/2\rangle$, single atom. Data from 2018-09-05

780A light was turned off during the gap time while 480 light kept on. This sequence measures ac stark shift imposed by 780 photon on $|2, 0\rangle \leftrightarrow |84d_{3/2}, m_j = 3/2\rangle$, and in this particular case was $\delta = 2\pi \times 3.39\text{MHz}$. Coherence time may contain more information, such as Rydberg-Rydberg dephasing or time-varying electric fields.

6.6 Single atom Ground-Rydberg Rabi oscillation

Good Ground-Rydberg Rabi oscillation is usually at the paramount importance, as we aim for high fidelity Rydberg state preparation and quantum gates. Typical two photon Rabi frequency we get is $\Omega = 2\pi \times 1\text{ MHz}$ with single photon Rabi frequencies of $\Omega_{780} \sim 2\pi \times 200\text{ MHz}$ and $\Omega_{480} \sim 2\pi \times 20\text{ MHz}$, with intermediate detuning of $\Delta \sim 2\pi \times -2.07\text{ GHz}$, but may vary depends upon Rydberg levels and beam parameters. From the previous apparatus typical Ground-Rydberg coherence is $\sim 6 - 10\mu\text{s}$, and in the new apparatus we typically get a factor of two or three

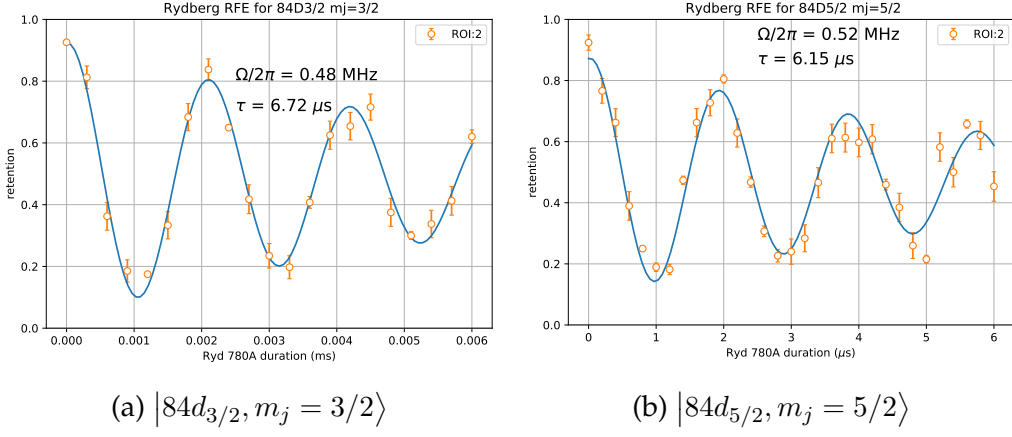


Figure 6.12: Ground-Rydberg Rabi Oscillation 84d states

shorter, and we are on the way to improve it.

6.7 Electromagnetic interference on Rydberg atoms

Transitions between adjacent Rydberg states have large dipole matrix element and energy separation in GHz scale. Therefore Eletro-Magnetic Interference(EMI) from modern wireless devices or high-speed electronics can affect the atoms. We have experimentally observed EMI affecting two new Rydberg levels, $111d_{5/2}$ and $97d_{5/2}$. Previous grad Larry reported[65] $102d_{5/2}$ is also susceptible to GSM cellular band. As a reference to avoid EMI, see the Figure 6.13.

This bug may be turned into a feature by employing Electromagnetically Induced Transparency(EIT) to be used as an atomic rf receiver[67–71].

Rydberg-Rydberg shifts provides means to calibrate a static electric field that atoms experience. With a microwave system capable of driving 5-8 GHz transition, the magnitude of field can be extracted from spectral shift between Rydberg-

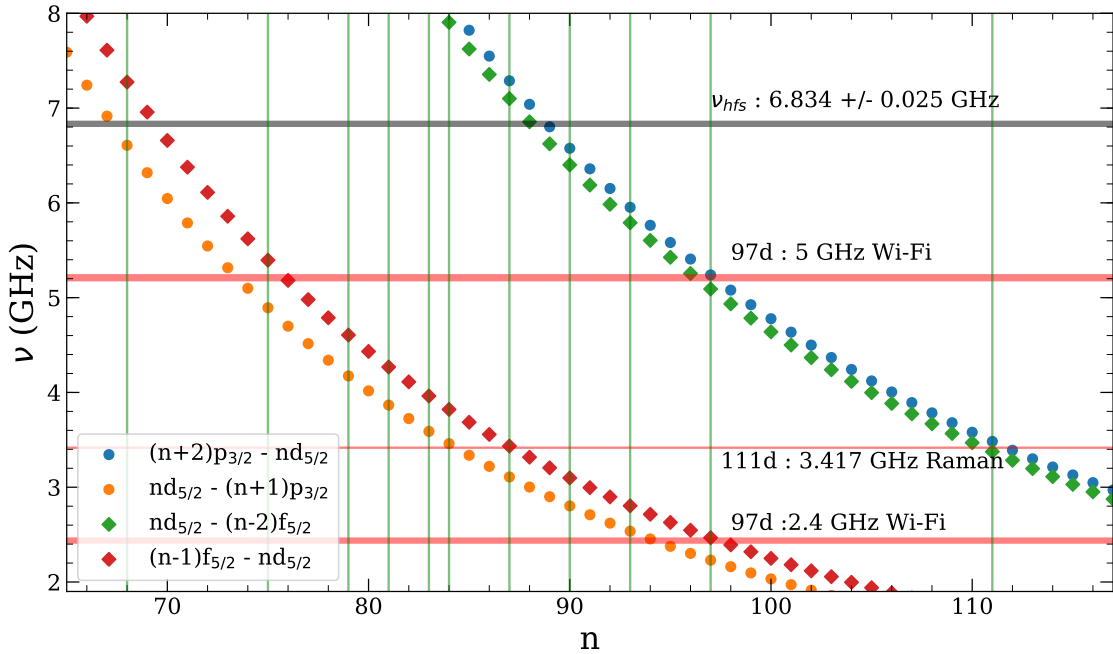


Figure 6.13: Dipole-allowed transitions from $nd_{5/2}$ state and strong rf sources in the lab. Vertical lines (Green) are accessible states limited by frequency tuning range as of 2019-04-08. Rydberg-Rydberg transition frequencies are calculated by ARC[66]

Rydberg transition.

6.7.1 External fields on 111d state

3.417 GHz RF radiation was causing dephasing of Ground-Rydberg Rabi oscillation of $|111d_{5/2}, m_j = 5/2\rangle$, as shown on Figure 6.14a. 3.417 GHz RF is only a few tens of MHz detuned from the transition $|111d_{5/2}, m_j = 5/2\rangle \leftrightarrow |113p_{3/2}, m_j = 3/2\rangle$, which is at 3.48 GHz. Two-level picture breaks down due to an extra field coupling two Rydberg states, creating three level Λ system. The Rabi frequency for the extra field was much stronger, thereby as soon as the ground state is excited to 111d,

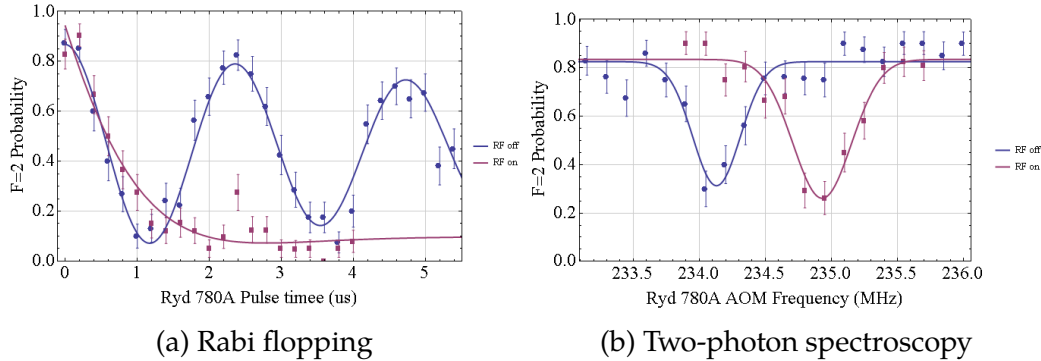


Figure 6.14: Rabi flopping and two-photon spectroscopy of $|2, 0\rangle \leftrightarrow |111d_{5/2}, m_j = 5/2\rangle$ transition, with and without near-resonant 3.417 GHz rf. Field on (Purple) and off(Blue). Spectral feature shifts by $2\pi \times 1.6$ MHz. Without the field, Ground-Rydberg Rabi frequency is $\Omega = 2\pi \times 421$ kHz and decay time $11\mu\text{s}$. Data from 2014-07-31.

the microwave field transfers the Rydberg population to the other Rydberg state. This causes rapid dephasing between ground-Rydberg manifold. Furthermore, the microwave field is originating from a rf leakage, meaning the polarization and intensity are poorly controlled. Resulting effect is the time-varying spectral shift of Rydberg two photon resonance feature, shown on Figure 6.14a.

6.7.2 External fields on 97d state

Dephasing observed on $97d_{5/2}$ state is believed to be caused by 5 GHz Wifi band, and possibly 2.4 GHz as well. $|97d_{5/2}, m_j = 5/2\rangle$ has dipole-allowed transitions to $|99p_{3/2}, m_j = 3/2\rangle$ and $|95f_{5/2}, m_j = 5/2\rangle$ around 5.2 GHz, overlapping to **5 GHz wifi bands** ranging 5180-5240 MHz. It also has transitions to $|96f_{5/2}, m_j = 5/2\rangle$ around 2.4 Ghz, which are very close to **2.4 GHz (802.11b/g/n/ax) wifi bands** ranging from 2412-2462 MHz.

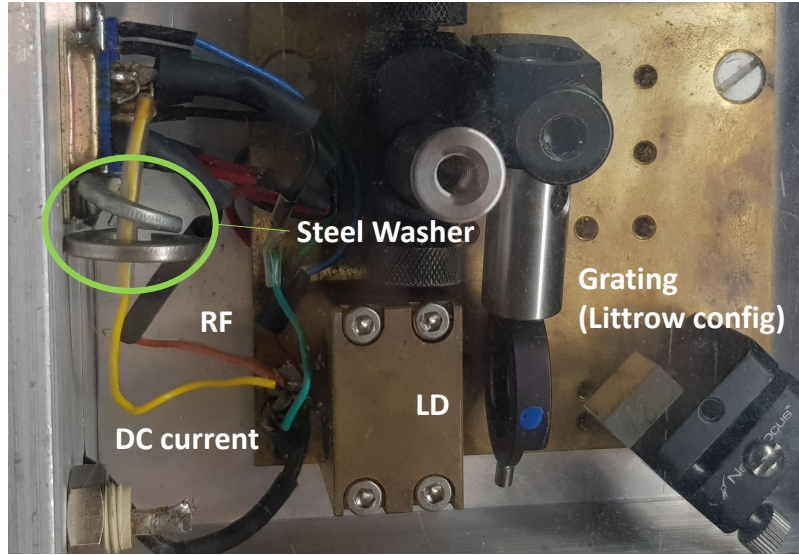


Figure 6.15: Raman external cavity diode laser system with rf modulation input. Steel washer[72] hanging on DC input connection helps impedance-matching 3.417 GHz rf input. However it acts as poor rf radiator that the efficiency susceptible to acoustic and mechanical noise.

Despite the EMI shielding surrounding the apparatus, there was bypassing route to atoms due to a 3 W rf amplifier located outside of the box, fed through the microwave horn pointing the atoms. We suspect the ambient rf noises were picked up by the amplifier, amplified, and headed to atoms. This hypothesis was tested by observing the dephasing dynamics of Rabi oscillations with different rf configurations, shown on Figure 6.16.

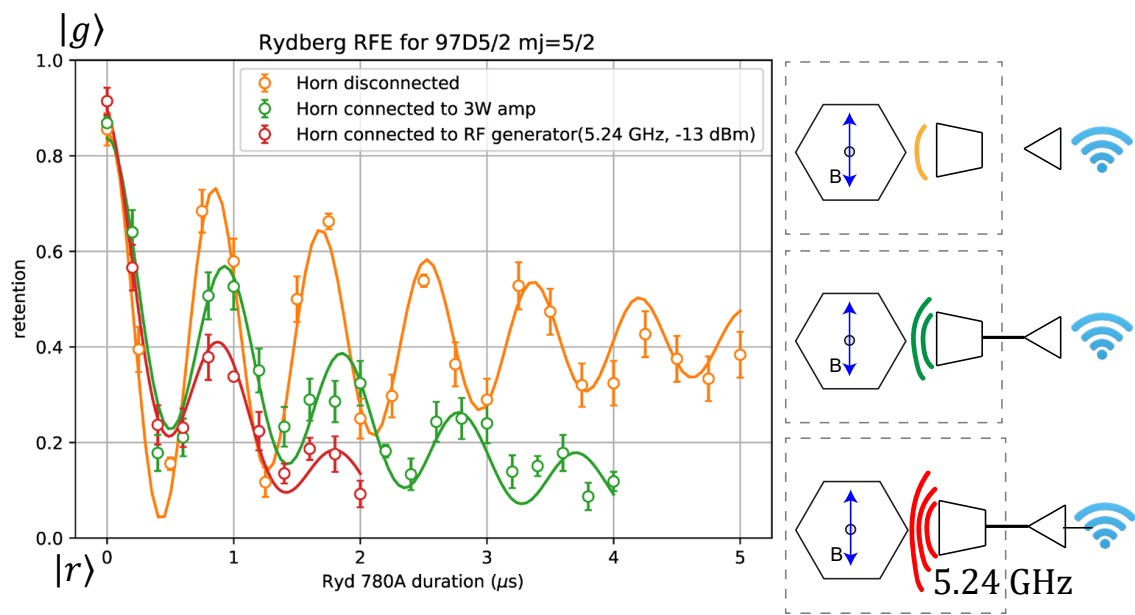


Figure 6.16: Severely dephasing Rabi oscillations between $|2, 0\rangle \leftrightarrow |97d_{5/2}, m_j = 5/2\rangle$ states due to external microwave source driving Rydberg-Rydberg transitions.

7 FREQUENCY DOUBLING

Single frequency, narrow-linewidth, high power light sources were needed to meet our experiment demand. Two wavelengths of our interests are 480 nm and 770 nm, each for Rydberg excitation and blue-detuned optical lattice respectively. Solid state lasers have limited power output at visible wavelengths, therefore we instead utilize nonlinear optical process to generate them from high power infrared lasers.

Photons do not interact with each other in the free space, but if nonlinear medium is employed, they can be combined and generate frequency upconverted photon. We use second harmonic generation which combines two photons of same energy to a single photon. This process is mediated by nonlinear crystal, efficiency enhanced by introducing a ring cavity. We begin with a framework which interconnects the incoming fundamental electric field \mathbf{E} , and harmonic field \mathbf{P} . The relationship is governed by $\chi^{(2)}$ susceptibility tensor and nonlinear coefficients d_{ij} .

$$\begin{bmatrix} P_X \\ P_Y \\ P_Z \end{bmatrix} = \begin{bmatrix} d_{11} & d_{12} & d_{13} & d_{14} & d_{15} & d_{16} \\ d_{21} & d_{22} & d_{23} & d_{24} & d_{25} & d_{26} \\ d_{31} & d_{32} & d_{33} & d_{34} & d_{35} & d_{36} \end{bmatrix} \begin{bmatrix} E_X^2 \\ E_Y^2 \\ E_Z^2 \\ 2E_Y E_Z \\ 2E_Z E_X \\ 2E_X E_Y \end{bmatrix} \quad (7.1)$$

In practice fundamental and harmonic fields are chosen to be linearly polarized, parallel to crystal axis and propagating along another axis. In this simplified

condition, harmonic polarization is

$$p_i = d_{ij} E_j^2 \quad (7.2)$$

where $i, j \in \{x, y, z\}$ or $\{1, 2, 3\}$.

For Type-I Non-Critical Phase Matching(NCPM) of LBO, harmonic field polarization is P_Y with fundamental field E_Z propagating along y-axis. Then above expression for the polarization can be simplified to

$$p_Y = d_{32} E_Z^2 \quad (7.3)$$

In case of PPKTP, fundamental and harmonic field have same z-polarization, and effective nonlinear coefficient is $d_{eff} = \frac{2}{\pi} d_{33}$, where the reduction factor of $\frac{2}{\pi}$ is introduced due to Quasi Phase Matching. Then the harmonic polarization is

$$p_Z = d_{eff} E_Z^2 \quad (7.4)$$

Typical interest in nonlinear conversion is the efficiency of the process. Simplest situation is where fundamental plane wave at angular frequency ω and beam size w enters nonlinear crystal of length l , index of refraction n for fundamental field. Then the power of harmonic wave is

$$\begin{aligned} P_{2\omega} &= P_\omega^2 \frac{2\omega^2 d_{NL}^2 l^2}{\pi \epsilon_0 c^3 w^2 n^3} \text{sinc}^2 \left(\frac{\Delta k l}{2} \right) \\ P_{2\omega} &= E_{NL} P_\omega^2 \end{aligned} \quad (7.5)$$

where $P_{2\omega}$ is the power of harmonic frequency, P_ω is the power of the fundamental, d_{NL} is nonlinear coefficient of the crystal, and Δk is phase mismatch between two fields, and E_{NL} is Nonlinear conversion efficiency. Phase mismatch is adjusted to be zero by tuning the crystal temperature for NCPM and QPM, or other means for other phase-matching techniques.

In reality, laser beams are modeled as Gaussian beams instead of plane waves. Capturing the evolution of beam profile and Gouy phase shifts, the conversion process is proportional to Boyd-Kleinman integral, show below. For the fundamental circular beam with its waist located at the center of nonlinear crystal, it is given by

$$h(z) = \int_0^z dz' \frac{e^{i\Delta z'}}{1 + \frac{iz'}{z_R}} \quad (7.6)$$

where $z_R = \frac{\pi n_1 w^2}{\lambda}$ is Rayleigh range of fundamental field taking account of refraction index n_1 in the crystal, and crystal center is $z = L_c/2$, where L_c is the total length of the crystal. General engineering goal would be to choose beam parameters that maximizes the integral $h(z = L_c)$, which maximizes single pass conversion efficiency, and optimal for cavity enhancement as well. Intuitive interpretation of BK optimum focusing is to focus the beam just right. Too tightly focused beam may exhibit efficient doubling process at very localized segment, but rapid divergence will make the entire crystal not utilized. Too loose focusing may utilize whole crystal segment, but too low intensity will make the efficiency low. Finding optimum beam parameter is lying somewhere between them.

7.1 960/480 PPKTP doubling cavity

PPKTP is widely used nonlinear crystal and with reported high conversion efficiency when an enhancement cavity is employed, in similar infrared wavelengths[73, 74].

7.1.1 Quasi-Phase matching

Periodically-poled structure allows harmonic beam coherently added up through the crystal. It has an advantage of tunable phase matching temperature by changing the poling period. Altering structure and orientation of beam and crystals are displayed in Figure 7.1. Use of poling comes with slight compromise on the nonlinear coefficient($d_{eff} = \frac{2}{\pi}d_{33}$).

In this design stage, we choose the beam waist that maximizes the Boyd-Kleinman integral, which $w_{BK} \sim 28\mu\text{m}$. PPKTP has known issues with thermal problem and gray tracking issues, such that too intense light may degrade the performance. For that reason, newly selected beam waist is $w_{960} \sim 35\mu\text{m}$. Obtained single-pass conversion efficiency is $E_{NL} = 0.00548\text{W}^{-1}$, see Figure 7.3 for temperature vs harmonic power.

7.1.2 Enhancement cavity Design

Design goal of the cavity is to support the desired resonator modes and ensure the generated harmonic beam has circular beam profile. This is because the output needs to be fiber-coupled for delivery, and spatial profile determines coupling to

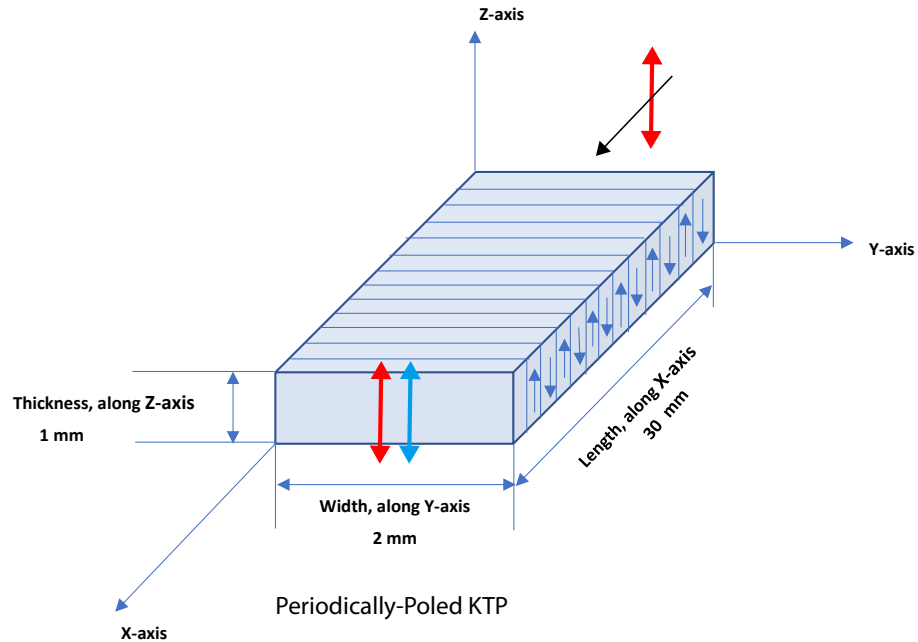


Figure 7.1: PPKTP dimension, orientations and poled domains. Fundamental and harmonic waves have same z-polarization propagating along x-axis. Due to mechanical design of current PPKTP holder, z-pol parallel to horizontal, and y-axis is parallel to the gravity. Illustration modified from draft provided by Moshe at Raicol Crystals

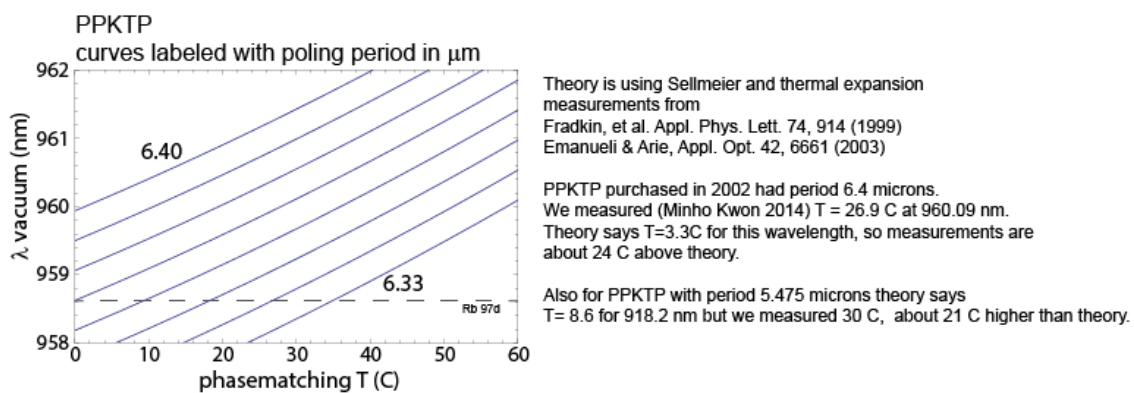


Figure 7.2: Poling period and phase-matching temperature, comparison between the measured and calculated.

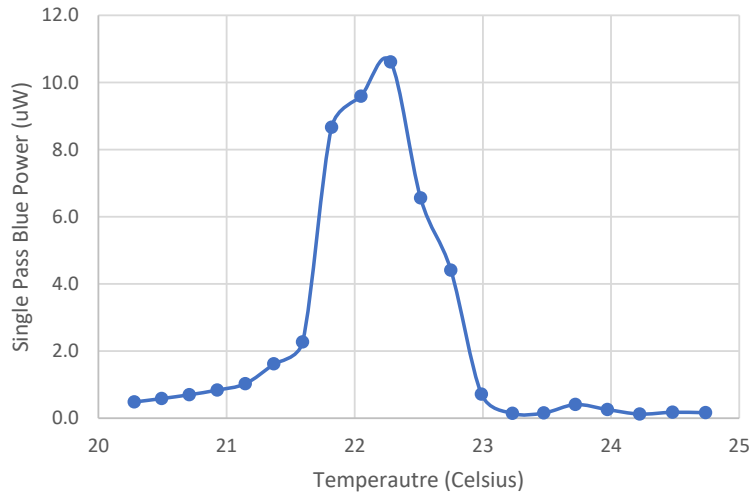


Figure 7.3: Single-pass PPKTP SHG. Fundamental optical frequency $f_{960} = 312717.13$ GHz and power 45.7 mW. Obtained single pass conversion $E_{NL} = 0.00548\text{W}^{-1}$. FWHM of the gain bandwidth is consistent with 3cm long crystal(1.29 C). Data from 2014-05-01

single mode fibers. Optimum cavity design should support TEM_{00} mode of beam waists ($w_{x,\omega} = w_{y,\omega} = w_{\text{BK}}$) at the center of the crystal same as the design waist, often satisfying Boyd-Kleinman condition. Firstly total cavity length L_T and spacing between two curved mirrors L_2 are determined to give desired, circular waist at the crystal center, see Figure 7.4.

Diagram for full optical layout, including input and locking optics, are illustrated in Figure 7.5, with the list of optics in Table 7.1.

Final step is choosing impedance-matched input coupler, M_4 , in the Figure 7.5. Linear power conversion efficiency $\epsilon = \frac{P_{2\omega}}{P_\omega}$ in enhancement cavity needs to take

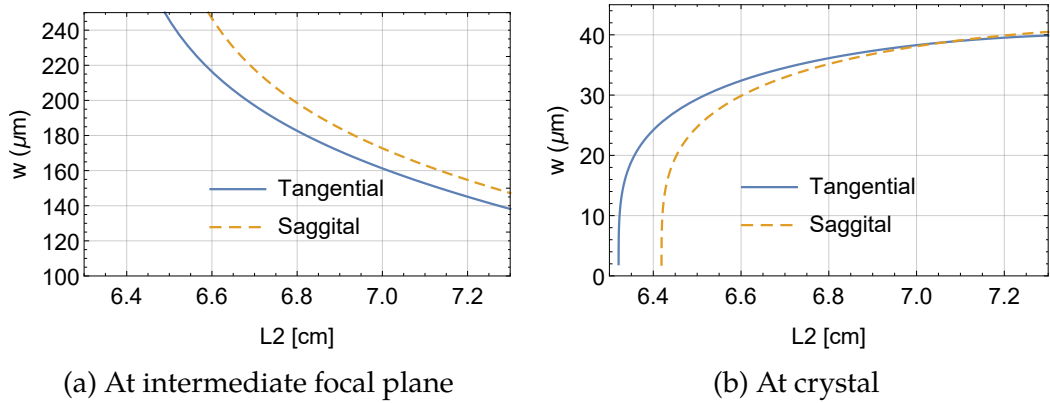


Figure 7.4: PPKTP doubling cavity. Tangential and Sagittal waist as a function of the curved mirror spacing, L_2

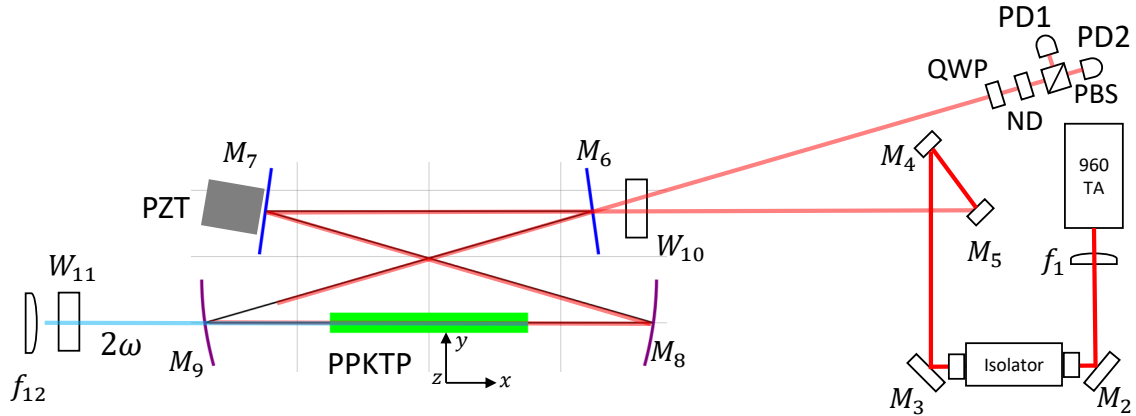


Figure 7.5: 960/480 bow-tie ring cavity and input optical setup

account depletion of fundamental. For formula is given as[75]

$$\sqrt{\epsilon} = \frac{4T_1\sqrt{E_{NL}P_1}}{[2 - \sqrt{1 - T_1}(2 - L - \sqrt{\epsilon E_{NL}P_1})]^2} \quad (7.7)$$

where T_1 is the input coupler transmission, E_{NL} is single pass non-linear coefficient, P_1 is mode-matched input power, L is linear loss excluding the input coupler.

Table 7.1: 960/480 Cavity Optics detail

Symbol	Description	Part Number
f_1	Mode-matching lens, f=1000mm	Thorlabs LA1464-B
M_2	980nm 45°, Laser Mirror	Edmunds 45-999
M_3	980nm 45°, Laser Mirror	Edmunds 45-999
M_5	Flat mirror	Thorlabs BB05-E03
M_5	Flat mirror	Thorlabs BB05-E03
M_4	Input coupler($T_{in} = 5.2\%$)	Toptica
M_5	Flat mirror	Toptica
M_6	Concave mirror, R=50mm	Toptica
M_7	Concave mirror, R=50mm	Toptica
M_8	Flat mirror	Toptica
f_{12}	Output collimator, f=100mm	Thorlabs AC254-100-A
W_{13}	BK7 480 window	Thorlabs WG11050-A
W_{14}	BK7 960 window	Thorlabs WG11050-B
PD1	Si Mounted PD	Thorlabs SM05PD1A
PD2	Si Mounted PD	Thorlabs SM05PD1A
PZT	Ring Piezo, 150V	Piezomechanik HPSt 150/14-10/12 HAg

Optimum choice of input coupler transmission T_1 can be analytically expressed as

$$T_1 = \frac{L}{2} + \sqrt{\frac{L^2}{4} + E_{NL}P_1} \quad (7.8)$$

Using our parameters on Table 7.2, impedance matched $T_1 \sim 6.8\%$ and our coupler has 5% transmission so discrepancy do exist, although cavity output is affected less than 10%.

By design, we observe circular harmonic beam, see Figure 7.6 and 7.7.

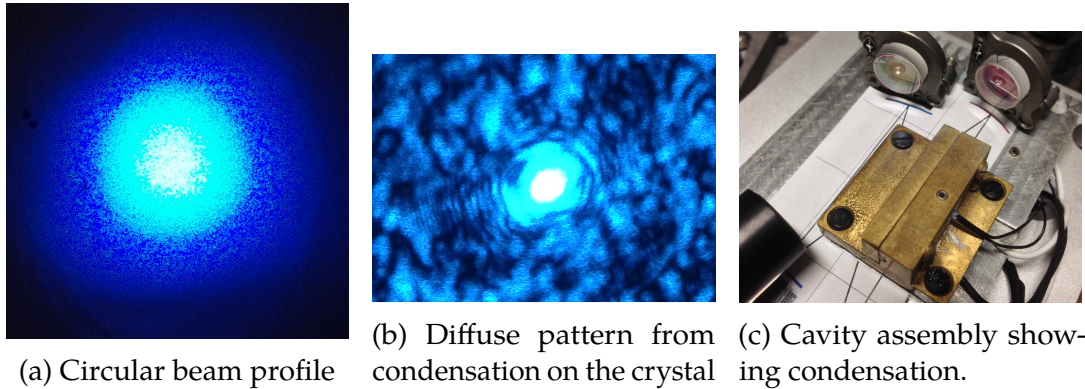


Figure 7.6: Spatial beam profile of 480 nm from the crystal

Table 7.2: Summary of numbers relevant to the performance of the 960/480 frequency doubler. PPKTP purchased from Raicol Crystals

Parameter	Value
Nonlinear Crystal	Periodically-Poled KTP
Crystal dimension($H \times W \times L_c$)	$1 \times 2 \times 30$ mm
Poling period	$6.375\mu\text{m}$
Nonlinear Coefficient d_{33}	13.7 pm/V
Effective Nonlinear Coefficient d_{eff}	8.72 pm/V
Input Power	$600 - 880$ mW
Output Power	$95 - 170$ mW
Mode Matching	$60 - 80\%$
Single-Pass Efficiency(calculated)	0.00277W^{-1}
Single-Pass Efficiency(measured)	0.00548W^{-1}
Cavity finesse(measured, off-resonant)	75
Free Spectral Range(FSR)	1.25 GHz
Input Coupler Transmission at 960 nm(T_1)	5%
Conversion efficiency(measured)	$22 - 24\%$
Distance between two curved mirrors(L_2)	6.8 cm
Total round trip length(L_T)	24 cm
Beam waist at crystal center (tan, sag)	$(36.1, 35.2) \mu\text{m}$
Beam waist at the intermediate plane (tan, sag)	$(183, 198) \mu\text{m}$

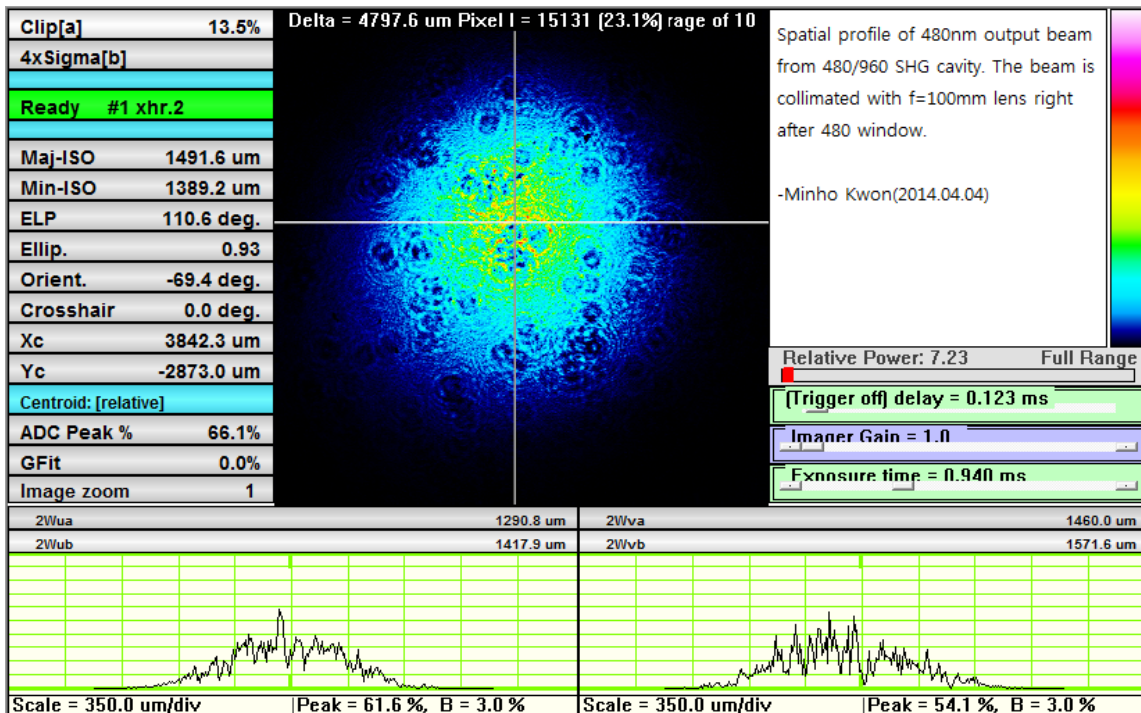


Figure 7.7: 480 nm spatial profile after collimated with f=100mm lens. Showing circular profile.

7.1.3 Hansch-Couillaud Cavity stabilization

960/480 Cavity length is stabilized by Hansch-Couillaud(HC) lock[76], whereas 1540/770 cavity uses Pound–Drever–Hall technique[77] to avoid distortion on error signal from thermal effects.

7.2 1540/770 LBO doubling cavity

High power, single frequency, continuous wave(CW) of 770nm light is generated by cavity enhanced Second Harmonic Generation(SHG) of 1540nm laser with Lithium Triborate(LBO) crystal. As of 2015-09-12, up to 13.97 W is produced from 18.8 W

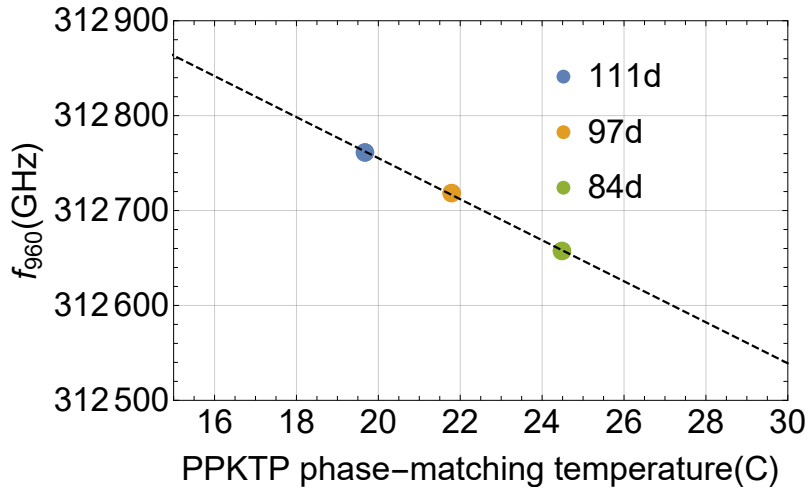


Figure 7.8: Phase matching temperature versus 960 laser frequency. PPKTP purchased from Raicol crystals 2014-04-29. Dashed line is a linear fit to the observed phase matching temperatures. $f_{960}(T^{\circ}\text{C}) = 312647 - 21.622(T - 25)$ (GHz) where T is the crystal temperature

of fundamental optical power. High power fundamental is provided by a 20 W fiber amplifier purchased from IPG Photonics(model:EAR-20K-C-LP-SF), seeded by RIO3135-3-46-1 purchased from Redfern Integrated Optics (RIO). In the developing stage, lasers from Optilab, model TLM-C-R and model DFB-B-20-P-1560, were used to seed the fiber amplifier. However those lasers were not stable enough to be used with an enhancement cavity, as shown in Figure 7.9.

This system is chosen for its high reliability and efficiency in a reasonable cost. Most common laser around 780 nm are diode lasers usually power limited up to 2 W. Moreover, highly astigmatic spatial profile further limits the power coupled to a single mode fiber. Instead we utilized mature technology established in the telecom band lasers (1540nm-1560nm). Within our research group, Martin Lichtman has made first attempt to build a SHG system (1560nm to 780nm) which achieved more

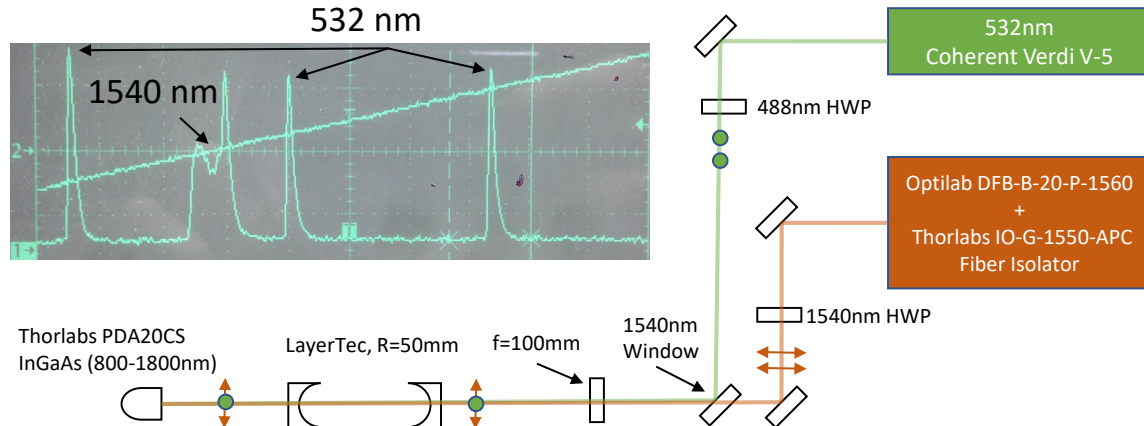


Figure 7.9: Bichromatic, doubly resonant scanning Fabry-Perot cavity setup to diagnose unstable 1540 nm DFB laser. Initially chosen 1540nm DFB laser not in single-frequency operational compared to DPSS 532nm Verdi laser

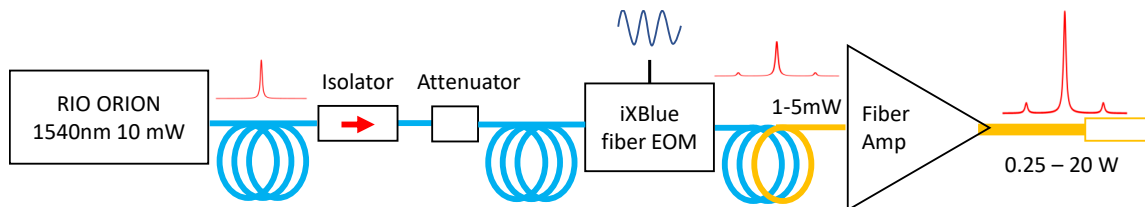


Figure 7.10: Fiber-optical configuration of 1540 nm coherent light source. Isolator is Thorlabs **IO-G-1550-APC** and 3dB attenuator is **FA03T-APC**

than 50% 10.4 W of 780nm from 20 W of 1560nm) conversion efficiency from a retro-reflected double pass setup with Periodically-Poled Lithium Niobate(PPLN) crystal. Even though the first attempt was successful, the system had issues with thermal effects arising from high nonlinearity of PPLN. Therefore, we have decided to rather use LBO crystal that is known to have minimal thermal effect[74], and utilize cavity build-up to achieve high conversion efficiency.

Table 7.3: Summary of performance of the 1540/770 frequency doubler at best working condition

Parameter	Value
Nonlinear Crystal	LBO($\theta = 90^\circ, \phi = 0^\circ$)
Crystal dimension(H×W×L _c)	3 × 3 × 30 mm
Nonlinear Coefficient	$d_{32} = 0.67 \text{ pm/V}$
Fundamental Input Power	~ 19 W
Mode matching	80 – 97.9%
Single-Pass Efficiency(calculated)	$1.344 \times 10^{-4} \text{ W}^{-1}$
Single-Pass Efficiency(measured)	$1.53 \times 10^{-4} \text{ W}^{-1}$
Cavity finesse(measured)	104 - 141
Cavity Free Spectral Range(FSR)	1.02 GHz
Input Coupler Transmission at 1540 nm(T ₁)	~ 5%
Conversion efficiency(measured)	74%
Total round trip length(L _T)	29.5 cm
Distance between curved mirrors(L ₂)	6.6 cm
Beam waist at crystal center (tan, sag)	(40.6, 40.6) μm
Beam waist at the intermediate focal plane (tan, sag)	(227, 248) μm

7.2.1 Type-I Non-Critical Phase matching

Type-I Non-Critical Phase Matching(NCPM) of LBO converts two z -polarized photons to a single y -polarized photon propagating along x -axis. For this application, bulk crystals cut with ($\theta = 90^\circ, \phi = 0^\circ$) were purchased from United Crystals and UVisIR.

LBO crystal is temperature tuned to modify refractive indices, dictated by Sellmeier equations[78]. Phase matching condition is simply those indices become identical $n_{z,1540}(T) = n_{y,770}(T)$, where n denotes refractive index for certain polarization and wavelength at given temperature. Calculated and measured phase matching temperature is shown on Figure 7.12. Since the phase matching occurs at an elevated temperature, we employed two stage temperature control to in-

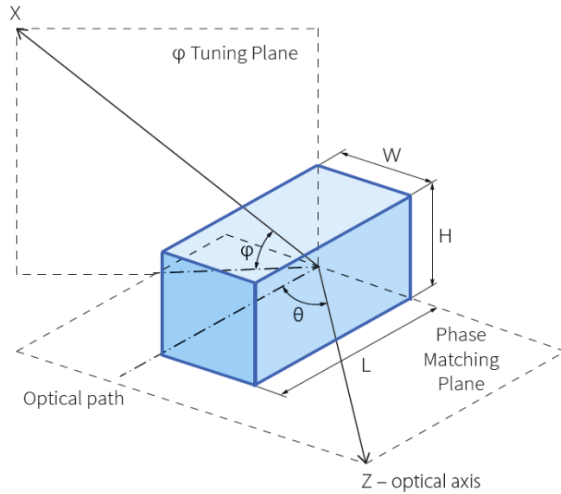


Figure 7.11: LBO axis definition. Image from [Altechna](#)

dependently stabilize the base plate (or cavity length) and crystal holder (LBO). Furthermore, any materials (screws, lid, baseplate) need to be free from outgassing and degradation at elevated temperature.

7.2.2 Cavity Design

Design goal is to support Boyd-Kleinman beam waist for our 3cm long crystal, $\lambda = 1540\text{nm}$, $w = 40\mu\text{m}$, in bow-tie ring resonator. Circular beam output is prioritized to achieve high efficiency single mode fiber coupling, by choosing the spacing between two curved mirrors $L_2 = 6.6\text{cm}$, shown in Figure 7.13. Complete optical layout of the cavity and input coupling part is presented, see Figure 7.14, and the list of optics in Table 7.4. CAD drawing is displayed on the Figure 7.16. Regarding the choice of impedance matched input coupler, calculated output power versus different coupler choice are presented, see Figure 7.15. They peak around $T_1 \sim 5\%$

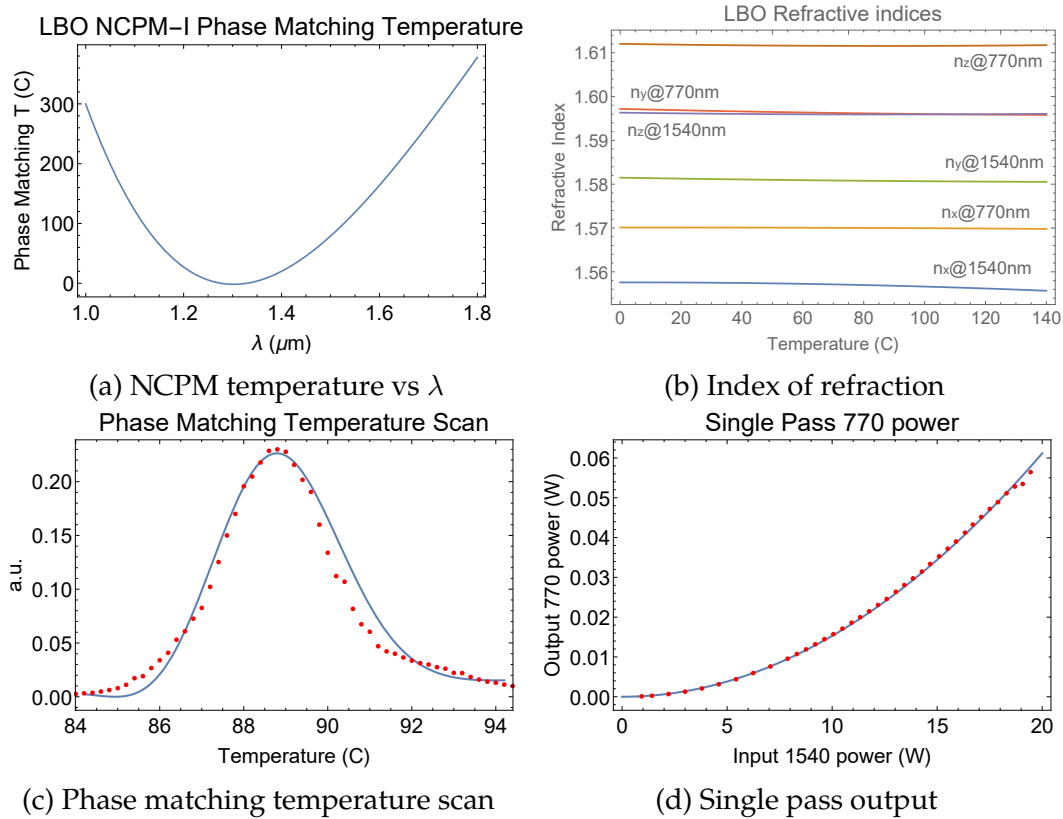


Figure 7.12: LBO indices of refraction. ($n_x \leq n_y \leq n_z$) parallel to crystallographic axes a, c and b. Type-1 Non-Critical Phase Matching(NCPM) temperature, and measured temperature tuning curve.

and we already have that, so the cavity is impedance matched. CAD design of full cavity assembly is displayed on Figure 7.16.

7.2.3 Pound-Drever-Hall Cavity stabilization

As of 2019-03-01, Pound-Drever-Hall(PDH) technique and is being used among Dither lock and Hansch-Couillaud techniques. Doubling cavity is stabilized by mechanically tuning the cavity length with a ring piezo glued onto the flat mirror.

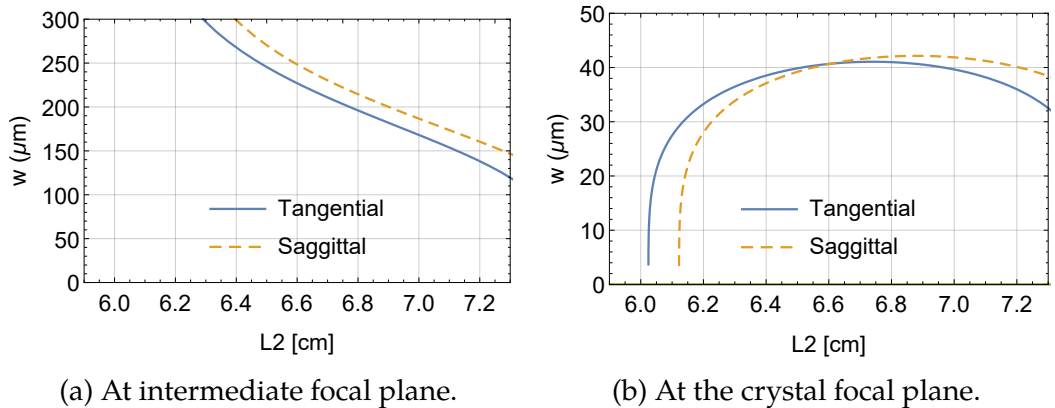


Figure 7.13: LBO doubling cavity. Tangential and Sagittal waist as a function of the curved mirror spacing, L_2 . Chosen $L_2=6.6$ cm.

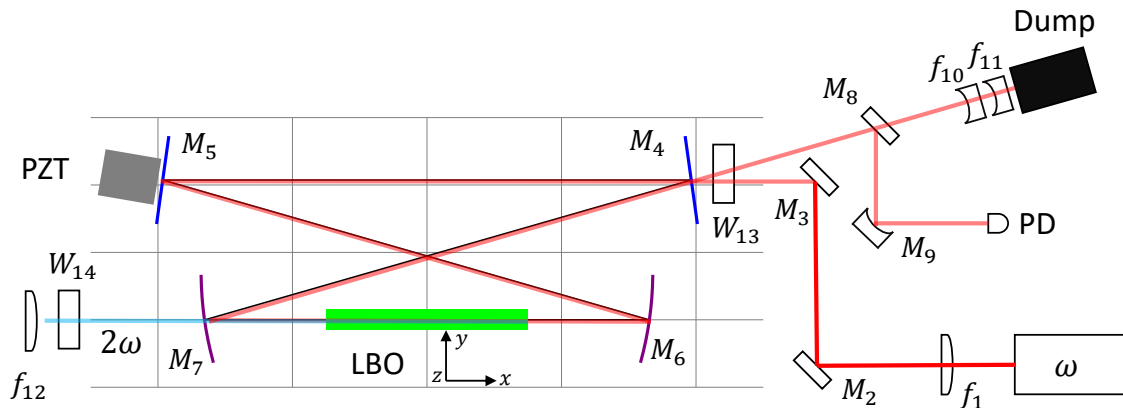


Figure 7.14: Bow-tie cavity for 1540/770 doubling cavity.

Since the application is atom trapping with far-detuned light, change in laser frequency is minimally concerned. This gives extra knob to further stabilize the doubling process. Fundamental laser frequency can be tuned to keep the cavity resonant by current modulation through the driver. With mechanical and electrical feedback, servo bandwidth of a few tens of kHz range is providing reliable and robust lock.

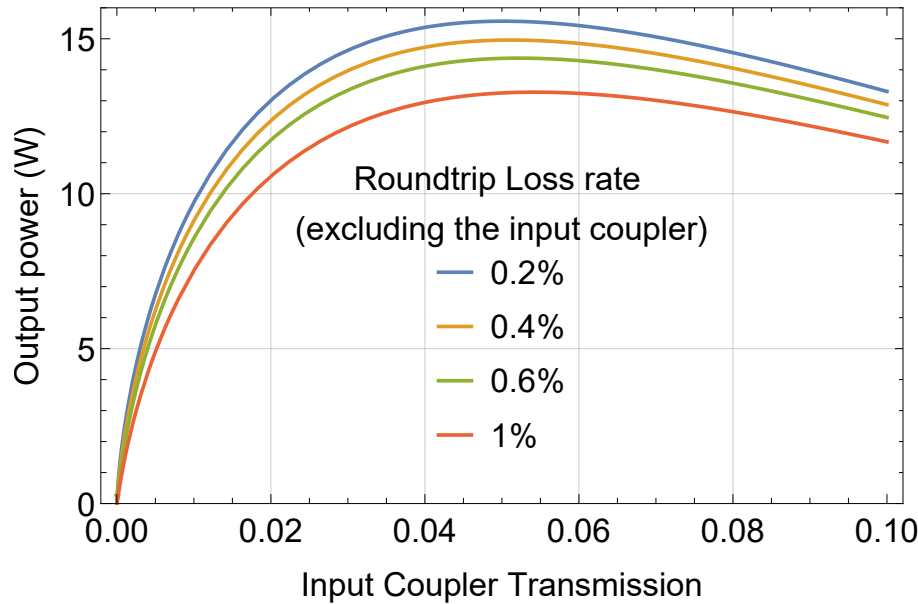


Figure 7.15: 1540/770 SHG cavity output power versus input coupler transmission

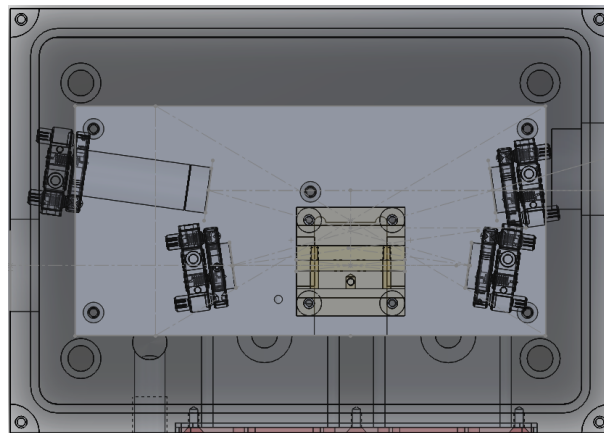


Figure 7.16: Mechanical design of 1540/770 SHG LBO cavity assembly, providing mirror mounting and temperature control. Ring piezo actually used is much shorter than displayed one, so the mount does not stick out from the Aluminum base plate.

Table 7.4: 1540/770 Cavity Optics detail

Symbol	Description	Part Number
f_1	Mode-matching lens, f=250mm	Thorlabs LA1461-C
M_2	Flat mirror	LayerTec 100007
M_3	Flat mirror	LayerTec 100007
M_4	Input coupler($T_{in} = 5\%$)	LayerTec 127999
M_5	Flat mirror	LayerTec 100007
M_6	Concave mirror, R=50mm	LayerTec 100828
M_7	Concave mirror, R=50mm	LayerTec 100828
M_8	Flat mirror	LayerTec 100007
M_9	Concave mirror, R=50mm	LayerTec 100828
f_{10}	Concave lens, f=-25mm	Thorlabs LC1054-C
f_{11}	Concave lens, f=-25mm	Thorlabs LC1054-C
f_{12}	Output collimator, f=150mm	Thorlabs LA1433-B
W_{13}	BK7 1540 window	Thorlabs WG11050-B
W_{14}	BK7 770 window	Thorlabs WG11050-C
Dump	Power dump	Thorlabs BT610
PD	5 GHz InGaAs detector	Thorlabs DET08C
PZT	Ring Piezo, 150V	Piezomechanik HPSt 150/14-10/12 HAg
HWP	Half waveplate, 1550 nm	Lambda RO WPO-12.7CQ-0-2-1550
HWP2	Half waveplate, 1550 nm	Lambda RO WPOM-12.7CQ-0-2-1550

Pound-Drever-Hall Technique

Pound-Drever-Hall(PDH) technique is chosen to provide offset-free error signal and high servo-bandwidth. Other locking techniques were implemented as well but due to their drawbacks, PDH is chosen. HC locking was very susceptible to the crystal heating, as it relies on birefringence of the crystal. This thermal transients issues combined with input-power dependent zero-crossing, HC lock did not provide good lock at high input optical power(>3 W). Dither lock did have better stability although its narrow capture range and dithering frequency at tens of kHz was mapped to dithered intensity noise in the frequency doubled light,

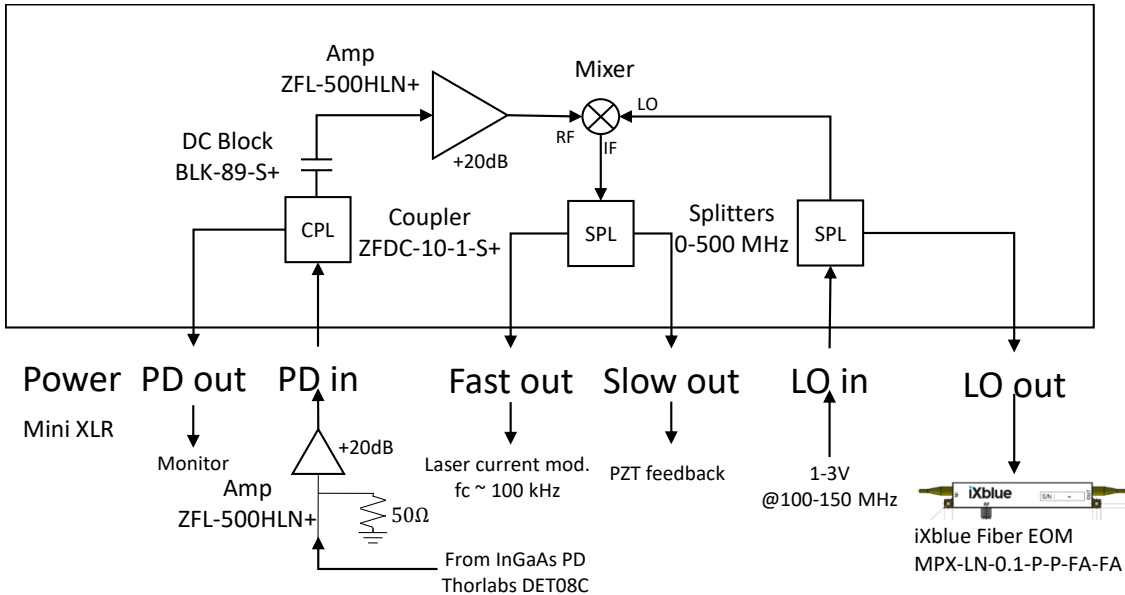


Figure 7.17: Creating PDH error signal for 1540/770.

which can lead to parametric heating[79] of trapped atoms. Phase-modulation is achieved by iXblue **MPX-LN-0.1-P-P-FA-FA** fiber EOM connected between the seed laser and the fiber amplifier.

Piezo-tuning sensitivity is 80nm/V(upto 150V) of cavity length, equivalent to optical tuning of 104MHz(@1540nm)/V. Laser modulation port has optical tuning of 63MHz(Ω @10kHz)/V. Due to high beam intensity, most of the cavity reflection is dumped to a beam trap, and small reflection from AR-coated window is collected to fast, biased InGaAs photodetector. We chose phase-modulation frequency Ω_{EOM} to be 130 MHz range thereby providing large capture range $f_{capture} = \frac{2f_{EOM}}{FSR}$, covering $\sim 26\%$ of the parameter space. Modulation depth is kept small such that the carrier has $> 97\%$ of the power while both sidebands contain $< 1.5\%$ each, as shown in

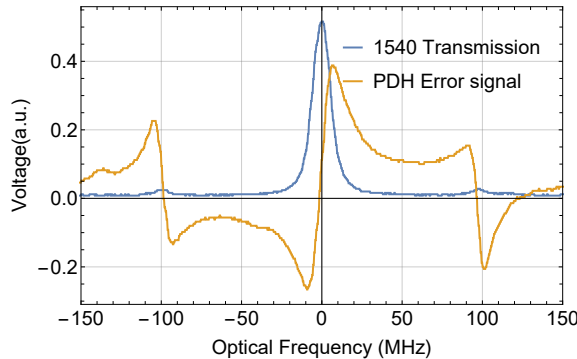


Figure 7.18: Cavity transmission of fundamental and PDH error signal.

7.18 This keeps the nonlinear process to be still power-efficient, and amplitude noise in 770 light due to optical beating is also minimized. To compensate Small modulation depth, PD electrical signal is boosted by an RF amplifier(Minicircuits ZFL-500HLN+), before it enters PDH box, where the signal gets further processed. Home-built standard PDH lockbox shown in the figure generates base error signal for slow and fast servo loop. Fine tuning of the vertical offset, magnitude and polarity of gain are set by home-built lockbox. Slightly modification on the fast-feedback has been done to boost the signal by factor of 50, as shown in Figure 7.19.

7.2.4 Optical setup

This section illustrates how the generated 770nm light is delivered from the cavity. Frequency doubled light emerging from the cavity can be modeled as a diverging Gaussian beam where the waist is located at the crystal center. Ultimately this light is coupled to a single-mode, polarization maintaining fiber patchcord and delivered to the apparatus. Good fiber coupling is particularly important for high

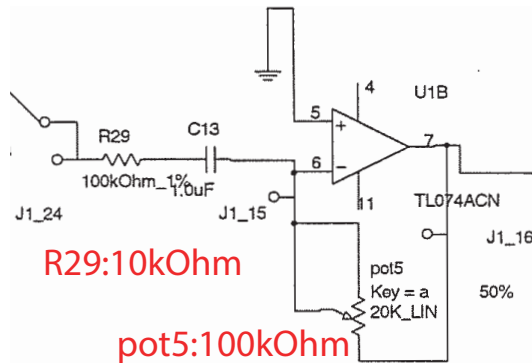


Figure 7.19: Modified fast servo gain state for 1540 770 PDH lock. Part of the circuit cropped from Generic Lockbox ver.1 schematic

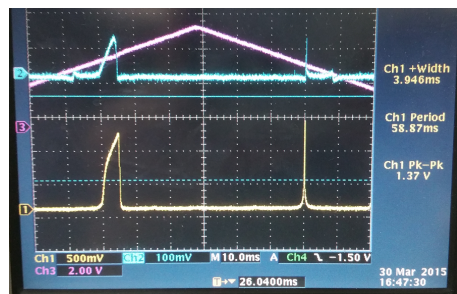


Figure 7.20: Thermal effects distorting the cavity transmission(Yellow) while ramping the cavity length(Purple). Light absorption heats the crystal up causing thermal expansion. Asymmetric transmission when the cavity length is scanned bidirectional is an indicative of thermal effect. This LBO crystal is purchased from xxx. Had extra absorption, leading to observable significant thermal effect.

power application, as uncoupled light will be absorbed by the cladding and may deposit significant heat, which may degrade the long-term coupling efficiency or polarization character of the fiber. 770 transverse beam profile highly circular 7.23, by design. After a collimating lens, polarization optics, and AOM, and auxiliary beam shaping optics, either +1st or -1st order is coupled to the PM fiber **OZ Optics PMJ-3A3A-633-4/125-3-2-1**. Typically we achieve 60% coupling efficiency.

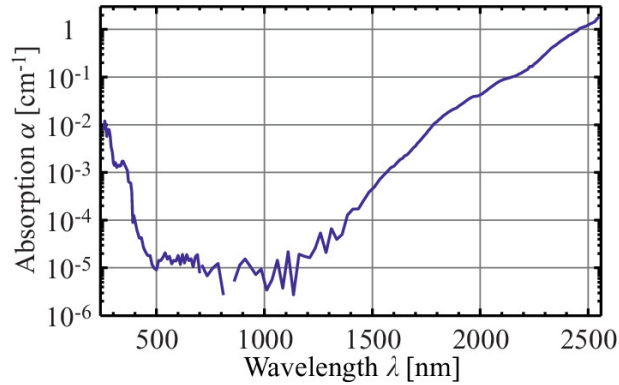


Figure 7.21: Reprinted from [80]. Wavelength-dependency of Photoacoustic absorption in LBO Crystal

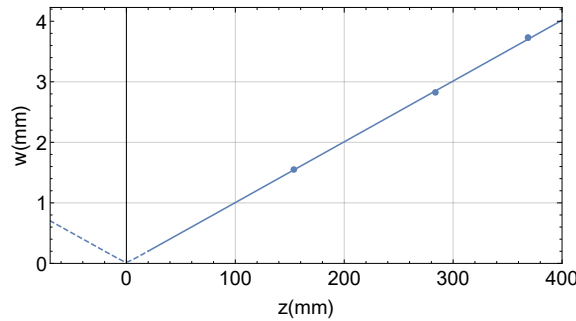


Figure 7.22: Beam parameter product measurement of 770nm from SHG cavity. Knife-edge measurement was performed to calculate half-diameter of beams at different distance(z) from the crystal. Fit gives $w(z) = 24.401\sqrt{1 + 0.169232z^2}$ μm , where z is in mm.

Table 7.5: 770 light source to fiber optical components

Symbol	Description	Part Number
f_1	Collimating lens $f=150\text{mm}$	Thorlabs LA1433-B
M_2	Flat mirror	
f_3	Telescope, first lens $f=340\text{mm}$	
AOM	Switching AOM, 80MHz	Gooch & Housego AOMO 3018-122
f_5	Telescope, second lens $f=150\text{mm}$	Thorlabs AC254-150-B
PBS	Polarization cleaning	
f_8	Fiber collimator, $f=11.07\text{mm}$	Thorlabs F220APC-780

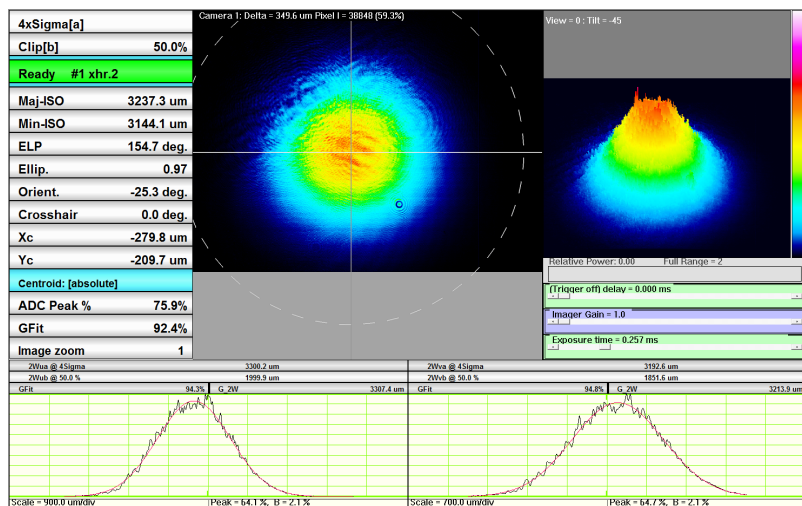


Figure 7.23: Spatial beam profile of 770 nm from the cavity. Ellipticity ~ 0.97 .

Part III

Ensemble Experiments and Calculations

8 ENSEMBLE QUBIT PREPARATION

Preparation of many-body entangled state can be achieved by many means. Entanglement class we are accessible to is a symmetric, singly excited state or so-called W-state, or $N = 1$ case of atomic Fock state[81]. Many excitation schemes are possible and demonstrated to prepare single ensemble Rydberg W-state. Straightforward way is to drive coherent Rabi oscillation between Ground and Rydberg state with accurately controlled pulse area. Due to imperfect result we got, more sophisticated scheme were explored, such as Adiabatic Rapid Passage[82], Stimulated Raman Adiabatic Passage(STIRAP)[83, 84], although the excitation fidelity were comparable. Here we come back to the straightforward approach which is merely driving Ground-Rydberg Rabi oscillation but adopted composite pulse schemes[85] which were originally developed for NMR experiments but applications are universal.

8.1 Collectively enhanced Rabi oscillation

Rydberg blockaded atomic ensemble exhibit \sqrt{N} collective enhancement in Ground-Rydberg Rabi oscillation, demonstrated by our group[81]. Due to limited ability to control atom loading, shot-to-shot atom number follows stochastic process. In-situ atom number measurement was also not possible as light assisted collision causes atom number to be different between the imaging and science phase. Therefore the results presented here are statistical average of experiments with a fixed atom loading rate. We found the atom number is best described by Poisson distribution, which gives the probability of having N -atom in a trap $P(N) = \frac{e^{-\mu}\mu^N}{N!}$, where μ is the

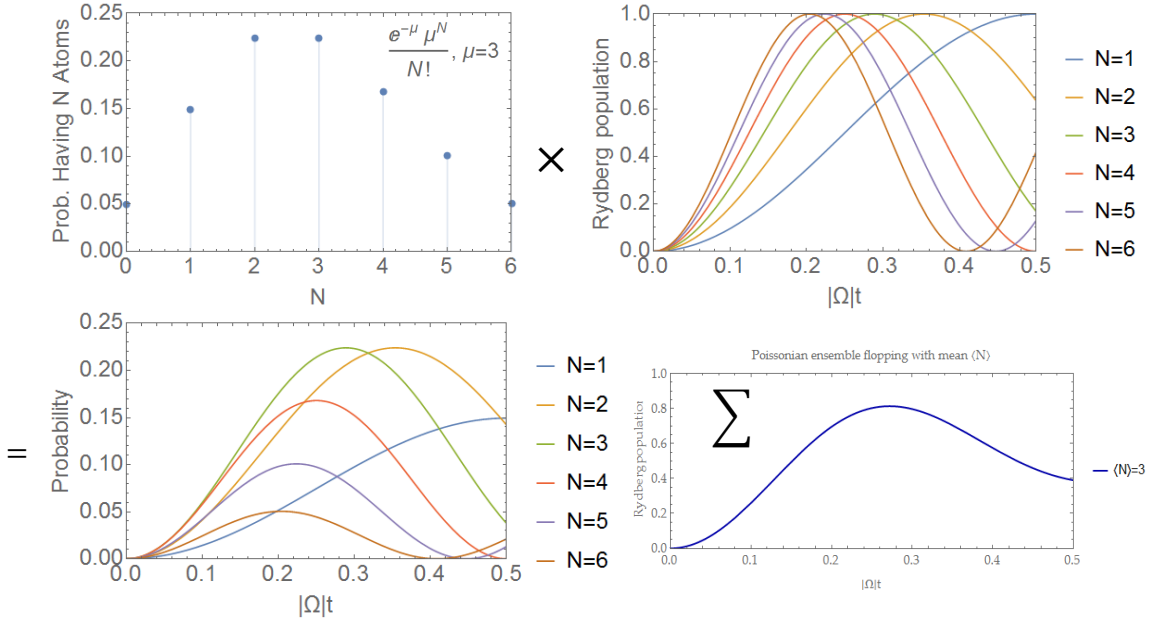


Figure 8.1: Poissonian atom number distribution leads to inhomogeneous collective enhancement, therefore when averaged, they look to be dephasing. Calculated for mean atom number $\bar{N} = 3$ case.

mean. In actual experiment, the result is washed-out looking Rabi oscillation curve, such as Figure 8.1, resulted from weighted average of many runs of collectively enhanced Ground-Rydberg Rabi oscillation.

Stochastic atom number fluctuation require dynamic, in-situ control of the duration t to make the effective pulse area ($A = \sqrt{N}\Omega t$). In order to apply a collective π -pulse, we simply take $t = t_\pi/\sqrt{\bar{N}}$, where t_π is single-atom π -pulse length and \bar{N} is the mean atom number. Fidelity of successful Rydberg excitation gets better as \bar{N} increases, as show on Figure 8.3b.

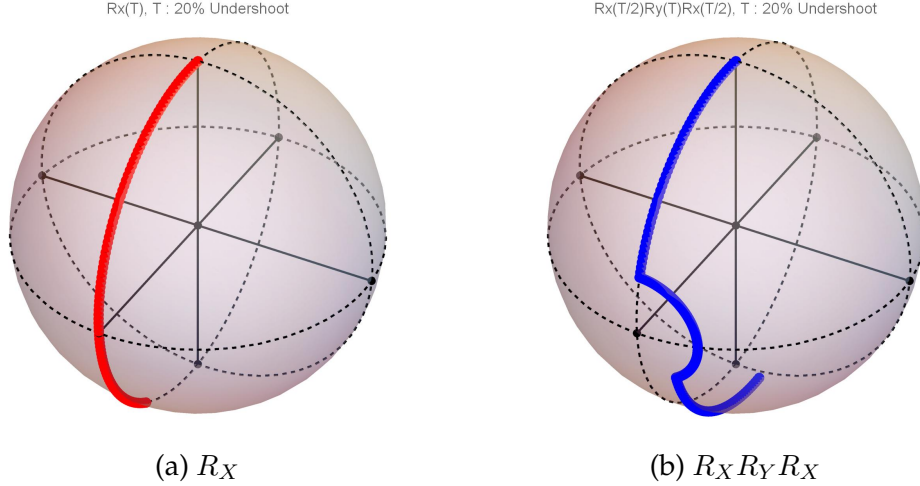


Figure 8.2: Visualized qubit rotation with normal and composite pulse sequence, assuming 20% undershoot in the pulse area. Desired operation is to flip the qubit from the north pole to the south.

8.2 Composite pulse

Deterministic Rydberg excitation requires perfect π -pulse or $R_x(\theta = \pi)$ rotation from Ground state, if coherent Rabi oscillation method is used. Error on pulse area $\delta\theta$ will make the qubit rotation $R_X(\theta + \delta\theta)$ to deviate from correct π -pulse, leading to imperfect excitation probability. Effect on the probability can be reduced to higher-order error when composite pulse scheme is adopted[85, 86], techniques initially developed for NMR experiments. Pulse category we are especially interested in are ones that reduces the impact of pulse area error, for example $R_X(\pi/2)R_Y(\pi)R_X(\pi)$ composite pulse scheme. This scheme requires three rotation about two different axis, and total pulse area that is twice of conventional single rotation as shown in the equation 8.2, and visualized in Figure 8.2.

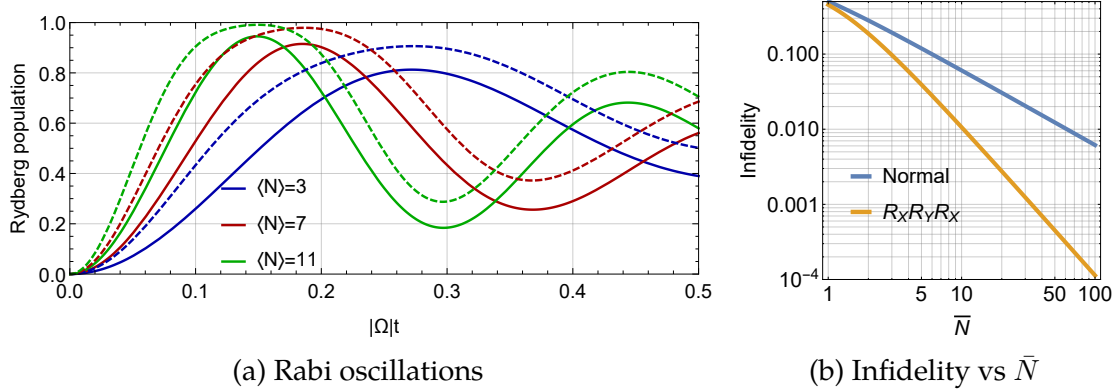


Figure 8.3: Ground-Rydberg Rabi oscillations of ensembles with Poissonian atom number distribution. Solid lines are normal pulse and dashed lines are using the composite pulses. No decay is applied.

$$R_{CP}(\theta) \equiv R_X\left(\frac{\theta}{2}\right) R_Y(\theta) R_X\left(\frac{\theta}{2}\right) \quad (8.1)$$

Then the probability of measuring the other state is

$$\langle \uparrow | R_{CP}(\theta) | \downarrow \rangle^2 = \frac{1}{2} (\cos \theta + 3) \sin^2\left(\frac{\theta}{2}\right) \quad (8.2)$$

Assuming a systematic error on the π -pulse area such that actual area being slightly off, $\pi \rightarrow \pi + \theta$, the error on the excitation probability is $\sim \frac{1}{16}\theta^4$, which is less sensitive than the convention scheme whose error goes $\sim \frac{1}{4}\theta^2$. Therefore when many \sqrt{N} -enhanced Rabi oscillations are concerned, we expect to observe higher probability of exciting ensembles to Rydberg states, as shown in the Figure 8.3

Composite scheme requires in-situ switching of the rotation axis, which can be achieved by shifting the optical phase of the addressing laser. Optical phase is dynamically controlled by changing the phase of RF signal driving the AOM

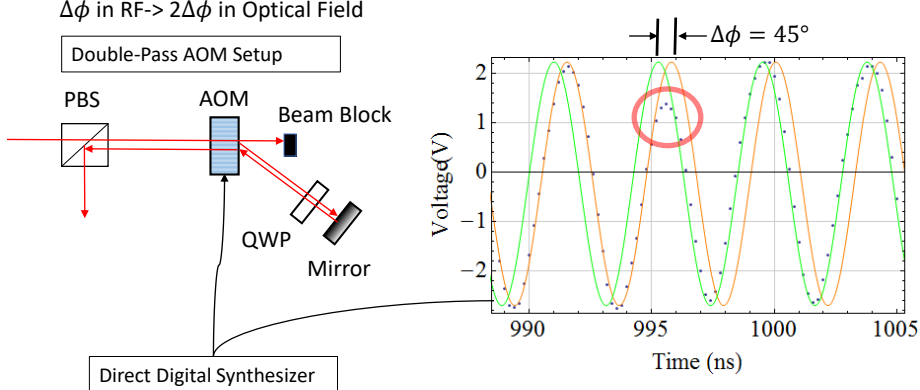


Figure 8.4: RF and electro-optical setup for composite pulse scheme

described in Figure 8.4. In a double-pass configuration ± 1 st-order configuration, optical phase experiences is twice of the RF phase change. Therefore 45° RF phase hop is translated into 90° optical phase change, or changing the rotation operator axis by 90° .

We have experimentally compared two pulse schemes in single-atom Rabi oscillation as shown in Figure 8.5a and Figure 8.5b. Plateau feature near the peak seen in the composite pulse confirms the composite pulse scheme behave as calculated.

8.3 Ensemble composite pulse Rabi oscillation

For ensemble case, see Figure 8.6. Although possible improvement has been reported [87], the maximum transfer probability were not observed in $N = 1$, $\langle N \rangle = 4.15, 7$ for us. Furthermore, $\langle N \rangle = 12$ case had lower transfer probability. We attribute this to additional dephasing caused by longer pulse, which compromises the advantage of the composite pulse.

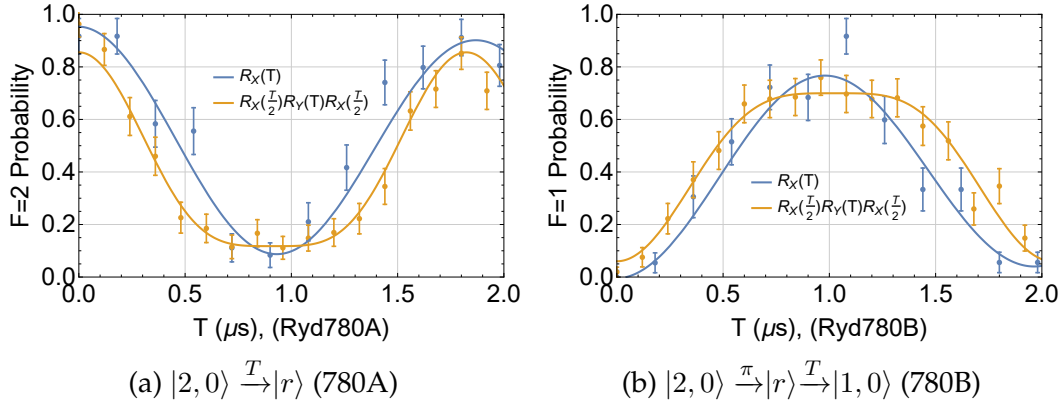


Figure 8.5: Comparison between normal and composite pulse on Single-atom(N=1) Rydberg Rabi oscillation. $|r\rangle = |111d_{5/2}, m_j = 5/2\rangle$. Data taken 2014-09-25

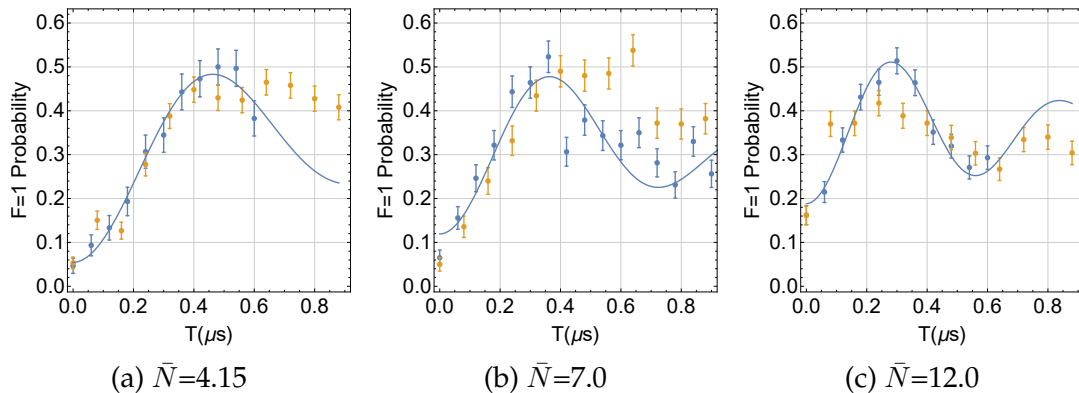


Figure 8.6: Comparison between normal- and the composite-pulse driving collective Rabi oscillations between $|2, 0\rangle$ and $|111d_{5/2}, m_j = 5/2\rangle$. Single-atom 780B π -pulse $|111d_{5/2}, m_j = 5/2\rangle \rightarrow |1, 0\rangle$ maps Rydberg population to $F = 1$ hyperfine manifold. X-axis indicates effective pulse length T , which is true pulse length for normal scheme and half of the total length for composite scheme. . Data from 2014-10-30.

9 COLLECTIVE SPIN DYNAMICS OF ENSEMBLE QUBIT

9.1 Microwave tomography as entanglement witness

9.1.1 Separable state rotation

General expression for N-separable atoms in two-level system can be represented as

$$\begin{aligned} |\psi\rangle_N &= \bigotimes_i |\psi_i\rangle \\ &= \bigotimes_i \left(\sin \frac{\theta_i}{2} |0_i\rangle + \cos \frac{\theta_i}{2} e^{-i\phi_i} |1_i\rangle \right) \end{aligned} \quad (9.1)$$

Suppose that we have N-atoms initialized to the logical “0” state $|0\rangle_N = |0\rangle^{\otimes N} = |F = 2, m_F = 0\rangle^{\otimes N}$, and have no population on “1” = $|F = 1, m_F = 0\rangle$ state. Those states are magnetic dipole transition thereby driven by magnetic part of the microwave. With microwave with pulse area θ , initial state $|0\rangle_N$ is coherently mapped to $|\psi\rangle_N = (\cos \frac{\theta}{2} |0\rangle + \sin \frac{\theta}{2} |1\rangle)^{\otimes N}$. Treating Fock states as spin excitations, Dicke states $|J, M\rangle$ provides alternative expression that can be mapped onto spherical phase space [88–90]. In this picture, Fock states of total number of atoms N and number of excitations n is mapped to $J = N/2, m = -(N/2) + n$, therefore visualized onto a sphere with radius $\hbar\sqrt{J(J+1)}$. Then our Fock states $|0\rangle_N$ ($|1\rangle_N$) are written as $|J = \frac{N}{2}, M = -\frac{N}{2}\rangle$ ($|J = \frac{N}{2}, M = -\frac{N}{2} + 1\rangle$). We are interested in tomographic signature when those N spin-1/2 is rotated on the Bloch sphere. Then

probability of having n-excitation after rotating 0-excitation state is

$$P(N, n, \theta) = \left\| \left\langle J = \frac{N}{2}, M = -\frac{N}{2} + n \middle| R_X(\theta) \middle| J = \frac{N}{2}, M = -\frac{N}{2} \right\rangle \right\|^2 \quad (9.2)$$

which is merely Wigner's small D-function $d_{m', m}^j(\theta)$ with $(j, m', m) = (\frac{N}{2}, -N/2 + n, -N/2)$. Probability of projecting each atom to “0” (“1”) state is $\cos^2 \frac{\theta}{2} (\sin^2 \frac{\theta}{2})$. From the symmetry, probability of measuring logical “0” after rotating the logical “1” state or $|W\rangle$. Since $|\psi\rangle_N$ is still a separable state, projections are independent to each other. Then probability projecting $|\psi\rangle_N$ to k-atoms in $|1\rangle$ state can be expressed as

$$P(N, k) = \frac{N!}{k!(N-k)!} \left(\cos^2 \frac{\theta}{2} \right)^{N-k} \left(\sin^2 \frac{\theta}{2} \right)^k \quad (9.3)$$

In the current destructive detection scheme, there is small chance ϵ per atom that $|0\rangle$ state can be detected as $|1\rangle$ due to Raman process. If we add this imperfectness into the equation, we get

$$P(N, k, \epsilon) = \frac{N!}{k!(N-k)!} \left[(1-\epsilon) \cos^2 \frac{\theta}{2} \right]^{N-k} \left[\epsilon \cos^2 \frac{\theta}{2} + \sin^2 \frac{\theta}{2} \right]^k \quad (9.4)$$

Following data(Figure 9.1) shows the probability of the projections $P(\bar{N}, 0)$, $P(\bar{N}, 1)$ and $P(\bar{N}, k \geq 2)$, where $P(\bar{N}, k \geq 2) = 1 - P(\bar{N}, 0) - P(\bar{N}, 1)$ because they add up to make the probability unity. They are averaged over Poisson distribution for the mean atom number $\bar{N} \sim 3.8$ atoms and $\epsilon = 2.5\%/\text{atom}$. It is instructive to visualize

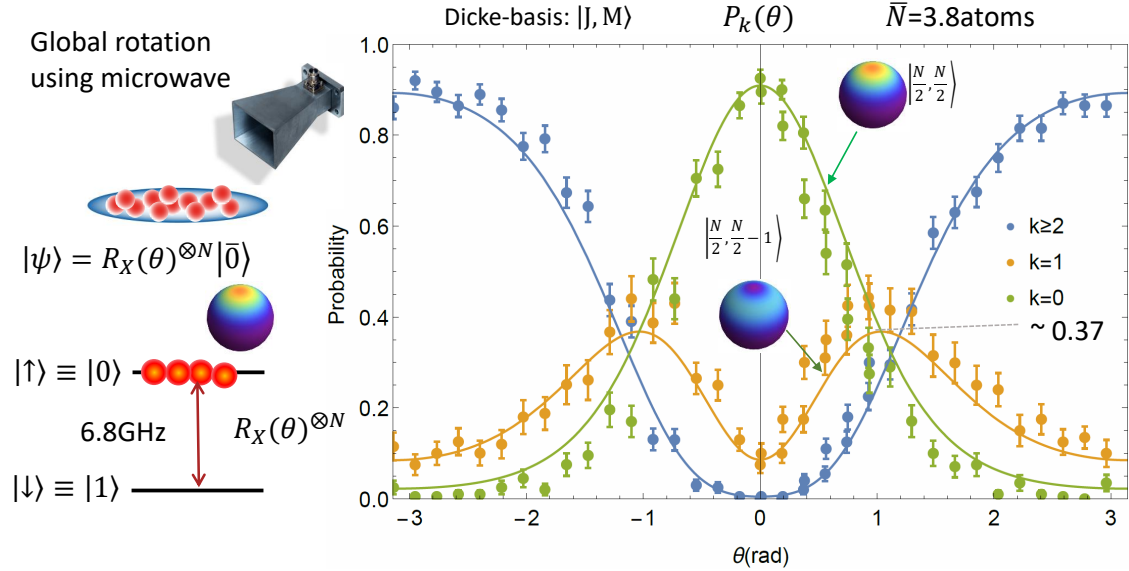


Figure 9.1: Microwave Tomography of the coherent spin state

those states onto spherical phase space. Husimi Q distribution[91] reads

$$Q(\theta, \phi) \equiv [(2J + 1)/4\pi] \langle \theta, \phi | \rho | \theta, \phi \rangle \quad (9.5)$$

where $|\theta, \phi\rangle$ is Bloch state, which can be written in Dicke state basis as the following.

$$|\theta, \phi\rangle = \sum_{m=-J}^J |J, m\rangle \binom{2J}{J+m}^{1/2} (\cos \frac{\theta}{2})^{J+m} (\sin \frac{\theta}{2})^{J-m} e^{-i(J+m)\phi} \quad (9.6)$$

9.1.2 Singly excited state Rotation

General expression describing N-atom two-level system in a pure state with a single excitation is

$$|\psi\rangle = \sum_i^N c_i |1\rangle_i \otimes |0\rangle^{\otimes(N-1)} \quad (9.7)$$

where c_i is complex number that satisfies normalization condition $\sum_i^N \|c_i\|^2 = 1$ and $0 \leq \|c_i\|^2 \leq 1$, and $\{|0\rangle, |1\rangle_j\}$ being basis states. This will include all possible singly excited states including separable or entangled cases. Rotating the state $|\psi\rangle$ maps to

$$R_X(\theta) |\psi\rangle = \sum_i^N c_i \left[\cos \frac{\theta}{2} |0\rangle + i \sin \frac{\theta}{2} |1\rangle \right]^{\otimes(N-1)} \otimes \left[i \sin \frac{\theta}{2} |0\rangle_i + \cos \frac{\theta}{2} |1\rangle_i \right] \quad (9.8)$$

Then the probability of projecting all atoms to $|0\rangle$ is

$$\begin{aligned} P_{|\psi\rangle,0}(\theta) &= |\langle \bar{0}_N | R_X(\theta) |\psi\rangle|^2 \\ &= \left[\sum_j^N i c_j (\cos \frac{\theta}{2})^{N-1} \sin \frac{\theta}{2} \right] \left[\sum_k^N i c_k (\cos \frac{\theta}{2})^{N-1} \sin \frac{\theta}{2} \right]^\dagger \\ &= (\cos \frac{\theta}{2})^{2N-2} (\sin \frac{\theta}{2})^2 \left[\sum_j^N c_j \right] \left[\sum_k^N c_k^* \right] \\ &= (\cos \frac{\theta}{2})^{2N-2} (\sin \frac{\theta}{2})^2 N |\langle W | \psi \rangle|^2 \end{aligned} \quad (9.9)$$

This probability is maximized for an input state $|W\rangle$, $P_{|W\rangle,0}(\theta) = N (\cos \frac{\theta}{2})^{2N-2} (\sin \frac{\theta}{2})^2$.

This can be contrasted to the localized excitation such that $|\psi\rangle = |\bar{1}\rangle_i$ or $c_j = \delta_{i,j}$, which has the overlap $|\langle W | \psi \rangle|^2 = 1/N$, giving the probability of measuring no

excitation after rotating $P_{|1\rangle_i,0}(\theta) = (\cos \frac{\theta}{2})^{2N-2}(\sin \frac{\theta}{2})^2$.

Particularly interesting feature happens for a set of states that are orthogonal to the symmetric state. We introduce a shorthand notation $|1_\perp\rangle$ that has zero overlap $|\langle W|1_\perp\rangle|^2 = 0$ to the symmetric state. These states cannot rotate back to zero-excitation state as the spin-rotations conserve angular momentum in Dicke state representation.

In case we have statistical mixture of localized single excitation, we employ a density matrix describing a fully incoherent, singly excited N-particle state, which can be written as

$$\rho_{incoh} = \frac{1}{N} \sum_j^N \rho_j \quad (9.10)$$

with $\rho_j = |\bar{1}_j\rangle\langle\bar{1}_j|$. Probability of measuring “0” after rotating ρ_{incoh} is

$$\begin{aligned} P_{\rho_{incoh},0}(\theta) &= \text{Tr} [R_x(\theta)^{\otimes N} \rho_{incoh} (R_x(\theta)^{\otimes N})^\dagger |0_N\rangle\langle 0_N|] \\ &= \text{Tr} [\rho_{incoh} (R_x(\theta)^{\otimes N})^\dagger \langle R_x(\theta)| |\bar{0}\rangle\langle\bar{0}| R_x(\theta)] \\ &= \text{Tr} \left[\rho_{incoh} \bigotimes_i^N \left(\cos^2(\frac{\theta}{2}) |0_i\rangle\langle 0_i| + \sin^2(\frac{\theta}{2}) |1_i\rangle\langle 1_i| \right) \right] \quad (9.11) \\ &= \text{Tr} \left[\frac{1}{N} \sum_j |1_j\rangle \cos^{2N-2}(\frac{\theta}{2}) \sin^2(\frac{\theta}{2}) \langle 1_j| \right] \\ &= \cos^{2N-2}(\frac{\theta}{2}) \sin^2(\frac{\theta}{2}) \end{aligned}$$

which shows the $1/N$ reduction compared to the symmetric coherent superposition state $|W\rangle$.

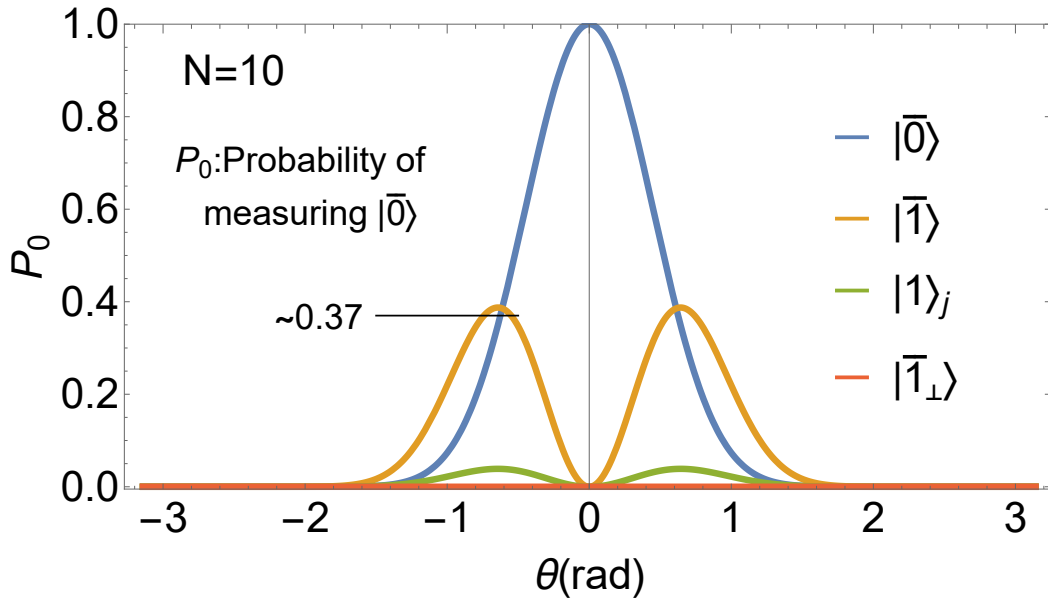


Figure 9.2: Microwave Tomography of possible constituents of Atomic Fock state: Non-localized vs localized single excitation states. Plotted are for $N = 10$ atom case. States are written in Dicke basis.

9.2 W-state Rotation

We experimentally measured tomographical signature of the state prepared by Atomic Fock state protocol[81]. Having a Fock state only indicates there was a single excitation, which does not imply whether the excitation was localized(separable) or non-localized(entangled) state. Those states behave differently when microwave rotations are applied, as show in Figure 9.2. entanglement witness for more general cases such as Dicke states[92] Experiment results (Figure 9.3)imply that the prepared state can be described by statistical mixture of symmetric states, $|\bar{0}\rangle$ and $|\bar{1}\rangle$. So far we have assumed that the atom number does not change while they are Rydberg-excited or stored in Hyperfine manifold. However several collision processes do

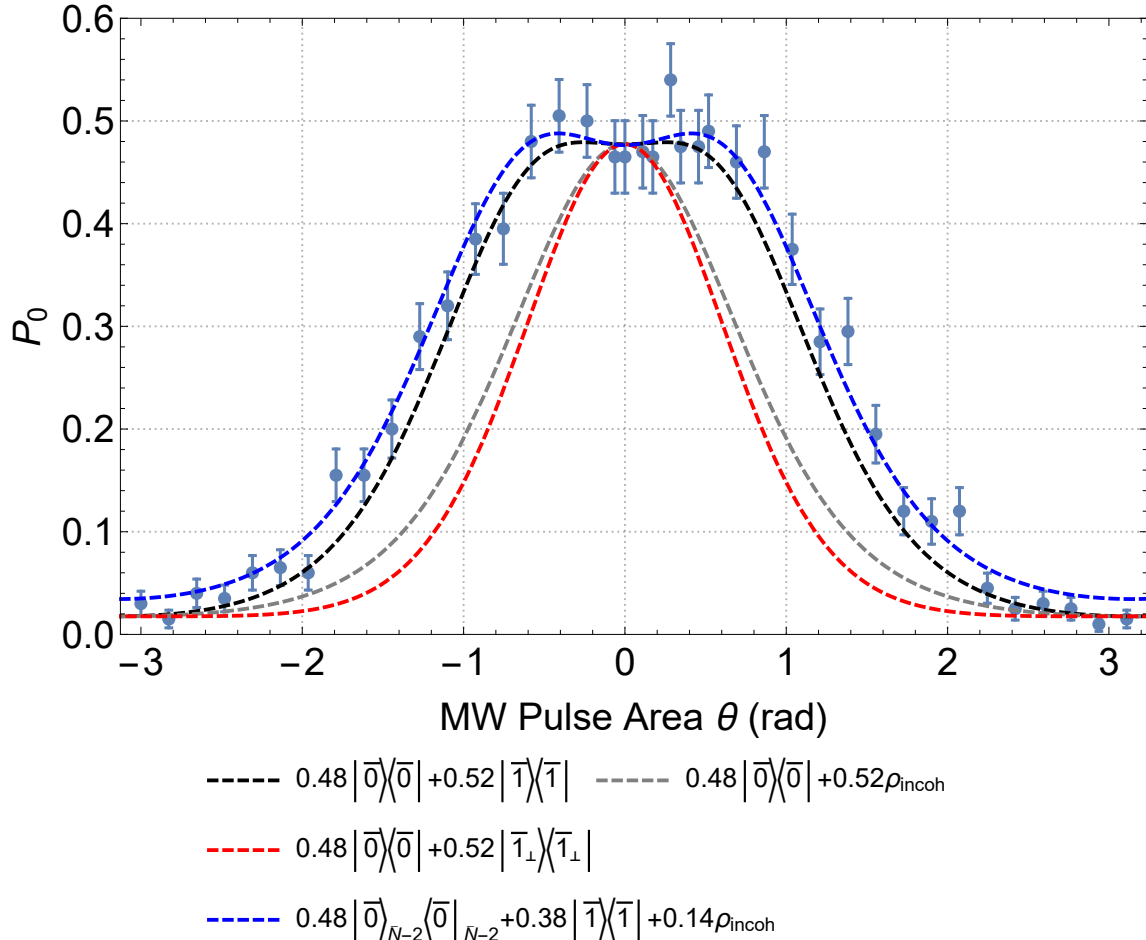
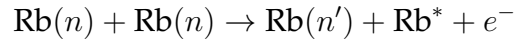


Figure 9.3: Probability of measuring 0 after rotating a state prepared by our W-state preparation pulses. Mean number of atoms $\bar{N} \sim 5.2$. State is reconstructed from linear combination of basis $\{|0\rangle, |\bar{0}\rangle_{\bar{N}-2}, |\bar{1}\rangle, |1_j\rangle, |\bar{1}_{\perp}\rangle\}$ that reproduces the observed tomographic signature. Basis states assumes Poissonian atom number distribution with mean \bar{N} , if not explicitly written. $\bar{N} - 2$ denotes reduced atom number. Blue curve is the best reconstruction, and the other lines are assuming the single excitation being localized or non-symmetric state. Microwave Rabi frequency $\Omega_{MW} = 2\pi \times 5.5\text{kHz}$. Data from 2015-05-30

exist which may lead a pair of atoms to escape from the trap. From the observed tomography (Figure 9.3), the reconstructed state $|\bar{0}\rangle_{N=2}$ could be resulted by pair-loss mechanisms, for example, Rydberg-Rydberg autoionization:



or Hyperfine-changing(ΔF) collisions:

$$|F = 2\rangle + |F = 2\rangle \rightarrow |F = 1\rangle + |F = 2\rangle + E_{\text{hfs}}$$

$$|F = 2\rangle + |F = 2\rangle \rightarrow |F = 1\rangle + |F = 1\rangle + 2E_{\text{hfs}}$$

Ryd-Ryd interaction leads to autoionization[46] of one Rydberg atom and the changes the state of the other Rydberg atom, making them inaccessible with the addressing lasers. For a pair of $111d$ atoms at mean distance $R \sim 500\text{nm}$ has $\Gamma_{\text{pair}} \sim 2\text{kHz}$ or lifetime of $\sim 500\mu\text{s}$, which is still a magnitude longer than the spontaneous decay time of Rydberg states. Inelastic collisions between ground state atoms can cause nuclear spin flip and releases an energy enough to kick atoms out of the trap. Since majority of atoms being at $|0\rangle = |F = 2, m = 0\rangle$ this is also likely pair-loss channel. Inelastic collision rate $\beta = 10^{-11}\text{cm}^3/\text{s}$ and peak atom density $N \times 10^{11}/\text{cm}^3$, the rate for each atom to experience the collision is $r_{\Delta F} = \rho\beta = N/\text{s}$ or the lifetime is $1/N$ sec. Then the collision-limited lifetime of N-atom W-state is $\sim 1/N^2$ sec, making $\tau \sim 20$ ms for 7 atoms.

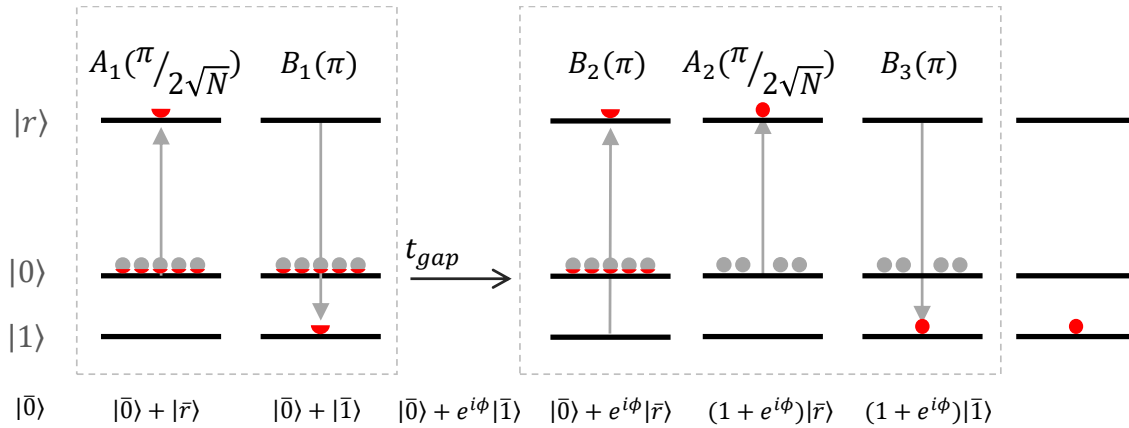


Figure 9.4: Experiment sequence to measure coherence time using Ramsey style interferometer

9.3 Coherence of ensemble qubit

Ramsey technique provides direct way to measure the atomic coherence of ensemble qubit. Rydberg W-state is prepared by a collective π pulse, then a single atom pi pulse maps the Rydberg excitation to Hyperfine manifold for long term storage. Experiment procedure is illustrated on Figure 9.4

W-state stored in the hyperfine manifold dephases due to finite coherence time between the clock states, where possible dephasing mechanism being atom-collisions, fluctuating ac stark shifts from atomic motions, and magnetic field fluctuations mapped to quadratic Zeeman shifts. For different gap time, dying oscillation is observed. We observed atom number dependency (N) on coherence time for separable states and entangled states. We performed another Tomography but this time allowing the prepared state to dephase. Time gap is inserted between the completion of W-state preparation protocol and the analyzing microwave ro-

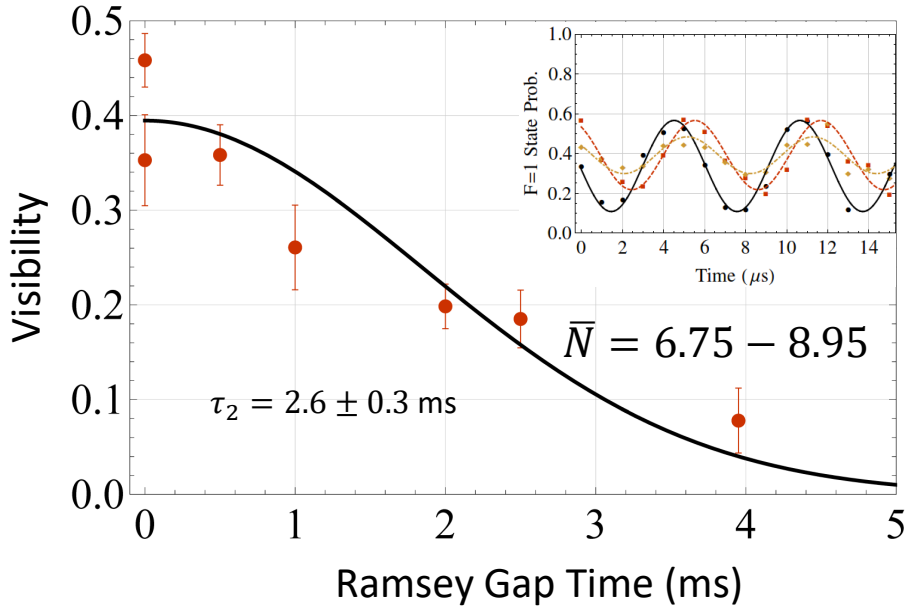


Figure 9.5: Ramsey interference measurement of qubit coherence for oscillation as a function of the gap time gives $T_2 = 2.6(3)$ ms. $\bar{N} = 7.6$. The circles are data points with 1σ error bars and the dashed and The gap time is the time t between the pulses. The solid lines are fits to the functions defined in the text. All data have been corrected for $\sim 1.5\%$ probability per atom of inset shows the Ramsey oscillations for gap times of 0 (solid the blow-away giving an unwanted transition from $|0\rangle \rightarrow |1\rangle$. The line), 0.5 ms (dashed line), and 2.5 ms (dashed-dotted line)

tation. Data shown on fi. 9.7 is consistent with the measured T_2^* such that the reduction of population($0.0167/0.206 \sim 0.081$) matches very well to the calculated $a(t = 5.5\text{ms}, T_2^* = 2.6\text{ms}) \sim 0.083$, using Equation. 6.8 fall off for given coherence. Although this run have lower W-state preparation than the other dataset Figure 9.3, decay agrees well.

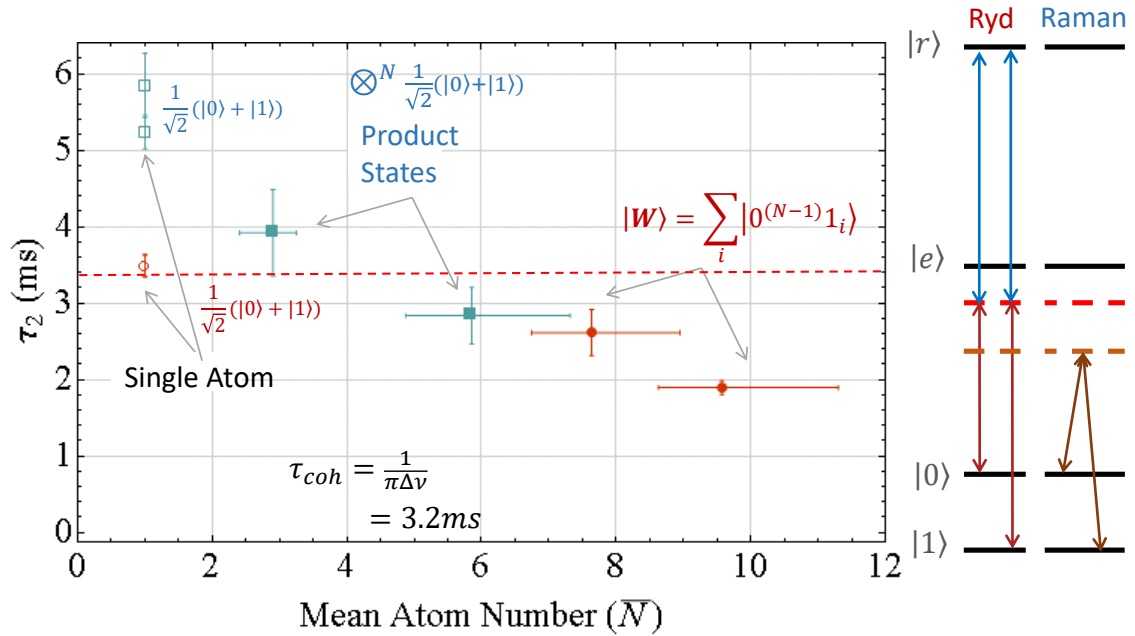


Figure 9.6: Atom number dependency of atomic ensembles in different entanglement class.

9.4 Limitations

Observed W-state preparation fidelity cannot be fully explained by inhomogeneous collective enhancement from atom number fluctuation. No improvement seen on composite pulse experiment suggests that the imperfectness is not due to pulse area errors, but from Rydberg physics we did not take account. Primary reason we suspect is the breakdown of Rydberg blockade, allowing multiple Rydberg excitation within an ensemble and making further optical manipulation not reliable. Due to 1-dim like trap geometry, interatomic axis are mostly parallel($\theta \sim 0^\circ$) to the quantization axis set by a weak magnetic field ($B_z = 3.7G$). Calculation (Figure 9.8) shows that the blockaded unperturbed pair-state, $|97d_{5/2}, m_j = 5/2; 97d_{5/2}, m_j = 5/2\rangle$, has

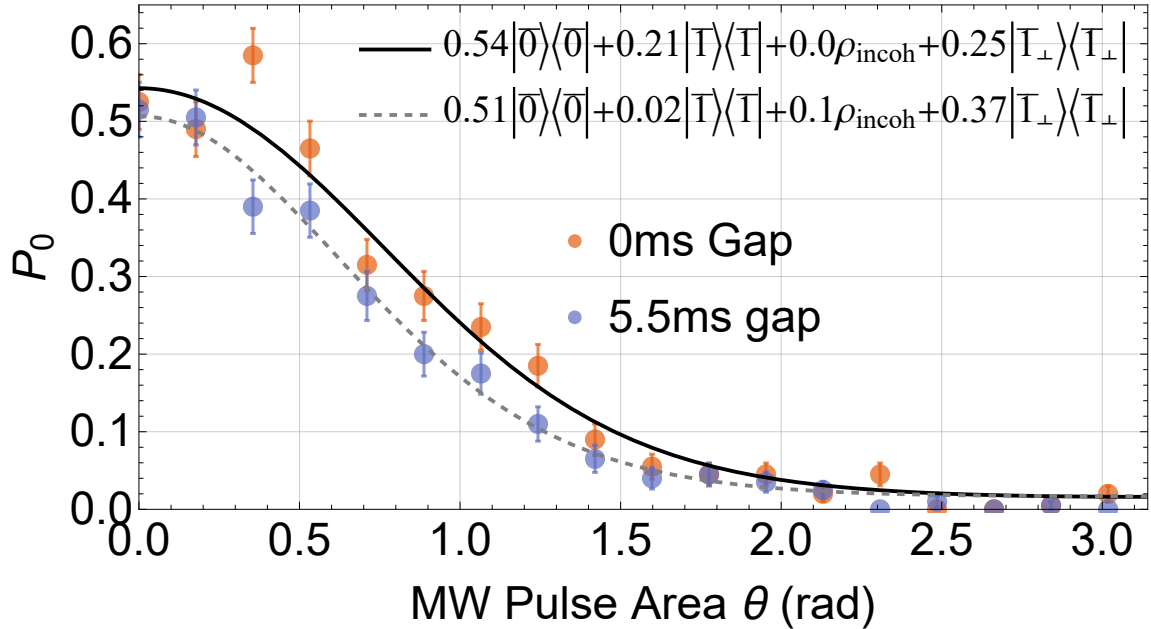


Figure 9.7: Evolution of tomographic signature of state prepared with W-state protocol. $\bar{N} \sim 5.2$. Lines are maximum likelihood reconstruction of the state from a set of basis $\{|0\rangle, |\bar{1}\rangle, |1_j\rangle, |1_{\perp}\rangle\}$, where $|1_j\rangle$ indicates localized single excitation. Data from 2015-06-09.

small but non-zero overlap to an unblockaded new pair-state around $R \sim 6\mu\text{m}$, resulting from dipole interaction to $|97p_{3/2}, m_j = 3/2; 97f_{7/2}, m_j = 7/2\rangle$.

Note that in our geometry ($\theta = 0$), dipole interaction conserves the projection of total angular momentum $M = m_{j_1} + m_{j_2}, \Delta M = 0$, where m_{j_1} and m_{j_2} are magnetic quantum number of Rydberg state of an atom-pair in interest. This greatly reduces the size of basis that can couple to, allowing one to calculate the pair-state energy level and overlap at reasonable computational resource. One of proposed actions to mitigate the Rydberg leakage is to choose other Rydberg state where the failure radius R_x can be avoided. However, R_x appears to be universal due to dipole-dipole coupling between $|nd_{5/2}, m_j = 5/2; nd_{5/2}, m_j = 5/2\rangle \leftrightarrow$

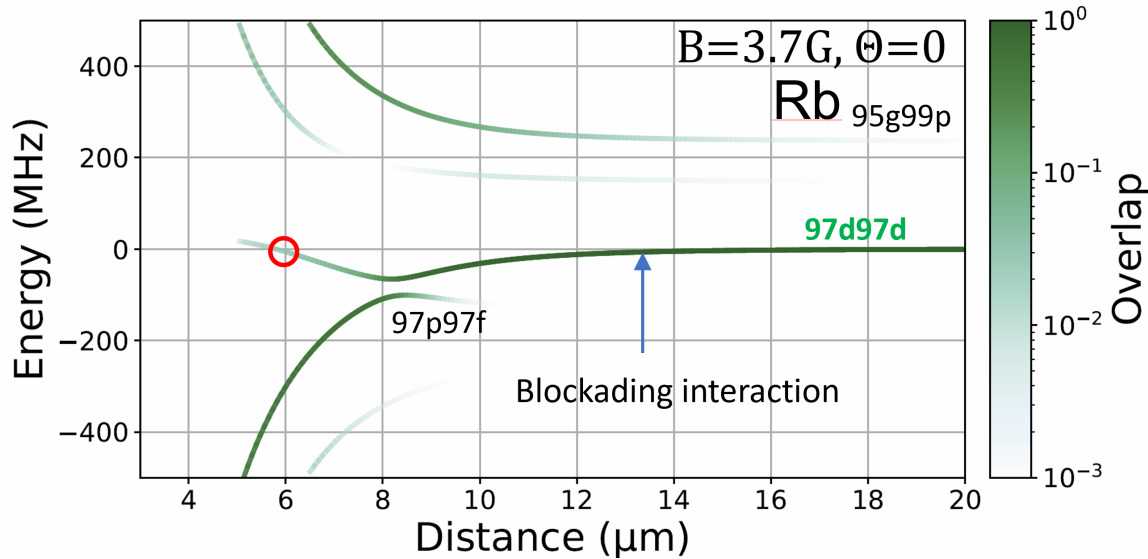


Figure 9.8: Pair-state calculation. Perturbed energy levels and overlap to unperturbed pair-state $|97d_{5/2}, m_j = 5/2; 97d_{5/2}, m_j = 5/2\rangle$ is plotted. Interatomic axis parallel to the quantization axis set by magnetic field. $\theta = 0^\circ$, $B_z = 3.7G$. Interaction with dipole-allowed neighboring pair-state, $|97p_{3/2}, m_j = 3/2; 97f_{7/2}, m_j = 7/2\rangle$, makes a perturbed pair-state to be unblockaded around $R = 6\mu\text{m}$ (Red circled). This pair-state has small yet non-zero state overlap to the unperturbed pair-state that is designed to be blockaded.

$|np_{3/2}, m_j = 3/2; nf_{7/2}, m_j = 7/2\rangle$, See Figure 9.9 for the case of $|84d_{5/2}, m_j = 5/2\rangle$.

Inserting 1D optical lattice on top of the existing dipole trap may restrict the interatomic distance away from the bad spot. We constructed 1D optical lattice with lattice constant $\Lambda = 1.59\mu\text{m}$. This will be also mitigate short range Rydberg interactions stemming from overlapping electronic wavefunctions. Other possible dynamics that can hurt the preparation fidelity are listed below.

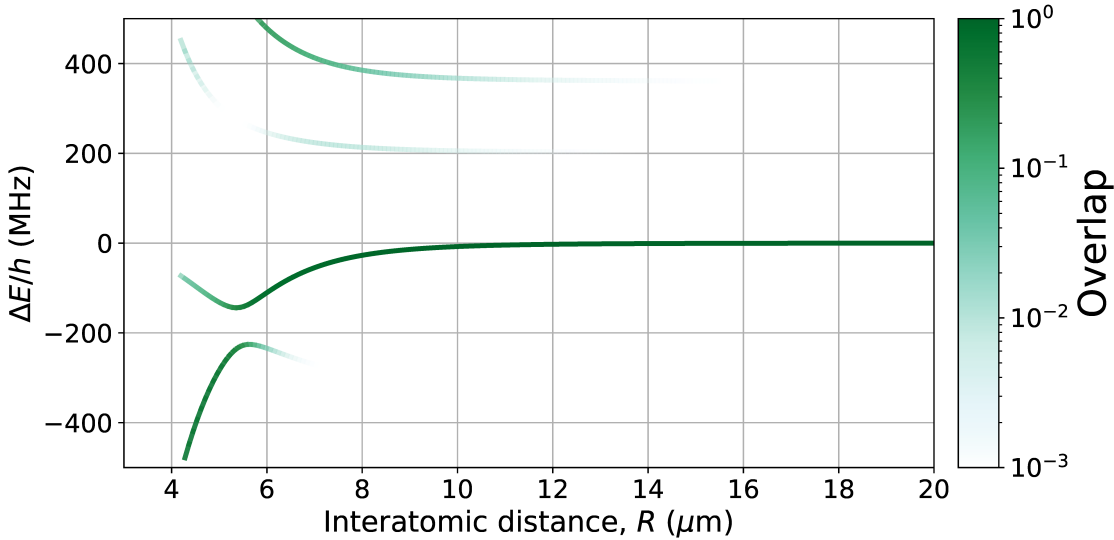


Figure 9.9: Pair-state calculation. Perturbed energy levels and overlap to unperturbed pair-state $|84d_{5/2}, m_j = 5/2; 84d_{5/2}, m_j = 5/2\rangle$ is plotted. Interatomic axis parallel to the quantization axis set by magnetic field. $\theta = 0^\circ$, $B_z = 3.7\text{G}$. Interaction with dipole-allowed neighboring pair-state.

Rydberg auto-ionization

Attractive molecular potential between $|nd; nd\rangle$ atoms can cause motion of stationary atoms, ultimately leading to ionizing collisions. This Rydberg-Rydberg ionization through dipole coupling[46, 93–96] become more prominent at high density sample. This mechanism will kick one or both Rydberg atoms out of the trap, if multiple Rydberg atoms were generated due to leakage. Consequently Rydberg excitation become localized, losing the entanglement.

Rydberg interaction induced dephasing

Strong dipole-dipole coupling[97, 98] happening at uncontrolled fashion can quickly yield dephasing of the state. This case is similar to having an external rf coupling multiple Rydberg states.

10 ENSEMBLE-ENSEMBLE BLOCKADE

Rydberg blockade and Rydberg-mediated quantum gates between single-atoms have been demonstrated[99, 100] Given our ability to prepare W-state in semi-deterministic fashion, we extend our scope to multi-ensemble experiments and demonstrate Rydberg blockade between two ensembles qubits.

10.1 Experiment Sequence

Experiments involve two optically trapped atomic ensembles in $|\bar{0}\rangle \equiv |2, 0\rangle^{\otimes N}$ state. One of the ensemble will be “Control” and the other is “Target”. Control ensemble in the ground state has negligible interaction on the Target ensemble, thereby Target Ground-Rydberg Rabi oscillation is not affected. However, if Control ensemble is excited to Rydberg W-state $|\bar{r}\rangle$, Target ensemble experiences van der Waals interaction, shifting the Rydberg energy levels. Large enough shift will prohibit Rydberg excitation on Target ensemble as well. Therefore π -pulse to map possible Rydberg population down to $|1, 0\rangle$ ground state will result no $|1, 0\rangle$ state, which is measured by pushing the $|2, 0\rangle$ population out of the trap.

We performed those experiments and results are described in the next section.

10.2 Experiment Results

Obtained experimental results are consistent with the prediction, shown on Figure 10.2. By switching the Control ensemble on or off, probability of preparing $|1, 0\rangle$ on

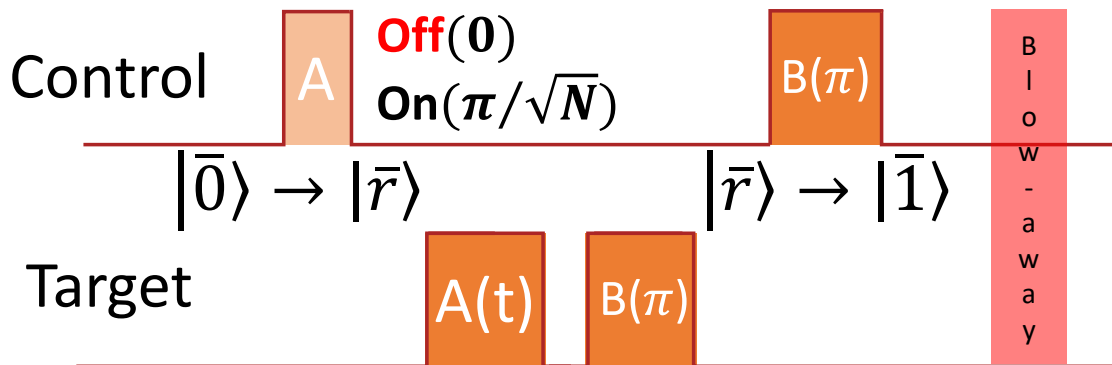


Figure 10.1: Ensemble blockade experiment configuration and pulse sequences. Control qubit is off for (Red), and is turned On(Black) by applying a collective π -pulse to excite to Rydberg W-state. Blow-away removes $|0\rangle$ population and remaining $|1\rangle$ is measured by fluorescence imaging.

the Target ensemble can be controlled. Amplitude of collective Rabi oscillation on the Target ensemble was suppressed by 89%. This is consistent with the probability to excite Control ensemble to contain Rydberg atom, limited by pulse area error and finite Ground-Rydberg coherence.

Successful N=1 Fock state preparation on Control ensemble after the blow-way suggests that Rydberg excitation indeed existed during the experiment. Limiting the scope to these data sets, Ensemble blockade fidelity is near-unity, shown on Figure 10.3.

10.3 Blockade leakage and Reverse blockade

We measured the probability of control ensemble returning to $|1\rangle$ after completion of Ensemble blockading, as the function of target excitation pulse area. Experiment results for different blockade strength are shown in Figure 10.4.

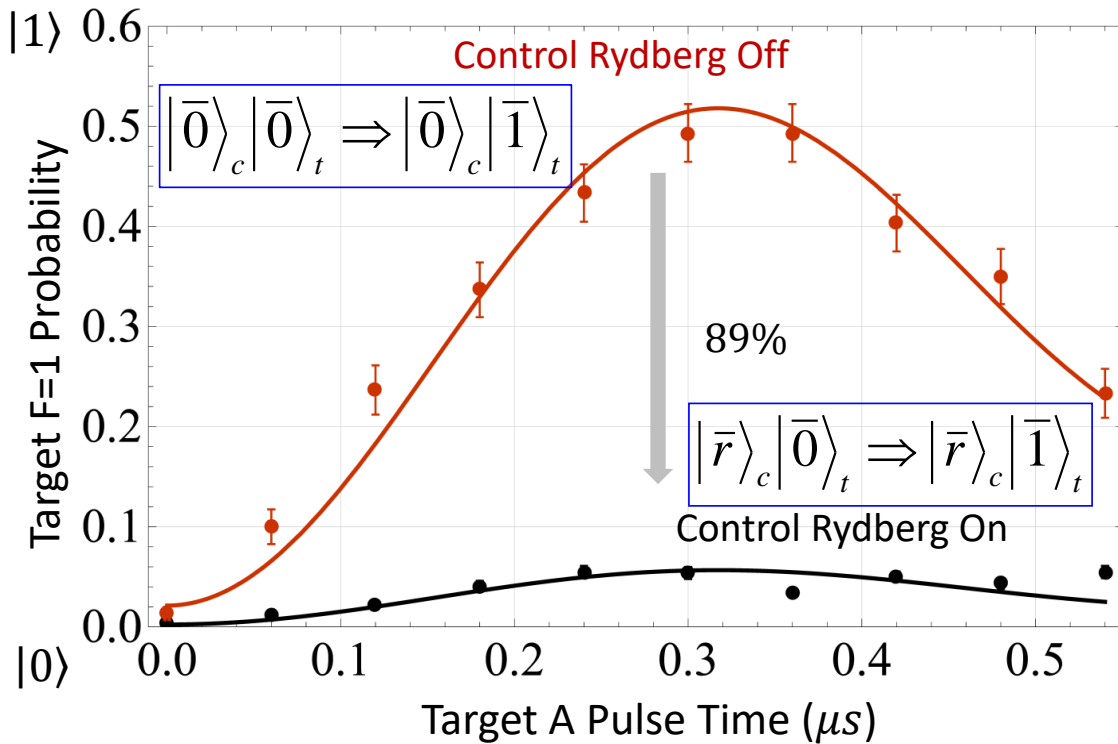


Figure 10.2: Collective Rabi oscillations on Target site while switching the Control qubit on and off

We observed the control ensemble refuses to return to the Ground state manifold. The failure rate increases as the target ensemble is driven longer, proportional to chance of having Target ensemble Rydberg excitation. We hypothesized this behavior to be stemmed from Rydberg double excitation (one in Control, and another in Target), due to van der Waals interaction not strong enough to fully blockade Target ensemble. Undesired Rydberg excitation on Target makes it perturber, and may blockade the attempt to de-excite Control ensemble back to Ground manifold. To test the hypothesis in experiment, three representative regimes are prepared, shown on Figure 10.4a. Tuning the Blockade strength can change the probability

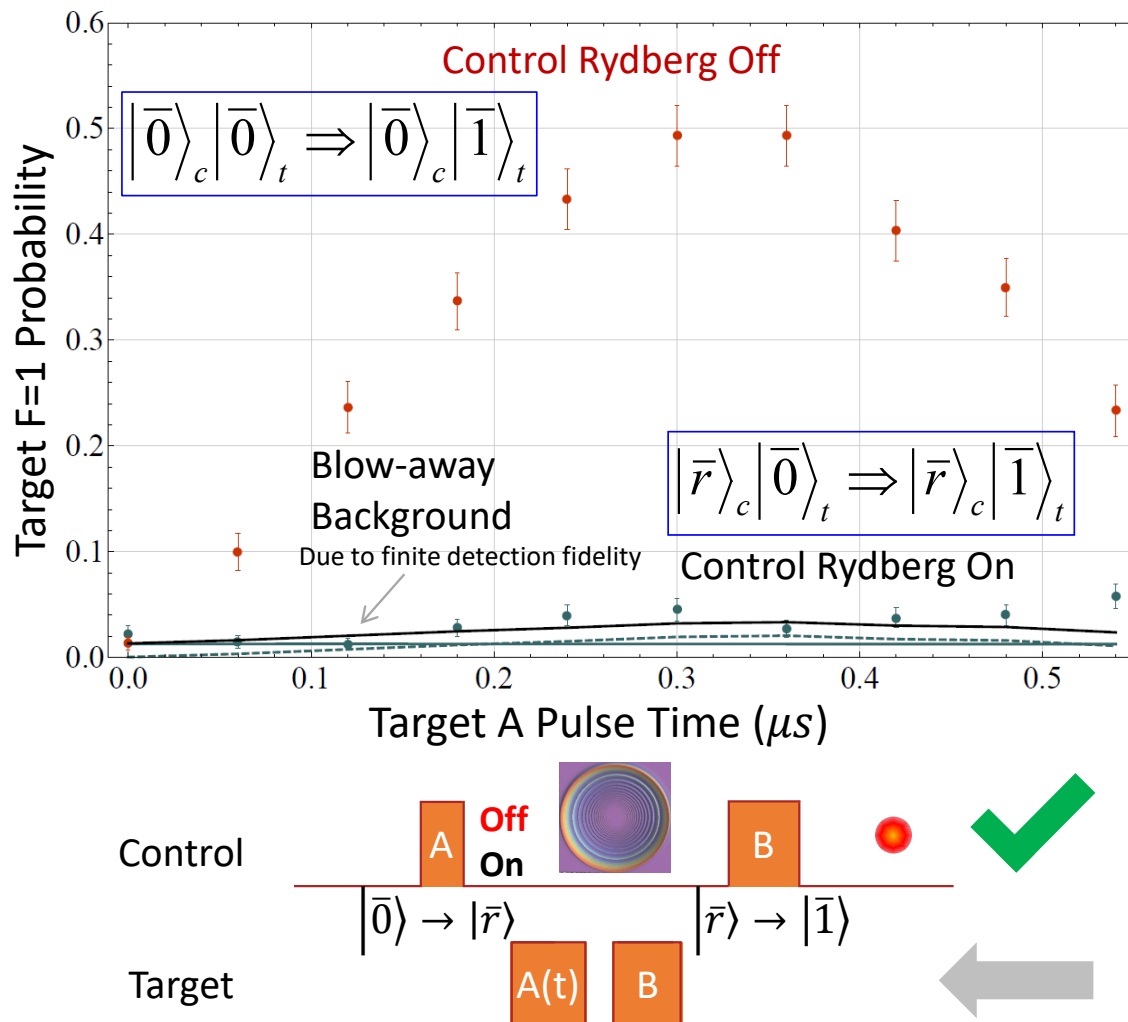
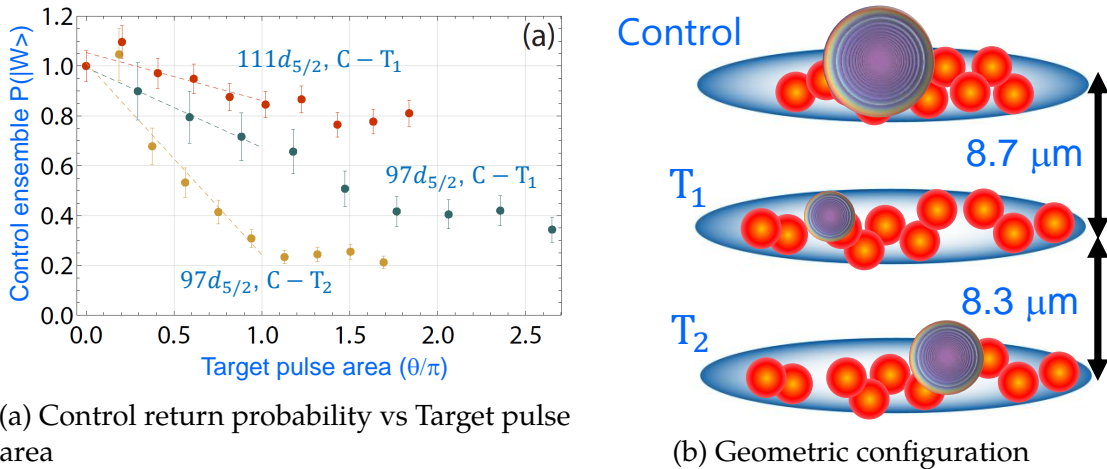


Figure 10.3: Collective Rabi oscillations on Target site while switching the Control qubit on and off. Post-selected on successful Control Transfer.



(a) Control return probability vs Target pulse area

(b) Geometric configuration

Figure 10.4: Reduction of Control ensemble returning to $|1, 0\rangle$ state, as a function of Target ensemble Rydberg pulse area.

of double Rydberg excitation, or Rydberg leakage on Target. This is achieved by changing inter-ensemble distance or choosing different Rydberg levels. Due to hard-wired dipole trap configuration, combinations of ensembles at different distances were assigned to the Control and Target.

1. Strong blockade regime : $|111d_{5/2}, m_j = 5/2\rangle, R = 8.7\mu\text{m}$
2. Intermediary regime : $|97d_{5/2}, m_j = 5/2\rangle, R = 8.7\mu\text{m}$
3. Weak blockade regime: $|97d_{5/2}, m_j = 5/2\rangle, R = 17\mu\text{m}$

In contrast to intra-ensemble case, atom pairs between two different ensembles experience weaker interaction because of angular dependency of $C_6(\theta)$. Furthermore, mismatch between interatomic axis and quantization axis set by magnetic field no longer forces $\Delta M = 0$, opening more interaction channels. Figure 10.5 shows the unperturbed pair-state $|97d_{5/2}, m_j = 5/2; 97d_{5/2}, m_j = 5/2\rangle$ will have

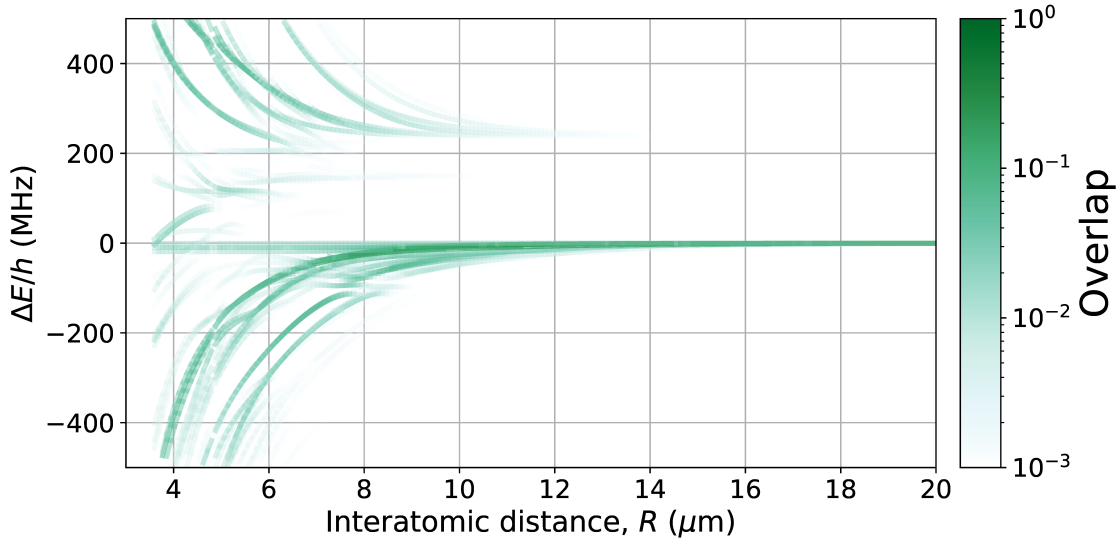


Figure 10.5: Pair-state calculation. Perturbed energy levels and overlap to unperturbed state $|97d_{5/2}, m_j = 5/2; 97d_{5/2}, m_j = 5/2\rangle$ is plotted. Interatomic axis perpendicular to the quantization axis set by magnetic field. $\theta = 90^\circ, B_z = 3.7\text{G}$

huge mixing, some of them might lead to Rydberg leakage. Avoiding this mixing seem extremely difficult. Results from 84d and 111d pair states are presented on Figure 10.6 and 10.7 respectively.

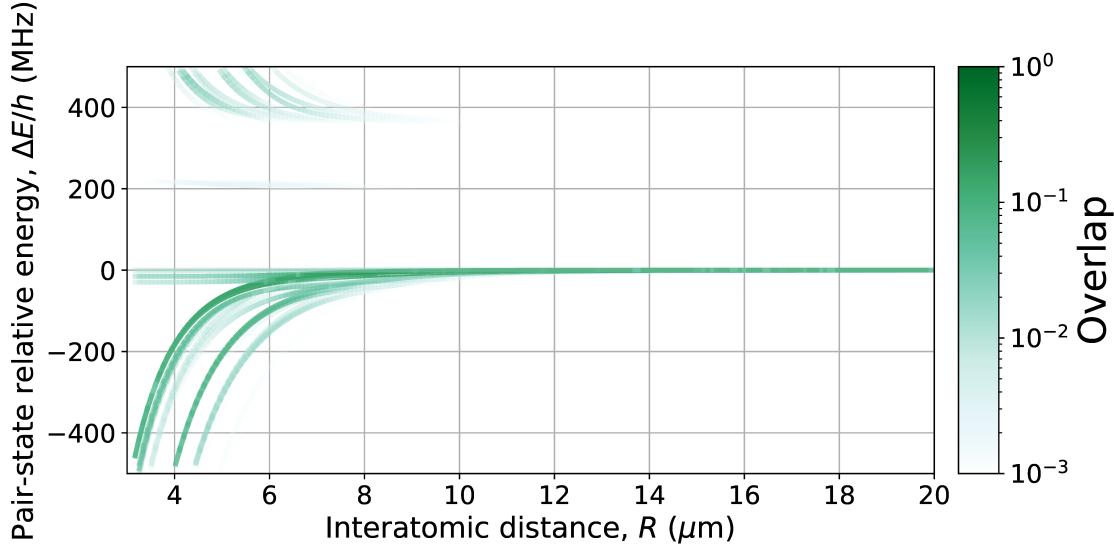


Figure 10.6: Pair-state calculation. Perturbed energy levels and overlap to unperturbed state $|84d_{5/2}, m_j = 5/2; 84d_{5/2}, m_j = 5/2\rangle$ is plotted. Interatomic axis perpendicular to the quantization axis set by magnetic field. $\theta = 90^\circ, B_z = 3.7\text{G}$

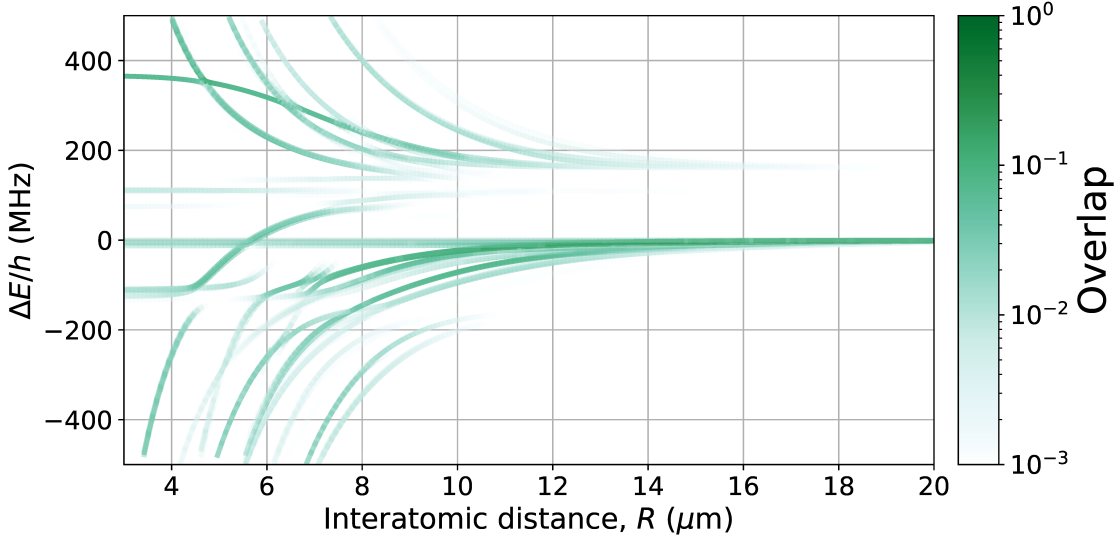


Figure 10.7: Pair-state calculation. Perturbed energy levels and overlap to unperturbed state $|111d_{5/2}, m_j = 5/2; 111d_{5/2}, m_j = 5/2\rangle$ is plotted. Interatomic axis perpendicular to the quantization axis set by magnetic field. $\theta = 90^\circ, B_z = 3.7\text{G}$

Part IV

Single-atom Qubit Experiments

11 STATE-DEPENDENT FLUORESCENCE DETECTION OF HYPERFINE QUBITS

This chapter is reproduction of [101]. The primary limitation to the non-destructive measurement is the number of photons that can be scattered before the atom leaks out from the original state caused by undesired coupling to the other states. We employ angular momentum selection rule to engineer the scattering to happen only between two states. Although this sounds conceptually simple, practical implementation requires careful characterization and in-depth understanding of atomic physics. We begin by presenting the main experiments and the results, followed by discussions on minimizing unwanted state coupling. Efforts are described from employing high purity circularly polarized light(Section 11.5.1), magnetic field shimming(Section 11.5.2), dealing with vector light shift (Section 11.5.3) and tensor light shift (Section 11.5.4). Then theoretical and quantitative calculations on scattering rate with unpolarized- and circularly polarized light are presented (Section 11.6). We briefly mention a site-selective quantum error correction scheme that is compatible with our state-dependent fluorescence detection.

11.1 Motivation

Quantum computation requires qubit state measurements to determine the result of a computation, and for measurement based quantum error correction. Measurement of the quantum state of an atomic hyperfine qubit is most often performed

by using a cycling, or near cycling, transition which repetitively transfers the qubit between a bright state $|B\rangle$ and an excited state $|e_B\rangle$. Detection of scattered photons due to illumination with light that is near resonant with the cycling transition projects the qubit into state $|B\rangle$. Conversely, if no photons are detected, the qubit is projected into the dark state $|D\rangle$. This idealized picture breaks down if the cycling transition is not perfectly closed, in which case an atom in state $|B\rangle$ may suffer a Raman transition to $|D\rangle$ thereby giving a measurement error.

Measurements that use a cycling transition rely on the availability of a metastable qubit dark state $|D\rangle$, or on shelving one of the qubit levels into a metastable dark state, as is done in trapped ion experiments[102]. In alkali atom experiments with qubits encoded in ground hyperfine levels the availability of a cycling transition generally relies on an angular momentum selection rule that is enforced by using probe light with a well defined polarization. This implies that the probe light propagates along a single axis in space which results in atomic heating due to the random direction of scattered photons. For a lossless measurement either the potential confining the atom should be sufficiently deep for the heating to be tolerable, as in experiments with trapped ions[103], or the detection system should allow for a state measurement after scattering only a small number of photons to minimize heating. This latter approach was demonstrated with optically trapped atomic qubits[104–106] using low noise single photon detectors. Alternatively, coupling of an atom to a high finesse cavity enables state detection with minimal heating and without loss of atoms[107]. It has been proposed to perform fast state measurements by coupling a single atom to a many atom ensemble, as a means of

increasing the effective photon scattering rate[28]. It is also possible to enforce a dark state condition with three dimensional probing light that cools the atoms, but this requires an inconvenient and complex sequence of steps[108].

In order to take full advantage of the large number of qubits available in neutral atom experiments it is desirable to be able to losslessly measure multiple qubits in parallel. This can be done by imaging scattered light from an array of qubits onto a sensitive imaging detector such as an electron multiplying charge coupled device (EMCCD). Although EMCCD cameras have high quantum efficiency they suffer from excess readout noise which has hitherto rendered parallel lossless state detection infeasible. To circumvent this limitation previous array experiments used a "blow away" technique where atoms in $|B\rangle$ are ejected from the array using a single unbalanced beam, followed by detection of the presence or absence of an atom. Atom detection is performed using a 3D light field that cools the atoms, but does not prevent state changing Raman transitions during the measurement. This approach provides state measurements, but requires that a new atom will have to be reloaded, half the time on average, which severely impacts the experimental data rate.

We show that low-loss detection of multiple atoms, in parallel, is possible using an EMCCD camera. This requires a careful choice of parameters to minimize both the motional heating rate (which is lower at large detuning) and the Raman depumping rate (which is lower at small detuning). The enabling advances include use of a moderately high numerical aperture (NA) collection lens, deep optical traps, and careful preparation of the polarization state of the probe light to minimize

Raman transitions from $|B\rangle \rightarrow |D\rangle$. Similar results to ours have been independently reported in [109].

11.2 Experiment Procedure

The experimental geometry and measurement sequence are shown in Figure 11.1. Atoms are prepared in the $|F = 1\rangle$ or $|F = 2\rangle$ hyperfine levels of the ^{87}Rb $5s_{1/2}$ electronic ground state, corresponding to $|D\rangle$ and $|B\rangle$ respectively. To prepare states of single atoms we begin by cooling in a standard magneto-optical trap (MOT) that is then overlapped with a 1D array of five optical dipole traps (ODTs) formed by focusing 1040 nm light to a waist of $w \simeq 2.5 \mu\text{m}$. The traps are (2.8, 4.4, 5.6, 3.9, 3.4) mK deep and are spaced by $\sim 9 \mu\text{m}$. The traps are pencil shaped with sizes $\sigma_z \sim 7 \mu\text{m}$, $\sigma_r \sim 0.7 \mu\text{m}$, with the long axis along the optical axis of the collection optics. Single atoms are loaded with probability 20-30% at a temperature of $\sim 100 \mu\text{K}$.

In order to measure the initial trap populations, the atoms are probed using 6 MOT beams with components near-resonant with $|B\rangle \leftrightarrow |e_B\rangle$ and $|D\rangle \leftrightarrow |e_D\rangle$ simultaneously, where $|e_B\rangle$ is the $F' = 3$ level and $|e_D\rangle$ is the $F' = 2$ level of the $5p_{3/2}$ excited state. Atom fluorescence is collected by a $NA = 0.4$ lens, and imaged onto an EMCCD camera (Andor iXon EM+ DU-860). The magnification was chosen such that the site separation is 2 pixels, and the signal from each ODT is integrated over a region of interest (ROI) defined by 5 camera pixels, as shown in Figure 11.2a). The advantage of a low magnification is that the same signal can be integrated

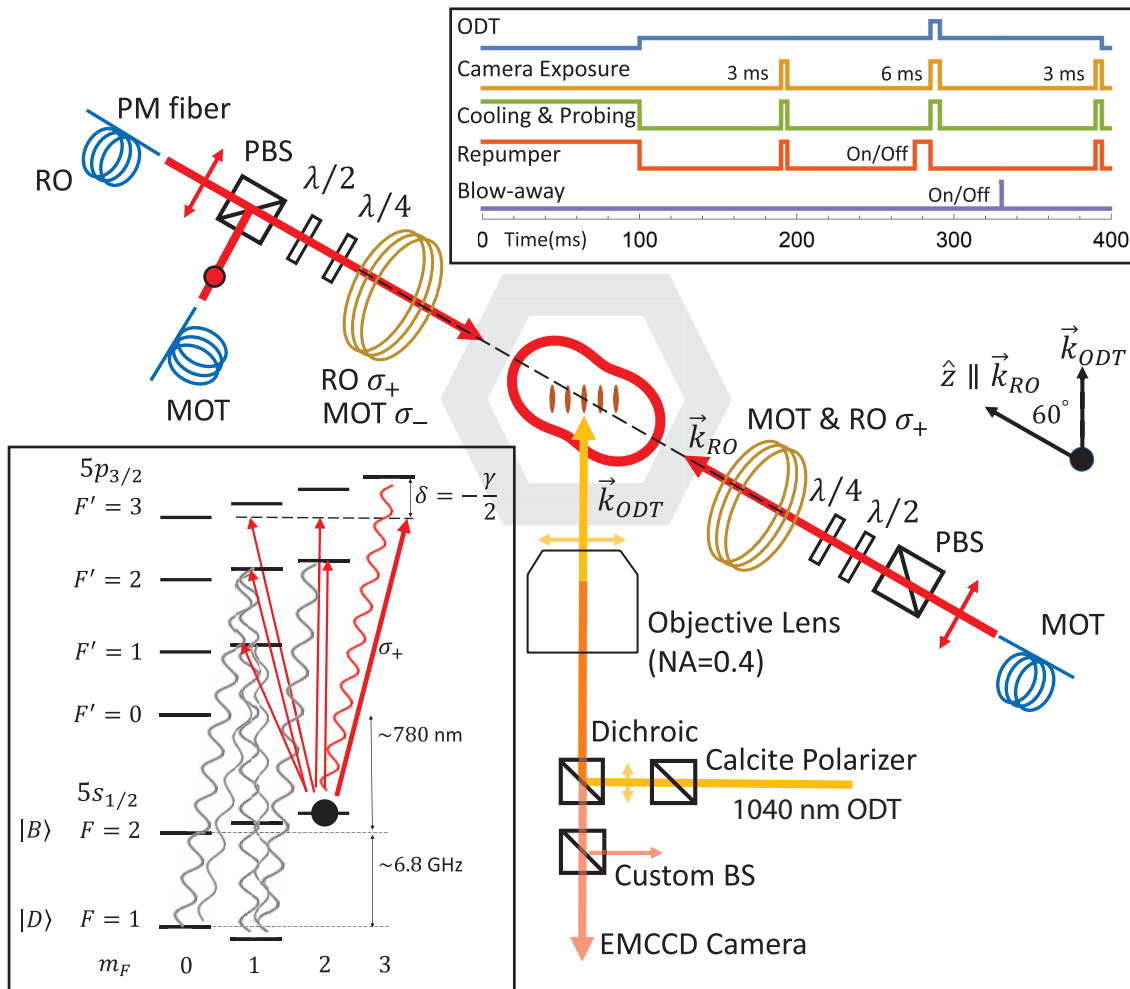


Figure 11.1: Experimental setup around hexagonal vacuum cell. The quantization axis $\hat{z} \parallel \vec{k}_{RO}$ is set by the bias magnetic field from a pair of coils. σ_+ polarized light propagates along \vec{k}_{RO} . The horizontally polarized trapping light is in the plane formed by \hat{z} and \vec{k}_{ODT} . Dichroic beamsplitters separate the trap light and fluorescence light which is imaged onto the camera.

over fewer pixels which lowers the electronic background noise. The excited states, $|e_B\rangle, |e_D\rangle$, are anti-trapped in the ODT, so to avoid heating the atom we toggle the ODT and the probe beams out of phase with a 50% duty cycle at 1.25 MHz. The photon detection efficiency is estimated to be 1.6 – 2.0%, accounting for the lens solid angle and dipole emission pattern (3.9 %), transmission through optics (74%), EMCCD quantum efficiency ($\eta = 75\%$), and fluorescence lying outside of the camera pixels used to define regions of interest (76-92%). Upon completion of the population measurement, there is a 100 ms delay for image transfer to the computer, after which the atoms are initialized in a random superposition of the Zeeman substates of one of the hyperfine levels, chosen by leaving either $|D\rangle \leftrightarrow |e_D\rangle$ or $|B\rangle \leftrightarrow |e_B\rangle$ on to depopulate the coupled state. To prevent low intensity leakage light from disrupting the initialized states mechanical shutters block unwanted light after initialization is completed. We estimate the state preparation fidelity for both states to be $> 99.5\%$ limited by the fidelity of blow away measurements that are performed at reduced ODT depth. After state initialization, a bias magnetic field $B_z \sim 20$ G making an angle of 60° from \vec{k}_{ODT} , the long axis of the ODTs, is switched on. The beams used for probing propagate along and counter to \vec{k}_{RO} , which is set to be parallel to \hat{z} with a possible small alignment error θ , see Figure 11.1. We use counter-propagating probe beams to mitigate the effect of heating due to near-resonant radiation pressure. In order to suppress Raman transitions both readout beams are σ_+ polarized which optically pumps the atoms into the lower state of the $|2, 2\rangle \leftrightarrow |3', 3'\rangle$ cycling transition. The beams are circularly polarized with small measured impurity of $\sim 6.3 \times 10^{-4}$ [110]. The counter-propagating

probe beams are generated from separate lasers with a relative frequency offset of 500 kHz. This technique avoids standing wave patterns, which can cause a time dependent drift in the single atom scattering rate and broaden the single-atom camera signal distribution. During the state measurement sequence the trap depths are temporarily doubled to enhance retention of the atoms. The combined intensity and detuning of the probe beams is set to saturation parameter $s_0 = 1$ and $\delta = \frac{\gamma}{2}$ red of the Zeeman shifted $|2, 2\rangle \leftrightarrow |3', 3'\rangle$ transition to provide maximal damping[111] with γ the excited state linewidth. The atoms are illuminated for 6 ms with the same 50% duty cycle as is used for the population measurement and fluorescence light is collected by the EMCCD for analysis. The resulting data are shown in Figure 11.2. The hyperfine state is determined on the basis of a simple threshold condition relative to the vertical dashed lines in Figure 11.2b),c). Although more extensive analysis that utilizes information gained from the temporal or spatial distribution of light in each region of interest can further reduce uncertainties[102, 109] our results show that the threshold condition alone is adequate for high fidelity measurements. After an additional 100 ms delay for image transfer, a third readout sequence probes the atoms again. Depending on the experiment, the third readout is either a second population measurement for probing atom loss or a destructive state selective measurement using a blow away beam for measuring the number of atoms depumped from $|B\rangle$ to $|D\rangle$.

	detected state (%)		final state (%)		
initial state	$ B\rangle$	$ D\rangle$	$ B\rangle$	$ D\rangle$	Lost
$ B\rangle$	(a) 95.6(6) (b) 98.0(4)	(a) 4.4(6) (b) 2.0(4)	98.6(1.9)	0.6 (1.6)	0.8(1.3)
$ D\rangle$	0.6(4)	99.4(4)	N/A	99.6(1.6)	0.4 (1.6)

Table 11.1: Results in the central site(#2) averaged over 2000 measurements. Data marked (a) are without correction, and data marked (b) are post-selected on the presence of an atom in the ROI in the third measurement, leaving only Raman depumping and state preparation as sources of error. The final state results are found from a third, state-selective measurement using a blow away beam.

ROI	Detected states (%)							
	#0		#1		#3		#4	
	$ \psi\rangle_i$	$ B\rangle$	$ D\rangle$	$ B\rangle$	$ D\rangle$	$ B\rangle$	$ D\rangle$	$ B\rangle$
$ B\rangle$	97.1(5)	2.9(5)	98.3(3)	1.7(3)	97.7(6)	2.3(6)	98.2(1.2)	1.8(1.2)
$ D\rangle$	0(0)	100(0)	1.0(5)	99.0(5)	0.5(4)	99.5(4)	0	100(0)

Table 11.2: Loss-corrected detection fidelities for the other four shallower traps. $|\psi\rangle_i$ is the initially prepared state.

11.3 Results

Full characterization of the non destructive measurement requires 4 experiments: 2 (state preparation $|B\rangle$ or $|D\rangle$) \times 2 (blow away on or off). The results of the 4 experiments for the center site are summarized in Table 11.1 for the center site and Table 11.2 for the other sites. We note that the results marked with a) include 2 % atom loss between each camera readout due to the finite trap lifetime $\tau \sim 5$ s and the 100 ms gap between each measurement. The background collision loss is not a fundamental limitation, and could be reduced by decreasing the chamber pressure or by shortening the image transfer time.

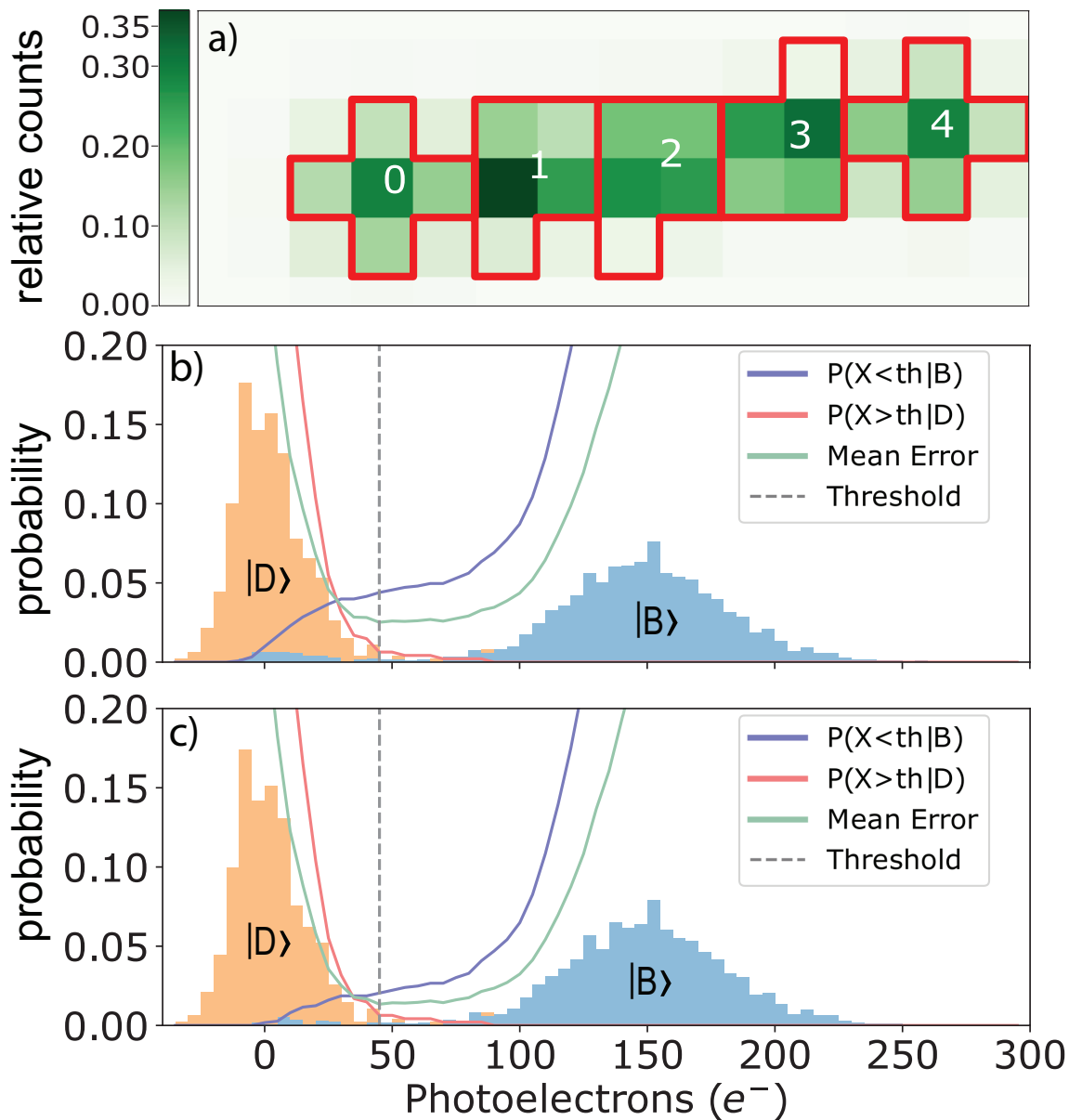


Figure 11.2: (a) Regions of interest are five pixels enclosed by red borders with the relative photon counts on each pixel shown by the green shading. Each 5 pixel ROI receives (76, 88, 89, 92, 76)% of the light from the corresponding trapped atom. Neighboring site fluorescence crosstalk is $\sim 2\%$. Each pixel represents a $4 \mu\text{m} \times 4 \mu\text{m}$ area and the site-to-site separation is $\sim 9 \mu\text{m}$. (b) Histograms of non-destructive readout in the central region (#2) for initial states $|B\rangle$ and $|D\rangle$. (c) The same data set post-selected on the presence of an atom in the ROI in the third measurement, leaving only Raman depumping and state preparation as sources of error. Signals in histograms are background-subtracted.

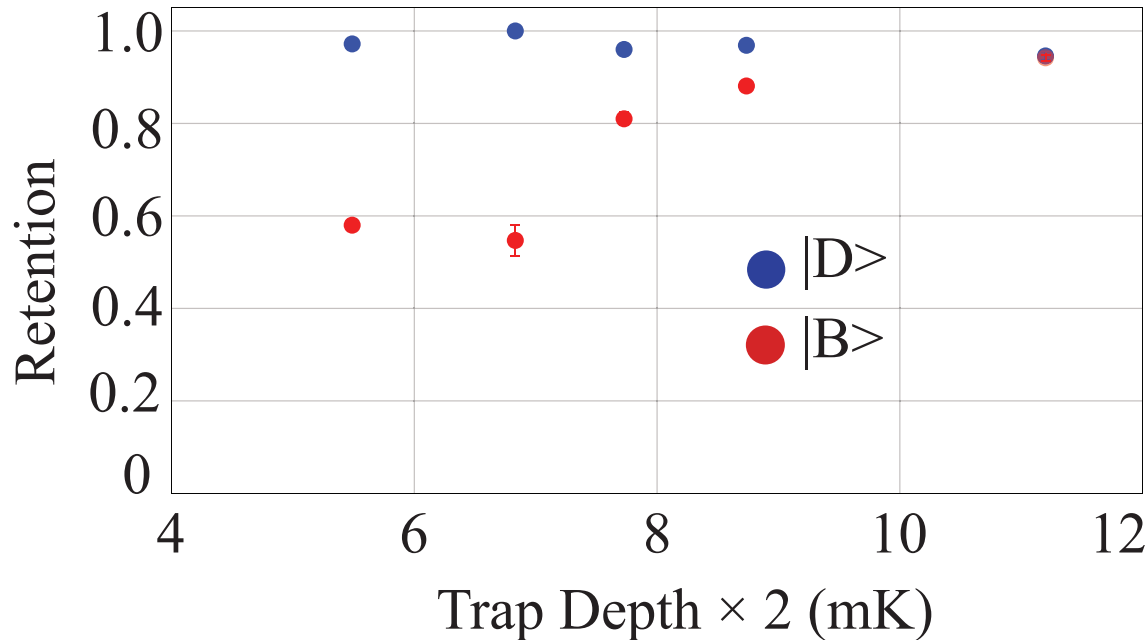


Figure 11.3: Probability of atom retention after non-destructive readout as a function of trap depth. Background gas collisions cause $\sim 4\%$ atom loss between the first and third measurements.

11.4 Discussion

In the experiments reported here the Zeeman states in each hyperfine level are equally populated, therefore depumping can occur in transit while optically pumping to the stretched state. This transient depumping is present even with perfect polarization and alignment. On average the amount of depumping will be very similar to what is expected for atoms prepared in $M = 0$ states, so our results are representative of measurements of qubit states. The relatively strong field $B_z \sim 20$ G, used to suppress effects from the vector light shift, causes the m_F states to have non-optimal detunings for transitions $|2, M_F\rangle \rightarrow |3', M_F + 1\rangle$ for $M_F \neq 2$ due to the Zeeman shifts. Decreasing the bias field will minimize the transient state depump-

ing, but we expect this to add to our state detection error at the $0.2 - 0.5\%$ level. This can be estimated by n_{op}/N_γ where $n_{op} \sim 10$ is the mean number of scattered photons to optically pump into $|2, 2\rangle$ and N_γ is a few thousand when not in the cycling state [110]. Despite the use of counter-propagating σ_+ beams, heating was still noticeable, limiting atom retention after the measurement, as is shown in Figure 11.3, and forcing us to use traps that are ~ 10 mK deep. This limited performance may be attributed to laser intensity noise, lack of sub-Doppler cooling mechanisms, and 1-D cooling. Future improvements including working with a higher NA lens to reduce the number of scattered photons needed for a measurement, and cooling the atoms into the Lamb-Dicke regime to suppress recoil heating will further reduce atom loss. Using blue detuned traps with intensity minima at the location of the atoms, as in [112, 113], would reduce the excited state tensor mixings, and obviate the need to turn the ODT on and off, thereby reducing any heating due to trap switching.

Ideally, qubit measurements should be projective, leaving the atom in an eigenstate of σ_z . This can be accomplished by following detection of an atom in $|B\rangle$, which ends up in $|2, 2\rangle$, with a sequence of stimulated Raman transitions or microwave pulses to return the atom to the $|2, 0\rangle$ hyperfine state.

11.4.1 Transient depumping

When starting from the non-stretched state a higher depumping rate is expected until the atom has been pumped into $|2, 2\rangle$, since the transitions can off-resonantly couple to $|2'\rangle$. A numerical simulation to estimate this source of error has been

performed using our experimental parameters: $s_0 \sim 1$, $\delta/2\pi = -3$ MHz from the Zeeman shifted cycling transition at $B_z = 20$ G, with polarization impurity of 6.3×10^{-4} , and equally distributed Zeeman state preparation. Results are shown in Figure 11.4. The scattering process is a sequence of quantum jumps that can be modeled as a Markov chain with finite state-change probability based on the coupling strength $|\Omega|^2$ and decay branching ratios. The effects from time-dependence of the probe intensity and the ODTs are ignored in the simulation. We see a sharp increase in dark state probability until the light optically pumps the atoms. We note that the transient depumping, which gives an error in state determination, could be eliminated by coherently transferring the atoms from the qubit state $|2, 0\rangle$ to the stretched state $|2, 2\rangle$ using microwave or Raman pulses.

11.4.2 Solution to Transient depumping

Coherent transfer of the computational basis(Clock states) to measurement basis(Stretched states) can be performed by a sequence of microwave pulses. Proposed sequence of microwave pulses, for our case, is $|2, 0\rangle \rightarrow |1, +1\rangle \rightarrow |2, +2\rangle$. In case of having two different quantization axes, one for computation and the other for qubit measurement, adiabatic reorientation of the bias magnetic field should precede.

11.5 Minimization of State-Mixing

Consider probing upper hyperfine ground level $F_g = J_g + I$ of alkali atoms with a cooling transition $J_g \rightarrow J_e = J_g + 1$. When using random polarization $N_\gamma =$

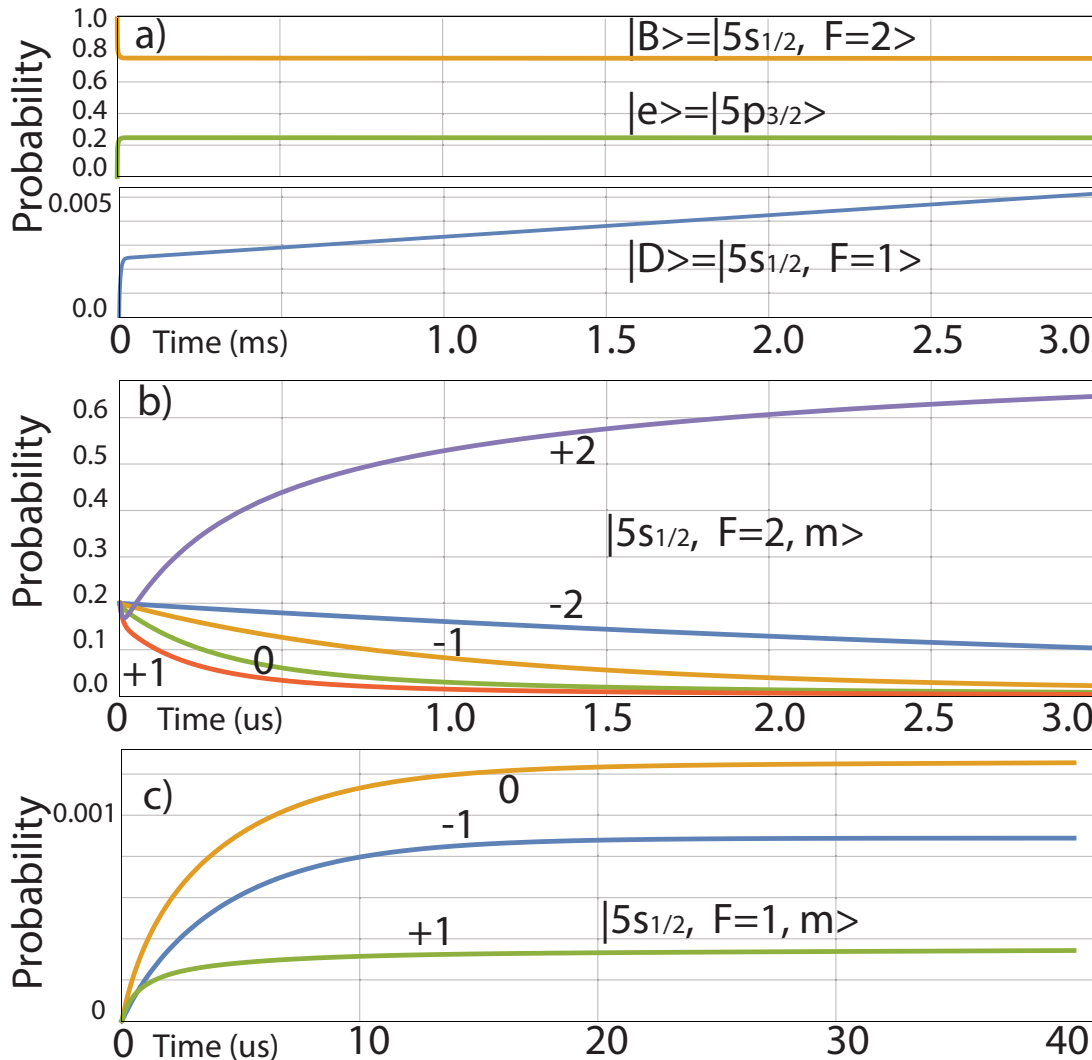


Figure 11.4: State dynamics during the state-selective readout. a) Probability of being in ground hyperfine levels and the excited level. Dark state probability is shown on a different y-scale. b) Transient optical pumping dynamics for the bright state manifold during readout. An initially random $|2, m_F\rangle$ state population is pumped to the stretched state. c) Transient dark state dynamics. Off-resonant coupling to $|2'\rangle$ is possible for all m_F states $m_F \neq 2$, so an increased Raman rate is expected until the atom is in $|2, 2\rangle$.

$\frac{38340}{1+4\delta^2/\gamma^2+s_0}$, where $s_0 = I/I_{s,eff}$ and $I_{s,eff} = 3.6 \text{ mW/cm}^2$ is the saturation parameter for randomly polarized light, see [110] for a derivation. With typical experimental parameters 10^4 photons could be scattered which would lead to approximately 100 photo-electrons, which is technically enough to clearly resolve the $|B\rangle$ and $|D\rangle$ photon histograms. However the $|B\rangle$ state histogram would leave a long tail from depumping events during the exposure that would overlap with the $|D\rangle$ state distribution. Therefore, in order to obtain clearly distinguishable photo-electron statistics we need the additional constraint that atoms scatter $\sim 10^4$ photons with minimal depumping, a condition that isotropic polarization does not satisfy.

To suppress the depumping, we have used σ_+ -polarized light along the quantization axis, as described above. In a real experiment polarization impurities and a small angular mismatch θ between \hat{z} , the direction of the magnetic field, and \vec{k}_{RO} , the axis of the readout beams, will still allow for a finite depumping rate.

11.5.1 Optimization of Light Polarization

Standard dielectric cube polarizing beam splitters (PBS) are used to set a linear polarization, and a pair of $\lambda/4$, and $\lambda/2$ retarders map the linear polarization to circular. Although in principle a $\lambda/4$ retarder is sufficient to map linear polarization to circular, we found that the use of an extra $\lambda/2$ retarder provided better adjustability leading to higher polarization quality. The quality is characterized by a rotating polarizer followed by a photodetector after the beam passes through the vacuum cell. Circularly polarized light transmits regardless of the PBS orientation, while linear polarization does not. Qualitatively the more circular the light is, the smaller

the oscillation amplitude as the detection polarizer is rotated. The retarders are rotated to minimize the amplitude of the oscillation. The contrast ratio of the visibility for maximally linear and maximally circular polarizations is used to quantify the purity of the polarization. Assume the polarization state has equal magnitude Cartesian components $E_x = E_y = E_0$ with a finite phase difference ϕ , represented as $\mathbf{E} = \begin{bmatrix} E_0, & E_0 e^{i\phi} \end{bmatrix}$ the intensity after passing through the rotating PBS is

$$I(\phi, \theta)/I_0 = \frac{1}{2} [1 + \cos(\phi) \sin(\theta)] \quad (11.1)$$

where θ represents the rotation angle of the PBS. The amplitude of the modulation is $\cos(\phi)/2$ which determines the relative phase. We now decompose the original electric field \mathbf{E} into σ_+ and σ_- as $E_{\sigma_+} = \begin{bmatrix} \frac{1}{\sqrt{2}}, & -\frac{i}{\sqrt{2}} \end{bmatrix} \cdot \mathbf{E}$, $E_{\sigma_-} = \begin{bmatrix} \frac{1}{\sqrt{2}}, & \frac{i}{\sqrt{2}} \end{bmatrix} \cdot \mathbf{E}$. Therefore the intensity ratio or polarization purity is

$$\frac{I_{\sigma_+}}{I_{\sigma_-}} = \left| \frac{E_{\sigma_+}}{E_{\sigma_-}} \right|^2 = \frac{1 + \sin(\phi)}{1 - \sin(\phi)} \quad (11.2)$$

With the rotating PBS setup, the DC and AC value of the intensity variation can be easily measured. We define the contrast as $C = \frac{\text{DC}}{\text{AC amplitude}} = \frac{1/2}{\cos(\phi/2)}$. Then the resulting intensity ratio is

$$\frac{I_{\sigma_+}}{I_{\sigma_-}} = \frac{1 + \sqrt{1 - 1/C^2}}{1 - \sqrt{1 - 1/C^2}} \quad (11.3)$$

and can be approximated as $4C^2$ for $C \gg 1$. Using generic polarizing optics we achieve contrasts of $C = 10 - 20$, corresponding to polarization purities of 400-

1600. Higher grade optics can readily improve the extinction. For example we have observed $C \sim 50$ with Glan-Taylor polarizers corresponding to 10^4 polarization purity. Full, general characterization of Stokes parameter can be found from [114].

11.5.2 Magnetic field optimization

The magnetic field must be closely matched to the probe light polarization. We adapt a procedure from reference [115], which uses the atoms to optimize the magnetic field vector, which defines the quantization axis \hat{z} , to coincide with \vec{k}_{RO} defined by the propagation vector of the probe light. The atoms are first optically pumped to $|F = 2, m_F = 2\rangle$ by a weak, circularly polarized, unidirectional beam with $B_z \sim 5$ G. One of the σ_+ -polarized probe lasers is tuned to $|F = 2\rangle \leftrightarrow |F' = 2\rangle$ and optically pumps the atoms into the $|2, 2\rangle$ dark state. When the alignment is optimal, the $|2, 2\rangle$ state is nearly dark and can only couple off-resonantly to $|3', 3'\rangle$, so depumping to $|1\rangle$ is minimized. If there is any mismatch, the dark state mixes with the bright states and scatters photons, eventually depumping into $|1\rangle$, which can be measured by the destructive blow away measurement. The growth in time of $|D\rangle = |1\rangle$ as a function of the depumping light $|2\rangle \rightarrow |2'\rangle$ quantifies the quality of the alignment, see Figure 11.5. The depumping time constants can be compared by preparing $|2, -2\rangle$ using the other MOT σ_- beam, and repeating the sequence. The ratio between the time constants can be used as a figure of merit for the alignment. We measure a ratio ~ 330 as seen from Figure 11.5

The figure of merit is the number of photons that the bright state can scatter before it falls into the dark state, as shown in Figure 11.7. We can quantify the

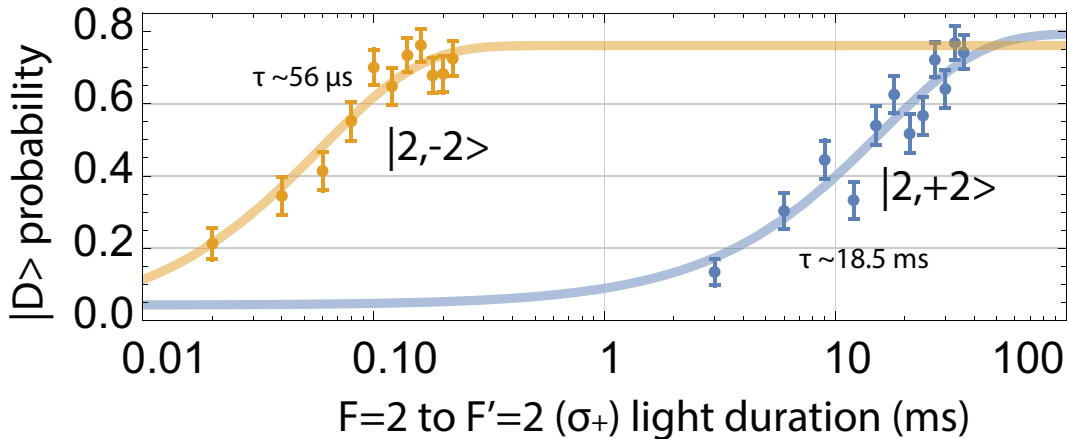


Figure 11.5: Growth of the probability of being depumped to the dark state ($F = 1$) for two different stretched Zeeman states $|2, +2\rangle$ (blue) and $|2, -2\rangle$ (yellow). The incident probe is unidirectional σ_+ , tuned to the center of the transition $|2, 0\rangle \rightarrow |2', 0'\rangle$ under bias field ~ 5 G.

chance of depumping by summing the rates over Raman depumping channels and comparing to the scattering rate on the cycling transition[110]. We estimate that we are able to scatter $N_{\gamma,\sigma} = 3.7 \times 10^5$ photons corresponding to an enhancement factor of ~ 20 over the unpolarized case with parameters $s_0 = 1$, $\delta = -\gamma/2$, and measured polarization purity $I_{\sigma_+}/I_{\sigma_-} = 1600$. It is also necessary to consider depumping due to the time-dependent vector and tensor light-shifts imposed by the ODT.

11.5.3 Fictitious magnetic field from vector light shift

Consider the AC stark shift ΔE_ψ of an atom in state $|\psi\rangle$ a illuminated by a single frequency optical field ω written as

$$\Delta E_\psi = -\frac{1}{4}\alpha_\psi(\omega)\mathcal{E}^2 \quad (11.4)$$

where α_ψ is the dynamic polarizability. See (Equation 2.20) for derivation. α_ψ can be decomposed into scalar($\alpha_\psi^{(0)}$), vector($\alpha_\psi^{(1)}$) and tensor($\alpha_\psi^{(2)}$) contributions as

$$\begin{aligned}\alpha_{nJF}(\omega) &= \alpha_{nJF}^{(0)}(\omega) + \mathcal{A}(\hat{k} \cdot \hat{z})m_F\alpha_{nJF}^{(1)}(\omega) \\ &\quad + \left[\frac{3(\hat{p} \cdot \hat{z})^2 - 1}{2} \right] \frac{3m_F^2 - F(F+1)}{F(2F-1)}\alpha_{nJF}^{(2)}(\omega).\end{aligned}\quad (11.5)$$

Here \mathcal{A} represents the circularity of light ranging continuously from 1(Right handed) to -1 (Left handed), and 0 for linear polarization. Unit vectors \hat{k} , \hat{p} and \hat{z} denote the orientations of wave vector, electric field and quantization axis defined by the bias magnetic field.

The effect of a vector light shift is equivalent to having a static magnetic field B_{fict} . We obtain an equivalent field by equating the shift to Zeeman shifts

$$-\frac{1}{4}\mathcal{A}m_F\alpha_{nJF}^{(1)}\mathcal{E}^2\hat{k} = \mu_B g_{nJF} m_F \vec{B}_{\text{fict}} \quad (11.6)$$

the equivalent fictitious field is given by:

$$\vec{B}_{\text{fict}} = -\frac{\mathcal{A}\alpha^{(1)}}{4\mu_B g_{nJF}}\mathcal{E}^2\hat{k} \quad (11.7)$$

with Landé g-factor g_{nJF} .

It is convenient to express the shift in terms of the mean trap depth for ground states as $U_{\text{trap}} = -1/4\alpha_{5s_{1/2}}^{(0)}\mathcal{E}^2$

$$\vec{B}_{\text{fict}} = \frac{U_{\text{trap}}}{\mu_B g_{nJF}} \left[\frac{\mathcal{A}\alpha_{5s_{1/2}}^{(1)}}{\alpha_{5s_{1/2}}^{(0)}} \right] \hat{k} \quad (11.8)$$

The equation gives both magnitude and orientation of the fictitious magnetic field. With finite circularity of the ODT light the bright state experiences

$$\frac{d\vec{B}_{\text{fict}}}{dU_{\text{trap}}} = 29.77 \left[\frac{\mathcal{A}\alpha_{5s_{1/2}}^{(1)}}{\alpha_{5s_{1/2}}^{(0)}} \right] \hat{k} \quad \text{G/mK} \quad (11.9)$$

where we have expressed the trap depth in temperature units.

The impact of this extra field is an effective time-dependent magnetic field during the 6 ms interrogation stage. While atoms are being probed, the traps are off and they are continuously pumped and projected to the stretched state, $|2, 2\rangle$ along the quantization axis \hat{z} originally set by the external static magnetic field \vec{B}_{ext} . When the traps are turned back on, $\vec{B}_{\text{ODT}} = \vec{B}_{\text{ext}} + \vec{B}_{\text{fict}}$ sets the quantization axis, and if these two axes are not parallel, $|2, 2\rangle$ is no longer an eigenstate. The state $|2, 2\rangle$ will undergo Larmor precession about the new axis with the frequency $\omega_L = \mu_B g_F B_{\text{ODT}} / \hbar$. The projection onto other Zeeman states in a rotated frame can be calculated from the Wigner-D function for a spin-2 particle. If the atom is projected to a non-stretched state when the next probe cycle begins, it will go through another optical pumping cycle and experience a temporarily increased depumping rate to $|D\rangle$.

To estimate the contribution of this effect to depumping let us begin with the initial stretched state $|2, 2\rangle$ and have it precess under magnetic field \vec{B}_{ODT} , governed by the Hamiltonian $H = \mu_B g_F \vec{F} \cdot \vec{B}_{\text{ODT}}$ where \vec{F} is the angular momentum operator.

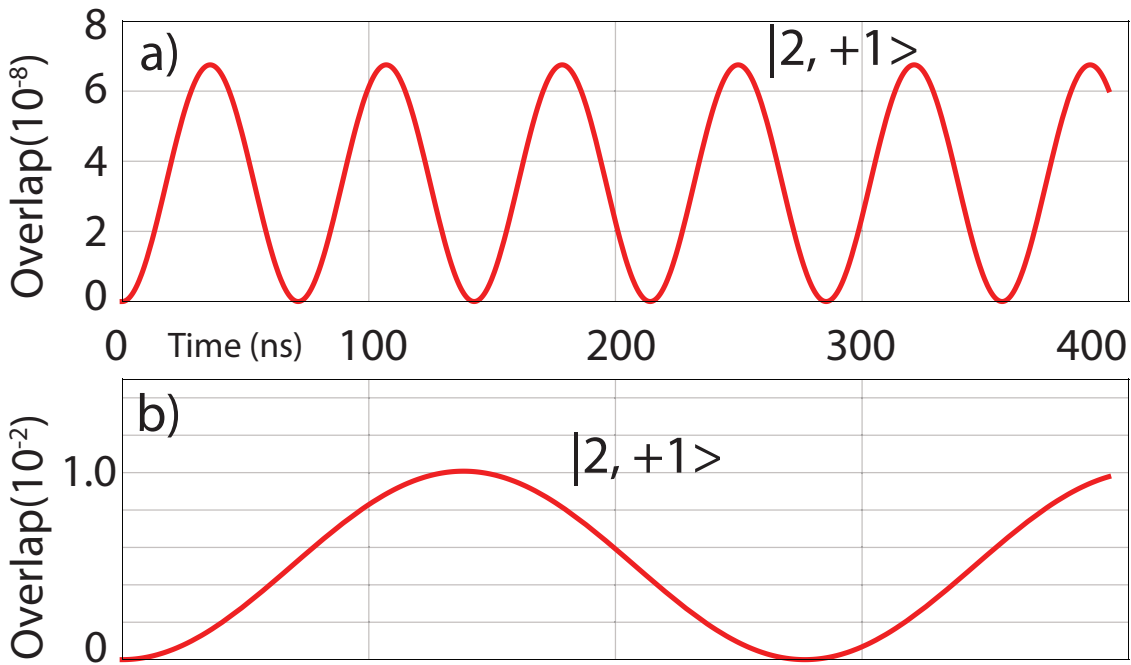


Figure 11.6: Larmor precession of $|2, +2\rangle$ showing finite overlap to $|2, +1\rangle$. a) For our experimental configuration: $\alpha = 60^\circ$, $B_{ext} = 20\text{G}$, $B_{fict} = 3\text{mG}$. b) Experiment configuration with more fictitious field. $B_{ext} = 5\text{G}$, $B_{fict} = 0.3\text{G}$. Both cases have negligible overlap to $m = -2, -1, 0$.

The angle θ_0 between \vec{B}_{ext} and the new field \vec{B}_{ODT} is

$$\theta_0 = \arctan \left(\frac{x \sin \alpha}{1 + x \cos \alpha} \right) \quad (11.10)$$

where α is the angle between \vec{B}_{ext} and \vec{B}_{fict} and $x \equiv B_{fict}/B_{ext}$ is the relative strength of the fields. For small axis mismatch, precession couples the closest m state, $|2, 2\rangle \leftrightarrow |2, 1\rangle$. Projection to the $m_F = 1$ state is time-dependent and dictated by the Larmor frequency. We consider maximal overlap to estimate maximal depumping

due to the fictitious field.

$$\left| \langle 2, 1 | e^{-\frac{iHt}{\hbar}} | 2, 2 \rangle \right|^2 \leq \left| D_{2,1}^2(2\theta_0) \right|^2 = 4 \cos^6 \theta_0 \sin^2 \theta_0 \quad (11.11)$$

Substituting θ_0 obtained from Eq. (11.10) shows the overlap is bounded by

$$\left| \langle 2, 1 | e^{-\frac{iHt}{\hbar}} | 2, 2 \rangle \right|^2 \leq \frac{4x^2 (1 + x \cos^6 \alpha) \sin^2 \alpha}{(1 + x^2 + 2x \cos \alpha)^4}. \quad (11.12)$$

For small vector shift ($x \ll 1$), the expression reduces to $\leq 4x^2 \sin^2(\alpha)$ showing a quadratic dependency. For our experiment, the vector light shift makes an angle $\alpha = 60^\circ$, and the relative strength of the fields x is 1.5×10^{-4} . These parameters give the maximal projection of precessed stretched state to the neighboring m -state to be 6.7×10^{-8} per cycle, which agrees with the numerical simulation shown in Figure 11.6a). What this means is that when the precessed state is illuminated by the light again, it has a probability of being projected to the $m_F = 1$ state of at most that number. Since we repeat the 800 ns long chopping cycle for 6 ms, ~ 7500 projections will occur. Multiplying with 7500 gives an expected number of m -changing scattering events 5.1×10^{-4} per readout, and each readout scatters $\sim 10^4$ photons. Therefore the vector light shift induced depumping is equivalent to having polarization contamination at the $\sim 10^{-8}$ level, orders of magnitude smaller than our measured contamination. This agrees with our observation that we failed to observe trap intensity dependent depumping, once the circularity in the ODT light was reduced from the parameters in Fig 11.6b).

Circular polarization of the ODT light results in a vector shift on the atoms

which adds a fictitious magnetic field, \vec{B}_{fict} , along \vec{k}_{ODT} , which can be expressed as

$$\vec{B}_{\text{fict}} = \frac{U_0}{\mu_B g_{|B\rangle}} \left[\frac{\mathcal{A} \alpha_{|B\rangle}^{(1)}}{\alpha_{|B\rangle}^{(0)}} \right] \hat{k}_{\text{ODT}}, \quad (11.13)$$

where U_0 is the trap depth, $g_{|B\rangle}$ is the Landé g-factor, and $\alpha_{|B\rangle}^{(0)}$, $\alpha_{|B\rangle}^{(1)}$ are scalar and vector polarizabilities. Circularity of polarization is characterized by \mathcal{A} , which ranges between $-1 \leq \mathcal{A} \leq 1$. The 60° angle between \vec{k}_{ODT} and \vec{k}_{RO} means that Larmor precession occurs, which reopens the depumping channels. In terms of the trap depth U_0 the fictitious field is

$$\vec{B}_{\text{fict}}/U_0 = 29.77 \left[\frac{\mathcal{A} \alpha_{|B\rangle}^{(1)}}{\alpha_{|B\rangle}^{(0)}} \right] \hat{k}_{\text{ODT}} \text{G/mK}. \quad (11.14)$$

For our experimental parameters, $\mathcal{A} \sim 2 \times 10^{-4}$, $\lambda = 1040 \text{ nm}$, $\vec{B}_{\text{fict}}/U_0 = 0.3 \text{ mG/mK}$. Therefore if one works with several mK deep traps and a weak bias field, a nonzero angle between \vec{k}_{RO} and \vec{k}_{ODT} must be accounted for. We verified that the depumping rate was independent of ODT power[110], suggesting that depumping is not due to the vector light shift for our parameters.

11.5.4 Excited manifold state mixing from Tensor light shift

Tensor light shifts couple M_F states in the excited level, creating a new set of energy eigenstates that are superpositions of unperturbed $|F, M_F\rangle$ states, which breaks the cycling character of the $|2, 2\rangle \leftrightarrow |3', 3'\rangle$ transition. Tensor polarizability 11.5 in

fine-structure basis can be converted to

$$\alpha_2^{(F)} = \alpha_2^{(J)} \frac{3K(K-1) - 4F(F+1)J(J+1)}{(2F+3)(2F+2)J(2J-1)}, \quad (11.15)$$

where $K = F(F+1) + J(J+1) - I(I+1)$. For $J < 1$ the tensor polarizability is zero. However for $J_e = 3/2$, $F_e = 3$ we get non-zero tensor shift. Given choice of linearly polarized ODT and \vec{k}_{RO} , the tensor shift exists for any non-zero intensity. As a natural solution to avoid tensor shifts during readout, the probe laser and ODT are switched out of phase so that the excited state is never populated when the ODT is on.

11.6 Resonant and off-resonant scattering rates

The Rabi frequency between a ground state $|n, l, J, F, m_F\rangle$ and an excited state $|n', l', J', F', m'_F\rangle$ is given by the expression

$$\begin{aligned} |\Omega_{F,m_F}^{F',m_{F'}}|^2 &= \left(\frac{e\mathcal{E}_q}{\hbar}\right)^2 (2F+1) \\ &\times \left| C_{Fm_F 1q}^{F'm'_{F'}} \left\{ \begin{array}{ccc} J & I & F \\ F' & 1 & J' \end{array} \right\} \langle n'l'J' \| r \| nlJ \right|^2 \end{aligned} \quad (11.16)$$

where $q = m_{F'} - m_F$, $C_{Fm_F 1q}^{F'm'_{F'}}$ is a Clebsch-Gordon coefficient, and $\{\}$ is a Wigner 6j symbol. Spherical component q of the optical field is $E_q = \frac{\mathcal{E}_q}{2} e^{-i\omega t} + c.c.$. Only coupling to $5p_{3/2}$ is considered due to the large fine structure splitting between $5p_{1/2}$ and $5p_{3/2}$. This allows the couplings to be expressed in terms of the common

reduced matrix element $\langle 5p_{3/2} \parallel r \parallel 5s_{1/2} \rangle$.

Using the normal scattering rate equation for a two-level system, the scattering rate for each specific transition and polarization can be written as:

$$r_{F,m_F}^{F',m_{F'}} = \frac{\gamma}{2} \frac{\frac{2|\Omega|^2}{\gamma^2}}{1 + \frac{4\delta^2}{\gamma^2} + \frac{2|\Omega|^2}{\gamma^2}} \Big|_{\Omega=\Omega_{F,m_F}^{F',m_{F'}}}. \quad (11.17)$$

Atoms excited to $|F'\rangle$ levels can spontaneously decay to $|F\rangle$ with branching ratio given by:

$$b_F^{F'} = (2J' + 1)(2F + 1) \left| \begin{Bmatrix} J & I & F \\ F' & 1 & J' \end{Bmatrix} \right|^2, \quad (11.18)$$

which satisfies the normalization condition $\sum_F b_F^{F'} = 1$.

After a single photon absorption-emission cycle of the bright state, the two possibilities are to decay back to $|B\rangle$ by a resonant process or to $|D\rangle$ by an off-resonant Raman process. In the following sections the relative strength between the cycling transition and the leakage into $|D\rangle$ is calculated for the cases of unpolarized and circularly-polarized probe light.

11.6.1 Unpolarized illumination

For the case of probing Zeeman degenerate atoms with unpolarized probe light, the rates for resonant and off-resonant processes are obtained by summing over the scattering rate weighted by the branching ratios with initial ground level $F_i = 2$ and final levels $F_f = 2$ or 1 .

$$r_{i \rightarrow f} = \sum_{F', m_{F'}} \sum_{m_{F_i}} r_{F_i, m_{F_i}}^{F', m_{F'}} b_{F_f}^{F'} \quad (11.19)$$

We will denote the resonant process $r_c = r_{2 \rightarrow 2}$ and the off-resonant process as $r_R = r_{2 \rightarrow 1}$. From the relative rate of both processes, we obtain a probability to depump for each scattered resonant photon $\beta = r_R/r_c$. Alternatively, we can express the rate in terms of the mean number of emitted photons before a depumping event as: $N_\gamma = 1/\beta$. For near-resonant light $\delta \ll \delta_{2' - 3'}$ we obtain the approximate expression for N_γ :

$$N_\gamma = \frac{38340}{1 + 4\delta^2/\gamma^2 + s_0}, \quad (11.20)$$

where δ is the probe detuning from the $2 - 3'$ transition, $s_0 = I/I_s$ and $I_s = 3.58 \text{ mW/cm}^2$.

11.6.2 Circularly-polarized illumination

For the case of Zeeman non-degenerate atoms and circularly polarized probe light, the probe optically pumps atoms into the stretched state $|2, 2\rangle$ where most of the scattering events take place. After the initial fast optical pumping, we can simplify the model to only consider transitions accessible from $|2, 2\rangle$. The dominant transition will be the cycling transition $|2, 2\rangle \rightarrow |3', 3'\rangle$ by design. The other transitions are only accessible due to polarization and alignment imperfections, which open off-resonant transitions to $|2', 2'\rangle$, $|2', 1'\rangle$ and $|1', 1'\rangle$. Since transitions to $|3', m'_F \neq 3'\rangle$, will scatter only to $|2\rangle$ and be pumped back to $|2, 2\rangle$, these states can be ignored in this analysis.

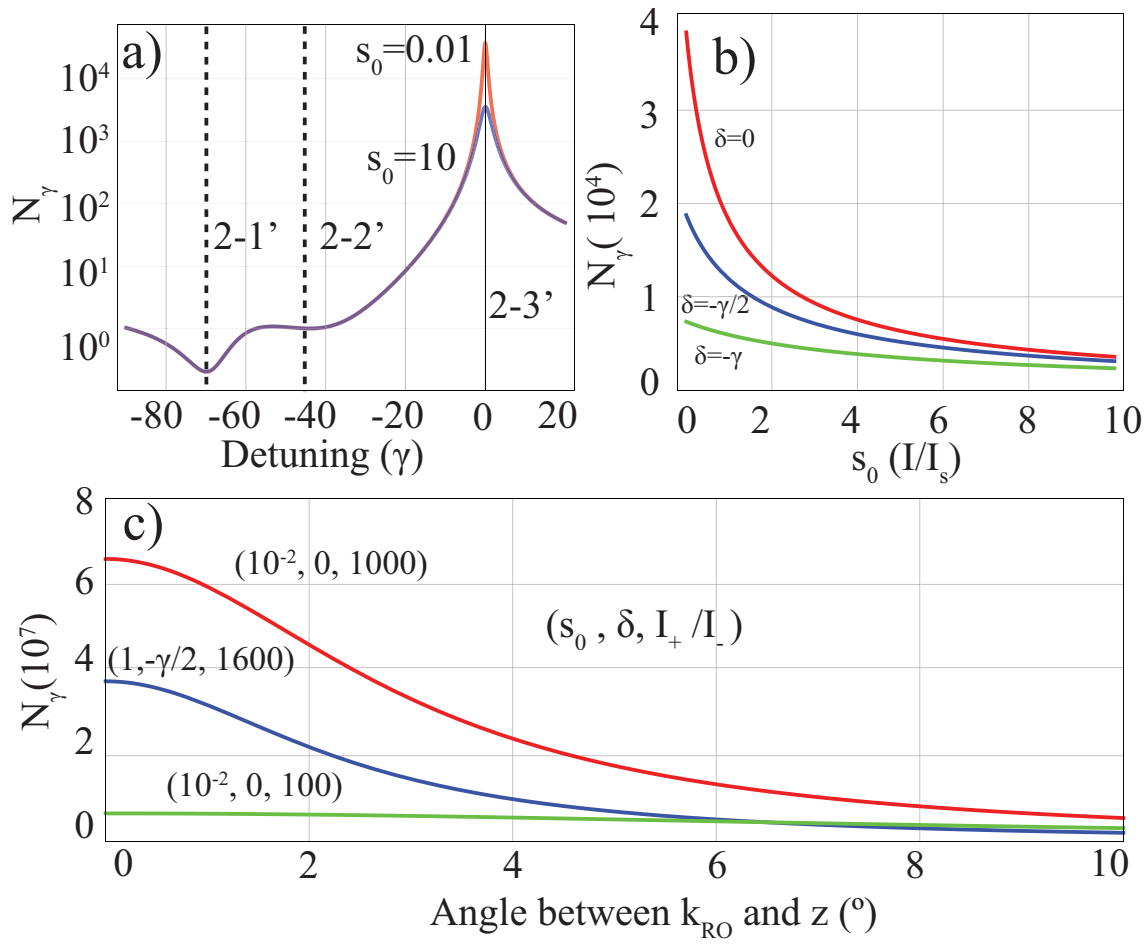


Figure 11.7: Dependence of mean number of resonant photons per Raman photon on probe light parameters. a) Detuning dependence spanning neighboring levels. b) Intensity dependence at three different detunings. c) Enhancement with σ polarized light for given saturation, detuning and intensity contrast I_+/I_- between σ_+ and σ_- .

To see the influence and sensitivity of polarization and alignment errors, we parametrize the polarization purity by the intensity fraction $(\epsilon_{-1}, \epsilon_1) = (1 - p, p)$ where ϵ_q denotes the fraction of spherical component q and $0 \leq p \leq 1$. The angular mismatch between the quantization-axis \hat{z} and \vec{k}_{RO} is represented by the angle θ . An angular mismatch θ projects the circular polarization to the z axis, allowing coupling to $\Delta m_F = 0$ transitions. For a given polarization purity and angular mismatch, one can calculate the projection using the Wigner-D function for a spin-1 particle. The perfectly matched case gives a projection $(w_{-1}, w_0, w_{+1}) = (1 - p, 0, p)$ where $\sum_{q=-1}^1 w_q = 1$. If θ is small, the resonant process rate r_c can be written as

$$\begin{aligned} r_c &= r_{2,2}^{3',3'}(w_{+1}) \\ &\equiv \frac{\gamma}{2} \frac{s_0 [p(D_{1,1}^1(\theta))^2 + (1-p)(D_{-1,1}^1(\theta))^2]}{1 + \frac{4\delta^2}{\gamma^2} + s_0 [p(D_{1,1}^1(\theta))^2 + (1-p)(D_{-1,1}^1(\theta))^2]} \end{aligned} \quad (11.21)$$

where $D_{m_1,m_2}^j(\theta)$ is the Wigner-D function and for the following derivation, they are explicitly written. Here $s_0 = I/I_{s,c}$, and $I_{s,c} = 1.66 \text{ mW/cm}^2$. Raman processes can occur via coupling to $|2', 2'\rangle$ by π -projection and to $|2', 1'\rangle$ and $|1', 1'\rangle$ by σ_- projection. Considering the branching ratios to the dark state, the Raman rate r_R is

$$r_R = \left[r_{2,2}^{2',2'}(w_0) + r_{2,2}^{2',1'}(w_{-1}) \right] b_1^{2'} + r_{2,2}^{1',1'}(w_{-1}) b_1^{1'} \quad (11.22)$$

Neglecting saturation effects on $2 \leftrightarrow 2'$ and $2 \leftrightarrow 1'$ transitions, we can simplify the

denominators and obtain

$$\begin{aligned}
r_R \simeq & \frac{\gamma}{2} \frac{1}{2} \left[\frac{s_0}{3} \left(p \sin^2 \frac{\theta}{2} + (1-p) \cos^2 \frac{\theta}{2} \right) \right. \\
& \left. + \frac{s_0}{6} \left((1-p) \cos^4 \frac{\theta}{2} + p \sin^4 \frac{\theta}{2} \right) \right] \\
& / \left(1 + \frac{4\delta_{2'-3'}^2}{\gamma^2} \right) \\
& + \frac{\gamma}{2} \frac{5}{6} \left[\frac{s_0 (1-p) \cos^4 \theta/2 + p \sin^4 \theta/2}{6} \right] \\
& \left[1 + \frac{4\delta_{1'-3'}^2}{\gamma^2} \right]
\end{aligned} \tag{11.23}$$

where $\delta_{2'-3'}$, $\delta_{1'-3'}$ are excited state hyperfine splittings. The denominators can be further simplified at large detuning, yielding

$$r_R = \frac{\gamma s_0}{2} f(\theta, p) \tag{11.24}$$

where

$$\begin{aligned}
f(\theta, p) = & \frac{\gamma^2}{48\delta_{2'-3'}^2} \left[2 \left(p \sin^2 \frac{\theta}{2} + (1-p) \cos^2 \frac{\theta}{2} \right) \right. \\
& \left. + \left((1-p) \cos^4 \frac{\theta}{2} + p \sin^4 \frac{\theta}{2} \right) \right] \\
& + \frac{5\gamma^2}{144\delta_{1'-3'}^2} [(1-p) \cos^4 \theta/2 + p \sin^4 \theta/2].
\end{aligned} \tag{11.25}$$

Again, taking the relative rate r_c/r_R gives the mean number of photons the bright

state can scatter before one depumping event. This can be approximated by:

$$N_{\gamma,\sigma}(\theta, p) \simeq \frac{p \cos^4 \frac{\theta}{2}}{p \sin^4 \frac{\theta}{2} + \sin^2 \frac{\theta}{2} + (1-p) \cos^4 \frac{\theta}{2}} \times \left(\frac{7}{4} \right) \left[\frac{38340}{1 + 4\delta^2/\gamma^2 + s_0} \right]. \quad (11.26)$$

valid when $\theta \ll 1, \delta \ll \delta_{2'-3'}, p \sim 1$. For the perfectly aligned case $\theta = 0$, depumping is suppressed by a factor of $\frac{4}{7} \frac{1-p}{p}$. Under non-zero magnetic field and optical potential one should include state dependent Zeeman and AC stark shifts in order to obtain more accurate results.

11.7 Site-Selective Readout for Error Correction

Error correction protocols require measurement of ancillary qubits interleaved with operations. In order to preserve the state of qubits that are not addressed during the readout, a modification of the shelving operation described in [108] could be implemented. Specifically, a global shelving operation that maps $|2, 0\rangle \rightarrow |1, 1\rangle$ could be performed with a π -pulse microwave or stimulated Raman laser with a large waist, as shown in Fig 11.8. An AC-Stark shift laser with pointing controlled by a acousto-optical deflector, could be used to shift a single target site out of resonance during the global microwave rotation, which will leave the state as a superposition of $|2, 0\rangle$ and $|1, 0\rangle$. Alternatively, a site-selective stimulated Raman laser with a small waist could be used to rotate multiple target sites from $|1, 1\rangle$ back to $|2, 0\rangle$. The hyperfine state can then be measured for a subset of qubits by the procedure described in the main text. The inverse shelving operation can then be performed to

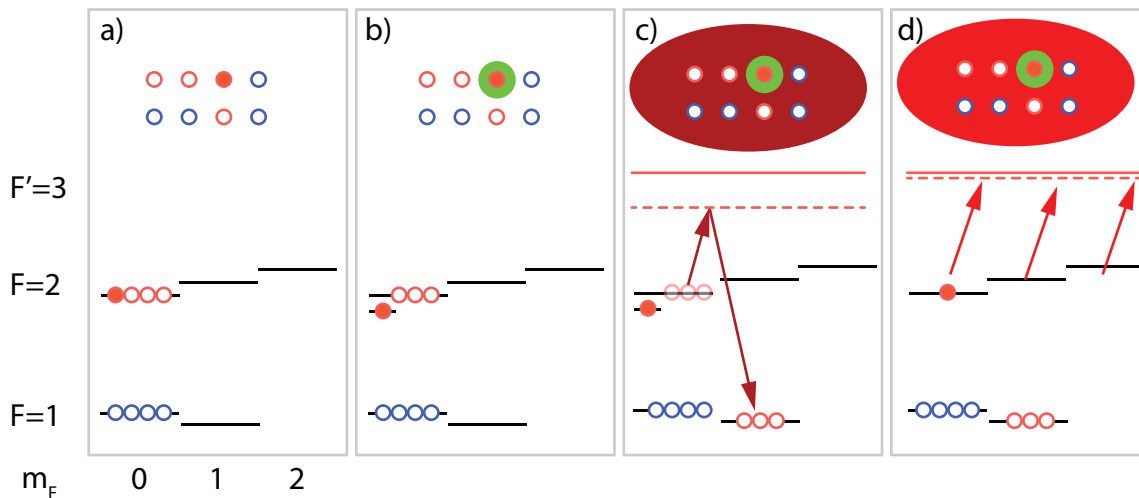


Figure 11.8: Proposed site-specific readout using shelving technique. a) Quantum register in arbitrary configuration. Solid circle is an ancillary atom to be measured. Unfilled circles are atoms that will not be measured. b) Localized beam(green circle) introduces qubit specific AC stark shift. c) Global Raman beam or microwave resonant to unshifted $|2, 0\rangle \leftrightarrow |1, 1\rangle$ transition can coherently shelve one of the clock states into $F = 1$ manifold. AC stark shifted atom will remain in its original state as it is off-resonant. d) Global σ^+ state-selective readout beam resonant to $|F = 2\rangle \rightarrow |F' = 3\rangle$ interrogates the unshelved atom.

map the shelved qubits back to $|2, 0\rangle$. In our configuration the readout and storage have different quantization axis, therefore proper spin rotations are required in advance.

12 AUTOMATIC ALIGNMENT SYSTEM

Reliable manipulation of atomic states require tightly focused addressing beams to be precisely positioned for atoms in each trap sites. In the old steel vacuum chamber apparatus, achieving and maintaining the positioning was very difficult and inefficient. Main technical challenge attributed to the large size of the optical setup and the poor HVAC of the lab, lack of thermal shielding, consequently requiring the routine readjustment of the beam alignment. Beam alignment experiment involves scanning beam positions with a lens or mirror, while watching the response from single atoms. These runs are expensive and furthermore, actuators were manually adjusted, providing finite precision.

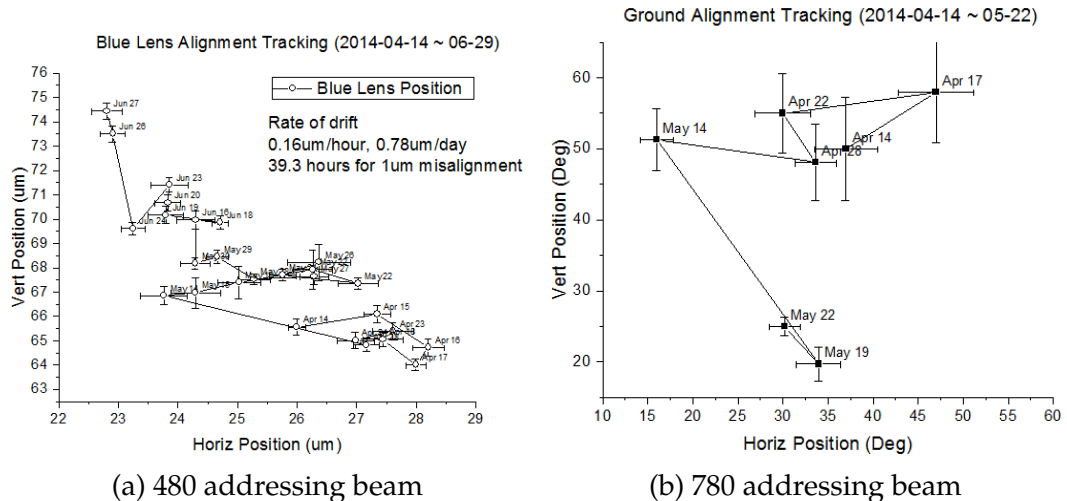


Figure 12.1: Long-term alignment drift of two Rydberg beams at atom plane. This is from old steel chamber setup, not the up-to-date apparatus. Data collected from 2014-04-14.

12.1 Configuration

Automatic alignment system is consisted of three sub-systems,

1. Motor control system
2. Image acquisition system
3. Reimaging optical system

Motor control system accurately sets the transverse position of the actuator attached on a lens mount. This moves the beam position at the atom plane in controlled fashion. Image acquisition system is takes pictures of beams, calculate the correction, and sends the desired correction to the motor control to move beam to the desired set point. Top level view of motor control and image acquisition system is shown in Figure 12.2. Reimaging optical system is a chain of optics to reimagine beams at the atom plane to an auxiliary CCD camera.

12.1.1 Motor control system

Slip-stick piezo screw actuators with home-built closed-loop operation are used to accurately set the transverse position of the alignment lenses. Commercial solutions for closed-loop slip-stick actuators exist and could be used, but the cost per channel increases significantly. Other actuator types, such as piezo stacks and motors could also be used, but are less preferable since neither technology could be turned off and still maintain alignment, and both can have significant vibrations.

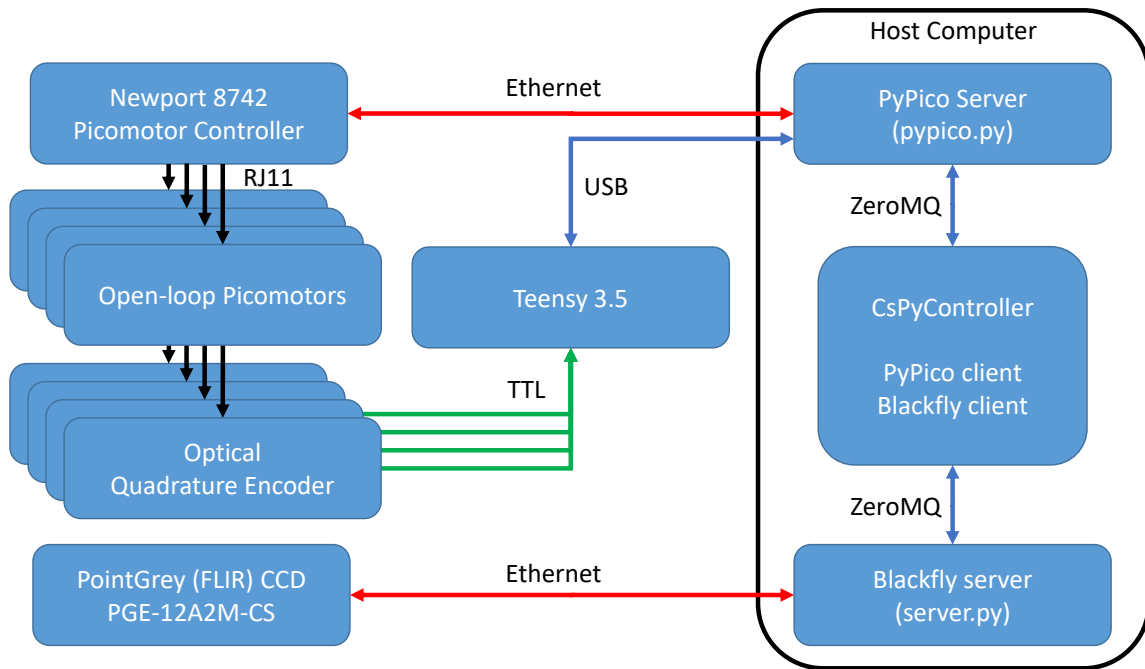


Figure 12.2: Top level view of the AAS system as of 2019-03-22. Decoder part has been updated since the initial setup[56]

Additionally, piezo stacks are limited in range compared to screw based systems. Manual alignment is, of course, also possible at the cost of accuracy and bandwidth.

To achieve closed-loop operation, an optical quadrature rotary encoder (Avago HEDR-55L2-BH07) with 2048 counts/rev is coupled to the end of the actuator screw via a custom “shaft-coupler”. Since each encoder count cycle has 4 state transitions, the screw shaft angle can be as accurate as 1 part in 8192 or 0.044 degrees. State transitions in the quadrature encoder outputs dictate the quantized relative angular motion of the screw. Therefore an additional decoder module must be used to keep track of the count signals produced by the encoder. We use a 32-bit 120MHz Micro Controller Unit(MCU, Teensy 3.5) to keep track of the position of the rotary encoder.

It retrieves and decodes the signals from multiple rotary encoders and records the current count for each channels. [GitHub repository](#) can be found for [Teensy 3.5](#), using its built-in counter.

Teensy is Arduino-compatible board equipped with powerful and faster CPU(32bit 120 MHz), compared to original Arduinos. Digital pins are 5-V tolerant and most of the pins can be used as counters. This allows us to implement better performing encoder-decoder system at much compact, consolidated platform. Previous platform was consisted with three different pieces, Quadrature Encoders([HEDR-55L2-BY07](#)), Decoders([HCTL-2032-SC](#)) and Arduino Mega(16bit 32 MHz) for serial communication and calculation. One can find [code](#) that needs to be loaded into the Teensy.

Communication between the MCU and a host computer is via a TCP/IP socket over USB. To close the feedback loop for the piezo-actuator, a python server has been written which handles communication between the client, the piezo-actuator control unit, and the decoder MCU. The server listens on a ZeroMQ Reply socket using TCP/IP for SCPI style commands. When a movement command is received from the client, a series of piezo movements are successively applied until the actuator has been successfully translated to the new setpoint or an error (such as overshooting the setpoint) has occurred. The control server is designed to approach the setpoint while only advancing the screw to eliminate the effects of backlash. The slip-stick rotation of the screw is a stochastic process and correcting for overshooting the setpoint will lead to backlash errors, therefore we use a proportional gain, P , in the feedback loop less than 1. Typically a gain of $P = 0.7 - 0.8$ will converge on the

setpoint with high reliability, but P should ideally be determined experimentally based on the variance of the screw movement. If the setpoint requires backward motion, a single backward movement to overshoot the setpoint is performed before the approach loop, so that only forward movement is necessary during the loop. The loop exits either when the setpoint is within 1 decoder count or if the setpoint has been exceeded and the current position is returned to the client. If the final position exceeds some acceptable error window around the setpoint, an error message is returned to the client when returning the position.

12.1.2 Image acquisition system

In order to compensate for transverse alignment drifts in the optical system, a camera([BFLY-PGE-12A2M-CS](#)) is used to re-image the lasers after they have passed through the vacuum chamber. Since the atoms are trapped at the focus of the ODTs, we will define drift as relative motion over time between a laser and the ODTs. The camera that samples the forward-propagating ODT and 780 nm lasers can correct 780 nm laser alignment drifts. This process is explained step-by-step in (Subsection [12.2.2](#)). Software part of the system is integrated into CsPyController for motor control and stand-alone python code for image processing, displayed in Figure [12.2](#).

12.1.3 Reimaging optical system

The requirement for individual site addressing and low crosstalk suggests that we address the atoms with a tightly focused beam propagating along the axial

Description	Part Number
Lens after 780 Pointing AOM, f=60 mm	LA1134-B
780 Telescoping lens 1, f=35 mm	LA1027-B
780 Telescoping lens 2, f=50 mm	AC254-050-B
Dichroic BS	
Lens after the dichroic, f=200 mm	AC254-200-B
Custom objective	NA = 0.4
Pyrex cell, thickness=7.3mm	JenOptik
Thad's custom triplet, f=110 mm	
Custom doublet, f=400 mm	
Dichroic BS	
Short-pass filter	
Long-pass filter	Edmunds 69-895
Flat mirror	
Achromatic Lens, f=100 mm	Thorlabs AC254-100-B-ML?
Achromatic Lens, f=500 mm	Thorlabs AC254-500-B-ML?
CCD camera	FLIR BFLY-PGE-12A2M-CS

Table 12.1: Reimaging setup for 1064 FORT and 780 addressing beams

direction of the ODTs, see Figure 12.3. As such, we use a co-propagating 780 nm laser path with beam waists of $w_x = 6.3$ and $w_y = 9.25 \mu\text{m}$. The asymmetry is caused by an astigmatism from the pointing AOM in the conjugate plane, which is used to adjust the spatial position of the laser along the x -axis on sub-microsecond timescales.

12.2 Alignment system characterization

This section illustrates characterizing each system after they are constructed. Detailed procedure and the result of misalignment detection using camera and atoms are discussed.

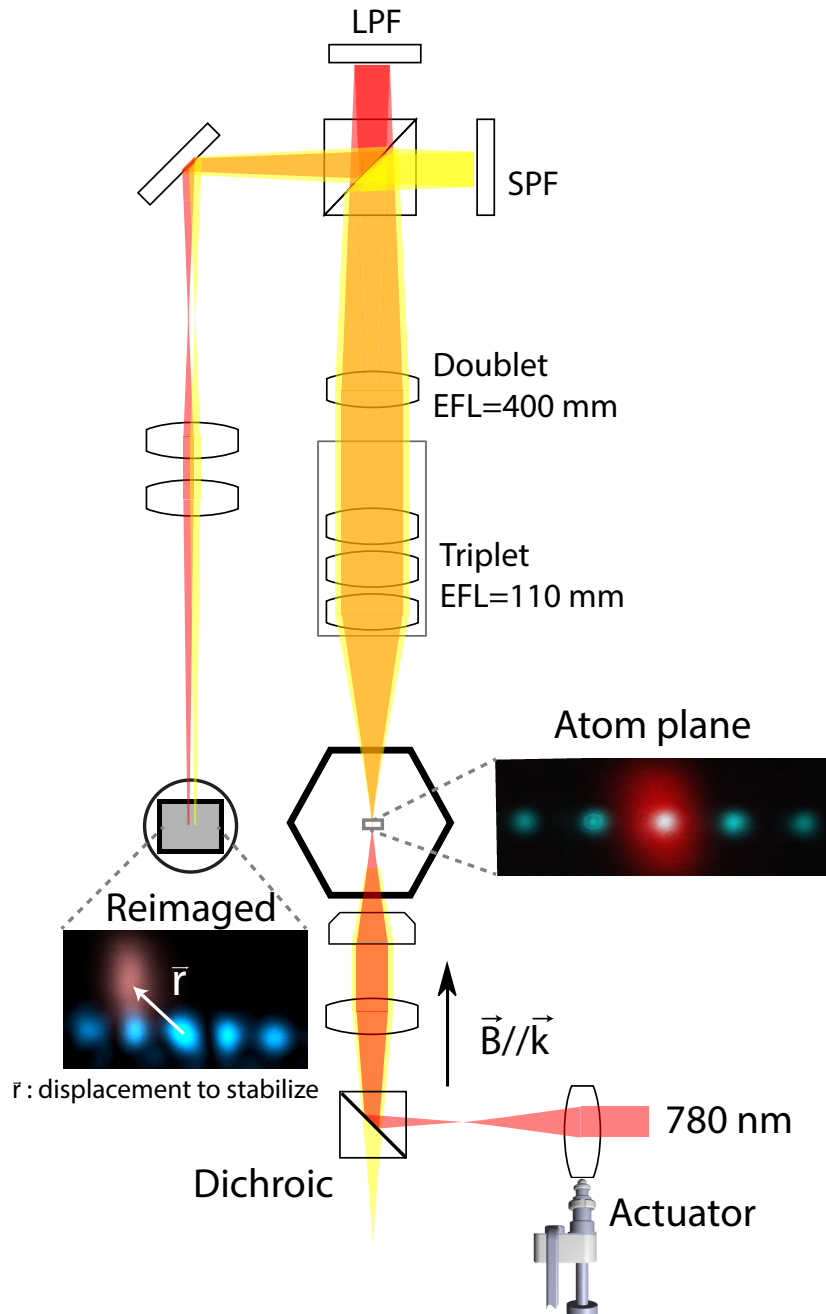


Figure 12.3: A schematic representation of the experimental apparatus. Atoms are trapped in the center of a hexagonal vacuum cell in 5 ODT trap sites spaced linearly. The array is formed by a single 1064 nm laser and a diffraction element. The 780 nm addressing laser is combined with the ODT laser using a Dichroic beam splitter (DBS) cube. One lens in each of the 780 and 480 nm path is placed in a computer controlled 2-axis transverse alignment stage, and is used to maintain the long-term relative alignment to the ODT laser. The EMCCD camera is used to image the atom trap population via fluorescence. The CCD camera is used to re-image both the ODT laser and 780 laser in separate 1 – 2 ms exposures.

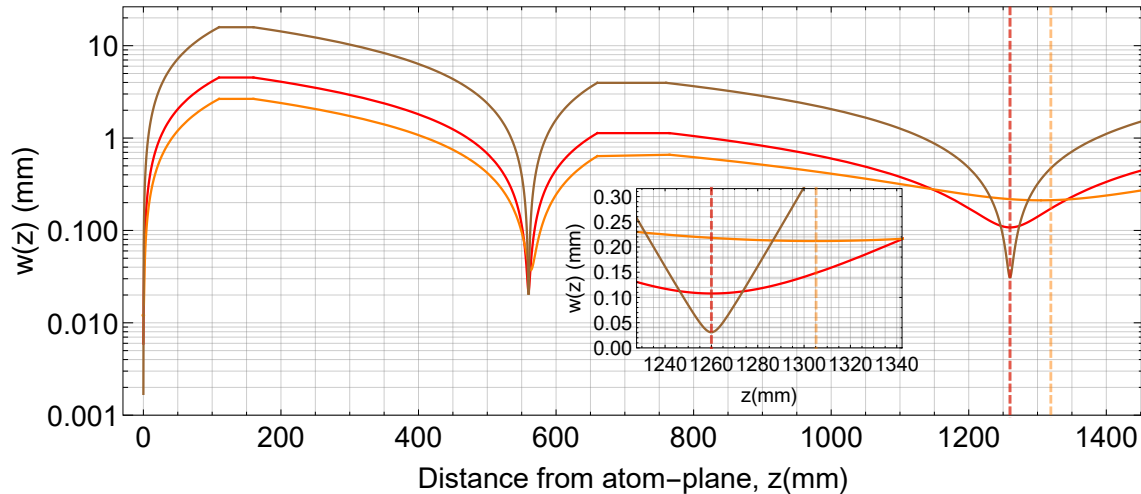


Figure 12.4: Confocal Setup. Propagation of 1064(Brown), 780X(Red), 780Y(Orange) gaussian beams from atom plane through the re-imaging system. Latest iteration. Calculation done with ABCD matrices. Wavelength-dependent path length is introduced to make the imaging system to be confocal for both wavelength. Camera located at $z = 1260$ mm, where the waists of 1064 and 780X are imaged. Due to astigmatic nature of 780Y, imaging plane is slightly off. Dashed lines indicate the image plane of the beam waists. Readers are advised to compare with Figure 12.18, non-confocal setup.

12.2.1 Closed-loop Picomotor operation

Piezo slip-stick based actuator provides programmable mechanical actuated motion to the optics. We use Newport's picomotor controller model 8742, open-loop version. Although Closed-loop version is available 8743-CL, they need to be paired with compatible closed-loop actuator 8310 which has hefty price tag and quite tall. Instead, we used open-loop version but implemented closed-loop operation by ourselves. Although home-made solutions look favorable as it requires low initial cost, one has to characterize and trouble-shoot everything to ensure reliable operation. As the first step, repeatability of our closed-loop system has been tested.

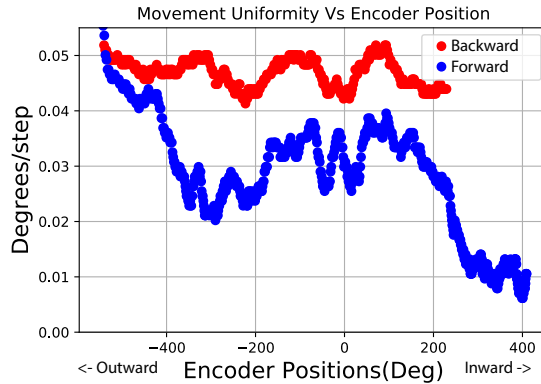


Figure 12.5: Open-loop picomotor repeatability

12.2.2 Misalignment detection with cameras, 780 photons

For each experiment cycle(~ 200 ms), it includes trigger pulses to make synchronized measurement of auxiliary camera image and the corresponding light sources(1064nm, 780nm and 480nm) one by one. Successful acquisition cycle will contain single camera shots corresponding to each beams. These temporarily stored, or buffered images are processed as soon as they are acquired. Firstly wavelength dependent magnifications($M_{1064} = 18.33$, $M_{780} = 18.05$) are used to convert camera pixel units to physical dimension at atom plane. Then images undergo sanity checks to ensure beams are properly exposed. Once they pass the tests, mild image processing is performed to make the beam to be more clearly identified. Conditioning processing basically removes background, or sets the brightness of lower 99% pixel to zero. X and Y centroids are calculated from this conditioned images. These centroids provide initial guess Gaussian fitting, which is more sophisticated yet computationally more expensive calculation. Since the conditioning may have distorted the beam, those Gaussian fits are applied to unprocessed image. we

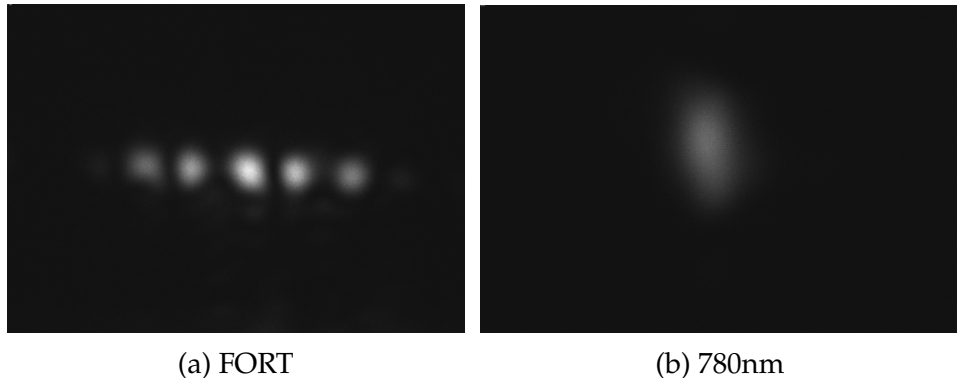


Figure 12.6: Reimaged beams onto the CCD camera

break down the 2D-Gaussian fit to two 1D-Gaussian fits applied to the integrated counts along columns or rows of pixels. Beam location from the Gaussian fits are final measurement, and passed to our data acquisition software. Detailed image processing and beam locator function is written in [BlackflyCamera.py](#). Exemplary Jupyter notebook can be found [here](#).

12.2.3 Misalignment detection with atoms, 780 photons

Near-resonant 780nm addressing beam induces ac stark shifts on atoms in $5s_{1/2}$ manifold. By experimentally mapping the shifts and extracting the spatial information, beam location can be calculated. The energy shifts of atoms in $5s_{1/2}F = 2, m_F = 0$ and $5s_{1/2}, F = 1, m_F$ can be written as

$$\Delta_{total} = \Delta_{1064} + \Delta_{780} + \Delta_{B^2} \quad (12.1)$$

where Δ_{1064} is ac stark shift from the π -pol 1064nm dipole trap, Δ_{780} is ac stark shift from the near-resonant 780nm addressing beam, and Δ_{B^2} is quadratic Zeeman

shifts. Since the measurable quantity is the phase accumulation between $|2, 0\rangle$ and $|1, 0\rangle$ states, the differential shift $\delta = \Delta_{total,|2,0\rangle} - \Delta_{total,|1,0\rangle}$ is only thing that matters. Then the breakdown of the differential shifts on the clock states is

$$\delta_{total} = \delta_{1064} + \delta_{780} + \kappa B^2 \quad (12.2)$$

where δ_{1064} and δ_{780} are differential ac stark shifts from dipole trap and addressing lasers respectively, $\kappa = 575.15\text{Hz}/\text{G}^2$ is coefficient[116] for 2nd order Zeeman effect, B is bias magnetic field.

Now, we look into ac stark shifts imposed by tightly focused, σ^+ -polarized, 780 nm light near-resonant to $5s_{1/2} \rightarrow 5p_{3/2}$ transition. In general $j = 1/2$ states have scalar and Vector shifts but Clock states are $m = 0$ thereby only scalar shifts are of our concern. Optical power of 780 light is chosen that Single photon Rabi frequency is around $2\pi \times 50 - 200$ MHz. Given $\Delta \sim -2\text{GHz}$, ac stark shift is from hundreds of kHz to a few MHz. This is orders of magnitude stronger than the other shifts we discussed earlier, and can be easily detected by Ramsey-style experiment, see Figure 12.7. Starting from upper clock state, π -polarized Microwave pulse with pulse area $\pi/2$ is applied to prepare superposition of upper and lower clock state. Then ac stark shifting beam(780) is turned on for duration t_{gap} to apply spatial-dependent shifts. Another $\pi/2$ Microwave is applied, followed by blow-away beam to perform state-selective readout.

Transverse spatial intensity distribution can be obtained by measuring the fringe frequency while 2D-scanning the beam position. Reconstructed distribution shown

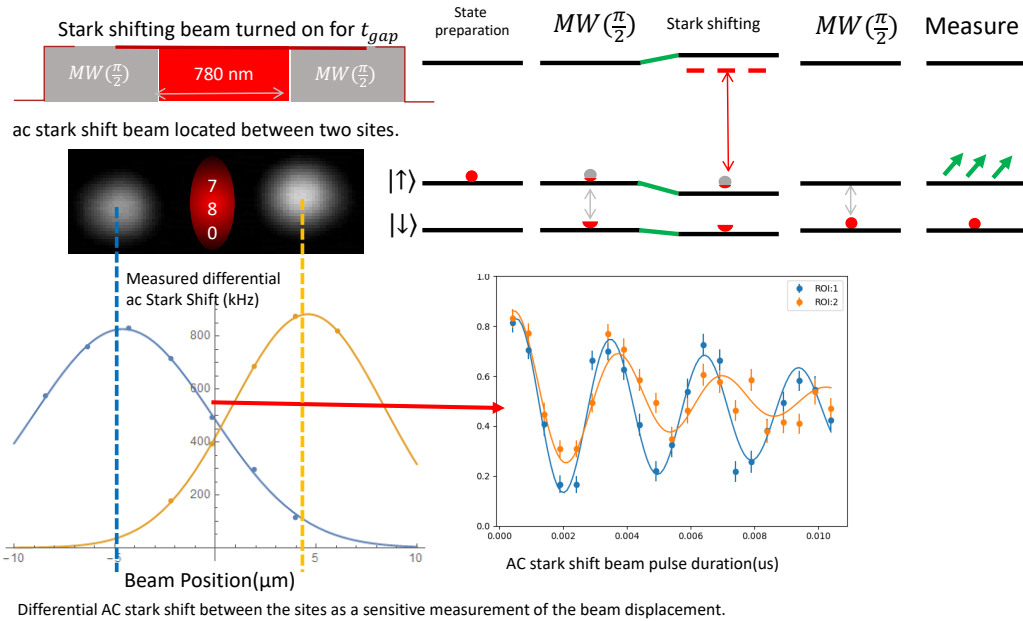


Figure 12.7: Detecting beam misalignment with atoms

12.3 is then used to map the measured frequency to spatial misalignment.

$$I(x, y) = I_0 \exp \left[-\frac{2x^2}{w_x^2} - \frac{2y^2}{w_y^2} \right] \quad (12.3)$$

$$\delta(x, y) = \delta_{780} \exp \left[-\frac{2x^2}{w_x^2} - \frac{2y^2}{w_y^2} \right]$$

From characterizations, transverse Gaussian beam sizes are $w_x = 6.3\mu\text{m}$, $w_y = 9\mu\text{m}$, $\delta_{780} = 825 \text{ kHz}$, site-to-site horizontal separation is $h_{1064} = 9.25\mu\text{m}$. Measured ac Stark shifts from multiple sites are collectively used to reduce the parameter space and earn exact position information. Then atom-based error signal is calculated

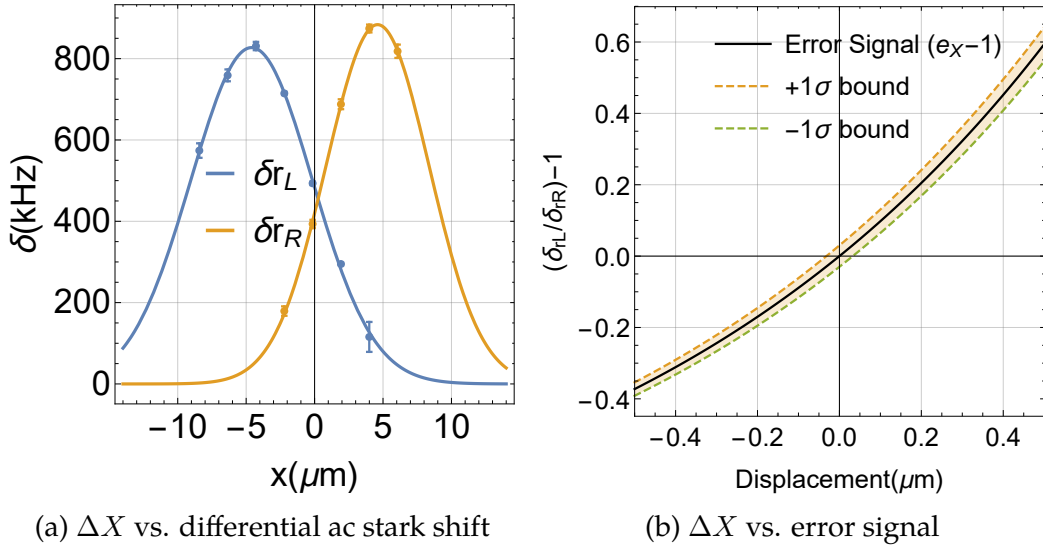


Figure 12.8: Horizontal position-dependent differential ac stark shift, and corresponding error signal

based on the extracted beam position from a reference point. The ac stark-shifting beam is deliberately positioned to be at the middle of two sites, namely r_L and r_R . This allows our measurement to be more sensitive to the drift along the axis connecting r_L and r_R , which is horizontal axis. Assuming origin to be at the center of them, coordinates for left and right sites are $(x_L, y_L) = (-h/2, 0)$ and $(x_R, y_R) = (+h/2, 0)$. Then for certain beam location (x, y) , differential ac stark shift experienced by atoms are

$$\begin{aligned}\delta_{r_L}(x, y) &= \delta(x - x_L, y - y_L) \\ \delta_{r_R}(x, y) &= \delta(x - x_R, y - y_R)\end{aligned}\tag{12.4}$$

Horizontal axis misalignment can be extracted from the ratio

$$e_x = \frac{\delta_{r_L}(x, y)}{\delta_{r_R}(x, y)} = \frac{\exp[-2(x - h/2)^2/(w_x)^2]}{\exp[-2(x + h/2)^2/(w_x)^2]} \quad (12.5)$$

where $h = 9.25\mu\text{m}$ is the FORT site-separation. Equation 12.5 has analytic solution $x = x_e = \frac{w_x^2 \ln e_x}{4h}$.

Next, y-position or vertical misalignment is $y=y_e$ that simultaneously satisfies the following equations to experimentally measured ac stark shifts on each sites.

$$\begin{aligned} \delta_{r_L,\text{measured}} &= \delta_{r_L}(x_e, y) \\ \delta_{r_R,\text{measured}} &= \delta_{r_L}(x_e, y) \end{aligned} \quad (12.6)$$

It is critical to verify the camera-based error signal is indeed correct representation. atom-based error signal for possible environmental parameters. Correctly reimaging gaussian beams of two different wavelength, this case 1064 and 780 nm, requires achromatic, confocal image relay. However, Due to our imperfect reimaging system, external perturbation such as thermal expansion may cause the reimaged beams to move around without actual misalignment in atom plane.

12.2.4 Misalignment detection with cameras, 480 photons

Current geometry does not allow the counter-propagating 480 beam to be imaged onto the same camera used for imaging ODT and 780 beams. Alternatively the EMCCD camera and the image relay used to image atoms can also image the 480 beam. The image relay is near-achromatic and confocal, and can benefit from already existing alignment reference, the single-atom fluorescence from traps. In a

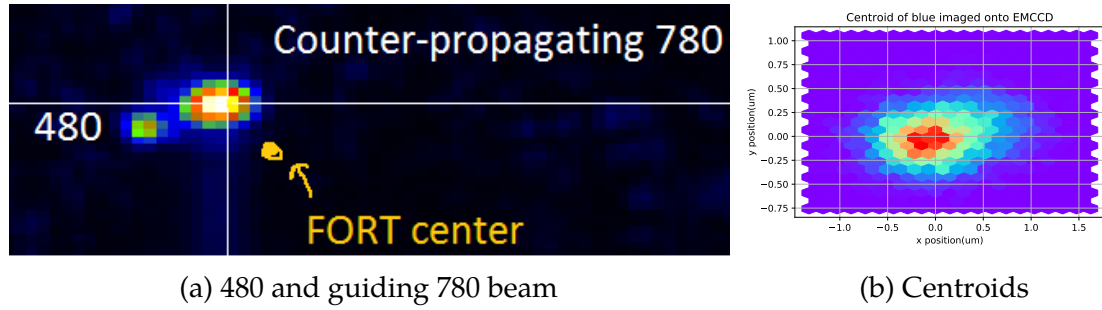


Figure 12.9: 480 beam on EMCCD camera and centroid analysis

typical condition EM Gain and $\sim 5 - 20$ mW of 480 optical power, $10 - 100\mu\text{s}$ of exposure and beam on time is sufficient to obtain properly exposed, high SNR image of the beam. Improper exposure may overfill the pixel wells and cause bleeding of image, ultimately compromising the ability to locate the beam. One drawback is low magnification of the image relay, limiting the resolution. Inevitable result is that the image of 480 beam to be highly pixelated, fits $> 99\%$ of counts within 3×3 pixel area, where one pixel corresponds to $\sim 4\mu\text{m}$ at atom plane. Achieving super-resolution is possible yet requires averaging over many measurement ($n = 50 - 300$) and sophisticated image analysis such as fitting to Gaussian or centroid calculations. Image analysis, feedback control(AAS2) and integration to CsPyController are completed.

12.2.5 Misalignment detection with atoms, 480 photons

Second photon for Rydberg excitation is far-detuned from the D1 and D2 line and closest electric-dipole allowed transitions are to $6p_{1/2}$ and $6p_{3/2}$, located ~ 420 nm. Small dynamic polarizability at 480nm makes the ac stark shift too small to

be measured at available beam intensity. Furthermore, differential ac stark shift between $F = 2$ and $F = 1$ state is even smaller as the ratio between the effective detuning $\sim 60\text{nm}$ to hyperfine splitting is much larger than the near-resonant 780 nm case. This inhibits us to perform experiments to independently characterize 480 pointing stability. Instead, we study the effect of misalignments on Ground-Rydberg dynamics and empirically extract the pointing stability from there. If the tightly focused 480 beam deviates from atom locations, atoms will see weaker light thereby two-photon Rabi frequency $\Omega_{2\gamma} \sim \sqrt{I_{780}I_{480}}$ will be slower. Also atoms are moving around due to their finite temperature sampling the spatial profile of the beam, which ultimately leads to extra dephasing of Ground-Rydberg Rabi oscillation.

12.3 Results

12.3.1 Relative pointing stability between 1064 and 780 beams

Performance of automatic alignment system is confirmed by continuously monitoring the ac stark shifts while the optical system is intentionally perturbed, mimicking environmental effects. In fact entire apparatus is enclosed by a temperature controlled box enabling precise, programmable control of the apparatus temperature. We run a temperature recipe that ramps the temperature up and down, and the response from atoms are analyzed for two conditions whether the alignment system is engaged(Closed-loop) or free-running(Open-loop).

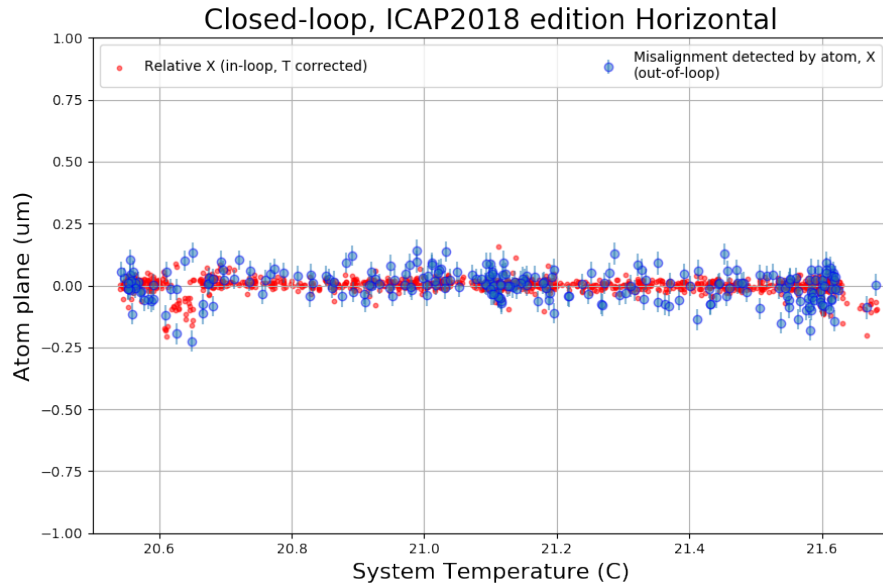


Figure 12.10: AAS closed-loop 1C horizontal variation, temperature corrected

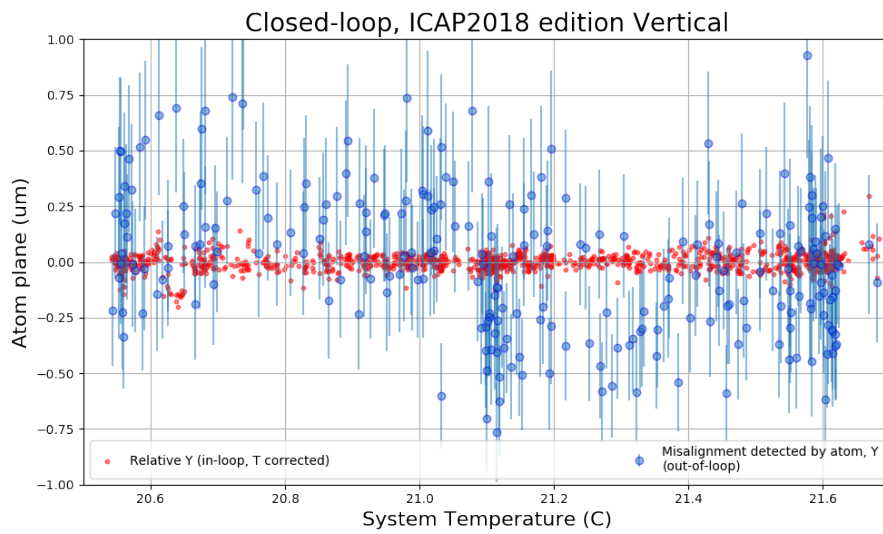


Figure 12.11: AAS closed-loop 1C vertical variation, temperature corrected

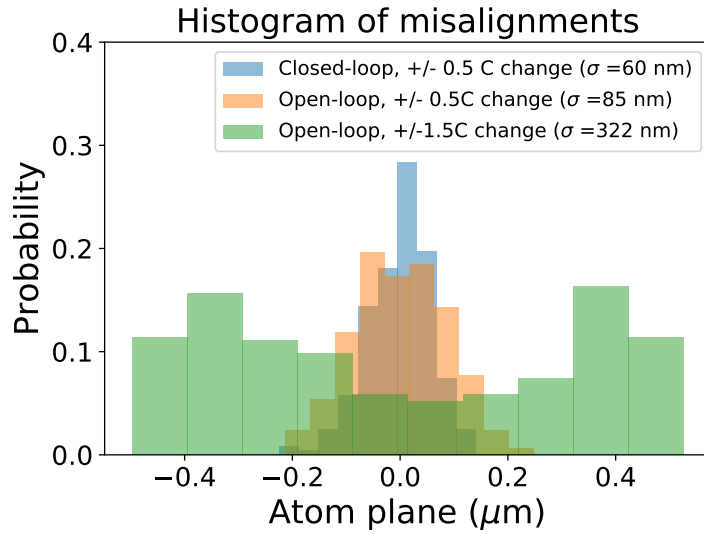


Figure 12.12: Histogram of misalignment for temperature ramping of the optical system. Plot generated 2018-07-16, data is from three different runs. 3C run

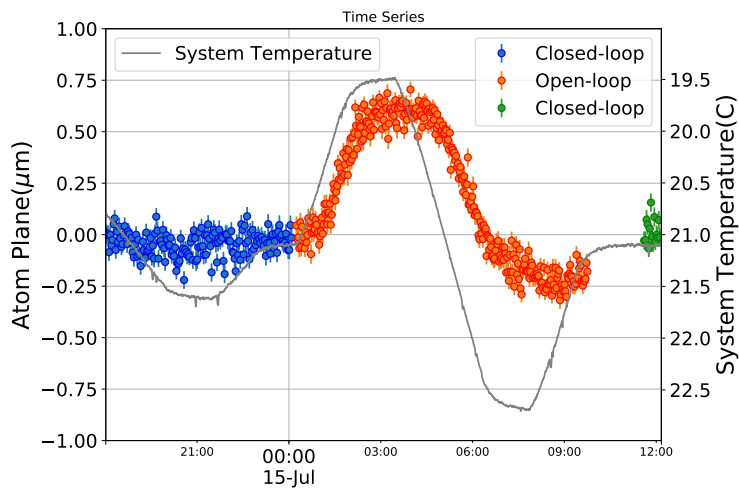


Figure 12.13: Timeseries of misalignment for temperature ramping of the optical system. At the beginning, closed-loop is engaged to keep the alignment. Then it was released, and re-engaged at the last to bring it back. It shows excellent repeatability. Plot generated on 2018-07-16, data is taken on 2018-07-15

12.3.2 Pointing stability of 480 beam

Detecting 480 Rydberg beam drift requires single-atom Ground-Rydberg Rabi oscillation with long coherence time. However as of 2019-03-20, rapid dephasing of Ground-Rydberg Rabi oscillation limits us to perform the experiment, therefore no data is available.

12.4 Limitations

12.4.1 Too much friction on X-Y translation stage

Precise, stable and repeatable positioning of the lenses are critical to achieve both passive and active pointing stability. The X-Y translation stage(Qioptiq [G065070000](#)) does not always touch the picomotor screw, either due to weak spring force or too much friction at the interface. To reduce the static and dynamic friction, small amount of Teflon lubricant(Blue Works Dry Lube) is applied at the interface between the 1" lens holder and spring-loaded pusher.

Although additional lubrication helped the mount from falling to ill-defined location, problems do occur at lower chance. To fully circumvent the issue being happening, software solution was implemented. Every time when picomotors are asked to move to new location, (θ_X, θ_Y) , actuators first move to $(\theta_X - 1^\circ, \theta_Y - 1^\circ)$, where (θ_X, θ_Y) are X & Y encoder reading in degrees, positive being inward(push) motion and negative being outward(pull) motion. Then they approach to the asked position by pushing forward for the remaining $\sim 1^\circ$ correction. Reason for both X and Y screws are asked to move is that they can give a nudge to escape from

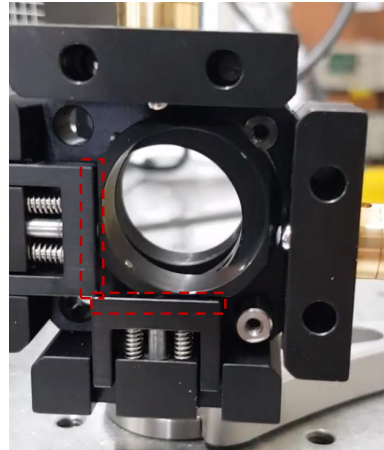


Figure 12.14: Qioptiq X-Y stage for beam positioning. Problematic interfaces are marked as red dashed rectangles.

the stuck when it happens. Completing the final correction by pushing the screw forward ensures the lens holder mates well with the other flat surface, and to minimize the backlash. With all these software aids the unreliable operations we had seen in the past are virtually solved, although X and Y motion do interrupt each other slightly.

12.4.2 Chromatic focal shift on confocal system

Ideal reimaging system will require optics to behave in same manner for wavelength we wish to capture, corrected for 480, 780 and 1064 nm. Unfortunately, the triplet objective lens(EFL=110mm) is only corrected for two wavelengths(480nm and 780nm), implying possible chromatic focal shift between 780 and 1064nm. This chromatic focal shift causes the image plane for those wavelengths to be dislocated, making simultaneous imaging difficult. Furthermore, wavelength-dependent magnification at the image planes requires additional calibration. We correct the dislocated image

plane by introducing wavelength-dependent path length, achieved by dichroic cube and long-pass(LPF) and short-pass filter(SPF). Although this enables the camera placed at the image planes of both wavelengths at the same time, uneven magnification still needs to be post-corrected for them.

12.4.3 Temperature Correction

Slight uncommon path between 1064 and 780 beams introduces external perturbations to impact their image by unequal amount. Since we take differential vector measurement, or using 1064 trap light as reference, this will lead to faulty camera error signal. Leading environmental effect that causes the problem is thermal expansion of the optomechanical system. Therefore we apply additional position correction, dependent on the system temperature. Optomechanical assembly temperature is monitored by multiple $10\text{k}\Omega$ thermistors and temperature logger(Measurement Computing [USB-TEMP](#)). Temperature correction term is empirically measured from the discrepancy between camera-based and atom-based error signal, while changing the box temperature in controlled manner. For temperature variation of $\pm 1.5^\circ\text{C}$, linear and quadratic corrections terms were necessary. For the first several runs correction terms appeared to be consistent over time, but beyond some point, they become not repeatable and higher-order correction seemed necessary. Data on this thesis is taken while the temperature correction was repeatable.

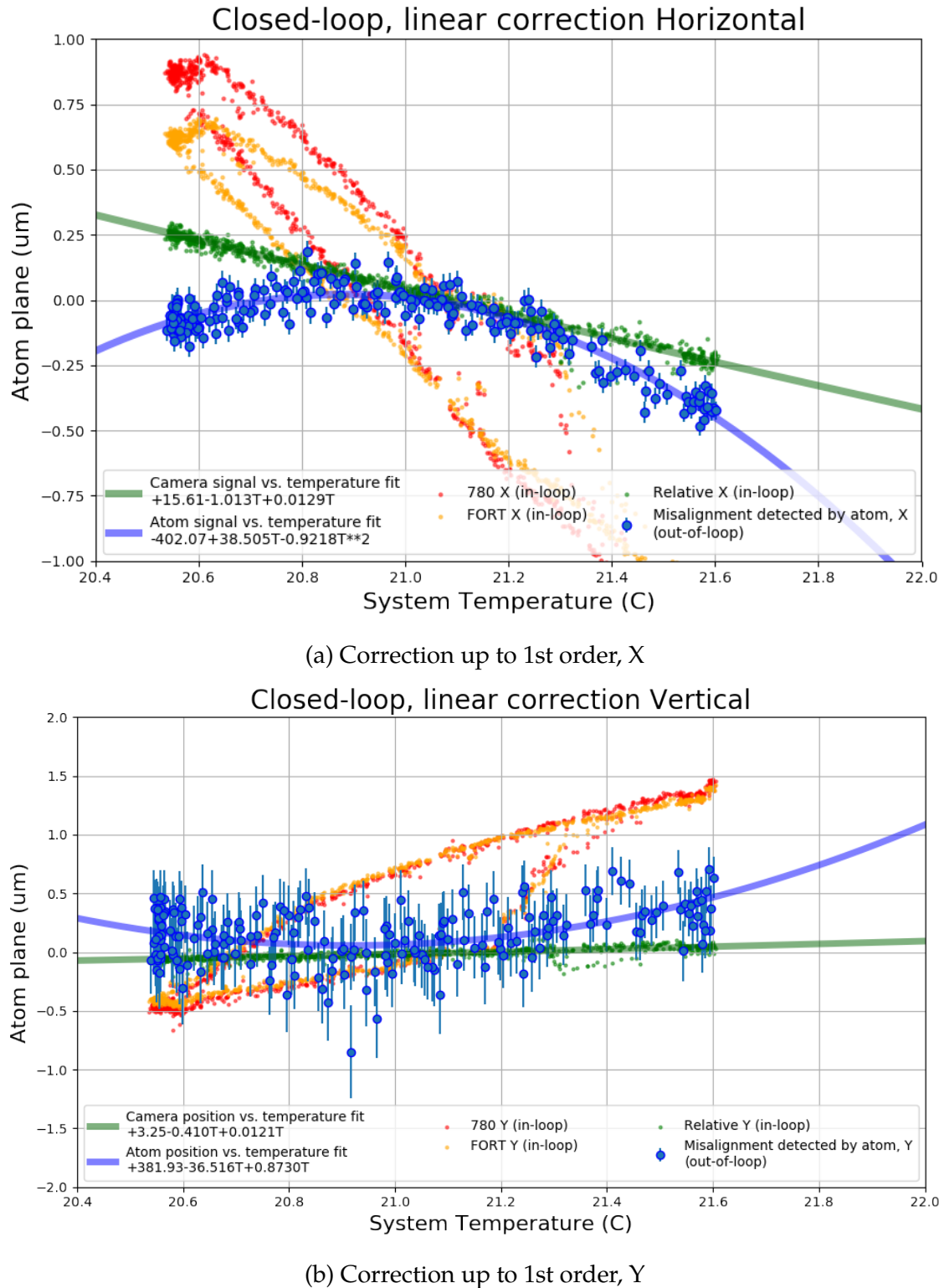


Figure 12.15: Closed-loop alignment versus temperature. Linear temperature correction. Data taken on 2018-07-14

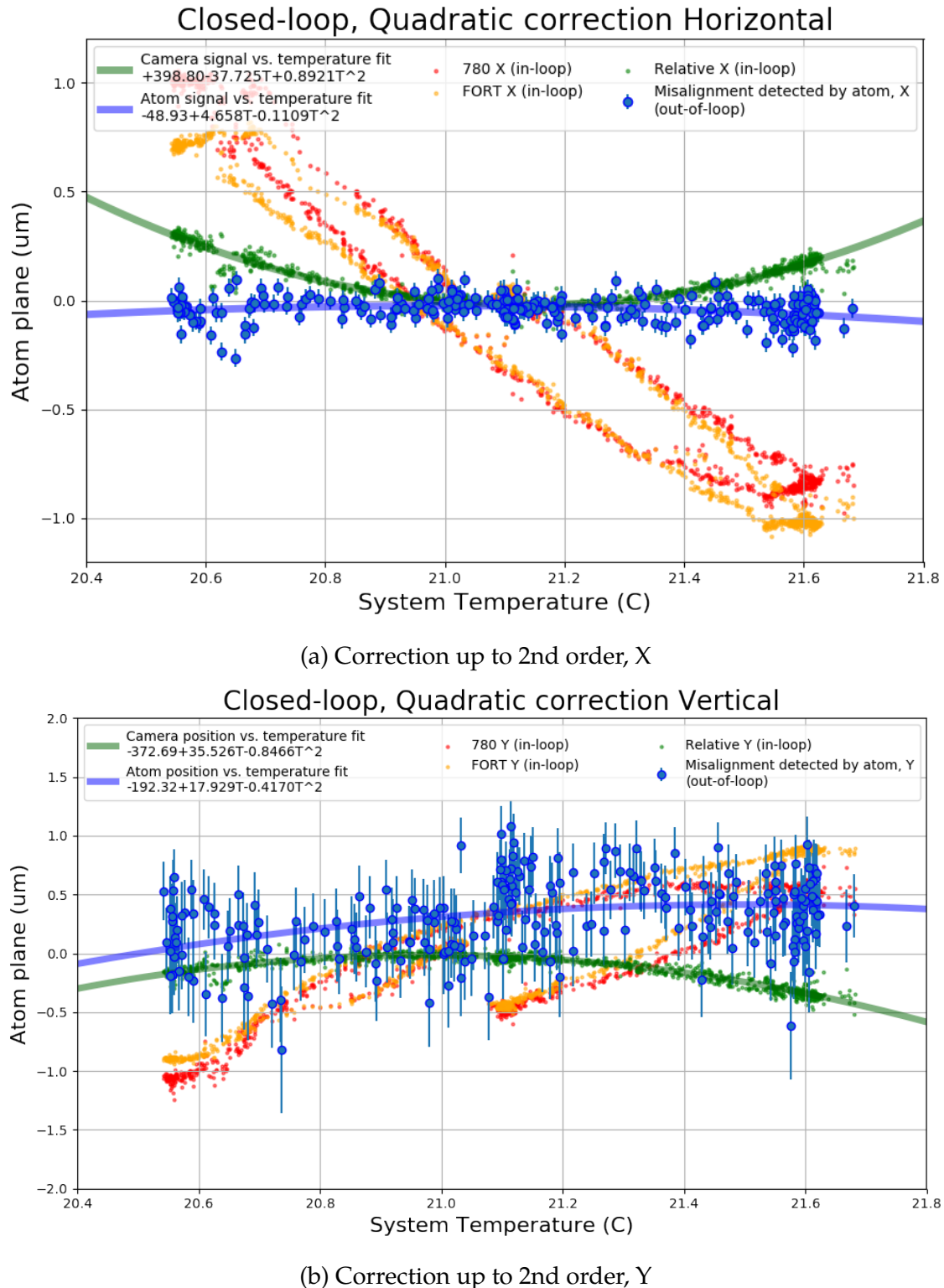


Figure 12.16: Closed-loop alignment versus temperature. Quadratic temperature correction. Data taken on 2018-07-14

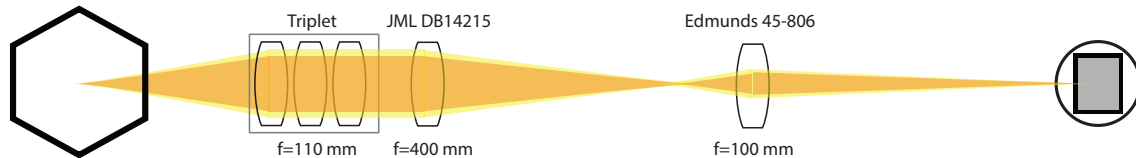


Figure 12.17: Previous-generation non-confocal reimaging system[56]. See Figure 6.1 for full optical setup.

12.4.4 Notes on non-confocal imaging system

Initially built reimaging system[56] was non-confocal configuration, and CCD camera was placed at a plane where 1064nm FORT and 780 horizontal waist are imaged. This unavoidably caused the other beam or axis to be defocused, and furthermore geometric image plane is not the same as the plane where the waist of gaussian beam is imaged[117]. ABCD matrix calculations (See Figure 12.18) with Gaussian beams show that achromatic, confocal, astigmatism correcting optical train is necessary to simultaneously image the 780 and 1064. Using the measured beam parameters of 780 ($w_{0,x} = 6.3\mu\text{m}$, $w_{0,y} = 10.2\mu\text{m}$, waist dislocated by $260\mu\text{m}$) and 1064($w_0 = 2\mu\text{m}$), locations of reimaged waist were displaced from geometric image plane by (780X, 780Y, 1064X&Y)=(-4.8 mm, +39.4 mm, -0.06 mm). This suggests that even aberration-free optics are used, nonconfocal configuration will alter the image planes between 780 and 1064 and astigmatism of 780 will limit only one of the axes to be correctly imaged.

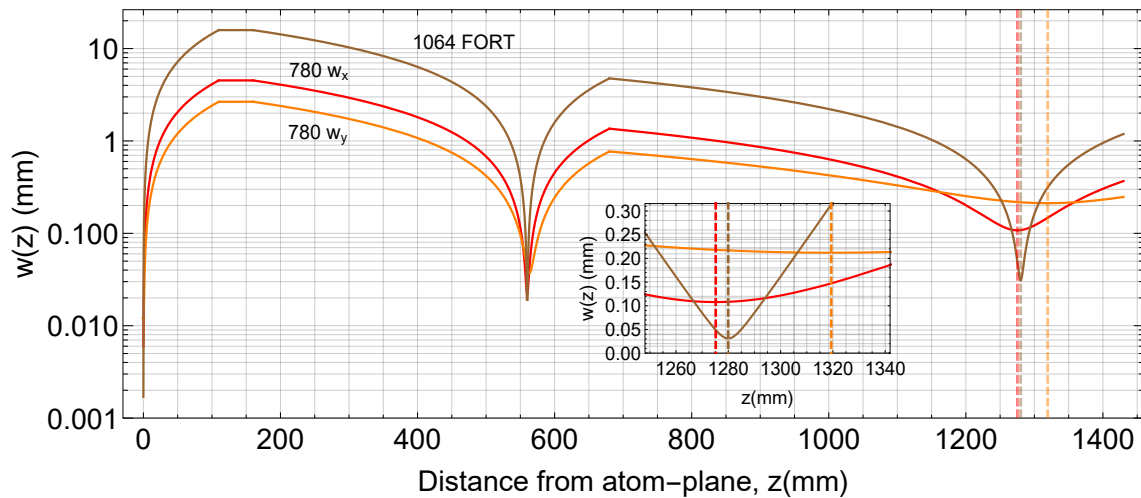


Figure 12.18: Non-confocal setup. Propagation of 1064(Brown), 780X(Red), 780Y(Orange) gaussian beams from atom plane through nonconfocal imaging system. Calculation done with ABCD matrices. Discrepancy in focal plane and waist-imaging plane in non-confocal imaging system when imaging coherent gaussian beam. Geometric image plane is at $z = 1280$ mm. Dashed lines indicate the image plane of the beam waists. May compare with the final, corrected setup Figure 12.4

Part V

Conclusion and Outlook

13 CONCLUSION

In this thesis, we present studies and demonstrations of critical building blocks of quantum computer and repeater based on atomic ensembles. We revisit each prong of Divincenzo's criteria alongside with our effort.

We have demonstrated semi-deterministic preparation W-state(ensemble qubit), thus getting a step closer to satisfying the second prong of divincenzo's criteria. State tomography and Ramsey experiment clearly identified that the majority of constituents in an ensemble are indeed W-state. Although the protocol is deterministic and enabled sub-poissonian Fock state preparation, observed 50-60% state preparation fidelity is lower than expected, taking account of known imperfections.

The missing fidelity is believed to be from molecular interactions between Ground-Rydberg and Rydberg-Rydberg atoms, modifying the dynamics. Lack of control between inter-atomic distance and atom number, combined with rich structure and broad mechanisms of molecular interactions, imposed significant challenge testing many hypothesis. As a symptomatic therapy, 1D blue-detuned optical lattice with a lattice constant $1.5\mu\text{m}$ is inserted. The spacing is comparable to the size of electronic wavefunction of Rydberg atoms, thus preventing atoms from overlapping each other. This offers better environment to pursue ensemble approach, because governing interactions can be restricted to dipole-dipole or van der Waals interactions, which can be more easily modeled. We have not experimentally testified the efficacy due to practical limitations.

The third prong is fulfilled by our first measurement of Ground W-state co-

herence time $T_2^* = 2.6$ ms for $\bar{N}=7.6$ atoms, not limited by fundamental physics. We believe the measured coherence time was limited by addressing laser coherence, hyperfine changing collisions, finite temperature and ac stark shift from optical trap. Most accessible improvement can be made on Hyperfine changing collisions by swapping the logical basis from $\{|0\rangle = |\uparrow; F = 2\rangle, |1\rangle = |\downarrow; F = 1\rangle\}$ to $\{|0\rangle = |\downarrow; F = 1\rangle, |1\rangle = |\uparrow; F = 2\rangle\}$, thus N-atom W-state contains only single excitation, rather than N-1 excitations. Observed coherence time is long enough to accommodate ~ 2600 Rydberg gate operations. At this point, spontaneous decay and dephasing of Rydberg state will become a challenge.

Our first demonstration of Rydberg blockade between two ensembles is significant progress toward universal gate operations between ensemble qubits, thus related to the fourth prong. We observe blockade fidelity of 0.89(uncorrected) and near-unity fidelity when post-selected on successful $N=1$ Fock state preparation of control ensemble. For weakly blockaded cases, Target ensemble become a perturber inhibiting the control ensemble to be de-excited from Rydberg W-state back to Ground states.

The fifth prong, qubit specific detection, can be related to our presented high fidelity, parallel, low loss, state-dependent fluorescence detection of hyperfine qubit. Itself is a significant step forward to single-atom qubit system for error correction, and boosting the data rate by recycling atoms. Expanding the technique for ensemble qubit is straightforward. The optical lattice will become handy suppressing two-body loss mechanisms (e.g. light assisted collisions and hyperfine changing collisions) to further extend the coherence time, and enable atom number resolving

fluorescence detection.

Demonstrations of the sixth and seventh prongs were not accessible given our ensemble qubit preparation fidelity requires further improvement. We studied directionality of cooperative single-photon emission from W-state. In the current super-wavelength lattice geometry and four-wave mixing scheme, $\sim 20\%$ of the emission will be in the main lobe. Better engineering of the lattice geometry, dipole-dipole interaction, phase-matching condition may lead the ensemble qubit to become attractive choice for quantum memory and repeater applications.

We report technical developments on apparatus, lasers, supporting hardware and software alongside with the advance in the quantum information science and atomic physics. Automatic beam alignment system is implemented to correct long-term drift of tightly focused addressing beams. Achieved 1σ pointing stability of 60 nm between dipole traps and 780 addressing beam. Two home-made, high-performing, cavity-enhanced frequency doubling system were constructed to meet experimental demand. We observe 960/480 system output as high as 180 mW with 600 mW fundamental, and 1540/770 system output as high as 13.97 W from 19 W fundamental.

A RYDBERG FILTERING CAVITY

We plan to construct medium-finesse Fabry-Perot cavity setup to optically filter unwanted frequency components from Rydberg lasers. As of 2019-04-19, the plan is to attach 1/2" concave mirrors to Invar spacer forming a ~ 100 mm-long non-confocal cavity. One mirror is mounted on a stacked ring piezo-transducer(PZT) for active stabilization. List of purchased optics is Table A.1. Scanning FP cavity with these optics probed by narrow-linewidth laser provides cavity finesse and cavity linewidth measurement as shown Fig. Cavity assembly will be hosted inside a vacuum can. Preliminary design is displayed in Figure A.2.

Description	Nominal spec	Part Number
780 mirrors	HR(780nm)>99.97%, R=100mm	LayerTec Ref no. X656235
960 high power mirrors	HR(910-970nm)>99.9%, R=150mm	LayerTec 100758

Table A.1: Purchased optics for filtering cavity setup

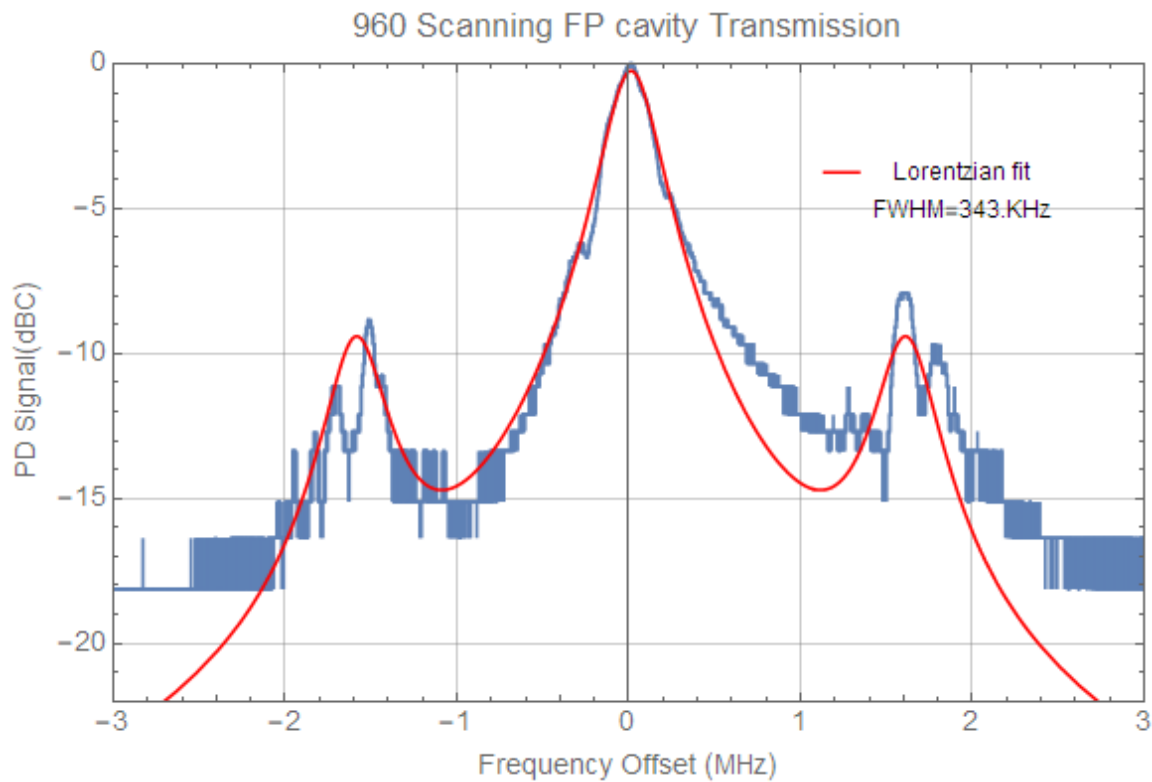


Figure A.1: Scanning FP transmission through 960 filtering cavity. Fitting to Lorentzian gives cavity linewidth of $\gamma/2\pi = 343$ kHz. Data acquired from Rigol Oscilloscope DS1054Z.

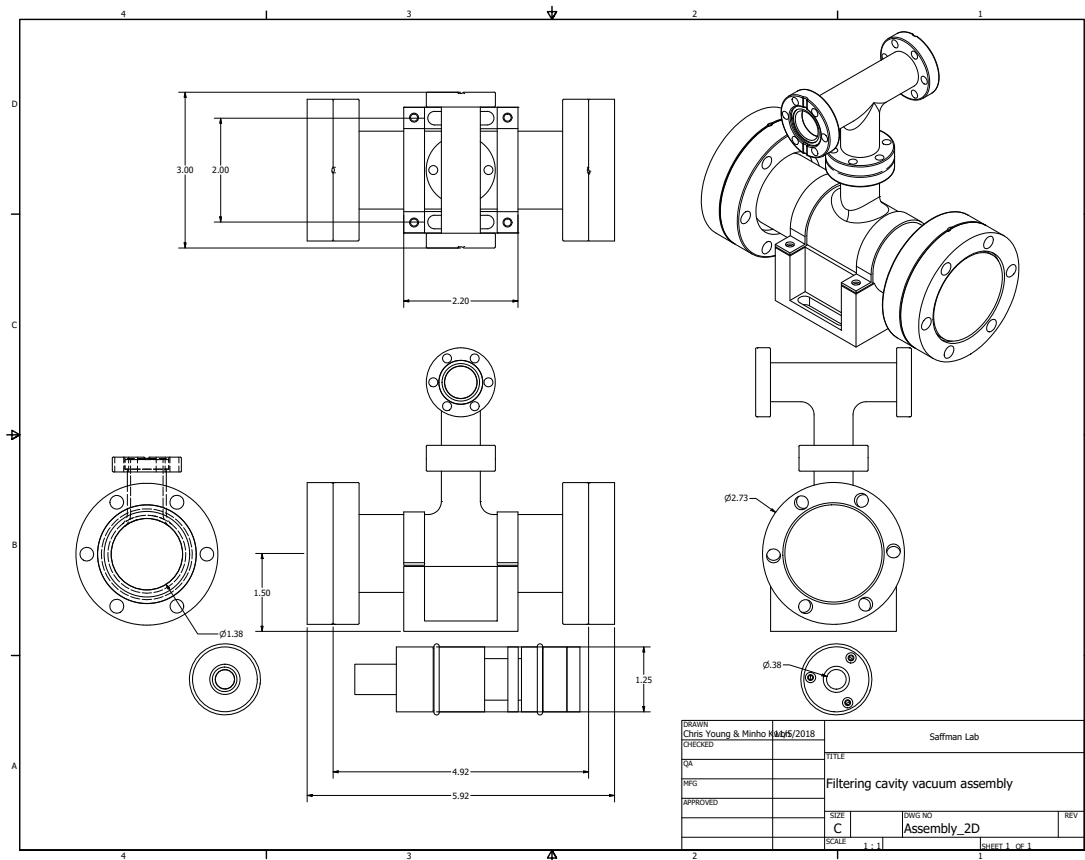


Figure A.2: Miniature vacuum assembly for hosting ~ 100 mm long filtering cavity. CF 2.75" form factor. Displayed units in inches.

B CAVITY LOCK MONITORS

Most of our lasers are Fabry-Perot laser diodes stabilized by an external feedback from a grating or an interference filter. Typical linewidths of these lasers are a few MHz, too broad for coherent Rydberg excitation. They are further stabilized by locking to a reference cavity. Depends on what axial and transverse mode being locked, the laser is stabilized to that frequency. It is critical to know what mode we are locked to, as it determines the optical frequency of the laser. Direct measurement of optical frequency is possible yet challenging, due to resolution limitation of wavelength meters (typically 100-500 MHz) or measurement overheads of frequency combs. As an additional piece of information to support those measurements for conclusive identification of modes, we monitor the spatial profile of cavity transmission. As an economical, compact, lab-friendly and programmable solution, we choose Raspberry Pi and a camera module for the cavity lock monitors. Raspberry Pi and Pi camera offer versatile and economical solutions for continuously monitoring many critical things in labs. Currently being used to watch spatial mode of cavity transmission.

B.1 Transmission monitor

Direct evidence of laser being referenced is to watch the laser transmitting through the reference cavity. We employ versatile CCD camera to monitor the spatial mode and amount that is transmitting.

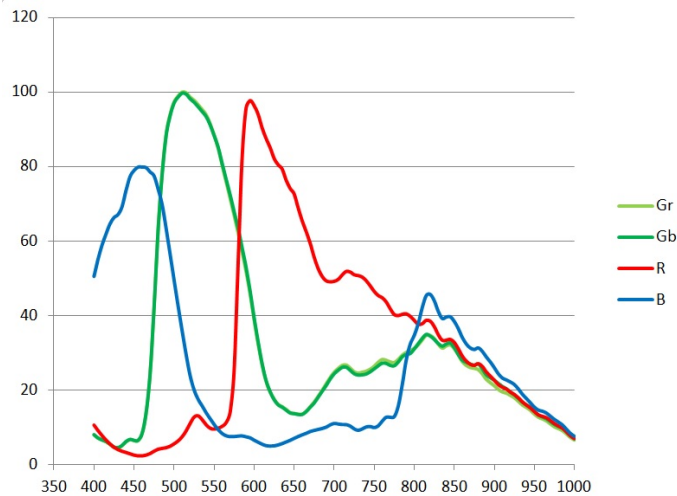


Figure B.1: Spectral sensitivity of Raspberry Pi NoIR Camera. Sony IMX219 sensor.

B.1.1 Raspberry Pi Camera

We use Raspberry Pi infrared Camera Module v2 (Pi NoIR) equipped with a Sony IMX219 8-megapixel sensor. Spectral coverage ranges 400-1000nm as shown B.1. Beyond this wavelength, detection might be possible but at reduced quantum efficiency. The camera works with all models of Raspberry Pi and well developed library [picamera](#) makes it easy to use.

B.1.2 Custom Mount

Custom Mount is 30mm cage-style, SM1 threaded, black-colored housing for Raspberry Pi cameras to be easily installed. The mount is a custom design created by Sebastian Malewicz, using SOLIDworks. The manufacturing was done through [eMachineShop](#). For future ordering of this part, a design in eMachineShop's CAD software already exists. Use this software to place an order, and please make

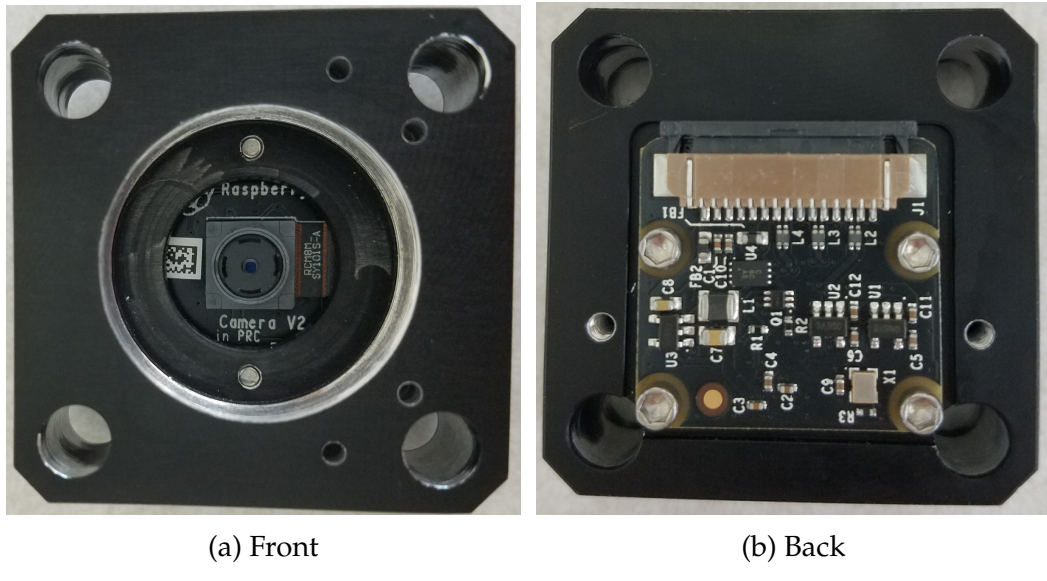


Figure B.2: Assembled Raspberry Pi camera and the custom mount. Built-in lens needs to be screwed out for spatial mode monitoring purpose.

sure that the smallest tolerances are selected and the part should be made out of aluminum. If the eMachineShop file is defective, please recreate based off of the corresponding SOLIDworks file. After receiving the completed parts, they must then be sent to be anodized for the optical black finish. Once anodization is complete, the mounts must be tapped on the front with a SM1 tap. Also the four 30mm cage holes in the corners must be reamed out such that the cage rod has a slip fit inside the hole. This ream is done with a 0.2365" diameter reamer. Reminder to please be careful while machining the mounts to prevent any unnecessary damage to anodized surfaces.

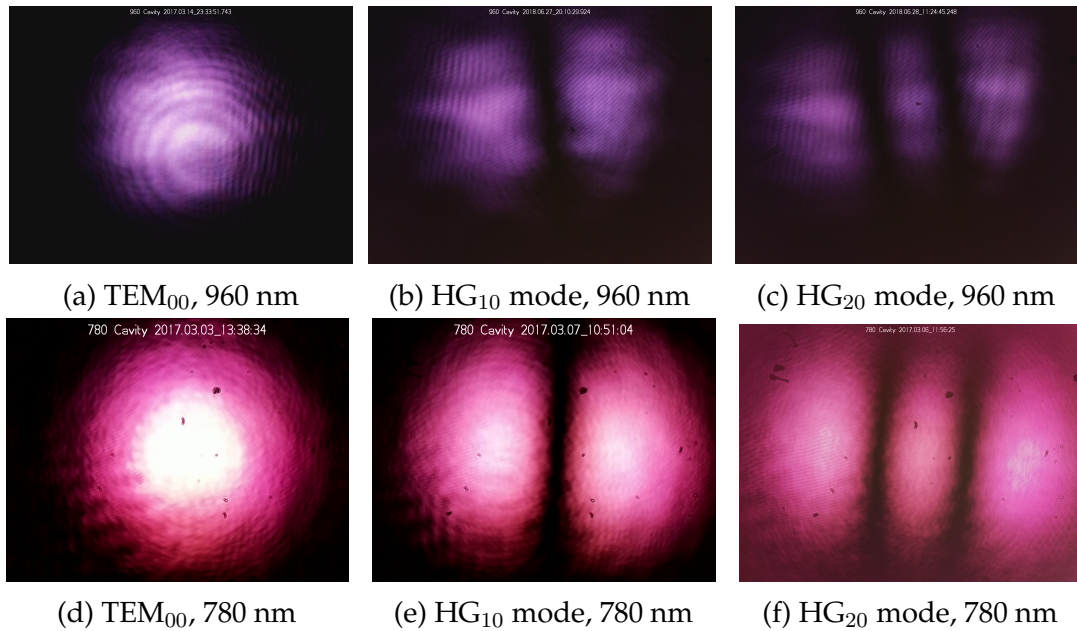


Figure B.3: Transmission through the reference cavity. Typically the input cavity coupling is optimize fundamental Gaussian mode.

B.1.3 Setting up

As a very first step, one should have Raspberry Pi and a camera ready for assembling.

Setting up Then one can set up an web interface [Web interface set up](#) Usually Raspberry Pi wouldn't have its own display and I/O. Handy remote desktop can be set up using [Enabling remote desktop access](#) and [troubleshooting](#).

B.2 Frequency monitor

Transmission monitor only tells us the laser is locked to a mode, not the mode we want to be. This extra uncertainty can be extinguished by employ a beamote monitor. Using the heterodyne setup, Figure D.1, we can obtain optical beat between 780 nm

Rydberg laser and cooling/repumper lasers that are locked to atomic spectroscopy. Programmable frequency counter **TTi TF930** watches the beat frequency and if it deviates from the acceptance window, it can raise warning for operators and stop the data acquisition process automatically.

C THE BOX

This Box isolates the main apparatus from environmental perturbations, such as room temperature change or background microwave noises. It has active temperature control of the air inside, and provides passive rf shielding. Deployed box is shown on Figure C.1.

C.1 Thermal control

Air temperature inside the box is actively stabilized thereby room temperature variation does not perturb the inner optomechanic assembly, ultimately improving the pointing stability of laser beams. Top level diagram can be found on Figure C.2. Fans are set to spin at constant RPM, and the radiator temperature varies to stabilize the thermistor reading. The thermistor is attached to central optomechanic assembly. Overcooled water is appropriately heated by Stiebel Eltron Mini 3-1, electrically controlled by PID controller (Omega CN32Pt 224-C24) and Voltage relay(SSR330AC25), and fed to the flowmeter(Omega FL46300) and to the radiator.

C.2 EMI shielding

Rydberg atoms have exaggerated sensitivity to electric field therefore minimizing the perturbation is critical achieving good state control. Two layers of shielding material are attached to the sides and top cover to protect the main apparatus against an ambient EMI. Outer layer is copper sheet reflecting external RF fields.

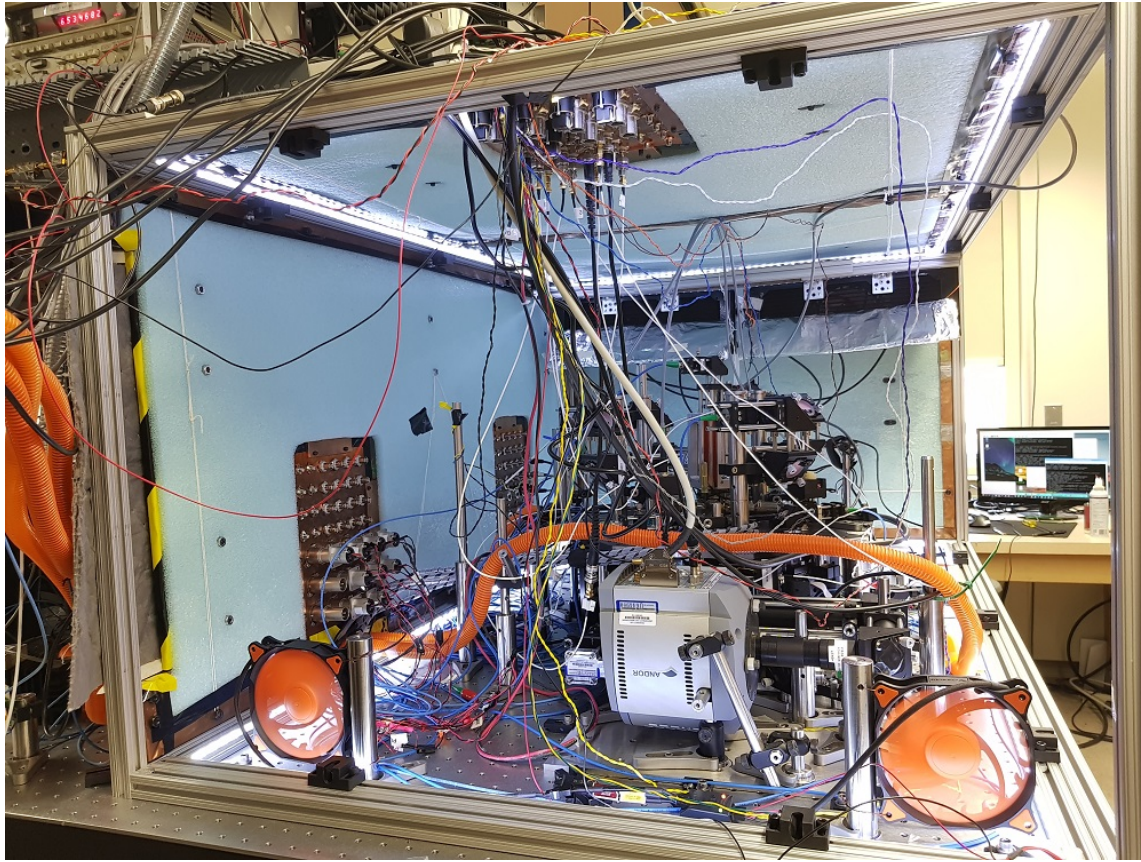


Figure C.1: Box enclosure and main apparatus seen from the side

Inner layer is an absorber foam [118](Laird Eccosorb QR-13AF) providing extra attenuation against the external RF fields and reducing unwanted reflection of 6.834 GHz microwave emanating inside the box.

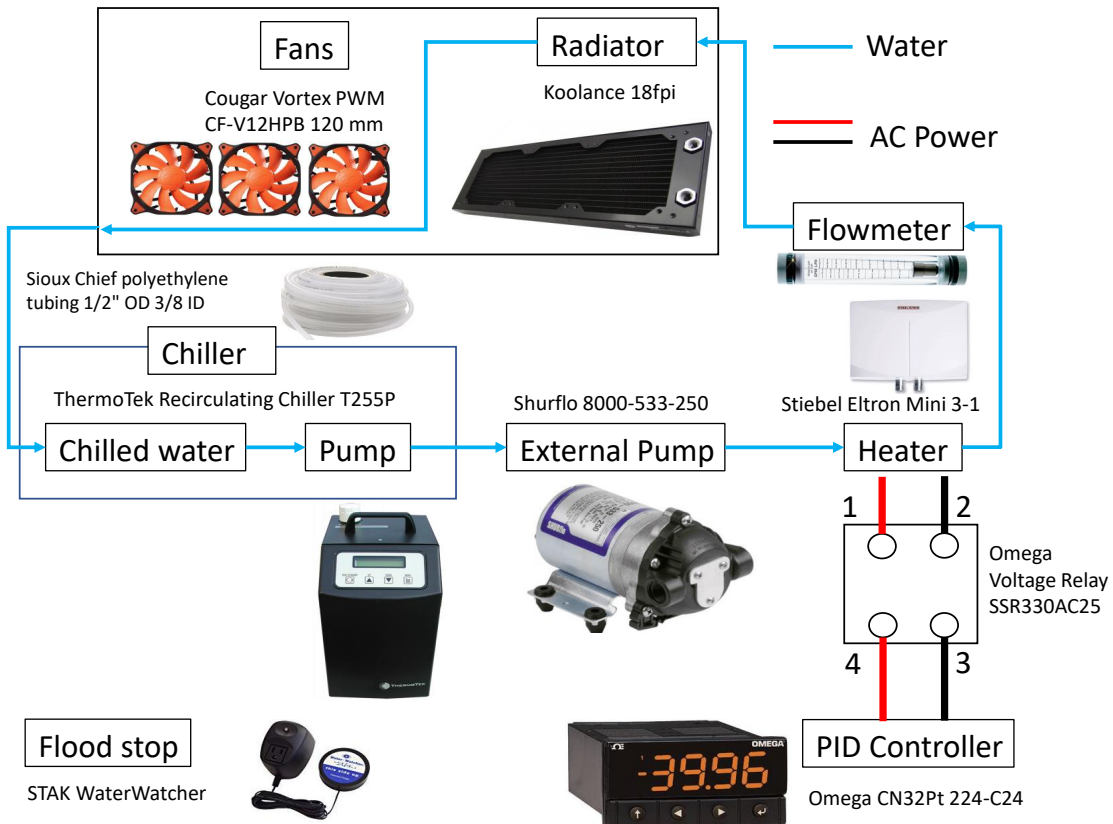


Figure C.2: Electrical and water connections.

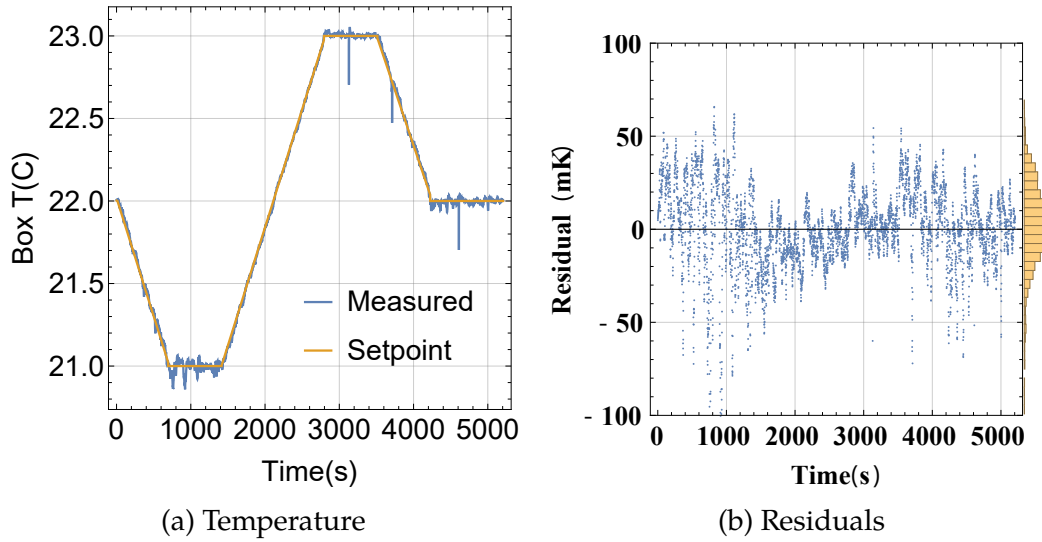


Figure C.3: Temperature stability of actively controlled box. Showing 23 mK(σ) excursion from dynamically changing set point of the air temperature inside the box. Sharp glitches are from bad electric connection to temperature sensor.

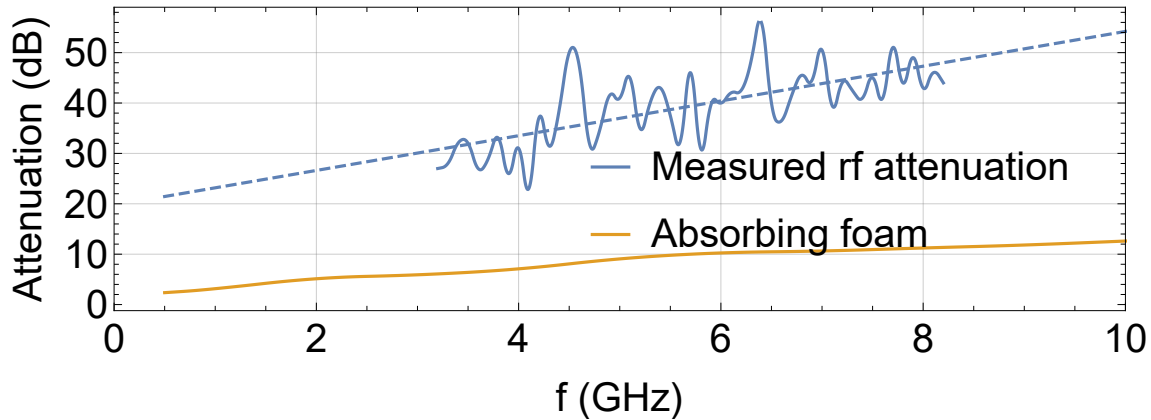


Figure C.4: RF attenuation of the box. Blue curve is measured attenuation of a single wall. Orange curve is attenuation from 1/4" Laird Eccosorb QR-13AF[118]. Dashed line is a linear fit to the data. Measured by Chris Young on 2018-12-17

D LASER CHARACTERIZATION

Coherent manipulation of atoms requires lasers driving transitions to have better phase coherence than the atomic coherence, typically limited by the lifetime of transitions and environmental fluctuations. We assess the quality of our lasers with a various technique described in the following section, and discuss the result and limitation on high-fidelity quantum gates.

D.1 Heterodyne measurements

Two spatially overlapped lasers interfere each other and if they are close in spectrum and photodetector has enough bandwidth to detect, optical beating can be mapped to electrical signal. Spectrum of the electric signal contain information about optical spectrum of the two lasers. Two different beams are combined into 2x2 fused fiber coupler [FUSED-22-633-4/125-50/50-3A3A3A3A-1-1](#) purchased from OZ optics. One arm is connected to high bandwidth photodetector [DET025AFC](#).

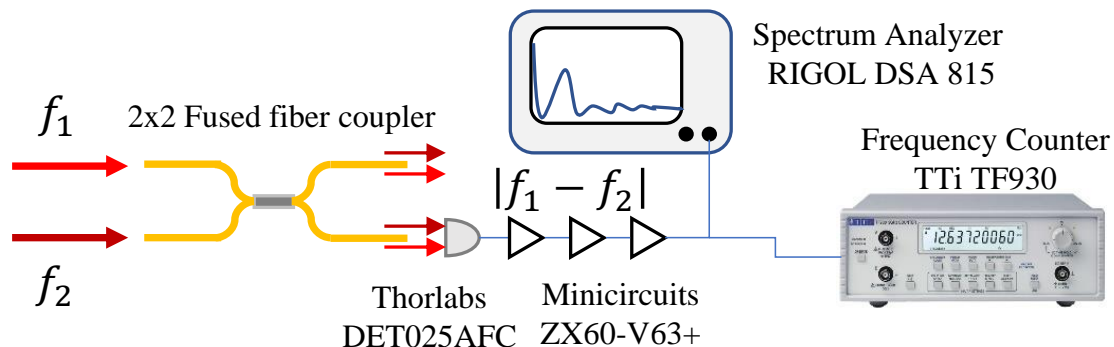


Figure D.1: Heterodyne setup

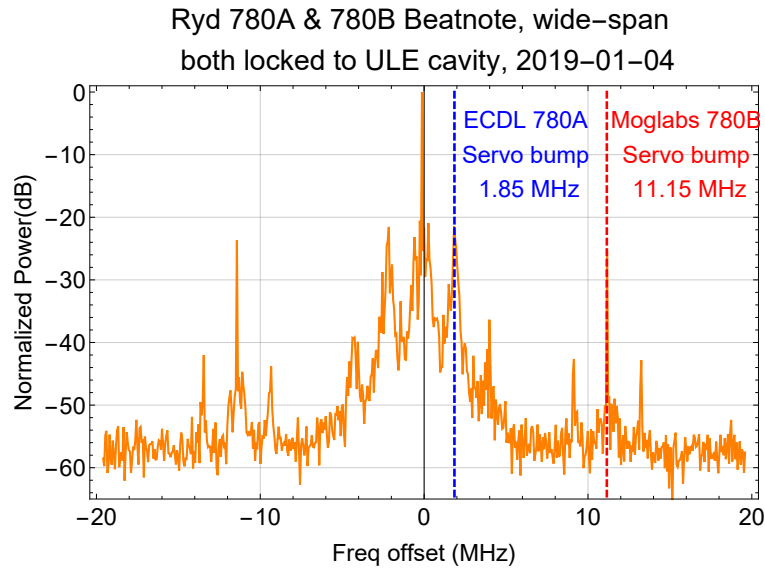


Figure D.2: Beatnote between two Rydberg lasers, 780A and 780B while they are stabilized to the ULE reference cavity

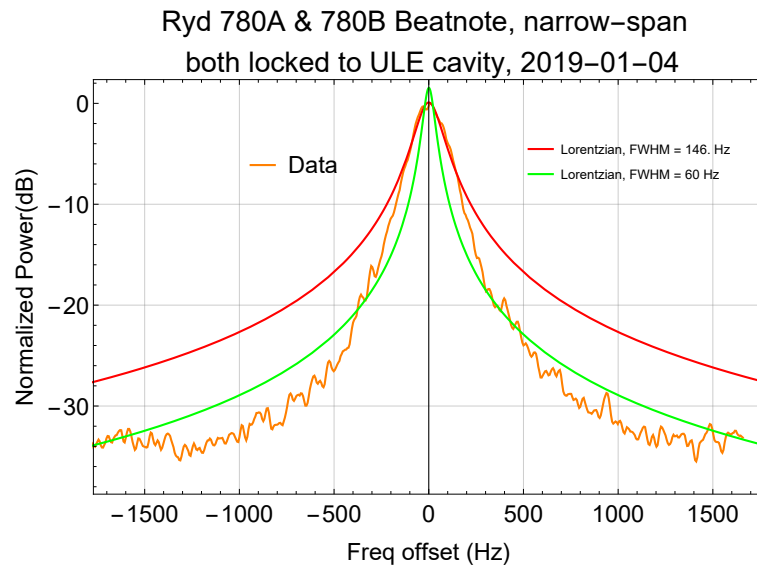


Figure D.3: Beatnote between two Rydberg lasers, 780A and 780B while they are stabilized to the ULE reference cavity, zoomed in

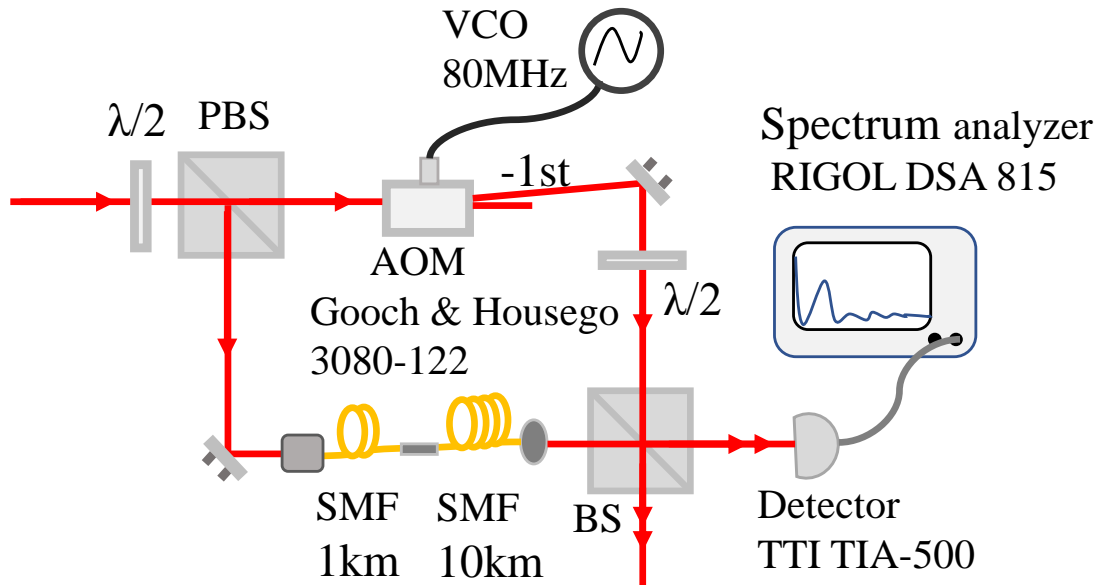


Figure D.4: Self-Heterodyne setup. Credit :Peiyu Yang

D.2 Self-heterodyne measurements

Sometimes working with two independent lasers are challenging. Alternative way is to replace one arm with a time-delayed, frequency shifted beam from the same laser. Delay line is a combination of 1km and 10km long fiber (Corning FC/PC **SMF-28** purchased from MetroTek. It is practically impossible to prepare delay line long enough to for very narrow linewidth lasers. For those instances where the delay time is far less than the coherence time, readers are advised to employ a technique from [119].

E LASER FREQUENCY CHART

It is often necessary to switch Rydberg levels. Usually the reasons are tune static field sensitivity, avoid rf interference, tune van der Waals C_6 coefficients and etc. This appendix provides what $nD_{5/2}$ levels are accessible without altering the existing setup too much. We keep 780 cavity modes and most of the frequency change is from 480 photon. Since we are frequency doubling 960 lasers and ULE cavity has FSR of ~ 500 MHz, 480 photons will change by ~ 1 GHz in energy when the mode hops to the adjacent axial modes.

Frequency comb measurements allowed us to calibrate 960 frequency at 97d, see Table E.1. Two absolute frequency measurements of 960 cavity mode were performed, separated by 1913 days, indicating the aging drift of $+233\text{mHz/s}$ (at 960 nm), or $-7.45 \times 10^{-16}/\text{s}$ of fractional drift. Beat note monitor measurement

Parameter	Value	Unit	Date
Rydberg 780A Cavity mode	384225.405	GHz	2019-02-07
Rydberg 780B Cavity mode	384233.40	GHz	2019-02-07
960 preshift AOM(-1st)	60.000	MHz	2019-02-07
960 Cavity mode (84d)	312657.7	GHz	2019-02-07
960 Cavity mode (97d)	312718.35347	GHz	2011-09-15
960 Cavity mode (97d)	312718.392	GHz	2016-12-10
960 Cavity mode (111d)	312761.2	GHz	2019-02-07
ULE cavity FSR (Larry)	499.812(2)	MHz	2011-09-15
ULE cavity FSR (Minho)	499.811371	MHz	2016-12-10
780A AOM center frequency(+1st)	250	MHz	2019-02-07
780B AOM center frequency(-1st)	350	MHz	2019-02-07
Red Pointing AOM frequency(+1st)	160	MHz	2019-02-07
Blue Pointing AOM frequency(-1st)	160	MHz	2019-02-07

Table E.1: Summary of Laser and AOM frequencies in the current setup.

provided absolute frequency of 780A cavity modes better than MHz precision. From these data, we can infer and further calculate what settings we need to use for accessing other Rydberg levels. Finite bandwidth of Rydberg 780A and 780B AOMs have been taken account, from n=50 to 118 range. Results are summarized in the Table E.2

$$f_{960 \text{ cavity mode}} = f_{960 \text{ laser}} - f_{960 \text{ preshift}}$$

$$f_{\text{Red}} = f_{780\text{A Cavity mode}} + 2 \times f_{780\text{A AOM}} + f_{780 \text{ pointing AOM freq}} \quad (\text{E.1})$$

$$f_{\text{Blue}} = 2 \times f_{960 \text{ laser}} - f_{480 \text{ pointing AOM freq}}$$

$$f_{\text{Total energy}} = f_{\text{Red}} + f_{\text{Blue}}$$

$nD_{5/2}$	780A AOM (MHz)	960 laser(GHz)	Total energy(GHz)
51	166.826	312231.136	1008688.012
52	258.856	312257.126	1008740.176
53	350.170	312281.617	1008789.340
56	198.574	312347.592	1008920.987
57	317.647	312367.085	1008960.210
60	274.286	312420.065	1009066.084
61	176.236	312436.059	1009097.875
62	298.157	312451.053	1009128.108
63	190.290	312465.548	1009156.881
64	398.694	312479.043	1009184.288
67	332.723	312516.528	1009259.127
68	201.771	312528.024	1009281.857
74	351.589	312586.502	1009399.112
75	259.153	312594.999	1009415.921
76	331.078	312602.996	1009432.059
79	203.985	312625.487	1009476.788
81	235.590	312638.982	1009503.841
82	127.097	312645.480	1009516.619
83	285.066	312651.477	1009528.930
84	221.034	312657.475	1009540.797
87	298.323	312673.969	1009573.940
90	221.444	312688.963	1009603.774
91	365.946	312693.461	1009613.060
92	357.697	312697.960	1009622.040
93	203.249	312702.458	1009630.728
97	243.748	312718.452	1009662.797
101	391.692	312732.447	1009691.082
102	167.915	312735.945	1009697.632
103	347.749	312738.944	1009703.989
106	346.602	312747.941	1009721.980
107	177.287	312750.940	1009727.639
109	103.766	312756.438	1009738.488
110	205.311	312758.937	1009743.689
111	236.007	312761.436	1009748.749
112	198.402	312763.935	1009753.672
115	199.599	312770.932	1009767.669

Table E.2: Calculated Rydberg two-photon resonance, at $B = 3.7G$ bias magnetic field. Note that 960 frequency going to the ULE cavity is 60 MHz higher, due to the pre-shift AOM. Total energy is energy difference between $|F = 2, m_F = 0\rangle \rightarrow |nD_{5/2}\rangle$. Blue colored are experimentally observed levels in our apparatus.

F HOME-MADE TEENSY TEMPERATURE CONTROLLER

Our lab has been using commercial TEC drivers from Newport and Arroyo which cost >\$1000. Since EOMs or AOMs have more tolerance on the temperature, use of such laser grade temperature controllers would be an overkill. Motivations are to replace them with appropriate solutions and decommission those laser grade temp controllers for other use. This project develops Arduino-based Digital PID loop using ADC/DAC to sense thermistor and output a voltage that controls a low power bipolar TEC driver(+/-1.5A). User interface is primarily touch interface. Temperature stability test protocol from NewPort [Application Note #38 Achieving Millikelvin Temperature Stability](#)

- Stand-alone operation, fanless, compact package.
- Single power supply dependency(5V). Bipolar, direct current up to +/- 1.5A@5V
- Reduced EMI from Linear + PWM driver(2.0MHz Switching freq)
- Multiple drivers can be stacked to single MCU

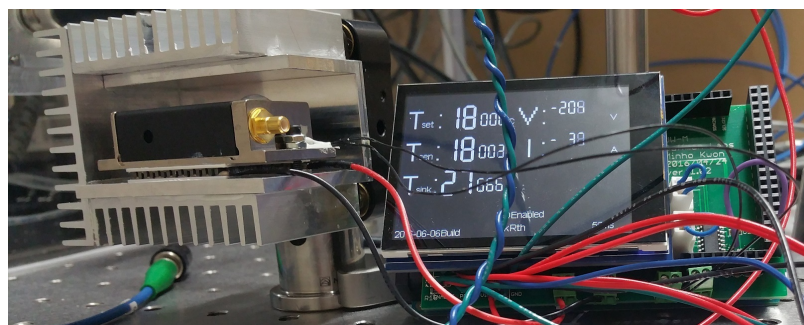


Figure F.1: Home-made TEC controller(Prototype) stabilizing the temperature of an acousto-optical modulator

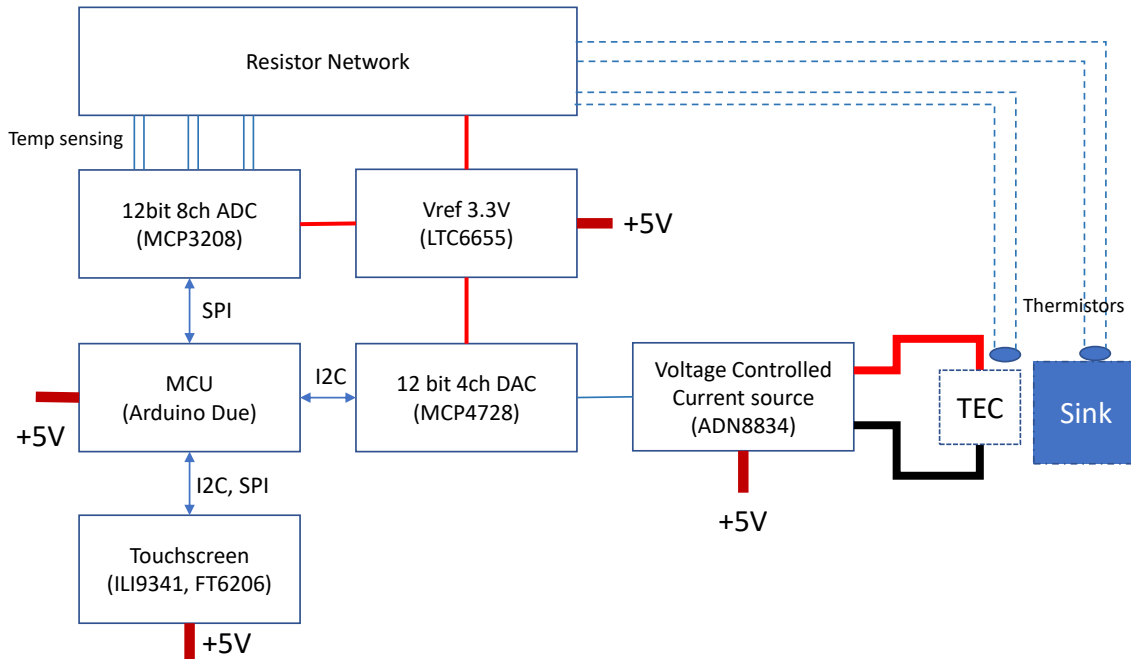


Figure F.2: Functional diagram of Temperature Controller

- 2.8" 320x240 Touchscreen interface.
- On/Off, Enable/Disable buttons to be failsafe when the touch interface fails.
- Two configurable analog voltage outputs. Can be used give a control signal to other circuit, or temperature monitoring.
- 10k/50k NTC thermistors supported
- Two thermistor inputs allow monitoring the object and sink simultaneously.
- 1σ stability $\sim 1 \text{ mK}$ (short-term)

Exemplary PID gain tuning curve is shown on Figure F.3.

Performance of the temperature controller is confirmed by out-of-loop measurement of object temperature, shown on Figure F.4.

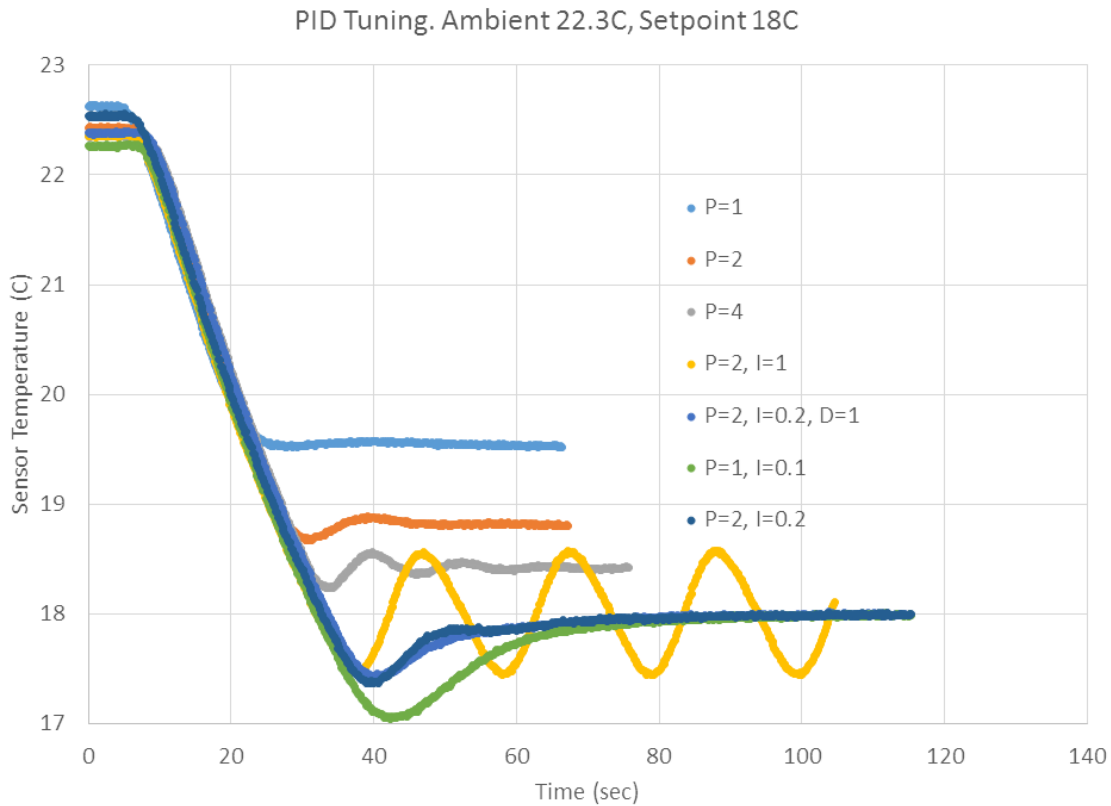


Figure F.3: Teensy TEC controller PID tuning curves. Data from 2016-03-16

I made a strategic choice– to discontinue the project– due to lack of profitability. Prototype has shown comparable performance what Arroyo's offers at much higher price. However after seeing many commercial products become available at very affordable price and considering the amount of extra work for perfection on this project, I recommend rather purchasing those commercial ones(being tested and equipped with nicer software). If you are looking for those commercial affordable TEC drivers, take a look at Thorlabs ,Meerstetter, and SmartPID (more casual). Prices ranges from \$50~\$250. If this project is to be resumed I would get away

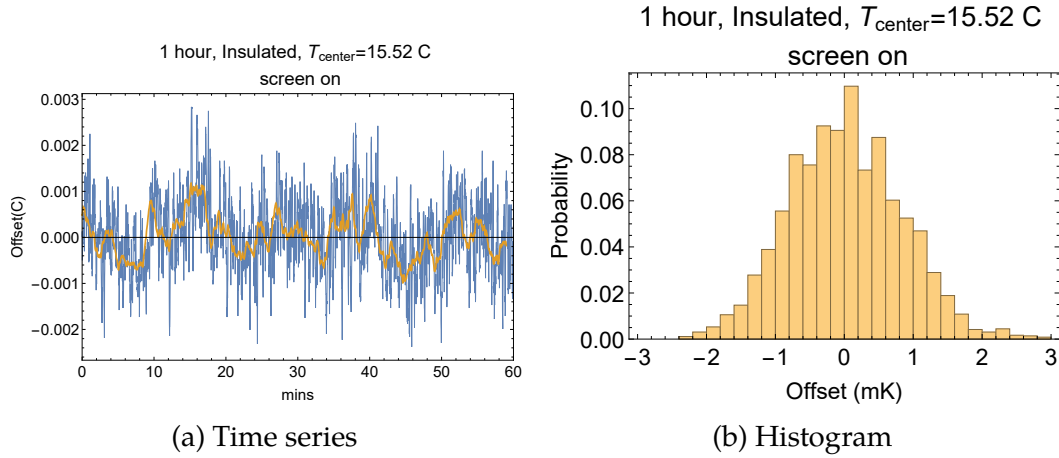


Figure F.4: Performance of home-made Teensy TEC controller exhibiting superb stability. Acquired temperature is from independent thermistor attached next to the thermistor being used by the controller.

from using touchscreens. They tend to generate digital noises into neighboring electronics. This will impose rework on user-interface (Front panel control & possibly Ethernet support). After new prototyping thorough testing before mass production is a must, as partially working device is the worst thing to have.

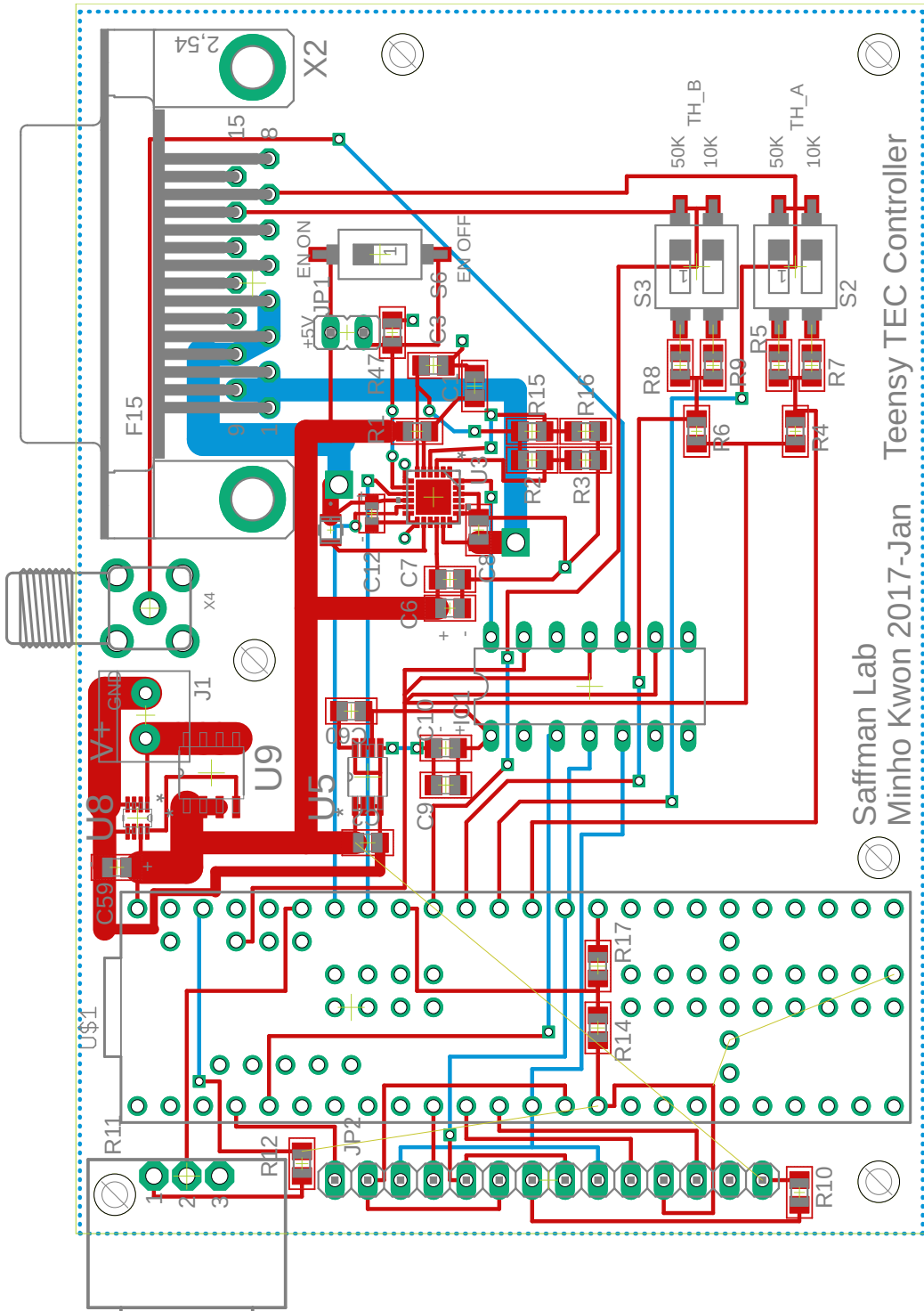


Figure F.5: Board layout of Teensy TEC controller

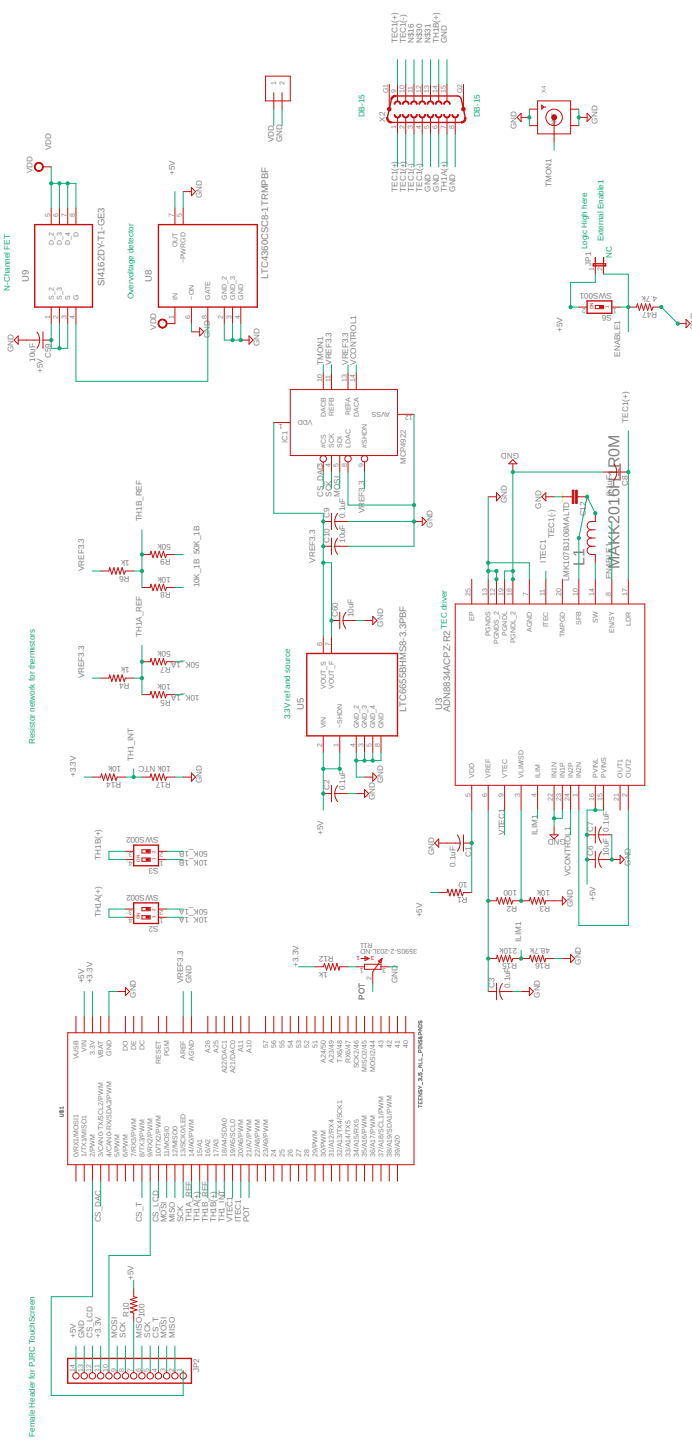


Figure F.6: Schematic of Teensy TEC controller

REFERENCES

- [1] M. Saffman. "Quantum computing with atomic qubits and Rydberg interactions: Progress and challenges". In: *Journal of Physics B: Atomic, Molecular and Optical Physics* 49.20 (2016). doi: [10.1088/0953-4075/49/20/202001](https://doi.org/10.1088/0953-4075/49/20/202001).
- [2] T Grünzweig, A Hilliard, M. McGovern, and M F Andersen. "Near-deterministic preparation of a single atom in an optical microtrap". In: *Nature Physics* 6.12 (2010), pp. 951–954. doi: [10.1038/nphys1778](https://doi.org/10.1038/nphys1778).
- [3] Alicia V. Carpentier, Yin H. Fung, Pimonpan Sompet, Andrew J. Hilliard, Thad G. Walker, and Mikkel F. Andersen. "Preparation of a single atom in an optical microtrap". In: *Laser Physics Letters* 10.12 (2013), p. 125501. doi: [10.1088/1612-2011/10/12/125501](https://doi.org/10.1088/1612-2011/10/12/125501).
- [4] Y. H. Fung and M. F. Andersen. "Efficient collisional blockade loading of a single atom into a tight microtrap". In: *New Journal of Physics* 17.7 (2015). doi: [10.1088/1367-2630/17/7/073011](https://doi.org/10.1088/1367-2630/17/7/073011).
- [5] Brian J. Lester, Niclas Luick, Adam M. Kaufman, Collin M. Reynolds, and Cindy A. Regal. "Rapid Production of Uniformly Filled Arrays of Neutral Atoms". In: *Physical Review Letters* 115.7 (2015), p. 073003. doi: [10.1103/PhysRevLett.115.073003](https://doi.org/10.1103/PhysRevLett.115.073003).
- [6] Marshall T. DePue, Colin McCormick, S. Lukman Winoto, Steven Oliver, and David S. Weiss. "Unity Occupation of Sites in a 3D Optical Lattice". In: *Physical Review Letters* 82.11 (1999), pp. 2262–2265. doi: [10.1103/PhysRevLett.82.2262](https://doi.org/10.1103/PhysRevLett.82.2262).
- [7] Nicolas Schlosser, Georges Reymond, Igor Protsenko, and Philippe Grangier. "Sub-poissonian loading of single atoms in a microscopic dipole trap". In: *Nature* 411.6841 (2001), pp. 1024–1027. doi: [10.1038/35082512](https://doi.org/10.1038/35082512).
- [8] M. D. Lukin, M. Fleischhauer, R. Cote, L. M. Duan, D. Jaksch, J. I. Cirac, and P. Zoller. "Dipole blockade and quantum information processing in meso-

- scopic atomic ensembles". In: *Physical Review Letters* 87.3 (2001), pp. 37901–1. doi: [10.1103/PhysRevLett.87.037901](https://doi.org/10.1103/PhysRevLett.87.037901).
- [9] E. Brion, K. Mølmer, and M. Saffman. "Quantum Computing with Collective Ensembles of Multilevel Systems". In: *Physical Review Letters* 99.26 (2007), p. 260501. doi: [10.1103/PhysRevLett.99.260501](https://doi.org/10.1103/PhysRevLett.99.260501).
- [10] Manuel Endres, Hannes Bernien, Alexander Keesling, Harry Levine, Eric R. Anschuetz, Alexandre Krajenbrink, Crystal Senko, Vladan Vuletic, Markus Greiner, and Mikhail D. Lukin. "Atom-by-atom assembly of defect-free one-dimensional cold atom arrays". In: *Science* 354.6315 (2016), pp. 1024–1027. doi: [10.1126/science.aah3752](https://doi.org/10.1126/science.aah3752).
- [11] Samuel Saskin, Jack Wilson, Brandon Grinkemeyer, and Jeff Thompson. "Narrow-line cooling and imaging of Ytterbium atoms in an optical tweezer array". In: *arXiv preprint* c (2018), pp. 1–6. URL: <https://arxiv.org/abs/1810.10517> <http://arxiv.org/abs/1810.10517>.
- [12] M. O. Brown, T. Thiele, C. Kiehl, T.-W. Hsu, and C. A. Regal. "Gray-Molasses Optical-Tweezer Loading: Controlling Collisions for Scaling Atom-Array Assembly". In: *Physical Review X* 9.1 (2019), p. 011057. doi: [10.1103/PhysRevX.9.011057](https://doi.org/10.1103/PhysRevX.9.011057).
- [13] Alexandre Cooper, Jacob P. Covey, Ivaylo S. Madjarov, Sergey G. Porsev, Marianna S. Safronova, and Manuel Endres. "Alkaline-Earth Atoms in Optical Tweezers". In: *Physical Review X* 8.4 (2018), p. 041055. doi: [10.1103/PhysRevX.8.041055](https://doi.org/10.1103/PhysRevX.8.041055).
- [14] Hyosub Kim, Woojun Lee, Han-gyeol Lee, Hanlae Jo, Yunheung Song, and Jaewook Ahn. "In situ single-atom array synthesis using dynamic holographic optical tweezers". In: *Nature Communications* 7 (2016), p. 13317. doi: [10.1038/ncomms13317](https://doi.org/10.1038/ncomms13317).
- [15] Daniel Ohl de Mello, Dominik Schäffner, Jan Werkmann, Tilman Preuschoff, Lars Kohfahl, Malte Schlosser, and Gerhard Birk. "Defect-free assembly

- of 2D clusters of more than 100 single-atom quantum systems". In: (2019), pp. 1–10. URL: <http://arxiv.org/abs/1902.00284>.
- [16] Daniel Barredo, Vincent Lienhard, Sylvain de Léséleuc, Thierry Lahaye, and Antoine Browaeys. "Synthetic three-dimensional atomic structures assembled atom by atom". In: *Nature* 561.c (2017), pp. 79–82. doi: [10.1038/s41586-018-0450-2](https://doi.org/10.1038/s41586-018-0450-2).
 - [17] Benjamin Rosenfeld, Jürgen Volz, Markus Weber, and Harald Weinfurter. "Coherence of a qubit stored in Zeeman levels of a single optically trapped atom". In: *Physical Review A* 84.2 (2011), p. 022343. doi: [10.1103/PhysRevA.84.022343](https://doi.org/10.1103/PhysRevA.84.022343).
 - [18] W. K. Wootters and W. H. Zurek. "A single quantum cannot be cloned". In: *Nature* 299.5886 (1982), pp. 802–803. doi: [10.1038/299802a0](https://doi.org/10.1038/299802a0).
 - [19] Nicolas Sangouard, Christoph Simon, Hugues de Riedmatten, and Nicolas Gisin. "Quantum repeaters based on atomic ensembles and linear optics". In: *Reviews of Modern Physics* 83.1 (2011), pp. 33–80. doi: [10.1103/RevModPhys.83.33](https://doi.org/10.1103/RevModPhys.83.33).
 - [20] L M Duan, M D Lukin, J I Cirac, and P Zoller. "Long-distance quantum communication with atomic ensembles and linear optics." In: *Nature* 414.6862 (2001), pp. 413–418. doi: [10.1038/35106500](https://doi.org/10.1038/35106500).
 - [21] Pierre Vernaz-Gris, Aaron D. Tranter, Jesse L. Everett, Anthony C. Leung, Karun V. Paul, Geoff T. Campbell, Ping Koy Lam, and Ben C. Buchler. "High-performance Raman memory with spatio-temporal reversal". In: *Optics Express* 26.10 (2018), p. 12424. doi: [10.1364/OE.26.012424](https://doi.org/10.1364/OE.26.012424).
 - [22] Jinxian Guo, Xiaotian Feng, Peiyu Yang, Zhifei Yu, L Q Chen, Chun-hua Yuan, and Weiping Zhang. "High-performance Raman quantum memory with optimal control in room temperature atoms". In: *Nature Communications* 10.1 (2019), p. 148. doi: [10.1038/s41467-018-08118-5](https://doi.org/10.1038/s41467-018-08118-5).

- [23] Lijun Ma, Oliver Slattery, and Xiao Tang. "Optical quantum memory based on electromagnetically induced transparency". In: *Journal of Optics* 19.4 (2017), p. 043001. doi: [10.1088/2040-8986/19/4/043001](https://doi.org/10.1088/2040-8986/19/4/043001).
- [24] J. Laurat, K. S. Choi, H. Deng, C. W. Chou, and H. J. Kimble. "Heralded Entanglement between Atomic Ensembles: Preparation, Decoherence, and Scaling". In: *Physical Review Letters* 99.18 (2007), p. 180504. doi: [10.1103/PhysRevLett.99.180504](https://doi.org/10.1103/PhysRevLett.99.180504).
- [25] D. N. Matsukevich, T. Chanelière, M. Bhattacharya, S. Y. Lan, S. D. Jenkins, T. a B Kennedy, and a. Kuzmich. "Entanglement of a photon and a collective atomic excitation". In: *Physical Review Letters* 95.4 (2005), pp. 22–25. doi: [10.1103/PhysRevLett.95.040405](https://doi.org/10.1103/PhysRevLett.95.040405).
- [26] M. Saffman and T. G. Walker. "Engineering single atom and single photon sources from entangled atomic ensembles". In: *Physical Review A - Atomic, Molecular, and Optical Physics* 66.March (2002), p. 065403. doi: [10.1103/PhysRevA.66.065403](https://doi.org/10.1103/PhysRevA.66.065403).
- [27] L. Li, Y. O. Dudin, and A. Kuzmich. "Entanglement between light and an optical atomic excitation". In: *Nature* 498.7455 (2013), pp. 466–469. doi: [10.1038/nature12227](https://doi.org/10.1038/nature12227).
- [28] M. Saffman and T. G. Walker. "Entangling single and N atom qubits for fast quantum state detection and transmission". In: *Physical Review A* 72.4 (2005), p. 042302. doi: [10.1103/PhysRevA.72.042302](https://doi.org/10.1103/PhysRevA.72.042302).
- [29] Marlan O. Scully, Edward S. Fry, C. H. Raymond Ooi, and Krzysztof Wódziewicz. "Directed Spontaneous Emission from an Extended Ensemble of N Atoms: Timing Is Everything". In: *Physical Review Letters* 96.1 (2006), p. 010501. doi: [10.1103/PhysRevLett.96.010501](https://doi.org/10.1103/PhysRevLett.96.010501).
- [30] I E Mazets and G Kurizki. "Multiatom cooperative emission following single-photon absorption: Dicke-state dynamics". In: *Journal of Physics B: Atomic, Molecular and Optical Physics* 40.6 (2007), F105–F112. doi: [10.1088/0953-4075/40/6/F01](https://doi.org/10.1088/0953-4075/40/6/F01).

- [31] Yevhen Miroshnychenko, Uffe V Poulsen, and Klaus Mølmer. "Directional emission of single photons from small atomic samples". In: *Physical Review A* 87.2 (2013), p. 023821. doi: [10.1103/PhysRevA.87.023821](https://doi.org/10.1103/PhysRevA.87.023821).
- [32] H. H. Jen, M.-S. Chang, and Y.-C. Chen. "Cooperative light scattering from helical-phase-imprinted atomic rings". In: *Scientific Reports* 8.1 (2018), p. 9570. doi: [10.1038/s41598-018-27888-y](https://doi.org/10.1038/s41598-018-27888-y).
- [33] Valentina Parigi, Vincenzo D'Ambrosio, Christophe Arnold, Lorenzo Marrucci, Fabio Sciarrino, and Julien Laurat. "Storage and retrieval of vector beams of light in a multiple-degree-of-freedom quantum memory". In: *Nature Communications* 6 (2015), p. 7706. doi: [10.1038/ncomms8706](https://doi.org/10.1038/ncomms8706).
- [34] Pierre Vernaz-Gris, Kun Huang, Mingtao Cao, Alexandra S. Sheremet, and Julien Laurat. "Highly-efficient quantum memory for polarization qubits in a spatially-multiplexed cold atomic ensemble". In: *Nature Communications* 9.1 (2018), p. 363. doi: [10.1038/s41467-017-02775-8](https://doi.org/10.1038/s41467-017-02775-8).
- [35] Bo Zhao, Markus Müller, Klemens Hammerer, and Peter Zoller. "Efficient quantum repeater based on deterministic Rydberg gates". In: *Physical Review A* 81.5 (2010), p. 052329. doi: [10.1103/PhysRevA.81.052329](https://doi.org/10.1103/PhysRevA.81.052329).
- [36] Neal Solmeyer, Xiao Li, and Qudsia Quraishi. "High teleportation rates using cold-atom-ensemble-based quantum repeaters with Rydberg blockade". In: *Physical Review A* 93.4 (2016), p. 042301. doi: [10.1103/PhysRevA.93.042301](https://doi.org/10.1103/PhysRevA.93.042301).
- [37] A. Grankin, P. O. Guimond, D. V. Vasilyev, B. Vermersch, and P. Zoller. "Free-space photonic quantum link and chiral quantum optics". In: *Physical Review A* 98.4 (2018), p. 043825. doi: [10.1103/PhysRevA.98.043825](https://doi.org/10.1103/PhysRevA.98.043825).
- [38] N. Šibalić, J.D. Pritchard, C.S. Adams, and K.J. Weatherill. "ARC: An open-source library for calculating properties of alkali Rydberg atoms". In: *Computer Physics Communications* 220 (2017), pp. 319–331. doi: [10.1016/j.cpc.2017.06.015](https://doi.org/10.1016/j.cpc.2017.06.015).

- [39] U. Fano, L. Fano, and D. C. Peaslee. "Basic Physics of Atoms and Molecules". In: *American Journal of Physics* 27.8 (1959), pp. 612–613. doi: [10.1119/1.1934937](https://doi.org/10.1119/1.1934937).
- [40] Constantine E. Theodosiou. "Lifetimes of alkali-metal—atom Rydberg states". In: *Physical Review A* 30.6 (1984), pp. 2881–2909. doi: [10.1103/PhysRevA.30.2881](https://doi.org/10.1103/PhysRevA.30.2881).
- [41] Eric Gerard Paradis. "High-Magnetic-Field Rydberg Atom Interactions." PhD thesis. The University of Michigan, 2013.
- [42] L. Ma, D. A. Anderson, and G. Raithel. "Paschen-Back effects and Rydberg-state diamagnetism in vapor-cell electromagnetically induced transparency". In: *Physical Review A* 95.6 (2017), pp. 1–6. doi: [10.1103/PhysRevA.95.061804](https://doi.org/10.1103/PhysRevA.95.061804).
- [43] Sebastian Weber, Christoph Tresp, Henri Menke, Alban Urvoy, Ofer Firstenberg, Hans Peter Büchler, and Sebastian Hofferberth. "Calculation of Rydberg interaction potentials". In: *Journal of Physics B: Atomic, Molecular and Optical Physics* 50.13 (2017), p. 133001. doi: [10.1088/1361-6455/aa743a](https://doi.org/10.1088/1361-6455/aa743a).
- [44] Robert J. Le Roy. "Long-Range Potential Coefficients From RKR Turning Points: C 6 and C 8 for B (3Π Ou +)-State Cl 2 , Br 2 , and I 2 ". In: *Canadian Journal of Physics* 52.3 (1974), pp. 246–256. doi: [10.1139/p74-035](https://doi.org/10.1139/p74-035).
- [45] Thomas Amthor. "Interaction-Induced Dynamics in Ultracold Rydberg Gases – Mechanical Effects and Coherent Processes". In: *Thesis* (2008). url: <http://www.freidok.uni-freiburg.de/volltexte/5802/>.
- [46] T. Amthor, J. Denskat, C. Giese, N. N. Bezuglov, A. Ekers, L. S. Cederbaum, and M. Weidemüller. "Autoionization of an ultracold Rydberg gas through resonant dipole coupling". In: *The European Physical Journal D* 53.3 (2009), pp. 329–335. doi: [10.1140/epjd/e2009-00119-4](https://doi.org/10.1140/epjd/e2009-00119-4).
- [47] Andrei Derevianko, Péter Kómár, Turker Topcu, Ronen M. Kroeze, and Mikhail D. Lukin. "Effects of molecular resonances on Rydberg blockade". In: *Physical Review A* 92.6 (2015), p. 063419. doi: [10.1103/PhysRevA.92.063419](https://doi.org/10.1103/PhysRevA.92.063419).

- [48] J.R. Johansson, P.D. Nation, and Franco Nori. "QuTiP 2: A Python framework for the dynamics of open quantum systems". In: *Computer Physics Communications* 184.4 (2013), pp. 1234–1240. doi: [10.1016/j.cpc.2012.11.019](https://doi.org/10.1016/j.cpc.2012.11.019).
- [49] Neil V. Corzo, Jérémie Raskop, Aveek Chandra, Alexandra S. Sheremet, Baptiste Gouraud, and Julien Laurat. "Waveguide-coupled single collective excitation of atomic arrays". In: *Nature* (2019). doi: [10.1038/s41586-019-0902-3](https://doi.org/10.1038/s41586-019-0902-3).
- [50] R. H. Dicke. "Coherence in Spontaneous Radiation Processes". In: *Physical Review* 93.1 (1954), pp. 99–110. doi: [10.1103/PhysRev.93.99](https://doi.org/10.1103/PhysRev.93.99).
- [51] Wei Feng, Yong Li, and Shi-Yao Zhu. "Effect of atomic distribution on cooperative spontaneous emission". In: *Physical Review A* 89.1 (2014), p. 013816. doi: [10.1103/PhysRevA.89.013816](https://doi.org/10.1103/PhysRevA.89.013816).
- [52] Anatoly a. Svidzinsky, Jun Tao Chang, and Marlan O. Scully. "Cooperative spontaneous emission of N atoms: Many-body eigenstates, the effect of virtual lamb shift processes, and analogy with radiation of N classical oscillators". In: *Physical Review A - Atomic, Molecular, and Optical Physics* 81.5 (2010), pp. 1–15. doi: [10.1103/PhysRevA.81.053821](https://doi.org/10.1103/PhysRevA.81.053821).
- [53] Line Hjortshøj Pedersen and Klaus Mølmer. "Few qubit atom-light interfaces with collective encoding". In: *Physical Review A* 79.1 (2009), p. 012320. doi: [10.1103/PhysRevA.79.012320](https://doi.org/10.1103/PhysRevA.79.012320).
- [54] K I Petsas, A B Coates, and G Grynberg. "Crystallography of optical lattices". In: *Physical Review A* 50.6 (1994), pp. 5173–5189. doi: [10.1103/PhysRevA.50.5173](https://doi.org/10.1103/PhysRevA.50.5173).
- [55] D. Porras and J. I. Cirac. "Collective generation of quantum states of light by entangled atoms". In: *Physical Review A* 78.5 (2008), p. 053816. doi: [10.1103/PhysRevA.78.053816](https://doi.org/10.1103/PhysRevA.78.053816).
- [56] Matthew F Ebert. "Neutral Atom Ensemble Qubits and Rydberg Blockade". PhD thesis. University of Wisconsin-Madison, 2017.

- [57] S. N. Atutov, R. Calabrese, V. Guidi, B. Mai, A. G. Rudavets, E. Scansani, L. Tomassetti, V. Biancalana, A. Burchianti, C. Marinelli, E. Mariotti, L. Moi, and S. Veronesi. "Fast and efficient loading of a Rb magneto-optical trap using light-induced atomic desorption". In: *Physical Review A* 67.5 (2003), p. 053401. doi: [10.1103/PhysRevA.67.053401](https://doi.org/10.1103/PhysRevA.67.053401).
- [58] C. Klempt, T. van Zoest, T. Henninger, O. Topic, E. Rasel, W. Ertmer, and J. Arlt. "Ultraviolet light-induced atom desorption for large rubidium and potassium magneto-optical traps". In: *Physical Review A* 73.1 (2006), p. 013410. doi: [10.1103/PhysRevA.73.013410](https://doi.org/10.1103/PhysRevA.73.013410).
- [59] Lara Torralbo-Campo, Graham D. Bruce, Giuseppe Smirne, and Donatella Cassettari. "Light-induced atomic desorption in a compact system for ultracold atoms". In: *Scientific Reports* 5 (2015), p. 14729. doi: [10.1038/srep14729](https://doi.org/10.1038/srep14729).
- [60] T. Arpornthip, C. A. Sackett, and K. J. Hughes. "Vacuum-pressure measurement using a magneto-optical trap". In: *Physical Review A* 85.3 (2012), p. 033420. doi: [10.1103/PhysRevA.85.033420](https://doi.org/10.1103/PhysRevA.85.033420).
- [61] Karl D. Nelson, Xiao Li, and David S. Weiss. "Imaging single atoms in a three-dimensional array". In: *Nature Physics* 3.8 (2007), pp. 556–560. doi: [10.1038/nphys645](https://doi.org/10.1038/nphys645).
- [62] Michael Hirsch, Richard J Wareham, Marisa L. Martin-Fernandez, Michael P Hobson, and Daniel J Rolfe. "A stochastic model for electron multiplication charge-coupled devices – from theory to practice". In: *PLOS ONE* 8.1 (2013), e53671. doi: [10.1371/journal.pone.0053671](https://doi.org/10.1371/journal.pone.0053671).
- [63] Aapo Hyvärinen and Erkki Oja. "Independent component analysis: algorithms and applications". In: *Neural Networks* 13.4-5 (2000), pp. 411–430. doi: [10.1016/S0893-6080\(00\)00026-5](https://doi.org/10.1016/S0893-6080(00)00026-5).
- [64] S. Kuhr, W. Alt, D. Schrader, I. Dotsenko, Y. Miroshnychenko, A. Rauschenbeutel, and D. Meschede. "Analysis of dephasing mechanisms in a standing-wave dipole trap". In: *Physical Review A* 72.2 (2005), p. 023406. doi: [10.1103/PhysRevA.72.023406](https://doi.org/10.1103/PhysRevA.72.023406).

- [65] Larry Isenhower. "Demonstration of Rydberg Blockade, A Neutral Atom CNOT gate, and Entanglement Generation". PhD thesis. University of Wisconsin-Madison, 2010.
- [66] Nikola Šibalić. "Rydberg atom ensembles under dephasing and dissipation: from single- to many-body dynamics". PhD thesis. Durhan University, 2017.
- [67] David A. Anderson, Rachel E. Sapiro, and Georg Raithel. "An atomic receiver for AM and FM radio communication". In: (2018), pp. 1–6. URL: <http://arxiv.org/abs/1808.08589>.
- [68] David H. Meyer, Kevin C. Cox, Fredrik K. Fatemi, and Paul D. Kunz. "Digital communication with Rydberg atoms and amplitude-modulated microwave fields". In: *Applied Physics Letters* 112.21 (2018), p. 211108. doi: [10.1063/1.5028357](https://doi.org/10.1063/1.5028357).
- [69] Kevin C. Cox, David H. Meyer, Fredrik K. Fatemi, and Paul D. Kunz. "Quantum-Limited Atomic Receiver in the Electrically Small Regime". In: *Physical Review Letters* 121.11 (2018), p. 110502. doi: [10.1103/PhysRevLett.121.110502](https://doi.org/10.1103/PhysRevLett.121.110502).
- [70] A. B. Deb and N. Kjærgaard. "Radio-over-fiber using an optical antenna based on Rydberg states of atoms". In: *Applied Physics Letters* 112.21 (2018). doi: [10.1063/1.5031033](https://doi.org/10.1063/1.5031033).
- [71] Christopher L. Holloway, Matthew T. Simons, Joshua A. Gordon, and David Novotny. "Detecting and Receiving Phase Modulated Signals with a Rydberg Atom-Based Mixer". In: March (2019), pp. 1–5. URL: <http://arxiv.org/abs/1903.10644>.
- [72] Erich Urban. "Coherent Manipulation of Single Atom Qubits Using Rydberg States". PhD thesis. The University of Wisconsin - Madison, 2009.
- [73] R. Le Targat, J.-J. Zondy, and P. Lemonde. "75%-Efficiency blue generation from an intracavity PPKTP frequency doubler". In: *Optics Communications* 247.4-6 (2005), pp. 471–481. doi: [10.1016/j.optcom.2004.11.081](https://doi.org/10.1016/j.optcom.2004.11.081).

- [74] Tobias Meier. "High-Power CW Green Lasers for Optical Metrology and Their Joint Benefit in Particle Physics Experiments". PhD thesis. Gottfried Wilhelm Leibniz Universität Hannover, 2011. ISBN: 978-3-8381-1434-7.
- [75] E. S. Polzik and H. J. Kimble. "Frequency doubling with KNbO₃ in an external cavity". In: *Optics Letters* 16.18 (1991), p. 1400. doi: [10.1364/OL.16.001400](https://doi.org/10.1364/OL.16.001400).
- [76] T.W. Hansch and B Couillaud. "Laser frequency stabilization by polarization spectroscopy of a reflecting reference cavity". In: *Optics Communications* 35.3 (1980), pp. 441–444. doi: [10.1016/0030-4018\(80\)90069-3](https://doi.org/10.1016/0030-4018(80)90069-3).
- [77] R. W.P. P. Drever, J. L. Hall, F. V. Kowalski, J. Hough, G. M. Ford, A. J. Munley, and H. Ward. "Laser phase and frequency stabilization using an optical resonator". In: *Applied Physics B Photophysics and Laser Chemistry* 31.2 (1983), pp. 97–105. doi: [10.1007/BF00702605](https://doi.org/10.1007/BF00702605).
- [78] K. Kato. "Temperature-tuned 90° phase-matching properties of LBO". In: *IEEE Journal of Quantum Electronics* 30.12 (1994), pp. 2950–2952. doi: [10.1109/3.362711](https://doi.org/10.1109/3.362711).
- [79] T. Savard, K. O'Hara, and J. Thomas. "Laser-noise-induced heating in far-off resonance optical traps". In: *Physical Review A* 56.2 (1997), R1095–R1098. doi: [10.1103/PhysRevA.56.R1095](https://doi.org/10.1103/PhysRevA.56.R1095).
- [80] Niklas Waasem, Stephan Fieberg, Janosch Hauser, Gregory Gomes, Daniel Haertle, Frank Kühnemann, and Karsten Buse. "Photoacoustic absorption spectrometer for highly transparent dielectrics with parts-per-million sensitivity". In: *Review of Scientific Instruments* 84.2 (2013). doi: [10.1063/1.4792724](https://doi.org/10.1063/1.4792724).
- [81] Matthew Ebert, Alexander Gill, Michael Gibbons, Xianli Zhang, Mark Saffman, and Thad G. Walker. "Atomic Fock State Preparation Using Rydberg Blockade". In: *Physical Review Letters* 112.4 (2014), pp. 1–5. doi: [10.1103/PhysRevLett.112.043602](https://doi.org/10.1103/PhysRevLett.112.043602).

- [82] Huaizhi Wu, Xi Rong Huang, Chang Sheng Hu, Zhen Biao Yang, and Shi Biao Zheng. "Rydberg-interaction gates via adiabatic passage and phase control of driving fields". In: *Physical Review A* 96.2 (2017). doi: [10.1103/PhysRevA.96.022321](https://doi.org/10.1103/PhysRevA.96.022321).
- [83] T. Cubel, B. K. Teo, V. S. Malinovsky, J. R. Guest, A. Reinhard, B. Knuffman, P. R. Berman, and G. Raithel. "Coherent population transfer of ground-state atoms into Rydberg states". In: *Physical Review A - Atomic, Molecular, and Optical Physics* 72.2 (2005), pp. 1–4. doi: [10.1103/PhysRevA.72.023405](https://doi.org/10.1103/PhysRevA.72.023405).
- [84] David Petrosyan and Klaus Mølmer. "Stimulated adiabatic passage in a dissipative ensemble of atoms with strong Rydberg-state interactions". In: *Physical Review A - Atomic, Molecular, and Optical Physics* 87.3 (2013), pp. 1–5. doi: [10.1103/PhysRevA.87.033416](https://doi.org/10.1103/PhysRevA.87.033416).
- [85] Malcolm H. Levitt. "Composite Pulses". In: *Encyclopedia of Magnetic Resonance*. John Wiley & Sons, Ltd, 2007. doi: [10.1002/9780470034590.emrstm0086](https://doi.org/10.1002/9780470034590.emrstm0086).
- [86] Malcolm H. Levitt and Ray Freeman. "Compensation for pulse imperfections in NMR spin-echo experiments". In: *Journal of Magnetic Resonance (1969)* 43.1 (1981), pp. 65–80. doi: [10.1016/0022-2364\(81\)90082-2](https://doi.org/10.1016/0022-2364(81)90082-2).
- [87] Han-gyeol Lee, Hyosub Kim, and Jaewook Ahn. "Ultrafast laser-driven Rabi oscillations of a trapped atomic vapor". In: *Optics Letters* 40.4 (2015), p. 510. doi: [10.1364/OL.40.000510](https://doi.org/10.1364/OL.40.000510).
- [88] Jonathan P Dowling, G. S. Agarwal, and Wolfgang P. Schleich. "Wigner distribution of a general angular-momentum state: Applications to a collection of two-level atoms". In: *Physical Review A* 49.5 (1994), pp. 4101–4109. doi: [10.1103/PhysRevA.49.4101](https://doi.org/10.1103/PhysRevA.49.4101).
- [89] A We. "Entangled States of More Than". In: 344.April (2014), pp. 180–184. doi: [10.1126/science.1248905](https://doi.org/10.1126/science.1248905).

- [90] Johannes Zeiher, Peter Schauß, Sebastian Hild, Tommaso Macrì, Immanuel Bloch, and Christian Gross. "Microscopic Characterization of Scalable Coherent Rydberg Superatoms". In: *Physical Review X* 5.3 (2015), p. 031015. doi: [10.1103/PhysRevX.5.031015](https://doi.org/10.1103/PhysRevX.5.031015).
- [91] C. T. Lee. "Q representation of the atomic coherent states and the origin of fluctuations in superfluorescence". In: *Physical Review A* 30.6 (1984), pp. 3308–3310. doi: [10.1103/PhysRevA.30.3308](https://doi.org/10.1103/PhysRevA.30.3308).
- [92] Marcel Bergmann and Otfried Gühne. "Entanglement criteria for Dicke states". In: *Journal of Physics A: Mathematical and Theoretical* 46.38 (2013). doi: [10.1088/1751-8113/46/38/385304](https://doi.org/10.1088/1751-8113/46/38/385304).
- [93] T. Amthor, M. Reetz-Lamour, S. Westermann, J. Denskat, and M. Weidemüller. "Mechanical effect of van der waals interactions observed in real time in an ultracold rydberg gas". In: *Physical Review Letters* 98.2 (2007), pp. 1–4. doi: [10.1103/PhysRevLett.98.023004](https://doi.org/10.1103/PhysRevLett.98.023004).
- [94] Wenhui Li, Paul J. Tanner, and T. F. Gallagher. "Dipole-Dipole Excitation and Ionization in an Ultracold Gas of Rydberg Atoms". In: *Physical Review Letters* 94.17 (2005), p. 173001. doi: [10.1103/PhysRevLett.94.173001](https://doi.org/10.1103/PhysRevLett.94.173001).
- [95] M. P. Robinson, B. Laburthe Tolra, Michael W. Noel, T. F. Gallagher, and P. Pillet. "Spontaneous Evolution of Rydberg Atoms into an Ultracold Plasma". In: *Physical Review Letters* 85.21 (2000), pp. 4466–4469. doi: [10.1103/PhysRevLett.85.4466](https://doi.org/10.1103/PhysRevLett.85.4466).
- [96] W. Li, P. J. Tanner, Y. Jamil, and T. F. Gallagher. "Ionization and plasma formation in high n cold Rydberg samples". In: *European Physical Journal D* 40.1 (2006), pp. 27–35. doi: [10.1140/epjd/e2006-00189-8](https://doi.org/10.1140/epjd/e2006-00189-8).
- [97] E. A. Goldschmidt, T. Boulier, R. C. Brown, S. B. Koller, J. T. Young, A. V. Gorshkov, S. L. Rolston, and J. V. Porto. "Anomalous Broadening in Driven Dissipative Rydberg Systems". In: *Physical Review Letters* 116.11 (2016), pp. 1–5. doi: [10.1103/PhysRevLett.116.113001](https://doi.org/10.1103/PhysRevLett.116.113001).

- [98] T. Boulier, E. Magnan, C. Bracamontes, J. Maslek, E. A. Goldschmidt, J. T. Young, A. V. Gorshkov, S. L. Rolston, and J. V. Porto. "Spontaneous avalanche dephasing in large Rydberg ensembles". In: *Physical Review A* 96.5 (2017), pp. 1–11. doi: [10.1103/PhysRevA.96.053409](https://doi.org/10.1103/PhysRevA.96.053409).
- [99] E. Urban, T. a. Johnson, T. Henage, L. Isenhower, D. D. Yavuz, T. G. Walker, and M. Saffman. "Observation of Rydberg blockade between two atoms". In: *Nature Physics* 5.2 (2009), pp. 110–114. doi: [10.1038/nphys1178](https://doi.org/10.1038/nphys1178).
- [100] K. M. Maller, M. T. Lichtman, T. Xia, Y. Sun, M. J. Piotrowicz, A. W. Carr, L. Isenhower, and M. Saffman. "Rydberg-blockade controlled-not gate and entanglement in a two-dimensional array of neutral-atom qubits". In: *Physical Review A* 92.2 (2015), p. 022336. doi: [10.1103/PhysRevA.92.022336](https://doi.org/10.1103/PhysRevA.92.022336).
- [101] Minho Kwon, Matthew F. Ebert, Thad G. Walker, and M. Saffman. "Parallel Low-Loss Measurement of Multiple Atomic Qubits". In: *Physical Review Letters* 119.18 (2017), pp. 1–5. doi: [10.1103/PhysRevLett.119.180504](https://doi.org/10.1103/PhysRevLett.119.180504).
- [102] A. H. Myerson, D. J. Szwer, S. C. Webster, D. T C Allcock, M. J. Curtis, G. Imreh, J. A. Sherman, D. N. Stacey, A. M. Steane, and D. M. Lucas. "High-Fidelity Readout of Trapped-Ion Qubits". In: *Physical Review Letters* 100.20 (2008), p. 200502. doi: [10.1103/PhysRevLett.100.200502](https://doi.org/10.1103/PhysRevLett.100.200502).
- [103] H HAFFNER, C ROOS, and R BLATT. "Quantum computing with trapped ions". In: *Physics Reports* 469.4 (2008), pp. 155–203. doi: [10.1016/j.physrep.2008.09.003](https://doi.org/10.1016/j.physrep.2008.09.003).
- [104] A. Fuhrmanek, R. Bourgain, Y. R. P. Sortais, and A. Browaeys. "Free-Space Lossless State Detection of a Single Trapped Atom". In: *Physical Review Letters* 106.13 (2011), p. 133003. doi: [10.1103/PhysRevLett.106.133003](https://doi.org/10.1103/PhysRevLett.106.133003).
- [105] Michael J. Gibbons, Christopher D. Hamley, Chung-Yu Shih, and Michael S. Chapman. "Nondestructive Fluorescent State Detection of Single Neutral Atom Qubits". In: *Physical Review Letters* 106.13 (2011), p. 133002. doi: [10.1103/PhysRevLett.106.133002](https://doi.org/10.1103/PhysRevLett.106.133002).

- [106] Y.-Y. Jau, A. M. Hankin, T. Keating, I. H. Deutsch, and G. W. Biedermann. "Entangling atomic spins with a Rydberg-dressed spin-flip blockade". In: *Nature Physics* October (2015), pp. 8–11. doi: [10.1038/nphys3487](https://doi.org/10.1038/nphys3487).
- [107] J. Bochmann, M. Mücke, C. Guhl, S. Ritter, G. Rempe, and D. L. Moehring. "Lossless State Detection of Single Neutral Atoms". In: *Physical Review Letters* 104.20 (2010), p. 203601. doi: [10.1103/PhysRevLett.104.203601](https://doi.org/10.1103/PhysRevLett.104.203601).
- [108] I. I. Beterov and M. Saffman. "Rydberg blockade, Förster resonances, and quantum state measurements with different atomic species". In: *Physical Review A - Atomic, Molecular, and Optical Physics* 92.4 (2015), pp. 1–10. doi: [10.1103/PhysRevA.92.042710](https://doi.org/10.1103/PhysRevA.92.042710).
- [109] M. Martinez-Dorantes, W. Alt, J. Gallego, S. Ghosh, L. Ratschbacher, and D. Meschede. "State-dependent fluorescence of neutral atoms in optical potentials". In: *Physical Review A* 97.2 (2018), p. 023410. doi: [10.1103/PhysRevA.97.023410](https://doi.org/10.1103/PhysRevA.97.023410).
- [110] Minho Kwon, Matthew F. Ebert, Thad G. Walker, and M. Saffman. "Supplementary Material for Parallel low-loss measurement of multiple atomic qubits". In: *Physical Review Letters* 119.18 (2017), pp. 1–8. doi: [10.1103/PhysRevLett.119.180504](https://doi.org/10.1103/PhysRevLett.119.180504).
- [111] D. J. Wineland and Wayne M. Itano. "Laser cooling of atoms". In: *Physical Review A* 20.4 (1979), pp. 1521–1540. doi: [10.1103/PhysRevA.20.1521](https://doi.org/10.1103/PhysRevA.20.1521).
- [112] M. J. Piotrowicz, M. Lichtman, K. Maller, G. Li, S. Zhang, L. Isenhower, and M. Saffman. "Two-dimensional lattice of blue-detuned atom traps using a projected Gaussian beam array". In: *Physical Review A - Atomic, Molecular, and Optical Physics* 88.1 (2013). doi: [10.1103/PhysRevA.88.013420](https://doi.org/10.1103/PhysRevA.88.013420).
- [113] Y. Wang, A. Kumar, T.-Y. Wu, and D. S. Weiss. "Single-qubit gates based on targeted phase shifts in a 3D neutral atom array". In: *Science* 352.6293 (2016), pp. 1562–1565. doi: [10.1126/science.aaf2581](https://doi.org/10.1126/science.aaf2581).

- [114] H. G. Berry, G. Gabrielse, and A. E. Livingston. "Measurement of the Stokes parameters of light". In: *Applied Optics* 16.12 (1977), p. 3200. doi: [10.1364/AO.16.003200](https://doi.org/10.1364/AO.16.003200).
- [115] Miguel Martínez Dorantes. "Fast non-destructive internal state detection of neutral atoms in optical potentials". PhD thesis. 2016.
- [116] Daniel Adam Steck. *Rubidium 87 D Line Data*. 2001.
- [117] William H. Carter. "Focal shift and concept of effective Fresnel number for a Gaussian laser beam". In: *Applied Optics* 21.11 (1982), p. 1989. doi: [10.1364/AO.21.001989](https://doi.org/10.1364/AO.21.001989).
- [118] Fire Retardant and Microwave Absorber. *Eccosorb* ® QR-13AF. URL: <https://assets.lairdtech.com/home/brandworld/files/DSEccosorbQR-13AF.pdf>.
- [119] Yu Peng. "A Novel Scheme for Hundred-Hertz Linewidth Measurements with the Self-Heterodyne Method". In: *Chinese Physics Letters* 30.8 (2013), p. 084208. doi: [10.1088/0256-307X/30/8/084208](https://doi.org/10.1088/0256-307X/30/8/084208).